MARIELLE DE OLIVEIRA

NUMERICAL MODELING AND SIMULATION OF HORIZONTAL AXIS OFFSHORE WIND TURBINES

São Paulo
2023

MARIELLE DE OLIVEIRA

Versão Corrigida

Modelagem e Simulação Numérica de Turbinas Eólicas de Eixo Horizontal Offshore

Tese apresentada à Escola Politécnica da Universidade de São Paulo para obtenção do título de Doutor em Ciências

São Paulo
2023

MARIELLE DE OLIVEIRA

NUMERICAL MODELING AND SIMULATION OF HORIZONTAL AXIS OFFSHORE WIND TURBINES

Thesis presented to Escola Politécnica da Universidade de São Paulo in partial fulfillment of the requirements for the Doctor of Philosophy Degree

Concentration Area:

Energy and Fluids.

Supervisor:

Dr. Bruno Souza Carmo

São Paulo
2023

Este exemplar foi revisado e corrigido em relação à versão original, sob responsabilidade única do autor e com a anuência de seu orientador.

São Paulo, 12 de maio de 2023

Assinatura do autor: 

Assinatura do orientador: 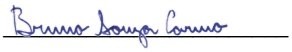

Catalogação-na-publicação

de Oliveira, Marielle
Numerical Modeling and Simulation of Horizontal Axis Offshore Wind Turbines / M. de Oliveira -- versão corr. -- São Paulo, 2023.
156 p.

Tese (Doutorado) - Escola Politécnica da Universidade de São Paulo. Departamento de Engenharia Mecânica.

1.Offshore Wind Turbines 2.Computational Fluid Dynamics 3.Blade resolved Simulations 4.NREL 5 MW & IEA 15 MW 5.Numerical Schemes and Solver Investigations I.Universidade de São Paulo. Escola Politécnica. Departamento de Engenharia Mecânica II.t.

I dedicate this thesis to my beloved Vó Mira (in memoriam), for having taught me always to have faith and follow my dreams.

ACKNOWLEDGMENTS

First and foremost, I thank God Almighty for enlightening me through this opportunity and granting me the capability to proceed successfully in this journey.

I would like to thank my supervisor, Professor Bruno Souza Carmo, who invited me to this field of research and whom I greatly admire as a researcher and person. Professor Bruno's knowledge, support, guidance, and opportunities to participate in different research groups helped me overcome the challenges during my Ph.D. program and improve my skills as a researcher. Special gratitude goes out to all the members of the NDF laboratory from the Mechanical Engineering department of The University of Sao Paulo, where I had the pleasure to work since 2018. These colleagues and friends were fundamental in so many ways for my achievements and personal development.

A huge thanks to my papers' coauthors for sharing their knowledge and contributing to this thesis, Professor Fábio Saltara, Professor Rodolfo T. Gonçalves, Dr. Leandro S. P. da Silva and specially to the best friend and co-worker I could have, Rodolfo C. Puraca.

Last but not least, I would like to acknowledge CAPES, the Coordination for the Improvement of Higher Education Personnel, for supporting my research at The University of Tokyo, under Process number '88887.307600/2018-00', and to FAPESP, the São Paulo Research Foundation, for supporting my PhD program under Process number '2018/26207-4'. I would also like to acknowledge the SDumont and NextGenIO supercomputers for providing me with the necessary computational resources to conduct the CFD simulations presented in this thesis. Additionally, I am grateful to the University of São Paulo for providing me access to its infrastructure and for the kind support from its team of Professors and collaborators.

This work is dedicated to God and to all the people who always supported me, in special my mother Maristela, my father Marco, my brother Marcos, my aunts Maria de Fátima, Léia, Wandeca, and to my beloved Felipe F. De Carli. Their unwavering support encouraged me to walk through this challenging journey.

"... E o rapaz mergulhou na Alma do Mundo, e viu que a Alma do Mundo era a parte da Alma de Deus, e viu que a Alma de Deus era a sua própria alma. E que podia, então, realizar milagres."

-- Paulo Coelho

RESUMO

À medida que a demanda global de energia aumenta, resultando em preocupações com poluição ambiental e crises energéticas, o uso de fontes renováveis de energia tem sido incentivado para reduzir os impactos causados pelo uso de combustíveis fósseis. Entre as fontes renováveis, a energia eólica offshore é uma solução promissora para contribuir para o fornecimento de energia devido a vários benefícios, incluindo velocidades do vento mais altas e consistentes em comparação com locais em terra. Turbinas eólicas offshore são normalmente maiores do que turbinas onshore, e para melhorar a eficiência e confiabilidade destes grandes equipamentos, simulações numéricas se tornaram uma ferramenta essencial para prever o comportamento aerodinâmico da turbina eólica em escala real sob diferentes condições de vento, devido às limitações dos testes experimentais em representar as condições de operação do sistema.

Desde a primeira simulação de alta resolução dos escoamento ao redor das pás de uma turbina eólica, diversas pesquisas considerando diferentes metodologias numéricas têm sido realizadas para compreender os efeitos aerodinâmicos tridimensionais transientes nas pás do rotor. A adequação de cada método numérico é determinada com base no objetivo específico de cada análise. Para investigar a geometria completa da turbina eólica, incluindo uma alta resolução da geometria das pás simulações que resolvem o escoamento ao redor das pás da turbina são cruciais para aprimorar a capacidade de prever a aerodinâmica da turbina eólica. Embora a metodologia de dinâmica dos fluidos computacional (CFD) tenha sido comprovada como eficaz para avaliar o comportamento aerodinâmico transiente do escoamento ao redor das pás da turbina eólica, bem como a geração de vórtices que formam a sua esteira, apenas algumas investigações usando tal método consideraram a geometria da turbina eólica em seu tamanho real de protótipo em escala de megawatts, devido à complexidade da simulação numérica e dos recursos computacionais necessários. Portanto, para maximizar a confiabilidade da metodologia de CFD como ferramenta no desenvolvimento de turbinas eólicas offshore, esta tese fornece uma base sólida sobre o impacto substancial dos métodos numéricos considerados no setup das simulações na precisão dos resultados obtidos e nos custos computacionais associados. As análises foram feitas para duas turbinas eólicas teóricas para aplicações offshore, a NREL 5 MW e a IEA 15 MW.

Palavras-Chave – Turbina Eólica Offshore. Dinâmica dos Fluidos Computacional. Simulações-resolvidas ao Redor das Pás. NREL 5 MW. IEA 15 MW. Investigações de Solver e Esquemas Numéricos.

ABSTRACT

As global energy demand continues to increase, resulting in concerns over environmental pollution and energy crises, the use of renewable energy sources of energy has been encouraged to reduce the impacts caused by the use of fossil fuels. Among the renewable sources, offshore wind energy is a promising solution to contribute to energy supply due to several benefits, including higher and more consistent wind speeds compared to onshore locations. Offshore wind turbines are typically larger than onshore turbines, and to improve the efficiency and reliability of these large machines, numerical simulations have become an essential tool to predict the aerodynamic behavior of the full-scale wind turbine under different wind conditions, due to the limitations of experimental tests in representing the operating conditions of the system.

Since the first high-resolution simulation of the flow around the wind turbine blades, extensive research considering different numerical methodologies have been conducted to understand the transient three-dimensional aerodynamic effects on the rotor blades. The suitability of each numerical method is determined based on the specific objectives of each analysis. To investigate the complete geometry of the wind turbine, including a high resolution of the blade geometry, simulations that resolve the flow around the turbine blades are crucial to enhance the ability to predict the wind turbine aerodynamics. Although the computational fluid dynamics (CFD) methodology has been proven effective in evaluating the transient aerodynamic behavior of the flow around wind turbine blades and generated wakes, only a few investigations using such method have considered the geometry of the full-scale prototype wind turbine in megawatt scale, due to the complexity of the numerical simulations and computational resources required. Therefore, to maximize the reliability of CFD methodology as a tool in offshore wind turbine development, this thesis provides a solid basis on the substantial impact of the numerical methods considered in the simulation setup on the accuracy of the results of the simulations and the associated computational costs. The analyses were conducted for two theoretical offshore wind turbines, the NREL 5 MW and IEA 15 MW.

Keywords – Offshore Wind Turbines. Computational Fluid Dynamics. Blade-resolved Simulations. NREL 5 MW. IEA 15 MW. Numerical Schemes and Solver Investigations.

LIST OF FIGURES

LIST OF TABLES

NOMENCLATURE

AMI	Arbitrary Mesh Interface
BEM	Blade Element Momentum
BNEF	BloombergNEF
CFD	Computational Fluid Dynamics
CFL	Courant-Friedrichs-Lewy
CL	Linear Interpolation
DES	Detached Eddy Simulation
DILU	Simplified Diagonal-based Incomplete LU preconditioner
DTU	Technical University of Denmark
FOWT	Floating Offshore Wind Turbine
FVM	Finite Volume Method
GAMG	Geometric-Algebraic Multi-Grid
GWEC	Global Wind Energy Council
HPC	High Performance Computing
IBAMA	Brazilian Institute of Environment and Renewable Natural Resources
IEA	International Energy Agency
INPE	National Institute for Space Research
IRENA	International Renewable Energy Agency
LES	LES Large Eddy Simulation
LUD	Linear-Upwind Differencing
LUST	LUST Linear-Upwind Stabilised Transport

N-S	Navier-Stokes
NASA	National Aeronautics and Space Administration
NREL	National Renewable Energy Laboratory
OWT	Offshore Wind Turbine
PBiCG	Preconditioned Bi-Conjugate Gradient
PISO	Pressure Implicit Split Operator
PPA	Power Purchase Agreement
SIMPLEC	Semi-Implicit Method for Pressure-Linked Equations Consistent
SIMPLE	Semi-Implicit Method for Pressure-Linked Equations
SST	Shear Stress Transport
UDS	Upwind Discretization Schemes
UMaine	University of Maine
URANS	Unsteady Reynolds-Average Navier-Stokes
WWEA	World Wind Energy Association

CONTENTS

PART I

INTRODUCTION

1 INTRODUCTION

Global energy demand constantly increases, resulting in environmental pollution and energy crisis concerns. In response, the use of renewable sources of energy has been encouraged to reduce the climate change impacts caused by the use of fossil fuels as sources of energy. There are several sources of renewable energy, such as hydropower, wind, ocean, solar and geothermal. Their exploitation can offer a significant amount of clean Energy and contribute to the green global energy transition. By the end of 2020, the global electricity matrix was composed of 29% of renewable Energy against 70% of fossil fuel-powered energy [1]. Additionally, by the end of 2021, the International Renewable Energy Agency (IRENA) reported a total global renewable energy generation capacity of 3,064 GW, an increase of over 256 GW in power capacity from renewable sources, with 94 GW coming from wind. Therefore, wind energy became one of the most cost-effective and viable alternatives to traditional energy production methods, representing at the beginning of 2022, a total of 850 GW of electric power from wind farms worldwide and a record in the offshore wind history with 21.1 GW of new installations, bringing the total of offshore wind capacity to 57.2 GB [2,3]. According to the Global Wind Energy Council (GWEC), it is expected that by the middle of 2023, wind energy will reach a noteworthy milestone on a global scale of 1 TW of installed capacity [4].

Prior to the numerical aspects of the offshore wind turbine investigations covered in this thesis, this chapter gives a general introduction to wind power development around the globe and the Brazilian perspective on the offshore wind market to highlight the motivation and main objectives of this work.

1.1 Wind Energy Development

The offshore environment holds a huge potential to contribute to the global energy supply and its exploitation has been supported by several institutions. The main sources of offshore renewable Energy include wind, wave, tidal and salinity gradient [5]. In order

to harvest these energies, offshore energy structures such as wave energy converters, ocean current/tidal turbines, and offshore wind turbines are being explored. These technologies are thriving due to the support of international collaborations as well as scientific and industrial communities. In this regard, IRENA is the first international, intergovernmental organization to focus exclusively on renewable Energy for both industrialized and developing countries [6]. Representing the wind power sector worldwide, the World Wind Energy Association (WWEA) has members in more than 100 countries. This non-profit association is dedicated to promoting the deployment of wind energy technology and supporting a future energy system based on the installation of wind turbines all over the planet, including offshore locations.

In Europe, from 1993 to 1999, the growth rate in the wind power industry was about 40% per year. By the end of 2000, around 17 GW of the world's electricity demand was generated by wind turbines operating in more than 50 countries. Of these, about 70% were installed in Europe. Denmark, Germany, and Spain were the lead countries, responsible for more than 80% of the European total wind power capacity [7].

Since 2008, the wind power progress has doubled, reaching a cumulative installed capacity of 300 GW [5]. In 2014 the policy support provided significant growth in the wind power sector, which was responsible for 2.5% of the global electricity demand, up to 18% in Spain, 20% in Portugal, and 30% in Denmark.

In 2014, the installed wind power was led by China with 75 GW, the USA with 60 GW, and Germany with 31 GW. Thus, statistics provided by GWEC indicated that 3% of the global electricity was generated from wind in 2016, and that number was rising.

According to the GWEC report [8], in 2017, the new wind power installations surpassed 50 GW, and the offshore sector had a record year of 4,3 GW of new installations, an increase of about 87% compared to the 2016 market, reaching a global installation of 18.8 GW, which represented 30% increase in the cumulative offshore capacity. In that year, the offshore segment represented about 8% of the global annual market and about 3.5% of the cumulative installed capacity, denoting advanced growth. Beyond the statistics, wind power was becoming a fully commercialized, unsubsidized technology.

As can be seen in Fig. 1.1, the new wind power plants that started operating in 2022 amassed 77.6 GW, resulting in a cumulative of 906 GW and a year-on-year growth of 9%. Additionally, 8.8 GW of new offshore wind capacity was connected to the power grids, bringing a total of 64.3 GW of offshore wind power installed [4].

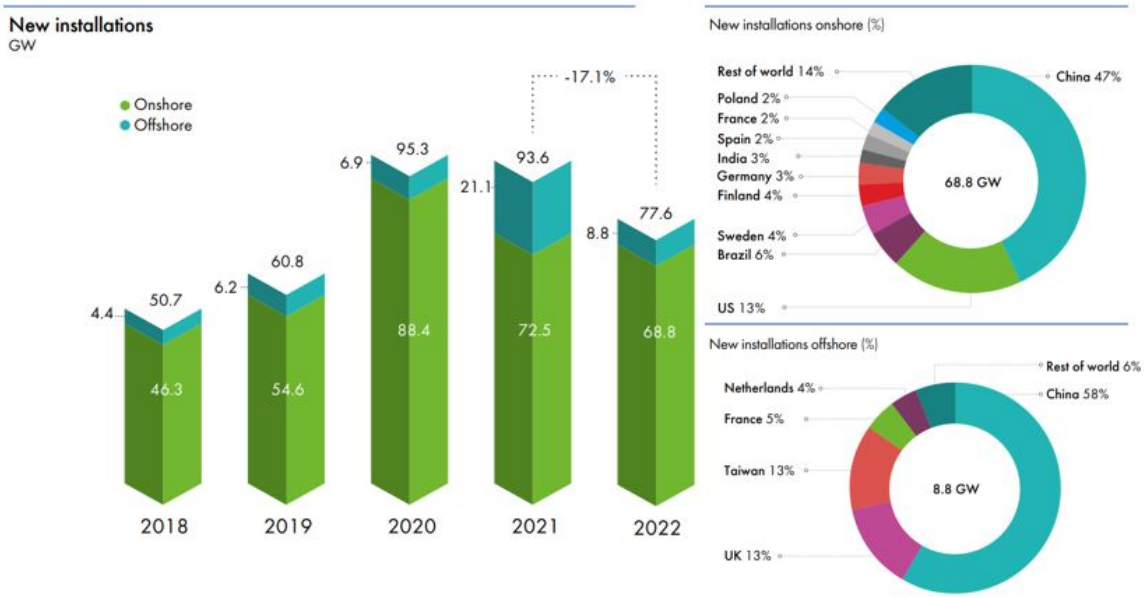

Figure 1.1: Global overview of new wind power installations grid-connected from 2018 until the end of 2022, adapted from GWEC [4].

Until 2026, the International Energy Agency (IEA) expects that more than 500 GW of new wind energy capacity will be installed, with a significant contribution from offshore wind energy. Additionally, GWEC forecasts that more than 90 GW will be added worldwide by 2026 [4]. Even though wind energy has taken about 33 years to reach 1 TW, according to BloombergNEF (BNEF), considering the offshore installations, the wind market will deliver another TW by 2030. Additionally, the UN Energy Compact signed by GWEC and IRENA, which aims to deploy the 2,000 GW of offshore wind to reach the net-zero target by 2050, also highlights the strong potential of the offshore wind market to promote economic development and enhancing the security of energy supply.

Therefore, from a global perspective, it is noticed that wind energy has developed into a mainstream source of electricity due to its technological potential that is expanding to the offshore sector and offers a real alternative to facilitate the transition to a more sustainable energy matrix across the globe.

1.1.1 The Brazilian Wind Market

Three decades ago, the installation of a 75 kW wind turbine on the island of Fernando de Noronha in the Northeast region of Brazil marked the beginning of the wind market in the country [9]. The first commercial wind plant in Brazil, Taíba Wind Station, was set up in 1999 in the State of Ceará, at Prainha with an installed capacity of 5 MW. The

Taíba wind park was composed of 10 Wobben-Enercon 500 kW wind turbines, with rotors of 40 meters diameter each and 45 meters of hub height. However, nowadays, with the operational height around 70 meters, the wind energy potential in the State of Ceará has increased to 24 GW, which allows an annual generation of 51.9 TWh/year [10].

In 2003, the Brazilian electric power grid, generation, and transmission predominantly belonged to the state. Besides that, there was a supremacy of hydropower plants, which represented about 91.4% of the installed power capacity. Due to the challenges for the national electricity demand in times of dry season, such as the power supply crisis in 2001, the exploitation of renewable resources has been intensified.

According to the GWEC, in 2018, Brazil represented 4% of the global onshore new installations, approximately 1,939 MW of installed wind capacity, which represented 3% of the global onshore energy production [11]. To date, the continuous growth of wind energy in Brazil has placed the country in 2022 the third position among the world's top five markets for new installations. Brazil also has the 6^{th} largest installed wind power capacity in the world [4]. Currently, wind energy ranks in the second position among Brazil's main energy resources, with a total of about 25 GW of installed capacity. This represents the supply to more than 30 million homes per month, considering only onshore installations [3, 4].

Besides the significant onshore potential in Brazil, the wind market is expanding to offshore sites where the wind resource is stronger, more consistent, and with less turbulence compared to onshore installations [5]. In this regard, as can be seen in Fig. 1.2, in March of 2023, the Brazilian Institute of Environment and Renewable Natural Resources (IBAMA) released the federal environmental licensing of offshore wind complexes, which has resulted in about 70 new projects being processed from different companies with a cumulative power capacity of approximately 180 GW [12, 13]. According to the licensing projects under development, the offshore wind farms will take place on the Brazilian coast in the northeast, southeast, and south regions, as illustrated in Fig. 1.2.

Also, the National Institute for Space Research (INPE) reported that the wind power capacity along the coast is around ten times higher than the onshore capacity, reaching 3,500 GW [14]. Moreover, the measurements from the National Aeronautics and Space Administration (NASA) satellites and data provided by Petrobras estimated the Brazilian offshore wind potential in the Southeast areas of 215 GW up to 100 m water depths [15], and 102 GW up to 50 m from the coast [14].

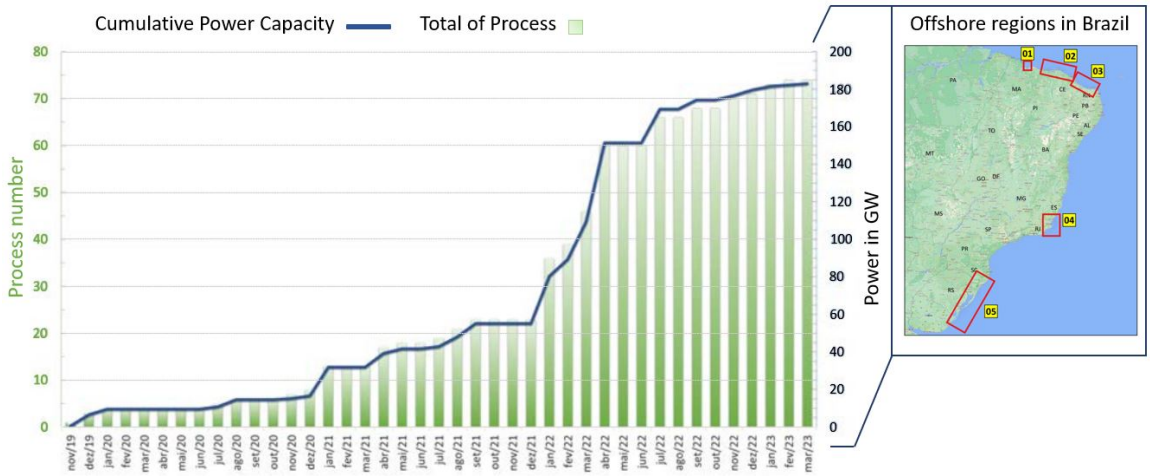

Figure 1.2: The Brazilian evolution of licensing demand for the upcoming offshore projects until March of 2023, adapted from IBAMA [13].

There are several configurations of Offshore Wind Turbines (OWT) foundations and platforms that are required to support the wind turbines, whereof these configurations vary mainly with the water depth. The most mature technology for offshore installations is the bottom-mounted foundation, which is required for shallow areas that are about 20 km from the coast and up to 60 m depth [16]. In 2016, among the offshore installations worldwide, 78.8% were composed of monopiles, 10.4% by gravity structures, 4.7% by jackets, and 4.1% by tripods [17]. However, as the costs of bottom-mounted structures increase significantly with the water depth, these concepts are restricted to shallow and transitional waters. Consequently, floating platforms have been investigated due to their applicability to deeper sea locations. Furthermore, as the offshore wind energy potential considerably increases in areas far from the coast, a substantial rise in the size of commercial wind turbines due to economy of scale is noticed, indicating that offshore wind energy will expand into deeper water applications. As a result, stronger development of floating offshore wind farms is expected in the near future [4, 18]. More detailed information about the offshore projects that illustrate the expansion of the Brazilian wind market to offshore installations, as presented in Fig. 1.2, can be found in the IBAMA map of projects under licensing process [13]. For instance, as the distance from the coast vary among the offshore projects that are going to be implemented in Brazil, it is expected that different concepts of foundations, including the floating platforms, will be required in the coming years to attend the offshore wind energy (OWE) industry requirements.

In this regard, as commercial wind turbines for offshore applications continue to increase in power capacity, such as SG 8 MW, Vestas 9.5 MW, and GE 14 MW [19–21], performing experimental tests during the design phase of such complex system, has become

increasingly difficult. As a result, high-fidelity Computational Fluid Dynamics (CFD) numerical models represent a valuable alternative to predict the flow characteristics of such complex systems by allowing the full-scale geometry in the numerical simulations. In addition, simpler numerical models, which require calibration, can also benefit from the results from high-fidelity computational analysis [22,23]. However, although CFD has been proven to be effective in examining the unsteady aerodynamic behavior of the flow around wind turbine blades and generated wakes, only a few investigations using such a method considered the wind turbine geometry in its full size of a megawatt-scale due to the complexity of the numerical simulation, and computational resources required [23,24].

Therefore, in this work, a CFD methodology is developed to predict the performance of the new generation of horizontal-axis offshore wind turbines, such as NREL 5 MW and IEA 15 MW, considering its geometry at full scale. However, in addition to predicting the wind turbine performance, including its aerodynamic loads and wake pattern, a detailed investigation regarding the influence of the solver in the results from the simulations is carried out to help cover the lack of information regarding these issues in the literature. In this regard, among the numerical arrangement parameters investigated are different spatial and temporal discretization strategies, the pressure-velocity coupling problem, different turbulence models, and different discretization schemes for the convective term.

1.2 Objectives and Research Contributions

As explained in the previous section, from the perspective of designing large wind turbines used for offshore applications, as the use of reduced-scale models and experimental testing may not accurately represent the physics of the full-scale prototype, numerical simulations in which the wind turbine is considered in its full-scale have become a valuable tool in the design process. In this regard, a real challenging task is associated with predicting the wind turbine performance and flow behavior around its blades for a certain operating condition, considering a high-fidelity numerical model where the solver parameters are evaluated to increase the accuracy of the simulation results.

Therefore, the primary goal of this work is to develop a robust CFD methodology to fully represent the fluid forces acting on the wind turbine and accurately predict its performance, including the evaluation of the aerodynamic loads with a high resolution of the flow features on the blades, and performing a detailed study of the influence of the numerical solver on the accuracy of the results and the computational costs associated.

Thus, the following objectives are part of the scope of this work:

1. To develop a high-fidelity numerical model based on a CFD methodology to predict the flow behavior and energy production of large horizontal-axis wind turbines used in offshore applications using open-source software;

2. To investigate different solver configurations to identify the most suitable numerical arrangement regarding temporal and spatial discretization strategies, considering a High-Performance Computing (HPC) environment;

3. To investigate the influence of different turbulence models in the accuracy of the results, considering different spatial and temporal discretization strategies to predict the aerodynamic forces and computational demand associated;

4. To evaluate the effect of different numerical schemes, such as pressure-velocity coupling algorithm and discretization schemes for the convective term, in the accuracy of the results and computational costs;

1.3 Scope and Structure of the Thesis

This thesis is composed of four main parts and contains the most relevant manuscripts that have been published or are currently under review for publication in international journals. Additional work relevant to the thesis is given in Appendices A.

- **Part I: Introduction - Chapter 1**, provides a literature overview of the global wind market, including the offshore scenario, and presents a general review of the historical development of the wind energy in Brazil including the future development of the offshore wind power in the country. The main objectives and contributions of the present study are also outlined, along with a list of publications.

- **Part II: Background Theory** deals with the description of wind energy technology, its physical aspects related to offshore installations, and the numerical methods that can be used to represent the problem.

  - **Chapter 2** describes the general aspects of the wind resources considered for modeling the offshore site of operation, as well as an explanation regarding the horizontal-axis wind turbines aerodynamics and the types of OWT concepts, which are related to the wind turbines investigated in this work.

  - **Chapter 3** provides a literature overview about the numerical methods that can be used to investigate the problem and emphasizes the importance of using a CFD approach to account for three-dimensional flow in the model.
  - **Chapter 4** describes the CFD methodology developed in this study, providing a detailed explanation of the Finite Volume Method (FVM) with respect to the pre-processing, solver, and post-processing stages of the simulations. Lastly, it presents the governing equations and discusses the numerical methods considered to evaluate the effect of the simulation's numerical arrangement on the accuracy of the results and computational costs.

- **Part III: Blade-resolved CFD Investigations**, illustrates all the blade-resolved investigations employed to evaluate the performance of two baseline wind turbines for offshore applications, the NREL 5 MW and the IEA 15 MW, considering the influence of the simulation's setup on the accuracy of the obtained results and computational demand required.

  - **Chapter 5** introduces a full explanation with respect to the solver configuration and its influence on the accuracy of the results and computational costs of blade-resolved simulations employed in the CFD methodology used to evaluate the performance of the NREL 5 MW considering the influence of the tower.
  - **Chapter 6** presents a study of the influence of the numerical scheme for the discretization of the convective term and different turbulence models on the accuracy of blade-resolved simulations employed to evaluate the performance of the NREL 5 MW considering rotor-only simulations.
  - **Chapter 7** presents the simulation results related to the numerical investigations carried out for the IEA 15 MW wind turbine for offshore application. Results for rotor-only simulations and considering the tower are presented along with the CFD methodology employed in each case.

- **Part IV: Concluding Remarks - Chapter 8,** summarizes the findings and main contributions of this thesis, along with the suggestions for future works whereof the methodology developed in this work can be useful.

1.3.1 List of publications included as part of the thesis

1. **DE OLIVEIRA, Marielle**; PURACA, Rodolfo Curci; CARMO, Bruno Souza. "A study on the influence of the numerical scheme on the accuracy of blade-resolved

simulations employed to evaluate the performance of the NREL 5 MW wind turbine rotor in full scale". *Energy*, v. 283, p. 128394, 2023.

2. **DE OLIVEIRA, Marielle**; PURACA, Rodolfo Curci; CARMO, Bruno Souza. "Blade-resolved numerical simulations of the NREL offshore 5 MW baseline wind turbine in full scale: A study of proper solver configuration and discretization strategies". *Energy*, v. 254, p. 124368, 2022.

3. **DE OLIVEIRA, Marielle**; PURACA, Rodolfo Curci; CARMO, Bruno Souza. "Assessment of turbulence models for the simulation of the flow through a megawatt-scale wind turbine rotor." *Proceedings of the EPTT 2022 13th Spring School on Transition and Turbulence, (EPTT2022)*, Blumenau, SC, Brazil, pp. 1-11.

4. **DE OLIVEIRA, Marielle**; DA SILVA, Leandro; PURACA, Rodolfo Curci; CARMO, Bruno Souza. "CFD investigation of the IEA offshore 15 MW reference wind turbine performance in full scale: A temporal discretization analysis". *Proceedings of the ASME 2023 International Conference on Ocean, & Offshore and Artic Engineering, (OMAE2023)*, Melbourne, Australia, pp. 1-12. (Accepted)

1.3.2 Additional publications during the Ph.D. candidature

1. DA SILVA, Leandro; **DE OLIVEIRA, Marielle**; CAZZOLATO, Benjamin; SERGIIENKO, Natalia; AMARAL, Giovanni; DING, Boyin. (2022). "Statistical linearisation of a nonlinear floating offshore wind turbine under random waves and winds." *Ocean Engineering 261*, pp. 1-15.

2. **DE OLIVEIRA, Marielle**; DA SILVA, Leandro; SALTARA, Fabio; GONÇALVES, Rodolfo Trentin, CARMO, Bruno Souza. "Temporal discretization investigation of the unsteady loading on an infinitely long cylinder in high Reynolds numbers using DES." *Proceedings of the ASME 2023 International Conference on Ocean, & Offshore and Artic Engineering, (OMAE2023)*, Melbourne, Australia, pp. 1-10.

3. DA SILVA, Leandro; SERGIIENKO, Natalia; , CAZZOLATO, Benjamin; MENG, F.; **DE OLIVEIRA, Marielle**.; DING, Boyin. (2023). "Motion suppression of a floating offshore wind turbine using heaving point absorbers: A case study in Australia." *Proceedings of the ASME 2023 International Conference on Ocean, & Offshore and Artic Engineering (OMAE2023)*, Melbourne, Australia pp. 1-11.

PART II

BACKGROUND THEORY

2 OFFSHORE WIND ENERGY: AN OVERVIEW OF GENERAL ASPECTS

The main objective of this chapter is to present the mechanical aspects of horizontal-axis wind turbines, including the basic understanding related to the transformation of the kinetic energy from the wind into mechanical shaft power, which drives a generator to produce electric power. Firstly, the analysis of the wind resources and the main characteristics of the technology are presented. Then, the actuator disc theory is used to understand the physics of the system necessary to model the problem and evaluate its performance. Lastly, the main OWT concepts are presented, along with a review of the numerical investigations considered to study the problem, whose needs motivated the analyzes presented in this thesis.

2.1 Wind Resource

The understanding of the wind resource is an important topic since the energy available in the wind is proportional to the cube of the wind speed. Thus, the identification of suitable sites and prediction of the viability of wind farms is the first stage of a wind energy project. The main issue related to the wind resource is the variability of the resource, which is intense over a significant range of scales in space and time [25]. For a given location, spatial variability describes the influence of the site's environment, while temporal variability, from a large-scale point of view, is related to how the wind speed may vary from one year to another.

According to Kelly [26], the main atmospheric parameters used by the numerical codes to calculate the wind turbine loads are the mean wind speed, the shear exponent, and the characteristic length scale of the turbulent eddies with the highest levels of energy. Amongst the conventional industrial wind measurements, the turbulence length scale parameter is difficult to measure. Thus, an understanding of the wind characteristics is required to identify a model that can represent this parameter accurately.

2.1.1 Turbulence

Amongst the environmental aspects that can affect wind turbine performance, turbulence is of great importance since it can affect both wind turbine power extraction and the lifetime of its components, such as blades and tower, due to the random fluctuations of the loads. However, even though turbulence is a complex process, difficult to represent through deterministic equations, this physical phenomenon needs to be addressed during the wind turbine design process [25, 27].

In this regard, since turbulence is a fluid flow phenomenon, it can be described by integrating the conservation of mass, momentum, and energy equations and taking into account a time integrator and proper initial and boundary conditions. However, since the fluid dynamics governing equations are nonlinear, small differences in the initial and boundary conditions can lead to significant discrepancies in the prediction of such chaotic processes. It is typically more advantageous to characterize turbulence by means of statistical quantities [25]. Regardless of the statistical description of the turbulence, some parameters are useful depending on the application.

2.1.1.1 Turbulence Intensity

The measure of the general level of turbulence is called turbulence intensity, and it depends on the roughness of the ground and the height above the surface. Once the height increases, the effects, which are a consequence of the interaction between the wind and the surface of the Earth, become weaker until it reaches a certain height where the airflow can be considered free of such influence. An estimate of the turbulence intensity can be obtained by

$$I = \frac{\sigma}{\overline{U}}, \tag{2.1}$$

where σ is the standard deviation of the wind speed, and $\overline{U}$ is the mean speed defined over 10 minutes or 1 hour [25]. Likewise, for numerical applications, such as boundary conditions for CFD simulations, another way to establish a representation of the turbulence intensity, but considering a dependence on the upstream history of the flow, is considering the flow as fully developed inside a duct given by the empirical correlation,

$$I \equiv 0.16 Re_{Local}^{-\frac{1}{8}}, \tag{2.2}$$

where,

$$Re = \frac{uL}{\nu}, \tag{2.3}$$

where Re is the Reynolds number, u is the velocity, L is the characteristic length and ν is the fluid kinematic viscosity. Thus, the local Reynolds number Re_{Local} is obtained considering local values for the parameters in the Eq. (2.3). Also, its worth mentioning that according to Basse [28], the representation of the turbulence intensity that is addressed to the flow history is relevant for flows that are governed by high Reynolds numbers, which is the case of the flows being analyzed in this work.

2.1.1.2 Turbulence Spectra

In order to complete the characterization of turbulence, the frequency content in the wind-speed variations is described by a continuous turbulence spectrum of scales. In this regard, time and length scales of turbulence can be identified by analyzing the frequencies and wavelengths using Fourier analysis of the flow time history.

Thereby, vortex stretching is the primary physical process that causes motion to spread across a broad range of wavelengths in turbulent flows [25, 29]. According to Wilcox [29], if the vortex elements are oriented in a direction that can stretch them through mean velocity gradients, then turbulence gains energy. The interaction between larger-scale turbulent motion and the mean flow is strongest for wavelengths that are not too small compared to the mean flow length scale, resulting in the larger-scale turbulent motion carrying most of the energy. Also, a cascade of energy arises from the larger eddies, which randomly stretch the vortex elements of smaller eddies.

From an engineering perspective, turbulent diffusion can considerably improve the transfer of mass, momentum, and energy, whereas large eddies, which persist for long distances, are responsible for increased diffusivity and stresses in turbulent flows. Enhanced diffusivity is perhaps the most significant aspect of turbulence, and its features play an important role in the formulation of any turbulence model [29].

2.1.2 Atmospheric Boundary Layer

Similar to the turbulence, the atmospheric boundary layer affects the wind turbine power output as well, mainly due to the wind shear profile, which is responsible for the wind velocity at the hub height, which represents the operational velocity of the wind turbine. Additionally, amongst the properties that have a major influence on the formation of the planetary boundary layer, turbulent structures are also present and represent a considerable transfer of momentum in the vertical direction [25]. Therefore, the wind shear profile of the atmospheric boundary layer can be estimated for a neutral

atmosphere considering the surface roughness height z_0, the velocity at the hub height v_0, and the reference height h_0 through the relation,

$$U_x = v_o \frac{\log(y/z_o)}{\log(h_o/z_o)}, \tag{2.4}$$

where U_x is the velocity in the x direction, and y represents the height variation. Some typical values of z_o parameter are shown in Table 2.1.

Table 2.1: Typical Lengths of Surface Roughness [25].

Type of terrain	Roughness length z_o (m)
Cities; forests	0.7
Villages	0.1
Open farmland	0.03
Flat grassy plains	0.01
Rough sea	0.001

2.2 Horizontal Axis Wind Turbine Aerodynamics

The technology involved in a wind turbine allows this device to interact with the environment, extracting kinetic energy from the wind and producing electricity. The energy extraction occurs due to the aerodynamic profile of the blades. In order to understand the physics of the system, a rotor region in the form of a disc containing the blades is assumed. To remove the kinetic energy from the wind, the mass of air that crosses this region is affected by a decrease in wind velocity. Additionally, the boundary of the rotor disc regions can be extended upstream as well as downstream to form a long stream tube of circular cross-section, as illustrated in Fig. 2.1.

As can be seen in Fig. 2.1, the approaching air upstream of the turbine inside the stream tube slows down compared to the air outside. Thus, at the rotor disc, its velocity is lower than the free-stream wind speed, and the stream tube expands to accommodate the slower-moving air. During this process, there is also a drop in static pressure; as a consequence, the region in which the air proceeds downstream with reduced speed and static pressure is called the wake region. In the stream tube, the pressure rises to compensate for the decrease in the kinetic energy until, eventually, far downstream, the static pressure returns to the atmospheric level [25,30]. Fig. 2.2 illustrates the variations in pressure and velocity along the stream tube.

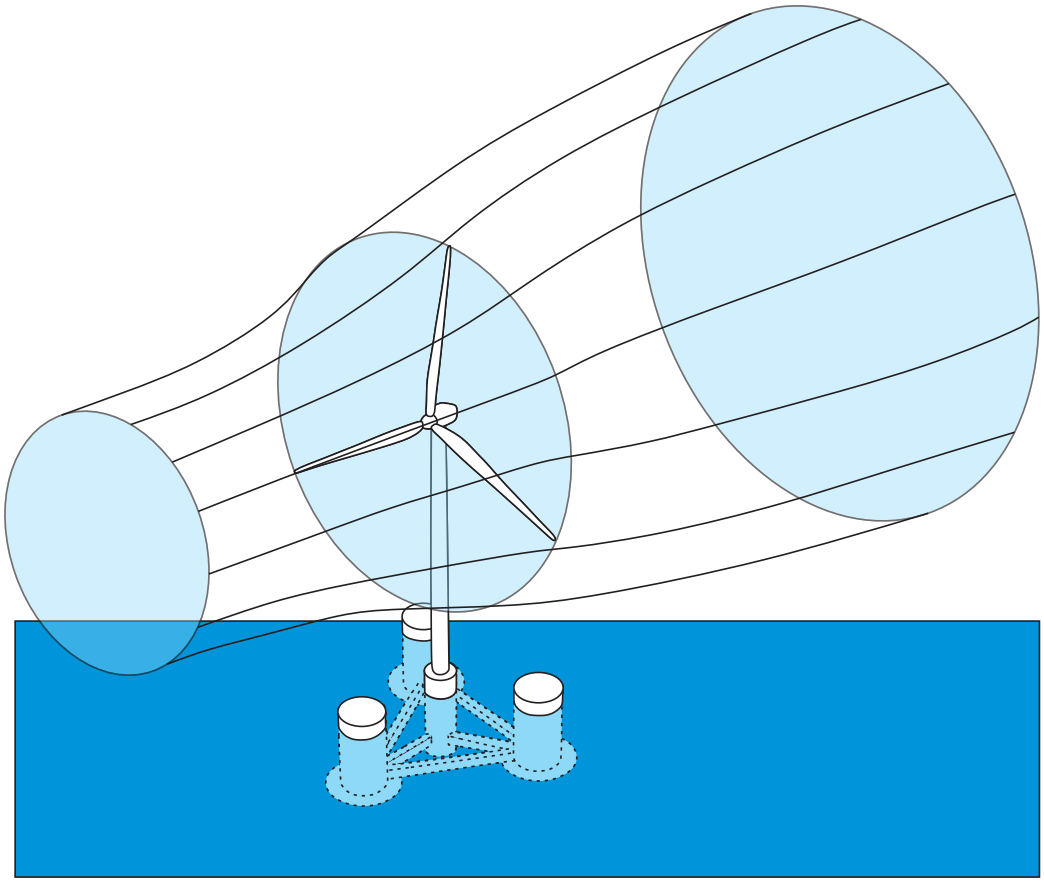

Figure 2.1: Representation of the stream tube of the flow through a wind turbine rotor.

2.2.1 Actuator Disc Approach

In order to understand the physics of the wind's kinetic energy absorption mechanism, the simplest approach to analyzing the aerodynamic behavior of a wind turbine without considering specific design characteristics is through the actuator disc theory. According to Burton et al. [25], in each time unit, the mass of air that passes through a cross-section of the stream tube is equal to ρAU, where U is the flow velocity, A is the cross-section area and ρ is the density of the air. Thus, the mass flow rate must be equal in all regions of the stream tube,

$$\rho A_\infty U_\infty = \rho A_d U_d = \rho A_w U_w, \tag{2.5}$$

where ∞ refers to the far upstream region, d refers to the disc, and w refers to the wake region (downstream of the disc). Figure 2.2 shows these three regions.

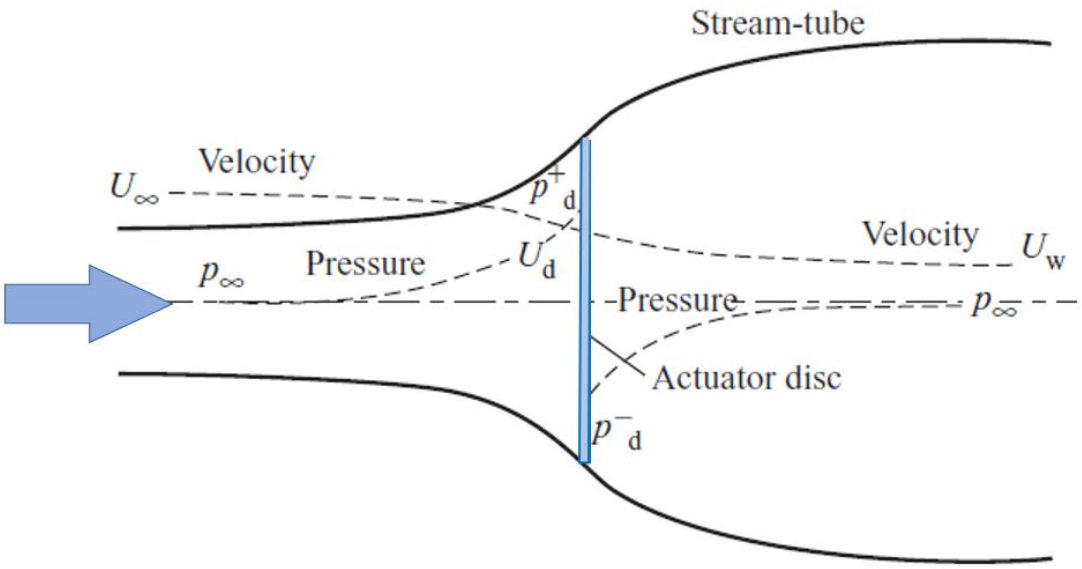

Figure 2.2: Streamtube energy extraction, adapted from [25].

The actuator disc induces a variation in the velocity, which is superimposed to the free-stream velocity, given by $-aU_\infty$, where a is the axial induction factor, also called the inflow factor. Thus, at the disc region, the resulting velocity in the stream direction is given by,

$$U_d = U_\infty(1-a). \tag{2.6}$$

Considering the streamwise velocity at the disc region determined by Eq. (2.6) and the momentum theory, some important parameters commonly used to qualify the operational conditions of wind turbines can be described as follows.

2.2.2 Momentum Theory

In order to estimate the variation in the momentum and, subsequently, the pressure at the disc region, it is necessary to consider the extraction of energy that occurs inside the stream tube. This pressure information is then considered to estimate the velocity relation in the far downstream and upstream regions. As stated by Burton et al. [25], the rate of momentum change can be determined by multiplying the total change in velocity by the mass flow rate as

$$\Delta Momentum = (U_\infty - U_w)\rho A_d U_d. \tag{2.7}$$

Conversely, the force responsible for the change in momentum is caused by the pressure difference across the actuator disc. Using this information and substituting Eq. (2.6) into Eq. (2.7), the force can be represented as

$$(p_d^+ - p_d^-)A_d = (U_\infty - U_w)\rho A_d U_\infty (1-a). \tag{2.8}$$

To obtain the pressure difference, Bernoulli's equation can be applied separately to the upstream and downstream sections of the stream tube. Thus, considering the upstream portion of the stream tube, the equation is given by,

$$\frac{1}{2}\rho_\infty U_\infty^2 + p_\infty + \rho_\infty g h_\infty = \frac{1}{2}\rho_d U_d^2 + p_d^+ + \rho_d g h_d. \tag{2.9}$$

Neglecting body force effects, Eq. (2.9) is simplified to

$$\frac{1}{2}\rho U_\infty^2 + p_\infty = \frac{1}{2}\rho U_d^2 + p_d^+. \tag{2.10}$$

Similarly, but considering the downstream portion of the stream tube, Bernoulli's equation is given by

$$\frac{1}{2}\rho U_w^2 + p_\infty = \frac{1}{2}\rho U_d^2 + p_d^-. \tag{2.11}$$

The relation between the velocities, which indicates the losses in the stream tube, can be obtained by subtracting Eq. (2.11) from Eq. (2.10) and then substituting the relation given by Eq. (2.8). Which results in the following equation:

$$U_w = (1-2a)U_\infty. \tag{2.12}$$

Therefore, based on Eq. (2.12), it can be inferred that half of the axial speed loss in the stream tube occurs upstream of the actuator disc, while the other half occurs downstream of the tube [25].

2.2.3 Power Coefficient

The power coefficient is defined as the ratio between the power converted by the wind turbine and the maximum power available in the wind stream [30]. Therefore, the wind turbine power can be evaluated by multiplying the force exerted by the air, F, by the resulting velocity at the disc as

$$Power = FU_d = (2\rho A_d U_\infty^2 a(1-a))(U_\infty(1-a)) = 2\rho A_d U_\infty^3 a(1-a)^2. \tag{2.13}$$

As the power available is given by $1/2\rho U_\infty^3 A_d$, the power coefficient is defined as follows:

$$C_P = \frac{Power}{\frac{1}{2}\rho U_\infty^3 A_d}. \tag{2.14}$$

The actuator disc approach allows us to rewrite the power coefficient using Eq. (2.13) and Eq. (2.14), resulting in Eq. (2.15):

$$C_P = 4a(1-a)^2. \tag{2.15}$$

The maximum possible value of the power coefficient, known as the Betz limit, is not related to design inefficiency but is instead limited by the fact that the stream tube must expand upstream from the actuator disc. To determine the maximum power coefficient, we must impose

$$\frac{dC_p}{da} = 0, \tag{2.16}$$

which results in an induction factor of $a_{max} = 1/3$. For this condition, the maximum power coefficient is,

$$C_{P_{max}} = \frac{16}{27} = 0.593, \tag{2.17}$$

which is known as the Betz limit.

2.2.4 Thrust Coefficient

The thrust coefficient can be similarly described by considering the force on the actuator disc due to the pressure drop. The equation for the thrust coefficient is as follows:

$$C_T = \frac{Thrust}{\frac{1}{2}U_\infty^2 A_d} = 4a(1-a). \tag{2.18}$$

The velocity reduction in the far downstream region from 2/3 to 1/3 is a consequence of the actuator disc model. However, if the airflow is completely stopped ($a \geq 1/2$), the momentum theory becomes invalid since the velocity in the wake region, given by $(1-2a)U_\infty$, becomes zero or negative. Furthermore, the actuator disc model assumes that the rotor comprises an infinite number of blades and the thrust is uniformly distributed over the rotor area. The model also neglects the effects of rotation on the wake formed. These assumptions limit the model's accuracy in representing real-world wind turbines with non-ideal characteristics. In such cases, alternative models need to be employed.

2.2.5 Horizontal Axis Wind Turbine Wakes

Downstream a horizontal axis wind turbine, the near and far wake regions are separated as a function of the spatial distribution and intensity of turbulence in the flow. Experiments have shown that the mean axial and rotational flow in the wake is responsible for the transport of the vortex structures generated and shed by the hub, tower, blades tip, and trailing edges. As a result, the wake behind the wind turbine is represented by an annular area with a strong velocity gradient [31]. The wind turbine wake can be sub-divided into three regions, the near wake, where the flow is dominated essentially by the rotor blades' aerodynamics and high turbulence, which includes the velocity deficit and the vortices structure generated by the rotor blades [32]. In the intermediate wake, where the tip vortices gradually lose identity, the flow from the undisturbed and core regions starts to interact, and the extra turbulence also starts to decay. Finally, the far wake region represents the equilibrium between the convective forces and the gradients of the turbulent momentum fluxes [33].

Figure 2.3 shows the wake expansion in an offshore site, in which the wakes were observed due to the re-condensation of the fog.

Figure 2.3: Wake expansion in an offshore site [30].

The complexity of the wind turbine wakes makes the modeling of this region a challenging task. Depending on the numerical method, each region of the wake requires distinct modeling approaches [32]. Moreover, unsteady aerodynamic effects, such as dynamic stall, dynamic inflow, and tower shadow, are also responsible for making such analysis more complex [31]. Additionally, the wind turbine wake is of extreme importance in delivering an accurate analysis regarding offshore wind farms. The wind farm layout is a critical factor and is established in the first stages of the project. As the number of wind turbines increases dramatically, the arrangement of the wind farm becomes strategic. The turbines can be placed along a single line, multiple lines, clusters, or grids. The farm layout contributes to the reduction of the wind energy average cost due to the benefits of scaling, land cost reduction, logistics, maintenance, and construction advantages [5]. However, a common challenge reported in the literature is the aerodynamic interaction among turbines which leads to a significant loss of energy production [30].

As an example, the aerodynamic interaction decreases the total energy converted to electricity compared to the same number of isolated turbines operating under the same wind inflow conditions due to the wind speed reduction and turbulence, which is known as wake effect or wake losses [34]. Based on that, wind farm planners have made a significant effort to reduce the aerodynamic interaction among turbines in an array to maximize the profitability of each project, hence maintaining competitiveness in this market.

2.3 Offshore Wind Turbine Concepts

The successful operation of many offshore wind farms around the world indicates a growing trend of installing more such facilities in the near future. The offshore wind turbine industry usually employs two primary kinds of foundations: bottom-mounted and floating foundations. As approximately 80% of the world's wind potential resources are available in areas with a water depth of over 60 m, and the bottom-mounted structures are appropriate for small water depths, typically up to 60 meters, it is expected that the installation of floating offshore wind farms will grow in the coming years [4, 35]. The floating designs are mostly adapted from offshore oil and gas industry practices. Presently, the offshore wind market offers three main design concepts, namely spar-buoy, semisubmersible, and tension-leg platform. According to [36], these designs are typically classified based on the floater structure's configuration to ensure static stability in the rotational degrees of freedom of pitch and roll.

Figure 2.4 illustrates the main designs of horizontal-axis offshore wind turbines foundations, including the bottom-mounted foundations, such as Monopile, legged Jacket, and the floating concepts, such as Tension Leg platform, Spar buoy, and semi-submersible.

Figure 2.4: OWT platform concepts by NREL [37].

Among the options for floating structures, semisubmersible platforms have a significant advantage over the other concepts, particularly in terms of installation. The assembly of the structure is done onshore and then towed to the offshore operational site, which is a beneficial factor for offshore wind farms due to installation costs and flexibility with regards to relocating the device based on weather conditions [5].

Although there are significant advantages to using floating foundations, only a few projects have actually deployed them in offshore locations around the world, mainly due to the motion of the floating platform that can significantly affect the performance of the floating wind turbine system [38]. In addition, compared to fixed-bottom wind turbines, platform motion can also raise tower loads and potentially decrease the structural lifespan of the system [39]. So far, besides Hywind Scotland, the first floating wind farm installed in 2017, Norway commissioned the TetraSpar floating foundation demonstration project with a capacity of 3.6 MW at the Metcenter Test site, which became the second floating offshore wind turbine in the country in 2021 [3,4]. Additionally, the Kincardine floating wind farm in Scotland connected 5 units of 9.5 MW FOWTs, while the Yangxi Shapa III offshore wind farm in China installed a single 5.5 MW floating prototype unit [4]. Therefore, in 2022, a total of 66.4 MW of floating wind capacity was commissioned, and a total of 16.5 GW

is expected until 2030 [4]. Since most of the commercial floating wind turbines are still in the early phase of development, with only a few prototypes having been installed, the industry, together with research communities, are working to develop new and improved technologies for floating offshore wind turbines to increase their efficiency, reduce costs, and make them more viable for commercial use. Thus, to support concept studies aimed at facilitating the improvement of offshore wind technology, the National Renewable Energy Laboratory (NREL) developed the specifications for two representative utility-scale wind turbines: the NREL offshore 5-MW baseline wind turbine and the IEA wind 15-MW offshore reference wind turbine [40, 41].

2.3.1 Reference Wind Turbines for Offshore Applications

In recent years, the significance of reference wind turbines, such as those developed by NREL [40, 41], has increased in the wind energy community due to their multiple roles. For instance, these theoretical wind turbines represent standard benchmarks that are openly defined with design parameters available to the public. This available information can be used as starting point for studies that investigate design methodologies for floating offshore wind turbines. Additionally, as an open design, reference wind turbines encourage cooperation between the industry and researchers, besides providing an opportunity to learn about basic design, components, and system trade-offs from the wind energy sector.

2.3.1.1 NREL Offshore 5-MW Baseline Wind Turbine

The NREL 5-MW reference wind turbine is a standardized, large wind turbine design intended to serve as a benchmark suitable for offshore wind energy development. Its purpose is to provide a common reference point that can be used to compare the performance of different wind turbine designs and technologies. The available information, which includes detailed design specifications such as blade length, tower height, and generator size, is used in this work to model and simulate the performance of a full-scale 5 MW wind turbine. The applicability of this reference wind turbine for offshore concepts can be verified through the NREL Offshore Code Comparison Collaboration Continuation (OC4) project, which involves the modeling definition of a semisubmersible floating offshore wind system [42]. The semisubmersible floating platform design was developed by the DeepCwind project, which aimed to generate test data to validate modeling tools for floating offshore wind turbines. According to NREL [43], several organizations contributed to the OC4 tasks project, including experts from the offshore structure and wind energy

communities, which provided multiple results, examining how the modeling approaches influenced the project. However, differences between the modeling approaches indicate that more effort is still required to represent the complex system better.

Figure 2.5 shows the OC4 floating system proposed by NREL, from which, in this work, the reference wind turbine is investigated. Additionally, Table 2.2 presents the main properties of the NREL 5-MW baseline wind turbine for offshore applications.

Power Rating	5 MW
Rotor Orientation, Configuration	Upwind, 3 Blades
Control	Variable Speed, Collective Pitch
Drivetrain	High Speed, Multiple-Stage Gearbox
Rotor, Hub Diameter	126 m, 3 m
Hub Height	90 m
Cut-In, Rated, Cut-Out Wind Speed	3 m/s, 11.4 m/s, 25 m/s
Cut-In, Rated Rotor Speed	6.9 rpm, 12.1 rpm
Rated Tip Speed	80 m/s
Overhang, Shaft Tilt, Precone	5 m, 5°, 2.5°
Rotor Mass	110,000 kg
Nacelle Mass	240,000 kg
Tower Mass	347,460 kg
Coordinate Location of Overall CM	(−0.2 m, 0.0 m, 64.0 m)

Table 2.2: NREL Offshore 5-MW Baseline Wind Turbine Properties [40].

2.3.1.2 IEA Wind 15-MW Offshore Reference Wind Turbine

Similarly to the previously presented NREL 5-MW reference wind turbine, NREL and the Technical University of Denmark (DTU) collaborated closely through the International Energy Agency (IEA) Wind Task 37 to develop the IEA 15 MW Wind reference wind turbine for offshore applications [41]. Additionally, the University of Maine (UMaine) leveraged its expertise and resources to contribute to this project developing the semisubmersible design for the floating platform concept. The main objective of this reference wind turbine is a standardized design, which was built considering valuable information from some industry contacts, that can be utilized in concept studies as the wind energy industry moves towards larger wind turbine design. Figure 2.6 shows the floating system proposed by NREL and UMaine. Additionally, Table 2.3 presents the main properties of the IEA 15-MW baseline wind turbine for offshore applications.

Figure 2.5: NREL DeepCwind floating wind system design [44].

Figure 2.6: The UMaine VolturnUS-S reference platform designed to support the NREL IEA-15 MW system definition [45].

Thus, the floating wind turbine system presented in Fig. 2.6 comprises a conventional horizontal axis, an upwind design with three blades, a rotor diameter of 240 meters, and a hub height of 150 meters.

Power Rating	15 MW
Turbine Class	IEC Class 1B
Specific Rating	332 W/m^2
Rotor Orientation	Upwind
Number of Blades	3
Cut-in Wind Speed	3 m/s
Rated Wind Speed	10.59 m/s
Cut-out Wind Speed	25 m/s
Design Tip-Speed Ratio	90
Minimum Rotor Speed	5.0 rpm
Maximum Rotor Speed	7.56 rpm
Maximum Tip Speed	95 m/s
Rotor Diameter	240 m
Airfoil Series	FFA-W3
Hub Height	150 m
Hub Diameter	7.94 m
Hub Overhang	11.35 m
Rotor Precone Angle	$-4.0°$
Blade Prebend	4 m
Blade Mass	65 t

Table 2.3: IEA Wind 15-MW Offshore Reference Wind Turbine Properties [41].

To be applicable for future technology development and analysis efforts, reference wind turbines must reflect the most advanced or upcoming technology in the field of wind energy. However, while the industry is moving beyond 10-MW designs, there is still a gap in the available information regarding the numerical methods that can accurately represent the physical behavior of this complex system regarding the aerodynamic loads acting on the large blades and its influence on the platform dynamics [41].

3 NUMERICAL METHODS FOR WIND TURBINE PERFORMANCE AND AERODYNAMIC ANALYSIS

Heretofore, the mechanism related to the wind kinetic energy conversion was described without taking into account the design of the blades. However, since the lift generated by the blades is used to rotate the rotor and drive the generator to produce electricity, the primary objective of this chapter is to present the numerical methods that use the blade properties to model a wind turbine and predict its performance. Initially, the rotor theory is used to illustrate how to predict the aerodynamic forces acting on the wind turbine blades, considering a two-dimensional approximation. Then, the CFD approach, which considers the unsteady and viscous three-dimensional aerodynamic effects on the wind turbine blades, is presented.

The prediction of the aerodynamic forces acting on the wind turbine blades can be made in multiple ways. The complexity of each method is converted into more accurate results and more reliable power estimations. Additionally, the diversity of the methods is essential during the development of a wind turbine project, as different methods are suitable for different project stages. For instance, BEM theory can be used as an approach to quickly analyze a possible aerodynamic design of a blade being developed, while the most expensive method to analyze the aerodynamic response of the blades, such as CFD, is commonly used to investigate the final design of a certain model.

3.1 Rotor Theory

The rotor theory is a fundamental principle in the design and analysis of wind turbines. This theory can be implemented in numerical codes and used as a tool for wind turbine designers and researchers to develop new designs for wind turbines under different conditions [31]. The rate of change of axial and angular momentum of all the air passing through the swept annulus of the wind turbine rotor is attributed to the aerodynamic lift

and drag forces acting on the span-wise elements of the wind turbine blades. The importance of the rotor theory relies mainly on the prediction of the required aerodynamic design for the blades to provide the necessary generator torque [25].

3.1.1 Blade Element Theory

In the Blade Element theory, it is assumed that the forces acting on a section of a wind turbine blade can be determined by considering the characteristics of a 2D airfoil, which is established by taking into account the angle of attack of the blade with respect to the air relative velocity at the cross-sectional plane of the blade element. This approach does not account for the 3D effects, meaning that spanwise flow is neglected [25].

Thus, to apply this analysis, the blade is decomposed into elements (sections), but the aerodynamic interactions between elements are not considered. Therefore, the lift and drag forces are determined solely by the airfoil profile. The drag (F_D) and lift (F_L) forces are parallel and perpendicular to an effective or relative wind, whereas the angle of attack (α) is the angle between the chord line and the relative wind. The angle between the plane of rotation and the relative wind is given by φ, which is composed of the sum of the angle of attack and section pitch angle, as shown in Fig. 3.1.

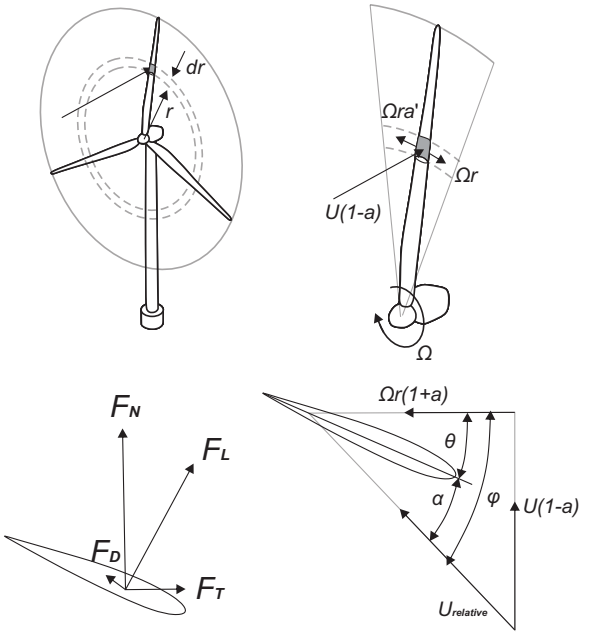

α - angle of attack
φ - relative wind angle
θ - pitch angle
$U(1-a)$ - wind velocity at blades
$U_{relative}$ - relative wind velocity

Figure 3.1: Horizontal axis wind turbine blade properties.

Hence, the incremental normal force to the plane of rotation (F_N), which contributes to the thrust force, and the incremental force in the tangential direction to the rotor swept

circle (F_T), which contributes to the torque are given respectively by

$$dF_N = dF_L \cos\varphi + dF_D \sin\varphi, \tag{3.1}$$

$$dF_T = dF_L \sin\varphi - dF_D \cos\varphi, \tag{3.2}$$

where dF_L and dF_D are increments of lift and drag forces. Considering a finite number of blades given by N_{blades}, and the expression of the lift force increment in terms of its coefficient $dF_L = C_L \frac{1}{2} \rho U^2_{relative} c dr$, where c is the chord and dr is the increment of the blade radius, the normal force increment can be rewritten

$$dF_N = N_{blade} \frac{1}{2} \rho U^2_{relative} (C_L \cos\varphi + C_D \sin\varphi c dr). \tag{3.3}$$

Similarly, the differential toque on a distance r along the blade is given by Eq. (3.4).

$$dQ = N_{blade} \frac{1}{2} \rho U^2_{relative} (C_L \sin\varphi - C_D \cos\varphi c r dr). \tag{3.4}$$

3.1.2 Blade Element Momentum Theory

The BEM theory, which originates from the previously explained blade element and momentum theories, assumes that the wind turbine blades can be divided into small, independent elements that behave like two-dimensional airfoils, with aerodynamic forces calculated based on the local flow conditions. Then, by means of the momentum theory, it also assumes that the loss of pressure or momentum in the rotor plane is due to the work done by the airflow passing through the rotor plane on the blade elements. In practical implementations of the BEM theory, as the wind turbine blades are divided into several elements along the span, as it moves in the rotor plane, an annular region is created, as shown in Fig. 3.1, across which the momentum balance takes place. Additionally, the annular regions formed in the rotor plane by the rotating elements from the blades are also where the wake-induced velocities cause changes in the local flow velocity at the rotor plane [46].

Thus, the induced velocities calculated using the momentum theory affect the inflow in the rotor plane and ultimately impact the forces calculated by the blade element theory. These two theories form an iterative process to determine both the aerodynamic forces and the induced velocities in the vicinity of the rotor. By considering the BEM theory, it is assumed that there is no radial flow interaction. Hence, the theory presents limitations [25]. For instance, BEM theory assumes that the airflow field around the airfoil is always in a state of equilibrium and that the flow adjusts instantaneously to the changes in the

wake vorticity. However, in practice, it has been noticed that the airfoil response takes time to adapt to changes in the wake caused by variations in the operating conditions of the wind turbine [46].

Currently, to overcome the limitations, important corrections have been made in the original theory, which allows the BEM theory to be used widely through different codes, such as OpenFAST [47], as a reliable tool for the induced velocity and elemental forces estimation and wind turbines modeling taking into account the blades design properties a low computational demand [46]. Fig. 3.2 illustrates the flow chart for implementing the BEM algorithm.

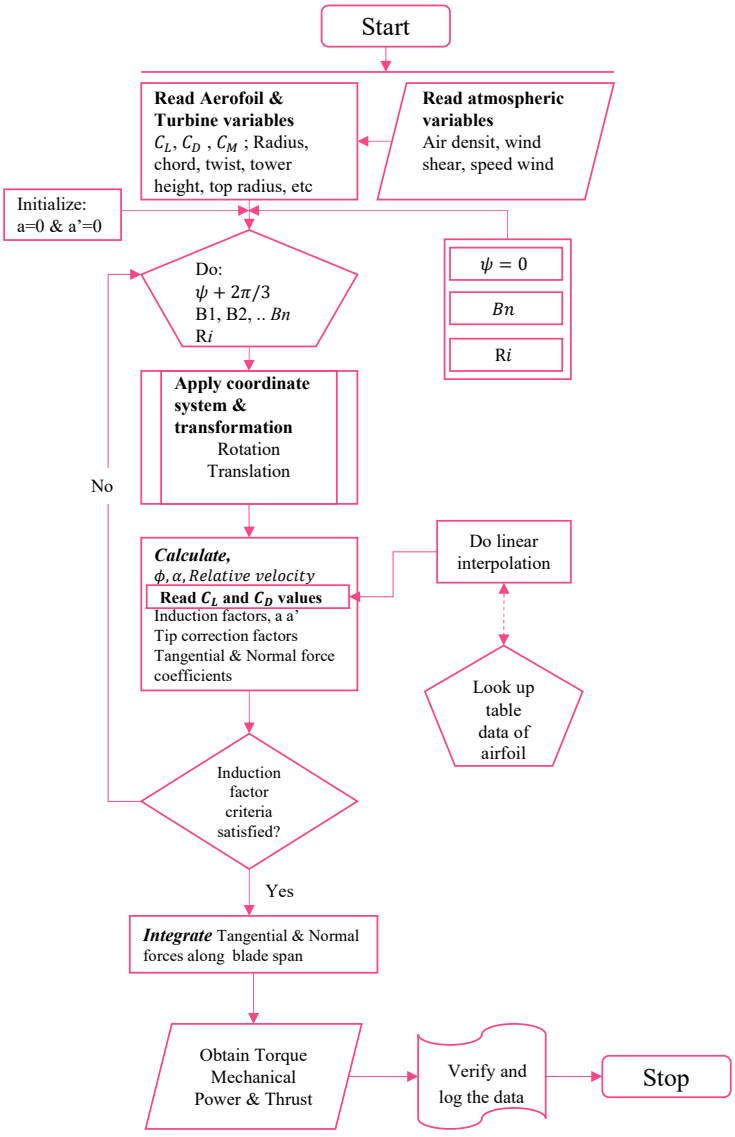

Figure 3.2: Flow chart for implementing BEM algorithm, adapted from [48].

3.1.3 OpenFAST Code

OpenFAST, which is composed of a set of computational modules to solve different dynamics of the wind turbine model, such as aerodynamics, hydrodynamics, control, and structural dynamics, is a powerful tool that enables the simulation of wind turbines. This integration amongst these numerical libraries allows a comprehensive nonlinear simulation of the aero-hydro-servo-elastic behavior of a wind turbine in the time domain. Developed and maintained by NREL [47], OpenFAST is capable of analyzing different wind turbine configurations, including rotor type, pitch or stall regulation, hub type, rotor position, and tower type, for turbines on land or offshore on fixed-bottom or floating substructures. The code incorporates the AeroDyn model, which contains the aerodynamic model for the rotor/induction model, blade airfoil aerodynamics, and the influence of the tower on the fluid local to the blade nodes, as well as tower drag. These aerodynamic models employ an improved version of the BEM theory, such as the quasi-steady state, to determine the effect of the wake through induction factors. In addition, this tool, which both industrial and research organizations have globally used, is also a calibrated and certified software by Germanischer Lloyd [49, 50].

Therefore, the OpenFAST code can be used as a robust framework to perform wind turbine simulations at a lower computational cost than high-fidelity CFD simulations. In this thesis, the OpenFAST code was utilized to accomplish a verification procedure for the CFD simulation results.

3.2 Computational Fluid Dynamics Approach

Although BEM methods are advantageous, with the increase in computational power, numerical methods that incorporate more advanced representations of unsteady aerodynamics, such as Computational Fluid Dynamics (CFD), have become more attractive to both industry and research communities. In addition, besides the accessibility of supercomputers, the effectiveness of open source CFD codes, such as OpenFOAM, has enabled the solution of the full three-dimensional Navier-Stokes equations, making CFD a promising approach for numeric investigation of wind turbine aerodynamics [23].

CFD is a powerful technique for studying different fluid flow systems, where a set of numerical methods are employed to solve the governing equations of fluid mechanics. Usually, the problem being investigated is represented by a computational domain that is discretized into several control volumes, composing a mesh, whereby the governing

equations are approximated by the numerical methods and solved within the control volumes. The use of this method allows the estimation of the flow properties, such as pressure and velocity fields, in a transient analysis throughout the computational domain.

3.2.1 Offshore Wind Turbine Modeling

In recent decades, wind farms around the world have seen a significant increase in the size of commercial wind turbines. As their power capacity has risen from 50 kW to 5 MW, the rotor diameter has also increased from 15 m to 120 m. As a result, such modifications in the wind turbine dimensions have called for improvements in the design tools. Simple static calculations and reduced order models present limitations when it comes to numerically describing the large-scale system. Thus, more advanced design tools are required to accurately model the complex system given by larger wind turbines [22].

For instance, several methods can be applied to model a wind turbine to predict its performance and aerodynamic loads. However, the suitability of each numerical method is determined based on the purpose of the analysis [23]. Experimental campaigns, such as the Unsteady Aerodynamic Experiment (UAE) by NREL, in which a heavily instrumented 20 kW wind turbine was placed inside the world's largest wind tunnel at NASA's Ames Research Center [51], have shown that the wind turbine faces complex aerodynamic loads and substantial three-dimensional effects. Although approaches such as the BEM method are commonly used to predict the rotor aerodynamics in different types of wind turbines analysis [52], for OWT investigations, the BEM theory has limitations in terms of capturing the interaction among the aerodynamic forces acting on the blades and the rotor's wake, due to the complexity of the turbulent region behind the rotor [53, 54].

Currently, the majority of OWT numerical simulations focus on investigating the influence on the prediction of the wind turbine performance, regarding the unsteady 3D aerodynamic effects on the rotor blades, as a consequence of transient effects, such as the dynamic response of the wake and dynamic stall [55]. Since the first blade-resolved simulation of a wind turbine [56], rotor-only simulations have been carried out through different CFD methodologies to understand the transient effects better.

For instance, numerical investigations of the NREL Phase II rotor [57], NREL Phase VI rotor [58], and MEXICO rotor [59] have shown that turbulence transition and precise definition of the trailing edge of the blade geometry significantly affect the prediction of the wind turbine performance. Therefore, the accurate representation of the three-dimensional effects present in the flow using a CFD approach became crucial to improve

the forecast wind turbine aerodynamics capability. Furthermore, performing experimental tests has become increasingly difficult as commercial OWT increases in power capacity, such as Vestas 9.5 MW and GE 14 MW [20, 21]. As a result, high-fidelity CFD numerical models represent a valuable alternative to predict the flow characteristics of such complex systems by allowing full-scale geometry in the numerical simulations. In addition, simpler numerical models, which require calibration, can also benefit from the results from high-fidelity computational analysis [22, 23].

In this regard, although CFD has been proven to be effective in examining the unsteady aerodynamic behavior of the flow around wind turbine blades and generated wakes, only a few investigations using such a method considered the wind turbine geometry in its full size of a megawatt-scale, due to the complexity of the numerical simulation, and computational resources required [24]. For example, previous research has investigated the multi-physical problem associated with the influence of the turbulence model on the prediction of the aerodynamic loads [60, 61], as well as the consideration of aeroelasticity effect [62–64]. Despite these studies have contributed with essential insights regarding the physics of the problem understanding, the solver arrangement was briefly addressed, and no investigation was conducted to explore the impact of the simulation setup on the accuracy of the results obtained with respect to the numerical schemes and solver parameters used. Additionally, considering the investigations conducted by [61], as the authors utilized the DES approach as a turbulence model for the numerical investigations, which demands significant computational resources, the mismatch between the numerical setup and mesh strategy employed significantly affected the simulation solution and results accuracy since the quasi-steady regime for power and thrust, which requires approximately 5-6 rotor revolutions to establish was not attained, even with the coarsest mesh.

Given the substantial impact of the numerical arrangement on simulation results and the associated increase in computational demand, further investigations are necessary to maximize the reliability of the CFD methodology as a tool. Besides analyzing the multi-physical problem, such analyses should also capture the influence of other numerical solver components on the solution's accuracy. This type of study is desirable and becomes crucial for simulations of wind turbines on full scale during offshore wind turbine projects.

4 COMPUTATIONAL FLUID DYNAMICS METHODOLOGY AND THE FINITE VOLUME METHOD

For the reasons explained previously in Chapter 3, a CFD methodology, which employs the Finite Volume Method (FVM), was developed to predict the performance of the new generation of horizontal-axis offshore wind turbines, such as NREL 5 MW and IEA 15 MW, considering their geometry in full scale. Besides predicting the wind turbine performance, including the evaluation of the aerodynamic loads with a high resolution of the flow features on the blades, a detailed study of the solver's influence on the accuracy of the simulation results and the computational costs associated was performed. In this regard, among the numerical arrangement parameters investigated are different spatial and temporal discretization strategies, the pressure-velocity coupling problem, different turbulence models and different discretization schemes for the convective term.

4.1 Finite Volume Method

Due to its ability to accurately capture the complex fluid dynamics related to the interaction between the wind turbine blades and the surrounding air, the Finite Volume Method (FVM) has been shown to be a mature and reliable method to investigate the performance of wind turbines [23, 24]. In this work, the FVM is employed to model the unsteady aerodynamic flow around the wind turbine and its generated wake to provide an effective means of investigating the performance of different offshore wind turbine designs at full scale. Therefore, the CFD investigations presented in this thesis employed the FVM, which is described in detail in this section.

4.1.1 Structure of the FVM Approach

The Finite Volume Method is a powerful numerical technique that is vastly used for solving partial differential equations. This approach connects several steps that enable the

discretization of the domain into small control volumes, the approximation of the partial differential equations within these volumes, and the solution of the resulting algebraic equations. According to Versteeg and Malalasekera [65], the structure of the CFD codes can be divided into three main parts: the pre-processing stage, which involves mainly preparing the geometry and defining the boundary conditions; the solver stage, where the discretized set of equations is solved using iterative or direct methods; last, the post-processing stage consists of analyzing and visualizing the results. These three main stages are presented in detail as follows.

4.1.2 Pre-processing Procedures Description

The initial stage of the CFD methodology is composed of the pre-processor steps. Although the interface between the user and the CFD code can be different, depending on the software being used, the pre-processor steps remain the same [65]. The first step is the definition of the geometry that represents all the regions of interest, called the computational domain. The next step is the mesh generation, which involves discretizing the computational domain into small, non-overlapping subdivisions called control volumes. At this stage, the user needs to specify the fluid properties and appropriate boundary conditions on the computational domain limits based on the physics of the problem.

Figure 4.1 illustrates the real system of an offshore wind turbine and its numerical representation in terms of computational domain and boundary conditions.

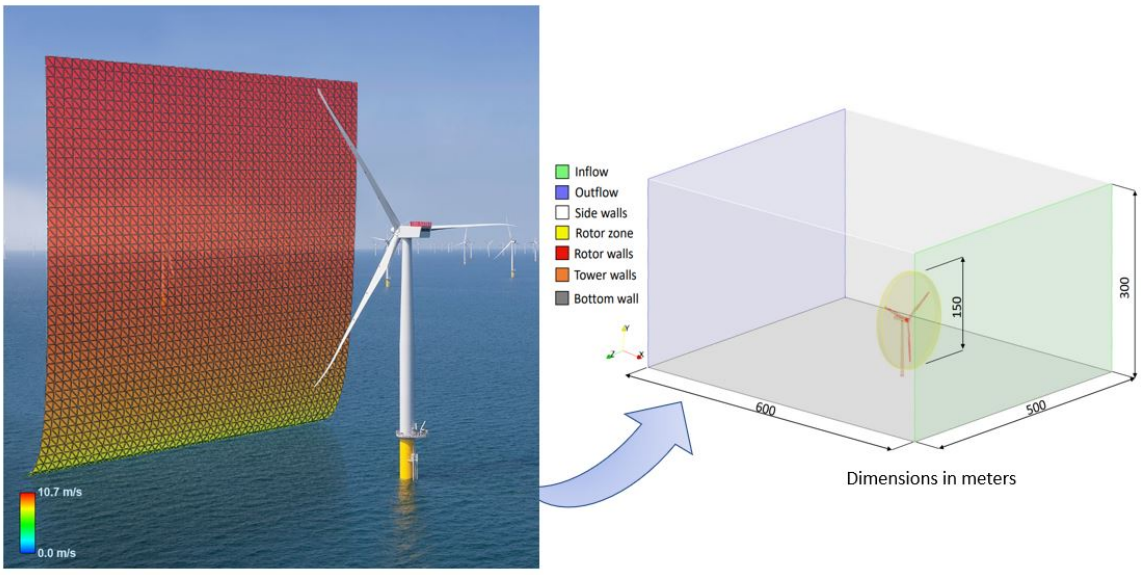

Figure 4.1: Offshore wind turbine representation of the real system in terms of the computational domain and boundary conditions, adapted from [66].

To solve the governing equations, boundary and initial conditions are necessary to obtain a solution for the problem being investigated. The two most common types of boundary conditions are Dirichlet and Neumann conditions. Dirichlet prescribes the value of the variable at the boundary; the Neumann condition prescribes the variable gradient. In a computational mesh, boundary conditions are necessary to give the appropriate numerical treatment for every boundary face and the dependent variable of the computational domain. Considering the example presented in Figure 4.1, the physical boundary conditions considered are discussed:

- **Inflow,** at this region, usually the velocity is prescribed while for consistency, the pressure gradient is considered null. In the case used as an example, in Fig. 4.1, at the inflow, the boundary condition for the velocity was of Dirichlet type, given by a prescribed logarithmic profile described by Eq. (2.4), where v_0 represented the velocity at 80 m high, chosen to be 10 m/s. Additionally, considering the location of the wind turbine in an offshore site, the roughness height z_0 was set to be 0.001 m, representing the ocean rugosity, y represented the height variation, and h_0 is the reference height considered as 80 m.

- **Outflow,** at this region, usually the pressure is prescribed as a fixed value equal to zero, and the other flow variables, such as the velocity and the turbulent quantities, have Neumann boundary conditions, usually a null gradient.

- **Symmetric plane,** at the side, top and bottom walls, the boundary condition for all the flow variables, such as velocity, pressure and turbulent quantities, was a symmetric plane. This condition corresponds to a null normal component and zero normal gradients for the tangential components.

- **Wall condition,** for the turbine walls, which included the rotor and tower walls moving wall velocity, and no-slip condition was imposed. The moving wall velocity condition sets the velocity to the desired value for moving walls when employing a moving mesh methodology. While the no-slip condition implies that the velocity of the fluid on the wall is equal to the velocity of the wall itself, thus Dirichlet condition as a fixed value equal to zero prevails since the tower of the turbine is not moving. In addition, as there is no flux through a solid wall, the condition for pressure is set as zero gradient. Also, when the turbulence model includes the use of wall functions, each turbulence property receives the proper wall function treatment.

- **Cyclic condition**, this condition is used to represent the coupling condition between two patches that have identical external boundaries but different inner struc-

tures. In the example case depicted in Fig. 4.1, at the rotor zone, the cyclic Arbitrary Mesh Interface (AMI) is applied to connect the dynamic part of the mesh, which refers to the rotor region, with the static part of the mesh, which is given by the other regions of the computational domain.

There is a wide range of boundary conditions, such as periodic, symmetry, and wedge, among others, which can be used depending on the physics of the numerical model considered to represent the problem being analyzed. More than 50% of the time required to build a CFD model is dedicated to defining the geometry and refining properly the computation domain. The CFD simulations, which employ the FVM, are capable of using different types of meshes, each with its distinct characteristics. The selection of the most suitable mesh type, such as structured, unstructured, or hybrid, depends on the problem's intricacy, as well as the desired level of accuracy and computational efficiency [65].

For instance, structured meshes are composed of elements that have regular shapes, such as cubes and hexahedrons, which are arranged in an organized pattern. This type of mesh is relatively simple to generate and presents favorable numerical aspects. However, its effectiveness is limited by the complexity of the geometry. Conversely, unstructured meshes employ non-uniformly shaped elements like triangles or tetrahedrons to depict intricate geometries. The process of generating them is more challenging and requires the use of algorithms to ensure its quality. Hybrid meshes, which blend structured and unstructured elements, are a good option to achieve a balance between accuracy and computational cost. Generating the most appropriate mesh is essential for the effectiveness of the CFD simulations. Based on the example illustrated in Fig. 4.1, a strategical partition of the computational domain and its mesh refinements are presented in Fig. 4.2.

As can be seen in Fig. 4.2, a strategical partition of the computational domain determines the size of the mesh element in each region. As an example, in parts of the domain far from the region of interest, the elements are larger, while as closer to the wind turbine, the mesh elements decrease in size until reaching the smallest size near the wind turbine geometry. This process requires meticulous treatment, strategy, and intense focus to achieve accurate and efficient results. Usually, optimal meshes are non-uniform and hybrid and include finer refinement in areas of interest where there is strong variation in fluid properties [67].

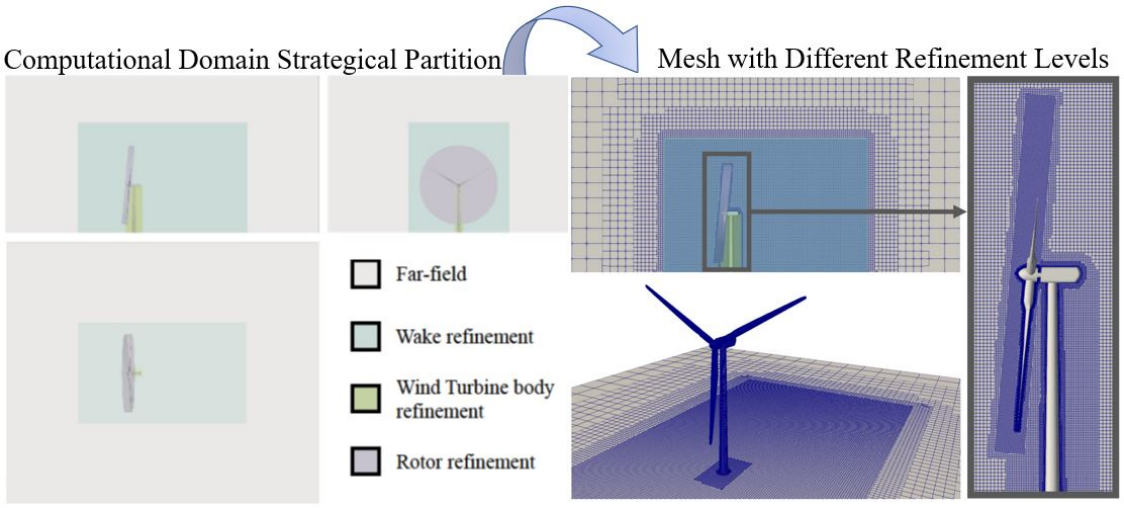

Figure 4.2: Computational domain regions and non-uniform mesh, adapted from [66].

4.1.3 Solver Procedures Description

At this stage, the discretized form of the governing equations is solved by an iterative or direct algorithm. To obtain the discretized form of the governing equations, several numerical procedures are considered. Usually, the first step is to integrate all the governing equations of fluid mechanics over all the cells in the computational domain. Then, convert the resulting integral equation into a system of algebraic equations through the so-called discretization process. Last, obtain the solution of the algebraic equations in each cell using a proper numerical scheme.

4.1.3.1 Discretization of the Governing Equations

In order to transform a set of continuous equations into a discrete set of algebraic equations applying the finite volume method, the computational domain must be discretized spatially. Additionally, for transient investigations, temporal discretization must also be employed. The spatial discretization is achieved by dividing the computational domain into several control volumes, as illustrated in Fig. 4.3, whereas, in the temporal discretization, several discrete time steps are considered to compute the simulation time.

According to Versteeg and Malalasekera [65], the governing equations, which are discretized into a set of algebraic equations, are solved at the center of the nodes in each cell by considering the flow properties of the neighboring cells. As shown in Figure 4.3, the control volume cells that compose the mesh are connected by their faces. A cell with the center node P has six neighboring nodes identified as W (west), E (east), N (north), B (bottom), and T (top), and six neighboring faces.

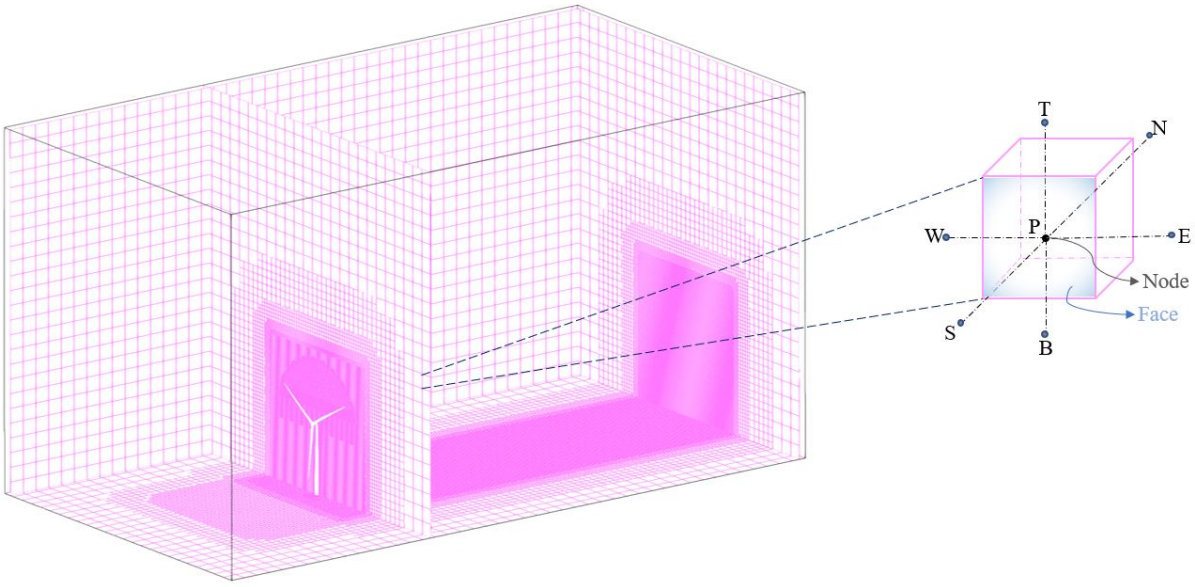

Figure 4.3: Spatial discretization of the computational domain and a generic three-dimensional control volume cell representation.

The approximations used to estimate a solution for the set of algebraic equations, which represent the original set of governing equations, are performed at specific locations between the cell's nodes and its faces based on the type of numerical scheme being used. As an example, a generic transport equation of a property Φ is used in Eq. (4.1) to illustrate the discretization process:

$$\underbrace{\frac{\partial \rho \Phi}{\partial t}}_{\text{time derivative}} + \underbrace{\nabla \cdot (\rho U \Phi)}_{\text{convective term}} = \underbrace{\nabla \cdot (\rho \Gamma_\Phi \nabla \Phi)}_{\text{diffusive term}} + \underbrace{S_\Phi(\Phi)}_{\text{source term}} , \tag{4.1}$$

where Φ is the quantity being transported, U is the velocity, ρ is the density, Γ_Φ is the diffusion coefficient and $S_\Phi(\Phi)$ is a source term. The transport equation for the property Φ, as given by Eq. (4.1), includes terms on the left-hand side that represents the rate of increase of Φ, where the convective term represents the net rate of Φ transport out of the control volume cell. On the right-hand side, the diffusion term represents the rate of increase of Φ due to diffusion, along with the contribution of the sources terms, which also increase the Φ property. The finite volume discretization is employed by reformulating Eq. (4.1) through integration over the control volume V_P and time as,

$$\int_t^{t+\Delta t} \left[\int_{V_P} \frac{\partial \rho \Phi}{\partial t} dV + \int_{V_P} \nabla \cdot (\rho U \Phi) dV \right] dt = \int_t^{t+\Delta t} \left[\int_{V_P} \nabla \cdot (\Gamma_\Phi \nabla \Phi) dV + \int_{V_P} S_\Phi(\Phi) \right] dt. \tag{4.2}$$

By applying Gauss's theorem, spatial integrals can be converted from volume to surface integrals. Therefore, the finite volume discretized equations can be solved by considering the appropriate numerical scheme for each specific term.

4.1.3.2 Spatial Discretization of the Transport Equation Terms

As aforementioned, the gradient terms from the volume integrals are converted into surface integrals via Gauss's theorem. By considering this approximation, the value from the gradient term is therefore approximated with second-order accuracy by summing the values of the property in all of the faces of the control volume as,

$$\int_{V_P} \nabla \Phi dV = \int_S \Phi d\mathbf{S} \approx \sum_f \mathbf{S}\Phi_f, \tag{4.3}$$

where Φ_f is the value of the property at the face, $\mathbf{S}$ represents the area vector pointing out of the control volume cell, which the magnitude is considered as equal to the face area, while $d\mathbf{S}$ is an infinitesimal element of surface pointing in the same direction. Similarly, the same approximation is proposed for the convection term by,

$$\int_{V_P} \nabla \cdot (\rho U \Phi) dV = \int_S (\rho U \Phi) \cdot d\mathbf{S} \approx \sum_f \mathbf{S} \cdot (\rho U)_f \Phi_P = \sum_f F\Phi_f, \tag{4.4}$$

where the term $\mathbf{S} \cdot (\rho U)_f$ is replaced by F, which represents the mass flux through a general face. The calculation of F is interpolated from the center of the volume cell to the face center values using a variety of numerical schemes, such as central differencing, Upwind, Hybrid, Power-law, QUICK, and TVD schemes. More details can be found in [65].

In addition, the discretization of the diffusion term is treated similarly to the convection term. By applying Gauss's theorem to convert the volume integration to surface integration and summing the contributions from all volume control faces. Thus, the following expression is obtained:

$$\int_{V_P} \nabla \cdot (\Gamma_\Phi \nabla \Phi) dV = \int_S (\Gamma_\Phi \nabla \Phi)) \cdot d\mathbf{S} \approx \sum_f \Gamma_\Phi (\mathbf{S} \cdot \nabla_f \Phi), \tag{4.5}$$

where for orthogonal grids, the term ∇_f is defined by

$$\nabla_f \Phi = \frac{\Phi_N - \Phi_P}{|\mathbf{d}|}, \tag{4.6}$$

where $\mathbf{d}$ is a vector, which represents the distance between the cell center of the control volume of interest, such as P, and the center of its neighboring cells, as N.

However, for non-orthogonal grids, the diffusion term is divided into two terms, in which the second term is a correction for the non-orthogonality, in order to preserve a second-order accuracy, as presented by Eq. (4.7):

$$\mathbf{S}\cdot\nabla_f\Phi = \underbrace{|\Delta|\nabla^{\frac{1}{f}}\Phi}_{\text{orthogonal contribution term}} + \underbrace{\mathbf{k}\cdot(\nabla\Phi)_f}_{\text{non-orthogonal correction term}} . \tag{4.7}$$

Considering this correction, the vector Δ and $\mathbf{k}$ are determined by satisfying the relation as $\mathbf{S} = \Delta + \mathbf{k}$, where vector Δ is chosen to be parallel to vector $\mathbf{d}$. Last but not least, the source term is approximated by a simple linearization process, so the integration of this term over the control volume is

$$\int_{V_P} S_\Phi(\Phi)dV = S_I V_P \Phi_P + S_E V_P, \tag{4.8}$$

where the subscripts I and E refer to implicit and explicit, respectively. In addition, the linearization process of the terms S_E and S_I depend on Φ, as $S_\Phi(\Phi) = \Phi S_I + S_E$, while P refers to the center of the control volume of interest.

4.1.3.3 Temporal discretization of the Transport Equation Terms

Finally, to complete the discussion about the discretization of the transport equation terms, the temporal term, which represents the time-dependent behavior of the system, must be considered. Usually, the choice of the time-integrator scheme depends on the type of equations being solved. For the purpose of this work, in which the flow is governed by high Reynolds numbers in the regions close to the wind turbine's blades, the implicit second-order upwind Euler scheme is considered to achieve a better convergence during the iterative process. The scheme is implemented by the Backward approach [68], in which the information from the current and previous time steps are stored, and the discretized form of the temporal derivative is obtained by considering the Taylor series expansion of Φ in time, around the new value of Φ, as $\Phi(t + \Delta t) = \Phi^n$. Thus, the term expansion is presented as follows,

$$\Phi(t) = \Phi^0 = \Phi^n - \frac{\partial\Phi}{\partial t}\Delta t + \frac{1}{2}\frac{\partial^2\Phi}{\partial t^2}\Delta t^2 + O(\Delta t^3) \tag{4.9}$$

Therefore, the discretized form of the temporal derivative term, in a first-order accuracy, is given by

$$\frac{\partial\Phi}{\partial t} = \frac{\Phi^n - \Phi^0}{\Delta t} + O(\Delta t^2). \tag{4.10}$$

To achieve second-order accuracy, the additional Taylor series term for the previous time step must be considered as,

$$\Phi(t-\Delta t)=\Phi^{00}=\Phi^{n}-2\frac{\partial\Phi}{\partial t}\Delta t+2\frac{\partial^{2}\Phi}{\partial t^{2}}\Delta t^{2}+O(\Delta t^{3}). \tag{4.11}$$

In order to eliminate the truncation error with scales of Δt, the Backward scheme is obtained by combining Eqs. (4.9) and (4.11). Thus, the second-order approximation of the temporal derivative term is obtained by,

$$\frac{\partial\Phi}{\partial t}=\frac{\frac{3}{2}\Phi^{n}-2\Phi^{0}+\frac{1}{2}\Phi^{00}}{\Delta t}. \tag{4.12}$$

According to Moukalled et al. [68], the coefficients considered in the time derivative approximation via Taylor series expansions achieve a second-order accuracy for the temporal discretization scheme. However, the boundedness of the solution is not guaranteed.

Additionally, the convergence stability of the temporal discretization methods is limited by the Courant number,

$$Co=\frac{\mathbf{U}_{f}\Delta t}{|\mathbf{d}|}, \tag{4.13}$$

where $\mathbf{U}_f$ is the control volume velocity at the face cell, Δt is the time step, and $\mathbf{d}$ is the vector that represents the distance between the center of the control volume cell of interest P and its neighboring cells centers. Therefore, the Courant number represents a measure of the flow information being carried, which transverses a control volume cell of the mesh in a given time step. Also, it is worth mentioning that the Courant-Friedrichs-Lewy (CFL) refers to the maximum allowable Courant number, which certain time-integrator schemes can employ, and also defines the time-step sizing of the transient simulation. Usually, explicit methods have CFL conditions close to the unit and small time-steps sizing, while implicit schemes allow larger CFL conditions and larger time-step sizing [65]. However, as in spatial discretization, the size of the control volume cells can influence the accuracy of the simulation solution; in temporal discretization, the time-step sizing plays the same rules in interfering the the accuracy of the obtained results.

4.1.4 Post-processing Procedures

Commonly, CFD simulations generate large amounts of data that are often difficult to interpret and visualize directly. The post-processing stage consists of analyzing the obtained data using different tools to transform the simulation results into meaningful and useful information that can be used to understand the behavior of the fluid flow.

Additionally, it is necessary to ensure the reliability of the results by employing validation and verification techniques. These methods quantify the error and uncertainty in CFD simulations. Usually, validation determines the accuracy of the implemented model by comparing the error with experimental data, while verification estimates whether the selected model accurately represents the real system by comparing the results between different numerical methods [65]. In this work, for all blade-resolved CFD simulations, a verification procedure was conducted by comparing the aerodynamic forces, in terms of generated thrust, power production, and distributed forces along the blade span, obtained from the CFD simulations with the results from OpenFAST code, which employs a different numerical method, as described previously in Section 3.1.3. Moreover, to ensure comparability between the results from the different numerical methods, both analyses were conducted considering the same operating and environmental conditions.

Furthermore, as the CFD simulations estimate the fluid properties in each cell of the computational domain, there are several ways to explore the flow characteristics. For instance, the ParaView software can be used to obtain iso-contours of the axial velocity, which are useful for visualizing the velocity field around the wind turbine and its wake. Figure 4.4 provides an example of such visualization of the flow features, showing a comparison of the instantaneous iso-contours of axial velocity obtained from a spatial discretization investigation, given by Mesh-1 and Mesh-2, of the NREL 5 MW.

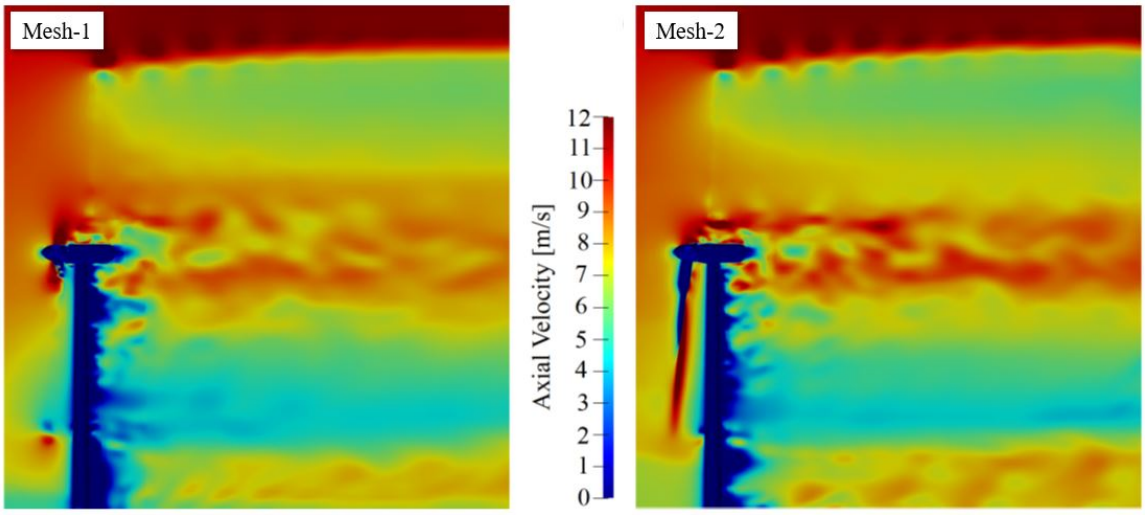

Figure 4.4: Instantaneous iso-contours of axial velocity gradients, obtained from a spatial discretization investigation of the NREL 5 MW, adapted from [66].

Similarly to the instantaneous iso-contours of the axial velocity, the iso-surfaces of a specific parameter of the flow can also be significant in capturing different features of the flow. Figure 4.5 illustrates the instantaneous iso-surfaces of the second invariant of the

velocity gradient tensor, the Q-criterion ($Q = 0.05$), obtained from a spatial discretization investigation of the NREL 5 MW, by Mesh-1 and Mesh-2.

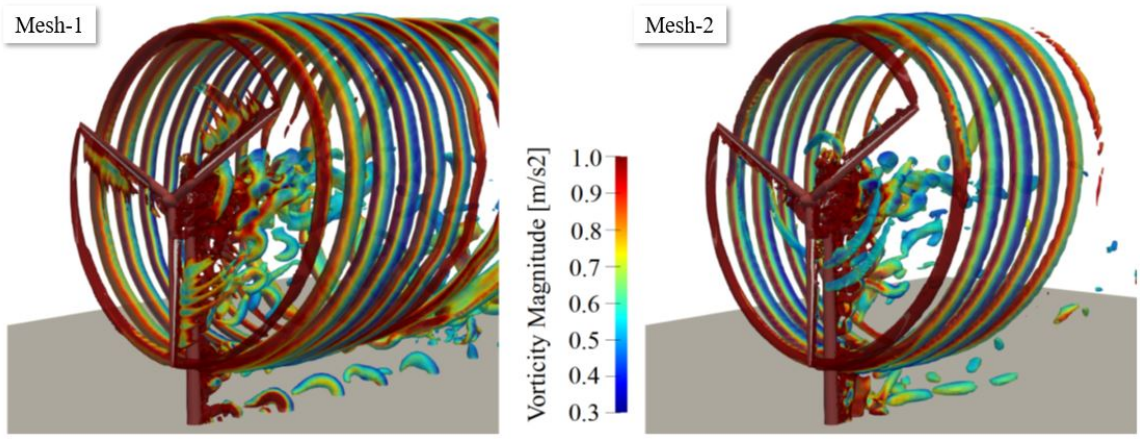

Figure 4.5: Instantaneous iso-surfaces of the Q-criterion colored by vorticity magnitude, from a spatial discretization investigation of the NREL 5 MW, adapted from [66].

Thus, there are many ways to explore the results of CFD simulations. The key is to use techniques that better suit the simulation data, allowing for a deeper understanding of the flow behavior, which is necessary in the design process of new systems and improving the performance of the existing ones.

4.2 Governing Equations

For the blade-resolved CFD simulations performed in this work, the governing set of equations is the continuity and Navier-Stokes equations, which represent for an incompressible flow the conservation of mass and momentum:

$$\nabla \cdot \mathbf{U} = 0, \tag{4.14}$$

$$\frac{\partial \mathbf{U}}{\partial t} + \nabla \cdot (\mathbf{U}\mathbf{U}) = -\nabla p + \nabla \cdot (\nu \nabla \mathbf{U}) + \mathbf{f}, \tag{4.15}$$

where t is time, ν is the kinematic viscosity, $\mathbf{U}$ is the velocity vector, p is the kinematic pressure, and $\mathbf{f}$ represents the surface tension and body forces such as gravity. As explained in the previous section, the finite volume method was employed to solve the governing equations of the specific problem being investigated in this work. In this regard, in this section, the terms from the governing equations which requires special attention, such as the nonlinear term of the momentum equation given by the convective term, the pressure-velocity coupling problem, and the dissipation term related to the turbulence, are discussed.

4.2.1 The non-linearity of the momentum equation

The discretization of the nonlinear convective term of the momentum equation, in which velocity is being transported by itself, represented by the second term in the left-hand side of Eq. (4.15), leads to

$$\nabla \cdot (\mathbf{UU}) = \sum_f \mathbf{S}(\mathbf{U}_f)(\mathbf{U}_f) = \sum_f F(\mathbf{U}_f), \tag{4.16}$$

$$\nabla \cdot (\mathbf{UU}) = a_P \mathbf{U}_P + \sum_N a_N \mathbf{U}_N, \tag{4.17}$$

where the coefficients a_P and a_N are related to the values interpolated at the faces of the control volume P and its neighbors indicated by N. The coefficients are a function of the control volume velocity at the face cell $\mathbf{U}_f$ and the same applies to the mass flux through a general face f, which must satisfy the continuity equation. Due to the complexity of the non-linear solvers and the computation effort required, a linearization of the convective term is recommended. In the linearization procedure, an existing velocity field that satisfies the continuity equation is considered to estimate the coefficients [69].

Despite its apparent simplicity, the discretization of convection has posed numerous challenges for numerical modeling in the past three decades. Up to now, several research works have resulted in a large number of convection schemes [68]. Although the literature regarding this topic is vast, in this section, two different schemes are discussed.

4.2.1.1 LUD and LUST schemes

Considering the wide range of convection discretization schemes, central discretization schemes (CDS) and upwind discretization schemes (UDS) are the two primary types of spatial discretization methods that are recommended for wind turbine simulations [23]. Usually, the choice of a discretization scheme depends on the turbulence model employed in the numerical simulations [24]. For the URANS-based simulations, it is typically recommended to use second-order accurate upwind discretization (UDS) methods, such as Linear-Upwind Differencing (LUD) scheme proposed by Warming and Beam [70], owing to their high level of stability. However, for LES-based models, non-dissipative central discretization (CDS) methods, such as Centered Linear interpolation (CL), are generally preferred over upwind-based schemes due to the introduction of a considerable amount of numerical diffusion in the numerical simulations from the upwind-based schemes that may interfere in the energy cascade of the turbulent structures from larger to smaller scales. That is to say, CDS is usually preferred over UDS to avoid the interaction of the turbulent

diffusion from the turbulence model with the numerical diffusion from the upwind-based scheme [69].

Furthermore, with the development of hybrid URANS-LES methods, which have been crucial for solving complex flow problems in engineering, significant efforts have been dedicated to developing advanced discretization methods for the convective term. Such methods exhibit central-like behavior and adjust to an upwind approach in regions dominated by strong gradients. For instance, the Linear-Upwind Stabilized Transport (LUST) scheme proposed by Weller [71] blends two second-order accurate schemes, providing superior numerical stability while maintaining the accuracy of the numerical solution [72]. However, although the hybrid central/upwind concept of the LUST scheme has shown promising results in DES simulations [73], there is currently a lack of information on its applicability in URANS simulations, specifically in terms of blade-resolved simulations of wind turbines, which are governed by high Reynolds numbers, in terms of results accuracy and the computational effort required. The LUD and LUST schemes are described in detail in Chapter 6, along with the numerical investigations conducted to assess their impact on the accuracy of the simulation results and computational costs, considering different turbulence modeling approaches.

4.2.2 Pressure-velocity Coupling Problem

As the compressibility effect, which occurs at the blade tip of large wind turbines, can be neglected [22], a pressure-based solver is employed to model the flow as incompressible. Therefore, to discretize the kinematic pressure term, a semi-discrete form of the momentum equation is considered,

$$a_P \mathbf{U}_P = \mathbf{H}(\mathbf{U}) - \nabla p, \tag{4.18}$$

where $\mathbf{H}(\mathbf{U})$ term represents the sum of the transport and source parts, respectively as

$$\mathbf{H}(\mathbf{U}) = -\sum_n a_n \mathbf{U}_n + \frac{\mathbf{U}}{\Delta t}. \tag{4.19}$$

Thus, considering the discretized form of the continuity equation given by,

$$\nabla \cdot \mathbf{U} = \sum_f \mathbf{S}\mathbf{U}_f = 0. \tag{4.20}$$

The velocity at the center of the cell of interest is obtained by considering Eq. (4.18) as,

$$\mathbf{U}_P = \frac{\mathbf{H}(\mathbf{U})}{a_P} - \frac{1}{a_P}\nabla p. \tag{4.21}$$

Hence, considering Eq. (4.21), the velocity at the cell's face, which is considered for the calculation of the fluxes are expressed by

$$\mathbf{U}_f = \Big(\frac{\mathbf{H}(\mathbf{U})}{a_P}\Big)_f - \Big(\frac{1}{a_P}\Big)_f (\nabla p)_f. \tag{4.22}$$

Therefore, the pressure equation is obtained by substituting Eq. (4.22) into the discretized form of the continuity given by Eq.(4.20) as,

$$\nabla \cdot \Big(\frac{1}{a_P}\Big) = \nabla \cdot \Big(\frac{\mathbf{H}(\mathbf{U})}{a_P}\Big), \tag{4.23}$$

$$\nabla \cdot \Big(\frac{1}{a_P}\Big) = \sum_f \mathbf{S}\Big(\frac{\mathbf{H}(\mathbf{U})}{a_P}\Big)_f. \tag{4.24}$$

Thus, the discretized form of the incompressible Navier-Stokes equations is obtained by rearranging the terms as:

$$a_P \mathbf{U}_P = \mathbf{H}(\mathbf{U}) - \sum_f \mathbf{S}(p)_f, \tag{4.25}$$

$$\sum_f \mathbf{S}\Big[\Big(\frac{1}{a_P}\Big)_f (\nabla p)_f\Big] = \sum_f \mathbf{S}\Big(\frac{\mathbf{H}(\mathbf{U})}{a_P}\Big)_f, \tag{4.26}$$

where a linear simultaneous dependence between velocity and pressure is observed, as the flow is incompressible and the density is constant, resulting in a lack of an equation to estimate the pressure field directly, consequently, a coupling between pressure and velocity introduces a restriction in the flow field solution.

In order to address the difficulty of pressure determination, Patankar [74] proposed a solution for the segregated method, which employs a staggered grid. In this approach, the velocity and pressure are estimated in different regions of the cell to stabilize the solver convergence. Based on this solution strategy, researchers have developed different versions of the PISO algorithm [75] and SIMPLE algorithm [67], which are the most common methods for solving the pressure-velocity coupling problem.

Usually, the SIMPLE algorithm and its variations, such as SIMPLEC, are employed in steady-state solvers, while the PISO algorithm and its variations are employed in transient simulations [65]. In the blade-resolved simulations conducted in this work, both methods were considered in the CFD simulations. Whereas SIMPLE [67] and SIMPLEC [76] algorithms were considered to initialize the numerical simulations, the iterative form

of the PISO algorithm [77] was employed for the transient analysis. Figure 4.6 illustrates the steps of the SIMPLE and SIMPLEC algorithms, which, according to Versteeg and Malalasekera [65], are the same. However, the SIMPLEC algorithm employs a different equation for the velocity correction, in which less significant terms are omitted. The steps of the PISO algorithm are presented in Chapter 5 along with the numerical investigation of the NREL 5MW wind turbine conducted to compare different solver strategies.

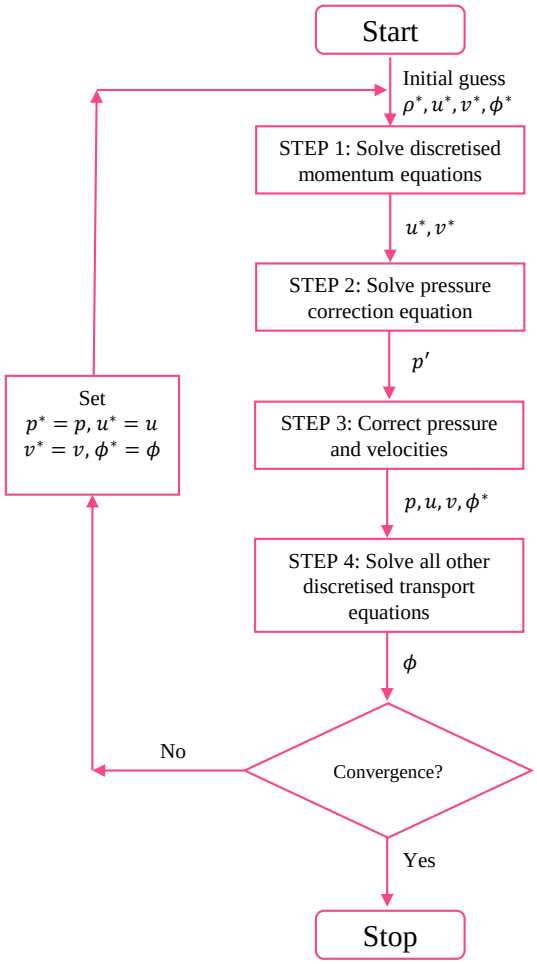

Figure 4.6: Flow chart of the SIMPLE and SIMPLEC algorithms, adapted from [65].

4.2.3 Turbulence Modeling

In nature, as well as in engineering applications, most of the flows are turbulent. Turbulent flows are time-dependent, chaotic, dissipative, and diffusive. Also, the vorticity fluctuations are three-dimensional, including a significant range of length scales, from the smallest vortices, which are characterized by Kolmogorov scales, to the flow structures that have sizes of the same order of the geometry [78].

Even though turbulence is a continuum phenomenon governed by the fluid mechanics equations, each flow pattern presents unique features, which in numerical simulations are associated with boundary and initial conditions, making a general solution of the Navier-Stokes equations for turbulent flows unavailable [78]. As the deterministic approach is not suitable to characterize turbulent flows, statistical methods are a convenient alternative due to the state of continuous instability, in which the turbulent flow can be described as separating the fluctuations from the properties of the mean flow [79]. However, applying statistical techniques to the momentum equations used to describe turbulent flows leads to a set of unknown variables, which requires the use of turbulence models and additional relations to be estimated [78]. In this regard, turbulence modeling remains one of the most important and challenging tasks in CFD, as it aims to provide accurate approximations of the physical behavior of turbulent flows.

4.2.3.1 Turbulence Models for Wind Turbine Simulations

Despite the increasing accessibility of high-performance computing (HPC) systems, the investigation of the flow around wind turbine rotor blades using blade-resolved modeling through CFD methodologies has revealed that obtaining a numerical solution of the Navier-Stokes (N-S) equations via direct numerical simulations (DNS) to analyze wind turbine performance remains infeasible [56, 57, 59]. In this regard, turbulence models have been vastly used to estimate wind turbine aerodynamic forces and wake behavior while keeping computational costs at a reasonable level to evaluate the most important turbulence effects [24]. Several options of turbulence models are available, differing primarily in accuracy and computational costs. For instance, the Large Eddy Simulation (LES) model offers an alternative approach for turbulence modeling, where the governing equations are solved using the mesh as a filter to solve the larger scales of turbulent motion. In comparison, smaller scales, known as subgrid-scales (SGS), are modeled instead [79].

Another option that arises from the statistical procedure applied to the Navier-Stokes equations is the Reynolds Averaged Navier-Stokes (RANS) model. The RANS equations are commonly employed as turbulence modeling techniques in engineering studies. The RANS equations can be used in steady and unsteady formulations, which has led to the introduction of the term Unsteady Reynolds-Averaged Navier-Stokes (URANS) nomenclature [80]. Also, due to the mathematical procedure involved, the Reynolds stress tensor, which is composed of six unknown quantities, results in a closure problem. Therefore, the relations used to solve de Reynolds stress tensor determine different types of URANS models. Among the ample variety of closure models, the SST k-ω model is commonly

employed to represent aerodynamic loads in the presence of adverse pressure gradients [81–83].

For instance, URANS k-ω SST turbulence model has been employed for wind turbine modeling in the OpenFOAM software, specifically for a small-scale wind turbine, and presented satisfactory agreement between the CFD results and the calibrated experimental tests in terms of the wind turbine's performance coefficients [84]. Usually, URANS-based models are preferred over LES or DNS approaches due to the lower computational costs associated, which are primarily determined by resolution requirements [79]. Although LES is advantageous in modeling anisotropic turbulent flow, where large-scale structures dominate, the model presents difficulties in determining flow properties in the wall region of the boundary layer [29, 80], even when implemented with a proper wall function [85]. Such limitation of the LES model restricts its application for blade-resolved simulations regarding the prediction of unsteady aerodynamic loads on the blades of wind turbines.

Therefore, the hybridization of LES into an improved approach, such as the Detached-Eddy Simulation (DES) model, has demonstrated reliable predictions of flow separation, recirculation zones, and vortex shedding in turbulent flows, providing better accuracy when compared with RANS and LES methods [86]. The application of DES to model aerodynamic problems is promising due to the possibility of employing the URANS-based models in the large areas of the boundary layer, while LES is efficiently applied at the regions where the momentum transfer is dominated by large structures, like the wake [80].

Nevertheless, despite the significant advantages of the DES model, only a few investigations have implemented blade-resolved CFD simulations of megawatt-scale wind turbines using the DES approach due to the difficulties of adequately connecting the turbulence model with other parts of the numerical arrangement, such as numerical schemes, spatial and temporal discretization refinements. Thus, in the investigations presented in Part III, a comparison between the URANS k-ω SST and the DES model was performed considering different numerical schemes of the convective term, in addition to different spatial and time discretization strategies.

4.2.3.2 Near-Wall Region Modeling

The features of turbulence close to the wall are highly different from those in other regions of the flow, so an appropriate model is required to model the near-wall region. To estimate the turbulent flow close to the wall, a proper mesh refinement must be considered to satisfy the requirement of the turbulence model based on the y^+ parameter.

The y^+ parameter is given by

$$y^+ = \frac{y u_\tau}{\nu}, \tag{4.27}$$

where u_τ is the friction velocity,

$$u_\tau = C_\mu^{1/4} \sqrt{k}, \tag{4.28}$$

and k is the value of turbulent kinetic energy at the center of the cell adjacent to the wall, obtained through the relation $k = k^+ \times u_\tau^2$. Fig. 4.7 illustrates the three distinct regions close to the wall that are denominated based on the variation of the y^+ parameter.

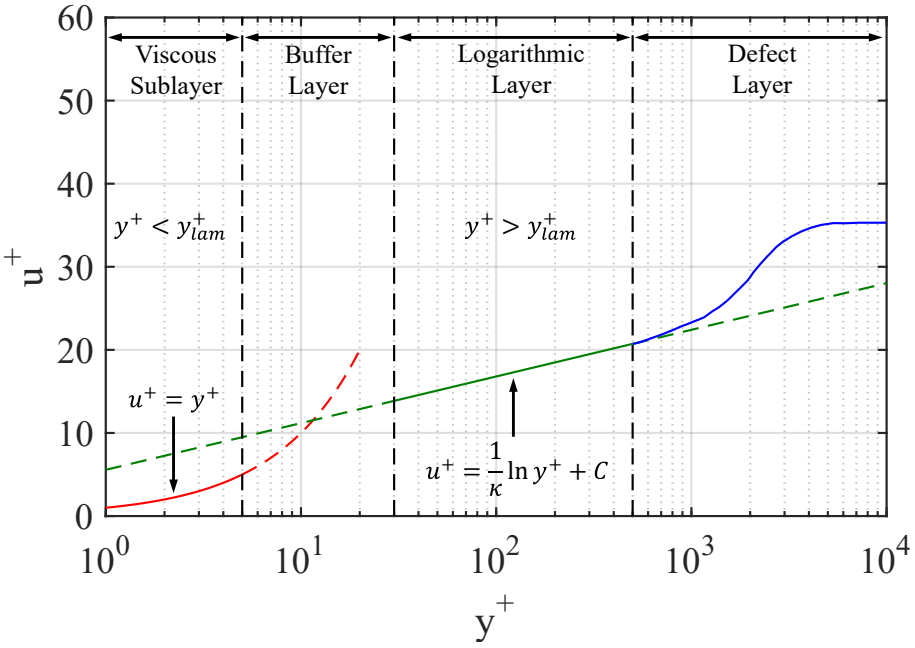

Figure 4.7: Velocity profiles at different regions of a turbulent boundary layer, adapted from [29, 66].

The approach employed to model the near-wall region in both turbulence methods investigated in this work considers that a high Reynolds number dominates the flow in this region. Wall functions were employed to estimate the turbulent quantities ν_t, k, and ω, whereby proper relations are used according to the value of y^+. The wall functions employed use the y^+_{lam} parameter as a reference for the y^+ value in the boundary layer. This approach, which is available in the OpenFOAM software, based on [87], avoids the buffer region, which brings stability to the turbulence modeling in the near-wall region by allowing the model to switch between the viscous and logarithmic regions of the boundary layer. More details of the approach are described in Chapters 5 and 6.

4.3 OpenFOAM Software

The variety of blade-resolved simulations investigations presented in Part III of this work were conducted using the open-source OpenFOAM software. The software acronym refers to (Open-source Field Operation And Manipulation).

OpenFOAM is an object-oriented C++ framework that enables the solution of a wide range of problems involving fluid mechanics through the finite volume discretization approach [68]. Most of the solvers and models required to develop a CFD model are already implemented in the software's utilities, making the use of the software direct and intuitive. The software's library arrangement, which includes a set of object classes, allows the users to manipulate all parts of the numerical arrangement, including the mesh, discretization schemes, and a wide variety of solvers parameters. Further details about the OpenFOAM software libraries and applications are presented by Moukalled et al. [68].

4.3.1 High-Performance Computing Environment

A High-Performance Computing (HPC) environment is a system designed to provide high levels of computing performance to solve complex and demanding computational problems that require large amounts of operations, memory, and storage. Several steps are considered when using the OpenFOAM software for parallel computing, such as decomposing the mesh and fields, running the application in parallel, and post-processing the decomposed case. In addition, the parallel execution uses the OpenMPI implementation of the standard message passing interface (MPI), and the user can choose the method for the decomposition and interfaces to external, third-party decomposition routines [88].

As OpenFOAM's parallel behavior varies depending on the type of problem being investigated and is not well understood [89], a scalability test is highly recommended before conducting the simulations. This type of test allows the identification of the best distribution of the mesh and fields over the number of available computer cores to ensure the best communication speed among them. Two supercomputers were used to perform the blade-resolved simulations presented in Part III of this work in an HPC environment. They were the NextGenIO supercomputer from the Edinburgh Parallel Computing Centre (EPCC), in which each node has two Intel Xeon Platinum 8260M Cascade Lake, 2.4 GHz, 48 cores and 192 GB of RAM and the Brazilian supercomputer SDumont, in which each node has two 12 core Intel Xeon Cascade Lake Gold 6252 processors, 3.7GHz, 24 cores and 256Gb of RAM.

PART III

BLADE-RESOLVED CFD INVESTIGATIONS

5 BLADE-RESOLVED NUMERICAL SIMULATIONS OF THE NREL 5 MW WIND TURBINE IN FULL SCALE: A STUDY OF PROPER SOLVER CONFIGURATION AND DISCRETIZATION STRATEGIES

Despite the proven effectiveness of CFD methodologies used to analyze the unsteady aerodynamic behavior of wind turbine blades and wakes, only a few studies utilizing this approach have considered the full megawatt scale of the wind turbine geometry due to the complexity of the numerical simulation and computational demand required. Previous research has investigated the multi-physical problem with a similar methodology and has contributed essential insights regarding the physics of the problem. However, the impact of the simulation setup on the accuracy of the obtained results, with respect to numerical schemes and solver parameters used, was only briefly addressed.

As the numerical arrangement can impact the accuracy of the simulation results, as well as its computational cost, this chapter aims to maximize the reliability of the CFD methodology as a tool to investigate the performance of wind turbines at full-scale. Therefore, an investigation with respect to the solver configuration and its influence on the accuracy of the results and computational costs of blade-resolved simulations is presented.

To perform the blade-resolved numerical investigation of the NREL 5 MW baseline wind turbine for offshore applications, including blade-tower interference, the iterative form of the PISO algorithm was considered in its generic form and with an extra step to correct the pressure before the beginning of the iterative process in each time step. The wind turbine was analyzed considering its full dimensions under the operating condition of optimal wind-power conversion efficiency for a wind speed of 10 m/s at hub height. The power production generated thrust and forces distribution along the blade span were estimated considering different spatial and temporal discretization strategies.

The blade-resolved CFD simulations developed in this chapter are presented through a paper published in Energy.

Energy 254 (2022) 124368

Contents lists available at ScienceDirect

Energy

journal homepage: www.elsevier.com/locate/energy

Blade-resolved numerical simulations of the NREL offshore 5 MW baseline wind turbine in full scale: A study of proper solver configuration and discretization strategies

M. de Oliveira*, R.C. Puraca, B.S. Carmo

University of São Paulo, Escola Politécnica, Dept. of Mechanical Engineering, Brazil

ARTICLE INFO

Article history:
Received 29 October 2021
Received in revised form
9 May 2022
Accepted 22 May 2022
Available online 28 May 2022

Keywords:
NREL 5 MW Wind turbine
Blade-resolved simulations
Iterative PISO Solver
Spatial and temporal investigations
Computational cost analysis

ABSTRACT

This paper presents a blade-resolved numerical investigation of the NREL 5 MW baseline wind turbine for offshore applications including blade-tower interference, analyzing the solver configuration and its influence on the results accuracy and computational costs. The wind turbine was analyzed considering its full dimensions under the operating condition of optimal wind-power conversion efficiency for a wind speed of 10 m/s at hub height. The power production, generated thrust, and forces distribution along the blade span were estimated. The computational analyses were carried out using a Computational Fluid Dynamics (CFD) methodology employing the Finite Volume Method (FVM) implemented in the OpenFOAM software considering different approaches of the Pressure Implicit Split Operator (PISO) solver and different mesh refinement strategies for the spatial discretization process, which resulted in two different meshes being investigated. For one of the meshes, a temporal discretization analysis was performed for three different CFL numbers. The iterative form of the PISO algorithm was considered in its generic form and with an extra step to correct the pressure before the beginning of the iterative process in each time step. Both approaches can be accomplished in OpenFOAM through the PIMPLE solver facilities for the treatment of the pressure-velocity coupling in unsteady problems. The analysis of the transient incompressible turbulent flow was conducted considering the same turbulence model for all CFD investigations, the URANS $k - \omega$ SST. A numerical verification was conducted in each analysis by comparing the CFD results against values obtained using the blade element momentum theory, implemented in OpenFAST. To conclude each analysis, a computational cost investigation was carried out. Finally, for the spatial and temporal discretization investigation, detailed information regarding the flow characteristics is presented. According to the accuracy of the results obtained through the CFD simulations, the best numerical arrangement is given by the iterative PISO with face flux correction as pressure-based solver and a temporal discretization which employs lower values of CFL, such as 1 or 2.

1. Introduction

Motivated by environmental issues such as global warming and air pollution, the use of renewable energy sources has become a relevant strategy to avoid these unfavorable impacts [1,2]. Among the options, wind energy has developed into a mainstream source of electricity due accelerated technology development and increase of productivity with scale. These aspects also led to the expansion of wind energy to offshore areas, which can present outstanding wind resources [3,4].

However, the growth in number and size of wind turbines does not come without challenges. The environment in which the wind turbines operate include atmospheric boundary layer and turbulence effects which vary spatially. Moreover, the substantial increase in the size of the commercial wind turbines due to the economy of scale, and the wind turbine blades-tower interaction, result in several uncertainties regarding the aerodynamic loads prediction and wake behaviour. Therefore, considering that the cost associated with offshore installations are superior, the need of better numerical codes to accurately predict the offshore wind turbine loads in the design phase become more important.

To date, few experimental campaigns have being performed to quantify the unsteady three-dimensional aerodynamic behaviour

* Corresponding author.
E-mail address: mariellededeoliveira@usp.br (M. de Oliveira).

https://doi.org/10.1016/j.energy.2022.124368
0360-5442/

Nomenclature

AMI	Arbitrary Mesh Interface
CFD	Computational Fluid Dynamics
CFL	Courant-Friedrichs-Lewy
DES	Detached Eddy Simulation
FVM	Finite Volume Method
HAWT	Horizontal Axis Wind Turbine
LES	Large Eddy Simulation
N−S	Navier Stokes
NASA	National Aeronautics and Space Administration
NREL	National Renewable Energy Laboratory
OWTs	Offshore Wind Turbines
PISO	Pressure Implicit Split Operator
SIMPLE	Semi-Implicit Method for Pressure-Linked Equations
SIMPLEC	Semi-Implicit Method for Pressure-Linked Equations Consistent
SST	Shear Stress Transport
UAE	Unsteady Aerodynamic Experiment
URANS	Unsteady Reynolds-Average Navier-Stokes
WT	Wind Turbine
Co	Courant number
P_k	Production of specific kinetic energy
Re_L	Reynolds number
Δt	Time step
Φ	Generic variable
ε	Specific dissipation rate of the standard k-ε turbulence model
κ	von Kármán constant
ν	Kinematic viscosity
ν_t	Kinematic eddy viscosity
ω	Specific dissipation rate of the original k-ω turbulence model
$\overline{\mathbf{U}'\,\mathbf{U}'}$	Reynolds shear stresses tensor
τ_1, τ_2	Time-scales
N	Point in the centre of the neighboring control volume **N**
P	Point in the centre of the control volume **P**
U	Velocity vector
$\mathbf{U}_f$	Control volume velocity at the face cell
$\mathbf{U}_p$	velocity at the centre of the cell
d	Vector between **P** and **N**
f	Body forces
$\tilde{P_k}$	Production limiter of specific kinetic energy
a_N	Matrix coefficient corresponding to the neighbour **N**
a_P	Matrix corresponding to the central coefficient **P**
h_h	Hub height
h_o	Reference height
k	Specific turbulent kinetic energy
k^+	Dimensionless turbulent kinetic energy
p	Kinematic pressure
u_τ	Friction velocity
y	Height variation
y^+	Dimensionless wall distance
z_0	Roughness height
U_h	velocity at the hub height
U_x	velocity in x direction
D	Wind turbine diameter
F	Mass flux through a general face
H	Tower height
R	Blade radius
S	Area vector pointing out of the volume cell
t	Time

of horizontal-axis wind turbine (HAWT), such as the National Renewable Energy Laboratory (NREL) test reported in Ref. [5], where aerodynamic loads of a 10 m rotor of a two-bladed, downwind turbine were evaluated in an outdoor field under several environmental conditions, and the other NREL test reported in Ref. [6], in which an Unsteady Aerodynamic Experiment (UAE) of a heavily instrumented 20-kW HAWT, placed inside the world's largest wind tunnel at NASA's Ames Research Centre, was carried out under homogeneous conditions, almost no blockage effects and an equivalent Reynolds number of approximately one million. The tests were able to provide high-quality data which have shown that HAWT undergoes significantly complex aerodynamic loads and that 3D effects are prevalent. Even though the tests were able to provide important data which have been use to validate and enhance engineering models, due to the ever increasing power capacity of offshore wind turbines (OWT), for instance, the Robin Rigg wind farm comprises 58 OWT of 3 MW, Block Island wind farm consists of 5 OWT of 6 MW each, and the Thorntonbank wind farm is composed by 54 6.15 MW OWT [7], the development of more robust numerical models capable of considering these three-dimensional effects in the design phase to better predict the OWT performance is necessary [6,8]. Among the numerical approaches in which such effects are taking into account, the CFD technique has been shown to be a mature, promising and reliable method to investigate the unsteady aerodynamic behaviour of the flow around wind turbine blades and generated wakes [9,10].

Up to now, since the first blade-resolved simulation of a wind turbine rotor blade [11], an extensively number of CFD investigations regarding rotor-only simulations have been made, such as for the NREL Phase II rotor [12], the NREL Phase VI rotor [13] and for the MEXICO rotor [8]. Previous investigations also showed that it is yet not feasible to resort to direct numerical simulations (DNS) to analyse wind turbine performance, so the numerical solution of the Navier-Stokes equations requires special treatment of turbulence, either by making use of Unsteady Reynolds-Average Navier-Stokes (URANS) turbulence models [14,15], by performing Large Eddy Simulations (LES) [16], or by adopting a hybrid approach, called Detached Eddy Simulation (DES) [17]. According to Ref. [8], the URANS model is sufficient to predict the flow correctly when the flow is fully attached, whereas for considerably separated flow, the DES model has been put forward as a promising solution in the rotor-only investigations since it improves the accuracy with less computational cost than LES [18].

However, when considering the blades, nacelle and tower geometries of a megawatt-scale turbine in CFD investigations, more effort to optimize the computational cost, while achieve accurate results with the numerical modeling must be made. For example, in the investigations performed by Ref. [16], the quasi-steady regime for the power and thrust, which typically requires around 5−6 rotor revolutions to be established, was not achieved even for the coarsest mesh. The results considering only 3 revolutions were compared with the reduced-order wind turbine simulation tool NREL's FAST code [19], and differences of around 6% for power and 20% for thrust were observed. To perform the numerical investigations, the authors considered as turbulence model the hybrid DES approach, which due to the mesh strategy employed,

presented a high computational demand. Considering that to investigate the wind turbine performance, the flow around the blades is modeled with an URANS approach in the DES turbulence model, this work only considers the URANS model to deal with turbulence in order to reduce the computational cost and to be able to predict the power and thrust considering the operational steady state.

Different URANS turbulence model options were tested by other authors to simulate the flow field around a HAWT blade, such as one-equation [20], and two-equations [15,21] models. Tests performed by Ref. [22] showed that the Spalart-Allmaras one-equation model was less sensitive in the near wall region in representing the viscosity effects in the boundary-layer, and between the two-equations models, the standard $k-\varepsilon$ has shown to be inadequate for the aerodynamics loads evaluation of HAWT blades. On the other hand, the Shear Stress Transport (SST) k-ω model from Ref. [23] is vastly recommended for the prediction of aerodynamic forces of wind turbine blades in 3D investigations [15], presenting good agreement with experimental results such as those from the MEXICO project [24], and from the NREL Phase VI test [25].

Besides the turbulence model, there are other important factors to be considered during the CFD investigation of a HAWT, which impact directly in the simulation convergence and computational cost of such analysis. For instance, regarding the solver considered to predict the flow behaviour, since the compressibility effect which occurs at the blade tip of large wind turbines can be neglected [26], the flow is treated as incompressible through a pressure-based solver. The treatment of the pressure-velocity coupling in transient incompressible flows results in a large set of algebraic equations and an iterative approach is required to segregate the dependent variables and the governing equations being solved in a sequential manner [27]. Therefore, the basic form of the solution algorithm remains the same even with the inclusion of time dependence, turbulence and other transport equations. Regarding the difficulty related to the pressure determination [28], suggested a solution for the segregated method based on staggered grids in which velocity and pressure are estimated at different points of the cell to stabilize the solver convergence.

Among the solver algorithms options to obtain a segregated solution, the different forms of the Pressure Implicit with Splitting of Operators (PISO) [29], and the Semi-Implicit Method for Pressure-Linked Equations (SIMPLE) [30] algorithms are the most common and recommended methods to solve the pressure-velocity coupling problem in incompressible flow investigations. A variety of the PISO and SIMPLE algorithms has been employed in the numerical investigation of wind turbines [10,31–33]. Both algorithms present different attractive alternatives, the better option is the one which works in balance with the computational demand and the accuracy required for the problem being investigated. According to Ref. [34], the non-iterative PISO algorithm, which was developed initially by Ref. [29] to solve unsteady transient flows, has been successfully adapted for iterative solutions involving the pressure-velocity calculations. In addition, the iterative methods play a crucial role to achieve convergence in problems involving dynamic mesh [35], which requires special treatment such as the Arbitrary Mesh Interface (AMI) technique, which is the method considered in the investigations presented in this work.

In OpenFOAM, the iterative form of the PISO algorithm is achieved through the PIMPLE solver utility by changing the parameter nCorrector from 1 to 2 in the simulation control dictionary. The iterative approach is advantageous as it includes an outer loop correction for the iterative process and a second correction for the pressure is performed before going to the next time step. The modeling performed in the present investigations considered a dynamic mesh and the transient analysis were solved considering the iterative approach of the PISO algorithm, which is presented in the next section.

Last but not least, according to Jasak [36], the boundedness of the solution for diagonally equal systems of equations will be preserved only for matrices which present positive coefficients. Therefore, in order to provide the required condition that make the solver to work correctly, attention regarding the spatial discretization such as the non-orthogonality of the mesh, which can be treated through the source term by considering the appropriate corrections. In addition, smooth mechanisms are also important to obtain stability during the numerical calculations of the unsteady Navier–Stokes equations, due to the non-linearity of the convective terms which lead to oscillations of the solution in the presence of large gradients [37]. Therefore, besides the non-orthogonality correction, considering the increase in the numerical stability and computing efficiency obtained by Ref. [38], where a smoothing procedure was incorporated to the solver SIMPLEC through the inclusion of an extra correction for the velocity which adjusts the linearized momentum equation. In this work, similarly, to Ref. [38], an extra correction for the pressure which also adjusts the correction coefficients in the prediction of the linearized momentum equations, is considered in the algorithm approach of the iterative PISO solver with face flux correction, to verify its influence in the solution stability, results accuracy, and computational cost.

Heretofore, the reported blade-resolved simulations of a megawatt scale wind turbine, such as the NREL 5 MW, focused primarily on the determination of the wind turbine performance by modeling the multi-physical problem. For example, we can find works on fluid-structure interaction analysis [39,40] and aerodynamics performance considering the pitch angle variation and the aero-hydrodynamic coupled problem [41–43]. However, in all investigations the solver is presented, but no investigation regarding the influence of the solver parameters on the accuracy of the results or computational costs are analyzed. With the increase in the wind turbines power to values of the order of 15 MW, the numerical modeling in full scale becomes even more challenging, and the need of an optimized solver more evident. Therefore, in order to cover these needs, the target of this paper is to present a methodology based on a solver investigation to perform blade-resolved CFD simulations to adequately predict the aerodynamic loads and the overall wind turbine performance considering the baseline NREL 5 MW wind turbine for offshore applications in full scale, under operating condition of optimal wind-power conversion efficiency. These simulations are computationally expensive and challenging to set up and converge, so we hope the discussion and results we will present in the next sections will help in the modeling and simulation of other large wind turbines. The access to the entire flow field may be very valuable to comprehend the physics and improve the performance of wind turbines, and this might have a huge social and economical impact, given the accelerated growth that is predicted for offshore wind energy in the coming decades.

2. Methodology

To perform the numerical investigations, two different spatial discretization strategies were considered. For the first mesh being analyzed, Mesh-1, an extra face flux correction was considered and its good performance made us to also employ it in the analyses carried out with the second mesh being investigated, Mesh-2. After comparing the results among the two different spatial discretization strategies, Mesh-2 was selected as the most suitable one when considering the balance between results accuracy and computational cost. At last, for Mesh-2 a time discretization investigation was performed considering different Courant-Friedrichs-Lewy

(CFL) numbers, with the purpose of analyzing the influence of this convergence parameter in the results accuracy and computational cost.

The investigations were carried out considering the 3D URANS approach and the $k-\omega$ SST turbulence model. As a verification procedure, the CFD results were benchmarked against the results obtained with OpenFAST [44], which implements the blade element momentum method, considering the same NREL 5 MW wind turbine at the same environmental conditions.

The remainder of this section is dedicated to describe the governing equations considered to model the problem and also the solver algorithm employed in each CFD investigation.

2.1. Governing equations

Considering the problem being investigated, the governing set of equations is composed by the conservation of mass and conservation of momentum equations, given respectively by:

$$\nabla\cdot\mathbf{U} = 0, \tag{1}$$

$$\frac{\partial\mathbf{U}}{\partial t} + \nabla\cdot(\mathbf{UU}) = -\nabla p + \nabla\cdot(\nu\nabla\mathbf{U}) + \mathbf{f}, \tag{2}$$

where t is time, ν is the kinematic viscosity, $\mathbf{U}$ is the velocity vector, p is the kinematic pressure and $\mathbf{f}$ represents the body forces.

2.2. Discretization of the governing equations by the Finite Volume Method (FVM)

In this section the governing equations are discretized through the FVM in order to highlight the aspects which require special attention, such as the non-linearity of the momentum equation and the linear dependence between velocity and pressure. Detailed information regarding the FVM can be found in Ref. [28]. The discretization of the non-linear term given by the convective term in Eq. (2) by the FVM leads to

$$\nabla\cdot(\mathbf{UU}) = \sum_f \mathbf{S}(\mathbf{U}_f)(\mathbf{U}_f) = \sum_f F(\mathbf{U}_f), \tag{3}$$

$$\nabla\cdot(\mathbf{UU}) = a_P\mathbf{U}_P + \sum_N a_N\mathbf{U}_N, \tag{4}$$

where $\mathbf{S}$ is the area vector pointing out of the volume cell with magnitude equal to the face area, F represents the term $\mathbf{S}\cdot(\rho U)_f$, which is the mass flux through a general face, whereas $\mathbf{U}_f$ is the control volume velocity at the face cell. The coefficients a_P and a_N are related to the values interpolated at the faces of the control volume P and its neighbors indicated by N, and are functions of the velocity $\mathbf{U}$. The same goes for F, which must satisfy the continuity equation. Because of the complexity of the non-linear solvers and the computation effort required, a linearisation of the convective term is recommended. Considering the type of flow being investigated, and following the recommendations by Refs. [34,36], the calculation of the F term is performed using an upwind numerical method to guarantee the boundedness of the solution by preserving positive coefficients in the linear algebraic equation matrices.

To discretize the kinematic pressure term in Eq (2), a semi-discrete form of the momentum equation is considered,

$$a_P\mathbf{U}_P = \mathbf{H}(\mathbf{U}) - \nabla p, \tag{5}$$

where $\mathbf{U}_P$ is the velocity at the centre of the cell, $\mathbf{H}(\mathbf{U})$ consists of the sum of the transport and source parts, as in

$$\mathbf{H}(\mathbf{U}) = -\sum_N a_n\mathbf{U}_N + \frac{\mathbf{U}}{\Delta t}, \tag{6}$$

where Δt is the time step.

The discretized form of the continuity equation, Eq. (1), is given by

$$\nabla\cdot\mathbf{U} = \sum_f \mathbf{S}\mathbf{U}_f = 0. \tag{7}$$

The velocity at the centre of the cell of interest is obtained by considering Eq. (5), resulting in

$$\mathbf{U}_P = \frac{\mathbf{H}(\mathbf{U})}{a_P} - \frac{1}{a_P}\nabla p. \tag{8}$$

In addition, by considering Eq. (8), the velocity at the cell face, which is necessary for the calculation of the fluxes, is expressed by

$$\mathbf{U}_f = \left(\frac{\mathbf{H}(\mathbf{U})}{a_P}\right)_f - \left(\frac{1}{a_P}\right)_f(\nabla p)_f. \tag{9}$$

The pressure equation is obtained by substituting Eq. (9) into the discretized form of the continuity given by Eq. (7). Hereby, the discretized form of the kinematic pressure term is given by

$$\nabla\cdot\left(\frac{1}{a_P}\right) = \nabla\cdot\left(\frac{\mathbf{H}(\mathbf{U})}{a_P}\right) = \sum_f \mathbf{S}\left(\frac{\mathbf{H}(\mathbf{U})}{a_P}\right)_f. \tag{10}$$

Finally, the discretized form of the incompressible Navier-Stokes equations are given by

$$a_P\mathbf{U}_P = \mathbf{H}(\mathbf{U}) - \sum_f \mathbf{S}(p)_f, \tag{11}$$

$$\sum_f \mathbf{S}\left[\left(\frac{1}{a_P}\right)_f(\nabla p)_f\right] = \sum_f \mathbf{S}\left(\frac{\mathbf{H}(\mathbf{U})}{a_P}\right)_f, \tag{12}$$

with the calculation of the face fluxes F given by

$$F = \mathbf{S}\mathbf{U}_f = \mathbf{S}\left[\left(\frac{\mathbf{H}(\mathbf{U})}{a_P}\right)_f - \left(\frac{1}{a_P}\right)_f(\nabla p)_f\right]. \tag{13}$$

It is important to notice that in the discretized form of the Navier-Stokes set of equations given, Eqs. (11) and (12), a linear simultaneous dependence between velocity and pressure is observed. To handle this inter-equation coupling problem, special treatment is required.

2.3. Pressure-velocity coupling problem

Since the flow is incompressible, the density is constant, inducing a lack of one equation to estimate the pressure field directly. The pressure can be interpreted as a Lagrange multiplier that enforces the velocity field to be divergence-free, which is equivalent to obey the mass conservation equation. As recommended by Ref. [28], for a segregated solution, the mass flow rate across the cell faces is given by the aforementioned variable F, which can be estimated without any interpolation process. Based on [34,36], the pressure-based solver chosen to perform the CFD investigations was the iterative form of the PISO algorithm which can be implemented in OpenFOAM through the PIMPLE solver utility. By changing the setup of this solver, it is possible to obtain a variety of pressure-based algorithms such as the non-iterative and

the iterative PISO, transient SIMPLE, SIMPLEC and others [10].

The iterative PISO solver is an attractive option since for each time step, the algorithm solves the pressure corrections twice in an iterative approach to reach the desired tolerance. In the investigations conducted for our Mesh-1, an extra correction for the F term was aggregated to the iterative PISO solver and tested to verify its influence in the accuracy of the results and associated computational cost. A detailed information regarding the algorithm sequence solved in each time step is presented in Fig. 1 for the two approaches which were tested. It is possible to notice that when considering the face flux correction an extra correction for the pressure is performed before the start of the iterative PISO steps.

2.4. Temporal discretization scheme

The choice for the time-integrator scheme depends on the type of equations being solved [36]. In this work we employ an implicit second order upwind Euler scheme to achieve a better accuracy in time marching. The temporal discretization is carried out through the Backward scheme [45], in which the information from the current and previous time step is stored. The discretized form of the temporal derivative is obtained by considering the Taylor series expansion of a variable Φ in time around the new value of Φ as $\Phi(t+\Delta t)=\Phi^a$ as in

$$\Phi(t)=\Phi^b=\Phi^a-\frac{\partial\Phi}{\partial t}\Delta t+\frac{1}{2}\frac{\partial^2\Phi}{\partial t^2}\Delta t^2+O(\Delta t^3). \tag{14}$$

Therefore, the temporal derivative discretized term in a first-order accuracy is given by,

$$\frac{\partial\Phi}{\partial t}\Delta t=\frac{\Phi^a-\Phi^b}{\Delta t}+O(\Delta t^2). \tag{15}$$

To achieve second-order accuracy, the additional Taylor series term from the previous time step must be considered. This relation is given by

$$\Phi(t-\Delta t)=\Phi^c=\Phi^a-2\frac{\partial\Phi}{\partial t}\Delta t+2\frac{\partial^2\Phi}{\partial t^2}\Delta t^2+O(\Delta t^3). \tag{16}$$

In order to eliminate the truncation error with the scale of Δt, the Backward scheme combines Eqs. (14) and (16), so the second order approximation of the temporal derivative is obtained:

$$\frac{\partial\Phi}{\partial t}=\frac{\frac{3}{2}\Phi^a-2\Phi^b+\frac{1}{2}\Phi^c}{\Delta t}, \tag{17}$$

where Φ is the variable being calculated, Δt is the time step, and the coefficients a, b and c are given by

$$a=1+\frac{\Delta t}{\Delta t+\Delta t_b}, \tag{18}$$

$$c=\Delta t\times\frac{\Delta t}{\Delta t_b\times(\Delta t+\Delta t_b)}, \tag{19}$$

$$b=a+c. \tag{20}$$

As usually, in this work the stability of the temporal discretization method was limited by the Courant number,

$$Co=\frac{\mathbf{U}_f\Delta t}{|\mathbf{d}|}, \tag{21}$$

where $\mathbf{U}_f$ is the control volume velocity at the face cell, Δt is the time step and $\mathbf{d}$ is the vector that represents the distance between the cell centre of the control volume of interest denominated by P, and its neighboring cell centre. Therefore, the Courant number represents a measure of the information quantity being carried, which transverses a volume cell of the mesh in a given time step. It is worth mentioning that the CFL refers to the maximum allowable Courant number that a certain time-integrator scheme can employ. Usually, explicit methods have CFL condition close to the unit, while for implicit schemes the parameter can be larger than 1 as it is less sensitive to numerical instabilities [34].

In the numerical investigations of our Mesh-2, different CFL numbers were considered in order to understand the sensitivity of the results accuracy, and computational cost with respect to this parameter.

2.5. Turbulence modeling

Finally, by considering the appropriated additional set of transport equations to represent the turbulence model, an approximate solution for the Navier-Stokes set of equations can be obtained. An ideal turbulence model should minimize the complexity of the flow field in order to capture the features of the most significant part of the system physics [46]. For the reasons already mentioned in the introduction, here we employ the URANS method which is a statistical procedure applied to the Navier-Stokes equations. By taking the average of the N−S equations, the closure problem arises, i.e. there are not enough equations to solve the nonlinear Reynolds stresses tensor term. This gives rise to the turbulence models which are necessary to close the set of equations of the URANS model. Among the options to express the Reynolds stresses tensor in terms of known quantities, the most widely used methods correlates the mean velocity gradient and the Reynolds stresses tensor. In this regard, the most popular approach is to use the Boussinesq hypothesis, which prescribes a relation between the turbulent tensor and the kinematic eddy viscosity where the transfer of momentum by diffusion in molecular level is similar to the transfer of momentum in a turbulent flow due to the turbulent fluctuations. The evaluation of the kinematic eddy viscosity ν_t, can be made through different ways such as algebraic relations, or by solving transport equations. However, the most common method is to obtain the kinematic eddy viscosity as a function of the specific turbulent kinetic energy and its specific dissipation rate which stands out for the so called two-equations turbulent model [46].

The CFD simulations conducted in this work employed the two-equations k-ω SST turbulence model from Ref. [23], due its ability of predict flows with strong adverse pressure gradient with higher performance when compared to the variation of the k-ω models from Ref. [46], and the baseline from Ref. [47]. Therefore, when considering the k-ω SST turbulence model, a new set of governing equations is obtained. These equations which also consider the low-Reynolds corrections are presented in details in Appendix A, along with all the turbulence model auxiliary relations and constants.

2.6. Near-wall region treatment

The features of the turbulence close to the wall are highly different from the other regions of the flow, thus an appropriated model to treat the near wall region is required. To estimate the turbulent flow close to the wall, a mesh refinement must be

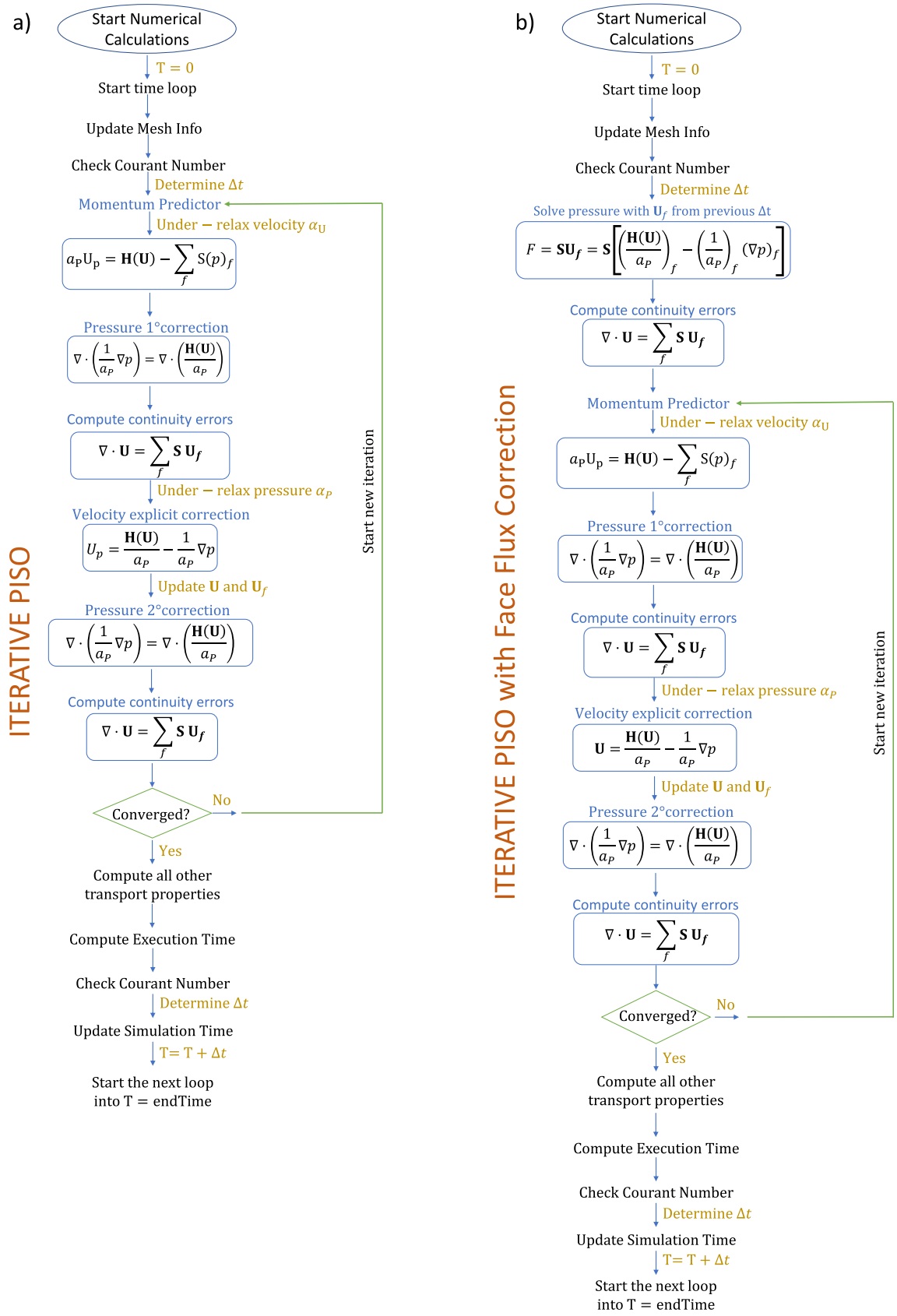

Fig. 1. Iterative PISO algorithm steps considered in the numerical investigation. a) Generic form, b) With face flux correction.

considered which must satisfy the requirement of the turbulence model based on the y^+ variable. In the current investigations, k and ω were modeled by the low Reynolds wall functions representing a model which can switch between the viscous and logarithmic regions of the boundary layer according to the position of y^+. In addition, ν_t is obtained using the Spalding wall function model [48,49], which also switch between viscous and logarithmic regions based on the value of y^+. A description of the near-wall regions, and the equations used to model the velocity close to the wall according to the y^+ in each one of the near-wall regions are presented in Appendix A.1.

3. Numerical simulations

In this section we detail the setup and parameters of the numerical investigations of the performance of the NREL baseline 5 MW offshore wind turbine in full scale. The data analyzed includes the power production, blade loading and wake aerodynamics pattern. The full wind turbine geometry is composed by three blades, the hub, the tower, and the nacelle, and more details about the design are available in Ref. [19]. Fig. 2 illustrates the case being investigated, which consists of the 5 MW wind turbine placed on an offshore site under the influence of a logarithmic non-turbulent wind profile.

3.1. Computational domain and boundary conditions

The full geometry was built using the software Solid Edge and imported into OpenFOAM, whereas all other parts of the computational domain were built around the wind turbine geometry using the snappyHexMesh utility. Fig. 3 illustrates the computational domain dimensions in meters and the boundary conditions, which were defined based in Ref. [50].

For all cases investigated the dimensions of the computational were the same: 500 m wide, 600 m long, 300 m high, and the rotor region 150 m to settle the rotor diameter which is considered as 124 m to taking into account the hub distance between the blades. The boundary conditions were also the same. At the inflow, the boundary condition for the velocity was of Dirichlet type, given by a prescribed logarithmic profile described as

$$U_x = v_o \frac{\log(y/z_o)}{\log(h_0/z_o)}, \tag{22}$$

where v_o is the velocity at 80 m high, chosen to be 10 m/s. Considering the location of the wind turbine in an offshore site, the roughness height z_o was set to be 0.001 m, representing the ocean rugosity. y represents the height variation and h_o is the reference height considered as 80 m. Still at the inflow, the boundary condition for the pressure was a null gradient (Neumann condition). For the turbulent quantities Dirichlet conditions were employed, with prescribed values estimated based on the most critical Reynolds number (at the blade tip), through the turbulence Reynolds number (Re_L) suggested by Ref. [51], used to estimate the turbulence length scale and the turbulence intensity. Based on that, the turbulence length scale for this region was 0.175 m, the turbulence kinetic energy $k = 3.2651\ \mathrm{m^2 s^{-2}}$, and the specific dissipation rate $\omega = 18.649\ \mathrm{s^{-1}}$, while the kinematic eddy viscosity was calculated based on the internal field everywhere. At the side and top planes, the boundary conditions for the velocity were symmetric plane condition, which corresponds to null normal velocity and zero normal gradient for the tangential velocity, pressure and turbulent quantities. For the turbine walls, no slip condition was imposed. At the rotor walls, the boundary condition for the velocity was of Dirichlet type. Since the mesh around this region is dynamic, a uniform rotor velocity of 1.1649 rad/s was prescribed, which is the rotor speed for a wind speed of 10 m/s. On the rotor walls and tower walls, Neumann boundary condition is applied for the pressure as a null gradient, while the turbulence properties receive the proper wall function treatment according with the y^+ value in the near wall region. At the outflow, the pressure was set to zero and the boundary condition for all other flow variables was null gradient.

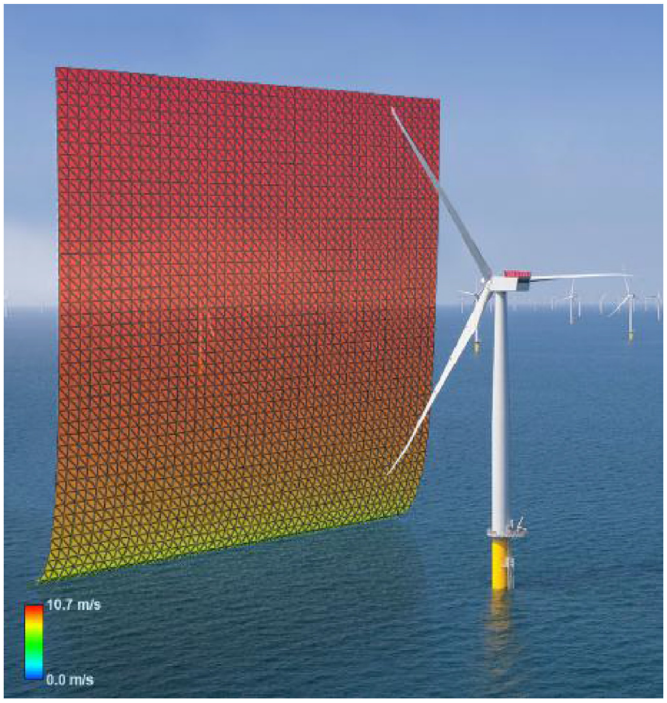

Fig. 2. Visualization of the case being investigated, which includes a 5 MW offshore wind turbine in full scale operating under a logarithmic non-turbulent wind profile.

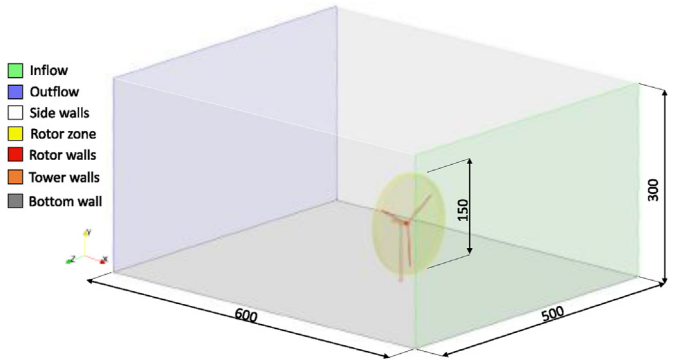

Fig. 3. NREL baseline 5 MW offshore wind turbine computational domain dimensions (in meters) and boundary conditions.

3.2. Spatial discretization

To perform the simulations, two different meshes, Mesh-1 and Mesh-2, were built considering different refinement strategies. Both meshes were built considering the same computational domain presented in Fig. 3. To build the non-uniform structured meshes, first the computational domain was decomposed in four main regions as presented in Fig. 4. Even though the partition of the computational domain regions was the same between the meshes

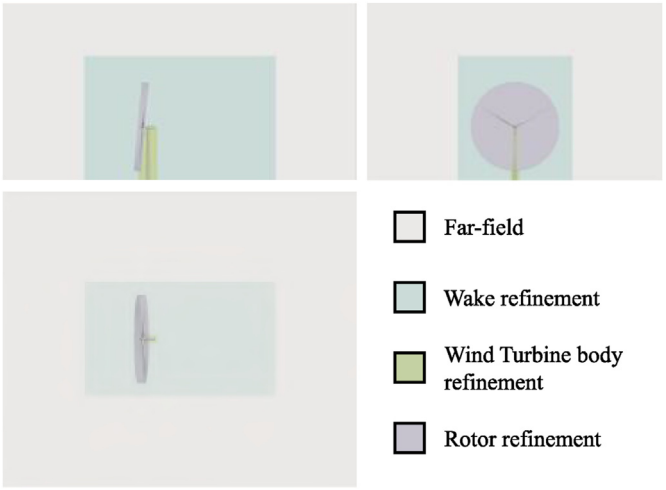

Fig. 4. Strategical partition of the computational domain to apply different mesh refinements.

being investigated, different cell sizes were adopted for each mesh. Table 1 presents the refinement applied in each region of the computational domain for both meshes being investigated. It is important to mention that both meshes have the same cell size close to the WT walls, in order to have y^+ parameter within the adequate range for the application of the turbulence model at the near-wall region. However, since the next steps of our research include the modeling of a free surface boundary condition in order to use this CFD methodology to model a floating offshore wind turbine (FOWT), Mesh-2 was built aiming a finer mesh in the inflow as well as the outflow region, to proper represent the free surface displacement. Therefore, to increase the refinement in the far-field region without the need of increase significantly the number of total cells in Mesh-2, the strategy chosen was to increase the cell size in the regions of the domain with low velocity and pressure gradients, based on the results obtained with Mesh-1. Regarding the mesh communication between the static and dynamic parts of the mesh, an arbitrary mesh interface (AMI) methodology [52] was considered for both meshes.

The main difference between the refinement strategies is in the rotor region, where the cells size was increased from 0.5 m for Mesh-1 to 1 m for Mesh-2, and in the wake region, where the cells size was increased from 1.5 m for Mesh-1 to 2 m for Mesh-2. Different cell sizes were adopted in the far field for both meshes, for Mesh-1 it started with element size of 25 m and decreased to 0.75 m close to the wind turbine. On the other hand, for Mesh-2 it started with element size of 8 m and decreased to 1 m close to the wind turbine. As a result, Mesh-1 and Mesh-2 were composed by 19, 942, 667 and 20, 744, 243 cells respectively. More details about the refinement strategy applied in each partition of the computational domain considered for each mesh being investigated can be seen in Fig. 5.

Table 1
Mesh sizing information (in meters) for each region of the computational domain for Mesh-1 and Mesh-2.

Region	Mesh-1	Mesh-2
Far-field	25	8
Wake refinement	1.5	2
WT body refinement	0.75	1
WT body surface	0.18	0.25
Rotor refinement	0.5	1
Blade surface	0.0625	0.0625
Total cells number	19,942,667	20,744,243

In addition, to perform the blade-resolved investigations considering the tower influence, a proper refinement close to the edges of the blades and tower, which must preserve the variation of the y^+ parameter in all these regions, is required. Fig. 6 illustrates the details of the meshes at different positions along the blade span indicated by R, and different distance from the ground indicated by H, when the blade is at azimuth angle of 180° which is in front of the tower. The information about the discretization properties at the different regions of the blade and tower is presented in Table 2, which includes the first cell height adopted in order to achieve the y^+ desired.

3.3. Numerical schemes

In all simulations the divergence terms were discretized using a second-order upwind scheme, chosen based on the modeling of similar problems to compute the convective fluxes [10,31]. Central differences were employed for the Laplacian terms, and the least-squares cell-based scheme was adopted for the gradient terms. The set of linear equations was solved based on [37,45], using the geometric-algebraic multi-grid (GAMG) algorithm for the symmetric matrices, and the preconditioned bi-conjugate gradient (PBiCG) with the DILU preconditioner for the non-symmetric matrices.

About the temporal discretization, as aforementioned, the second order implicit backward scheme was employed. The CFL number was limited and controlled by an adaptive time step to guarantee stability during the iterative process. Different CFL

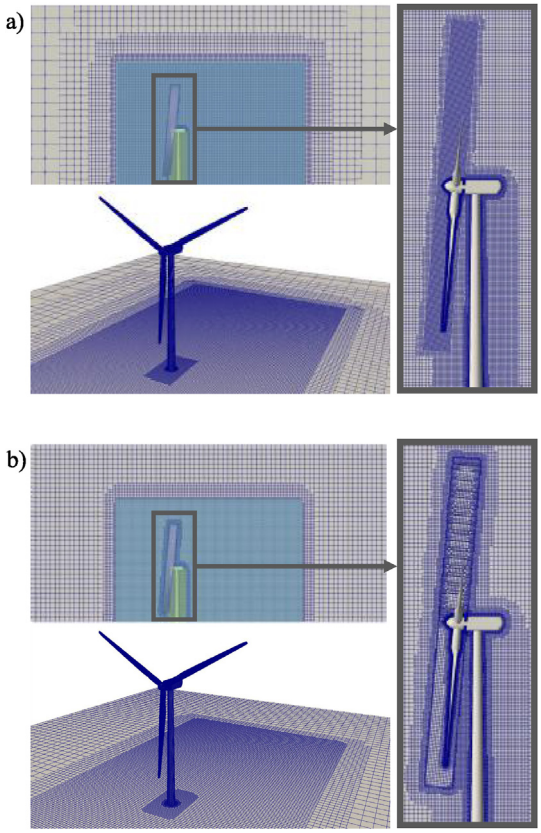

Fig. 5. Spatial discretization of the computational domain regions considered for a) Mesh-1, and b) Mesh-2.

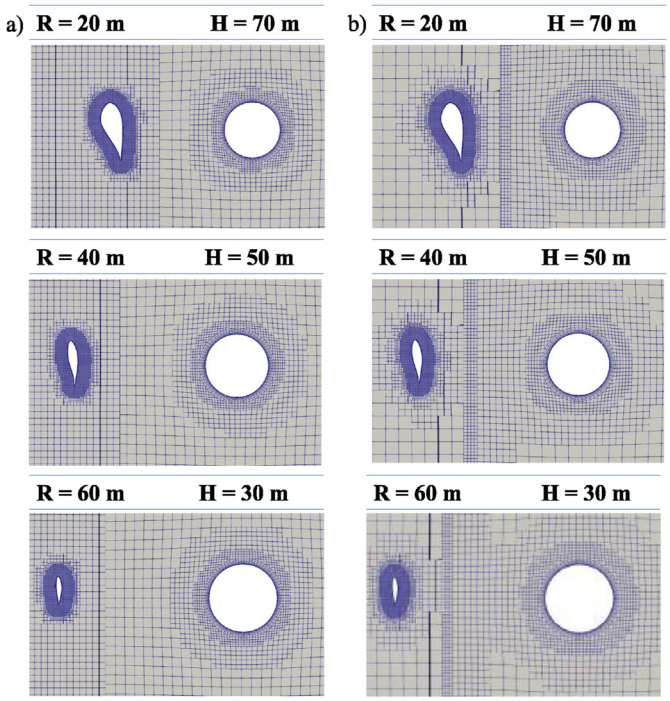

Fig. 6. Spatial discretization at different positions along the blade span, indicated by R and different distances from the ground, indicated by H, for a) Mesh-1 and b) Mesh-2.

numbers were applied for Mesh-2 to understand the sensitivity of the accuracy of the results and computational cost with respect to this parameter. This was possible because the CFL number can be larger than 1 for implicit schemes, since they are less sensitive to a numerical instabilities [36].

3.4. Solver information

For Mesh-1, two different iterative PISO algorithms were implemented, as presented in Fig. 1, which includes the iterative PISO in its generic form and the iterative PISO with face flux correction. For both investigations the pressure-based solver considered 5 sub-iterations for each time step and 2 corrections for pressure. The CFL number was limited to 2 for the transient analyses in both cases. For Mesh-2, only the iterative PISO with flux correction was considered.

The URANS $k-\omega$ SST turbulence model was employed in all cases and the iterations were considered converged according to Ref. [34], when the residuals of the set of estimated variables was equal or less than 10^{-6}. For each mesh, the initial conditions for the transient problem for all properties were the steady state solution for the problem after 500 iterations, obtained with the steady form of the SIMPLE algorithm. The computations were carried out in the Brazilian supercomputer Santos Dumont. To run the simulations the meshes were partitioned into 240 sub-domains using scotch decomposition, allocating 10 nodes in the cluster, where each node had two 12 core Intel Xeon Cascade Lake Gold 6252 processors, 3.7 GHz, and 256 Gb of RAM.

4. Results and discussion

First the results obtained with Mesh-1 regarding the different approaches of the iterative PISO solver as illustrated in Fig. 1 are presented. Next, a comparison between the different meshes using the same numerical setup is made to choose the more suitable one when comparing the computational cost and the accuracy of the results. Finally, Mesh-2 is used for an investigation about the temporal discretization.

4.1. Iterative PISO solver approaches

Here we compare the two different approaches of the iterative PISO solver, illustrated in Fig. 1, and the results are presented in two parts. First, comparisons of the generated thrust, power production and the forces distribution along the blade span obtained with both setups are presented, along with the results from the NREL OpenFAST code [44], considering the same environmental conditions. Subsequently, a discussion is made based on the computational cost associated with each approach of the iterative PISO solver tested.

4.1.1. Verification with OpenFAST

OpenFAST v2.5.0 [44] is a code capable of analyzing three-bladed HAWT, including the tower influence and different environmental conditions in the time domain. The code is a calibrated [53], and certified code by Germanischer Lloyd (GL) [54], which has been used both by research groups and in the industry worldwide for over 15 years, for the design and certification of wind turbines. It uses the blade element momentum theory and tip corrections to calculate the aerodynamic loads on the blades. In addition, the FAST code, previous version of the OpenFAST, was used by the NREL for the data acquirement, to map the performance of the theoretical wind turbine that is being investigated in this work, the NREL 5 MW reference wind turbine for offshore applications as presented in Ref. [19]. Therefore, we compare the results quantitatively with the results obtained in the OpenFAST, expecting that closer the results are from OpenFAST, closer we are from the expected numerical solution.

Fig. 7 illustrates a comparison of the wind turbine power production and the generated thrust for both algorithms of the iterative PISO tested, the generic form, and with an extra correction for pressure due to the face flux correction applied before the start of the solver loop. Besides, both CFD simulations results are benchmarked against the OpenFAST results.

Looking at the generated power and thrust comparison between the two approaches of the iterative PISO solver, Fig. 7, it is possible to notice that the generic form of the solver presented very similar

Table 2
Spatial discretization information at different positions along the blade span, indicated by R, and different distance from the ground, indicated by H, for Mesh-1 and Mesh-2.

	Blade	Tower	Blade	Tower	Blade	Tower
Position (Azimuth = 180°)	R = 20 m	H = 70 m	R = 40 m	H = 50 m	R = 60 m	H = 30 m
First cell height	1×10^{-3} m	1×10^{-2} m	1×10^{-3} m	1×10^{-2} m	1×10^{-3} m	1×10^{-2} m
Characteristic length	Chord	Diameter	Chord	Diameter	Chord	Diameter
	4.65 m	4.3 m	3.63 m	4.79 m	1.2 m	5.27 m
Re_{local}	7.2×10^6	2.8×10^6	11.3×10^6	3.1×10^6	11.7×10^6	3.3×10^6
Local air speed	23.2 m/s	9.9 m/s	46.6 m/s	9.65 m/s	69.9 m/s	9.28 m/s
y^+	60	260	120	253	180	242

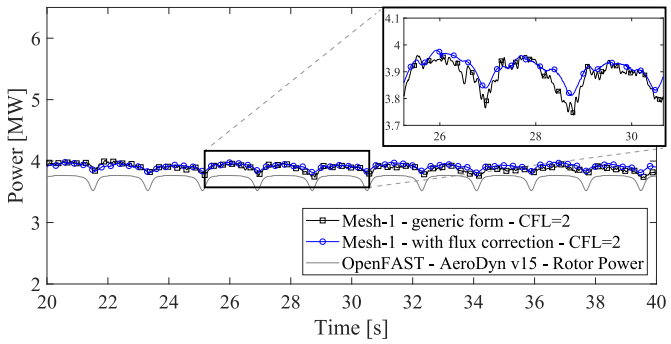

(a) Power.

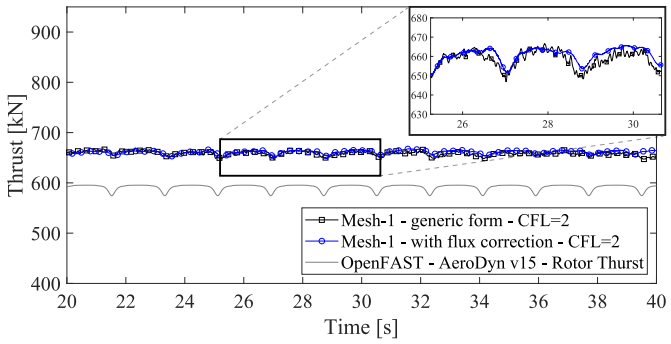

(b) Thrust.

Fig. 7. Generated power and thrust comparison between the iterative PISO solver using the generic form and with face flux correction approaches, benchmarked against OpenFAST results.

results in terms of low frequency components when compared to the approach with face flux correction, which can also be attested by looking at mean values in Table 3, for both power production and thrust. However, the time series presented significant noise for the generic form of the iterative PISO solver while for the approach with the extra pressure correction this behaviour was not observed. Since the wind profile considered in the investigation is non-turbulent, the instabilities captured in the generic form sign is interpreted as an oscillation caused by the numerical arrangement. Both algorithms presented higher mean values for both generated power and thrust when compared with OpenFAST results.

In addition, the distribution of the mean forces along the blades were also investigated and compared. As presented in Fig. 8, both methodologies of the iterative PISO solver presented similar behaviour in the normal and tangential forces prediction along the blade span, for both positions of the blade being analyzed. The 0° azimuth angle represents the blade aligned with the wind turbine in the z-direction pointing to the top wall of the computational domain, while the 180° azimuth angle represents the blade aligned with the wind turbine in the z-direction pointing to the bottom wall of the computational domain, which represents the position of the blade when it is crossing in front of the tower. Besides the quantitative analyses of the normal and tangential forces acting on the blades, we draw a comparison of instantaneous horizontal and vertical wind velocity profiles after 7 complete revolution at 4 different positions downstream in the wake region. These results are presented in Fig. 9 a) for the vertical plane and Fig. 9 b) for the horizontal plane. It is possible to observe that both methodologies of the iterative PISO solver led to similar results at all positions in the wake region. However, some fluctuations in the wind profile are present when considering the generic form.

Table 3
NREL 5 MW wind turbine performance comparison between the CFD simulations and OpenFAST code results.

	Mean	
	Power [MW]	Thrust [kN]
Mesh-1: generic CFL 2	3.88 ± 0.05	658.5 ± 4.4
Mesh-1: F corr. CFL 2	3.91 ± 0.04	664.4 ± 3.0
Mesh-2: F corr. CFL 1	3.49 ± 0.06	636.6 ± 5.5
Mesh-2: F corr. CFL 2	3.84 ± 0.05	636.6 ± 3.6
Mesh-2: F corr. CFL 4	4.08 ± 0.05	685.2 ± 3.4
OpenFast AeroDyn	3.72 ± 0.07	591.4 ± 5.9

A computational cost analysis considering the performance of each of the tested approaches showed that the extra face flux correction can be performed without significant extra computational demand as shown in Fig. 10. Both methodologies took approximated 11 h to complete the simulation of 1 s. The variation between the time to calculate one time step was on average 14.97 s for the generic form of the iterative PISO solver, against 15.61 s for the approach considering the face flux correction. In order to verify the computing efficiency independence regarding the spatial discretization, we tested both approaches of the iterative PISO algorithm for Mesh-2, in which the time to calculate one time step was on average 16.69 s for the generic form, against 17.02 s for the approach considering the face flux correction.

Therefore, considering the computational cost and numerical accuracy, we concluded that the most suitable solver option was the iterative form of the PISO algorithm with the face flux correction. The stability of the time series signals are important in these analysis due to the next steps of the CFD simulation, which as presented in Sec. 5.1, will increase significantly the instabilities during the numerical calculations, therefore the need of a smooth solution is necessary to be able of achieve convergence in the future investigations.

4.2. Investigation of spatial discretization strategies considering the iterative PISO solver with face flux correction

As presented in Figs. 5 and 6, different spatial discretization strategies were considered for Mesh-1 and Mesh-2. The results are presented in three parts. First a comparison of the generated thrust, power production and forces distribution along the blade span obtained with the different meshes are presented along with the results obtained with OpenFAST considering the same environmental conditions as performed in the CFD simulations. In sequence, the visualization of the flow features for each mesh is shown. Finally, a discussion is made based on the computational cost associated with each CFD case.

4.2.1. Verification with OpenFAST

A comparison for the wind turbine power production and generated thrust obtained through the CFD simulations, considering both spatial discretization strategies, and the results obtained with OpenFAST considering the same environmental conditions are shown in Fig. 11. It is possible to notice that both meshes presented similar results, slightly higher than those from OpenFAST. This can also be seen in Table 3. However, the results obtained with Mesh-2 were closer to those from OpenFAST.

It is also clear that power production results were very close to each other, while the generated thrust exhibited more noticeable

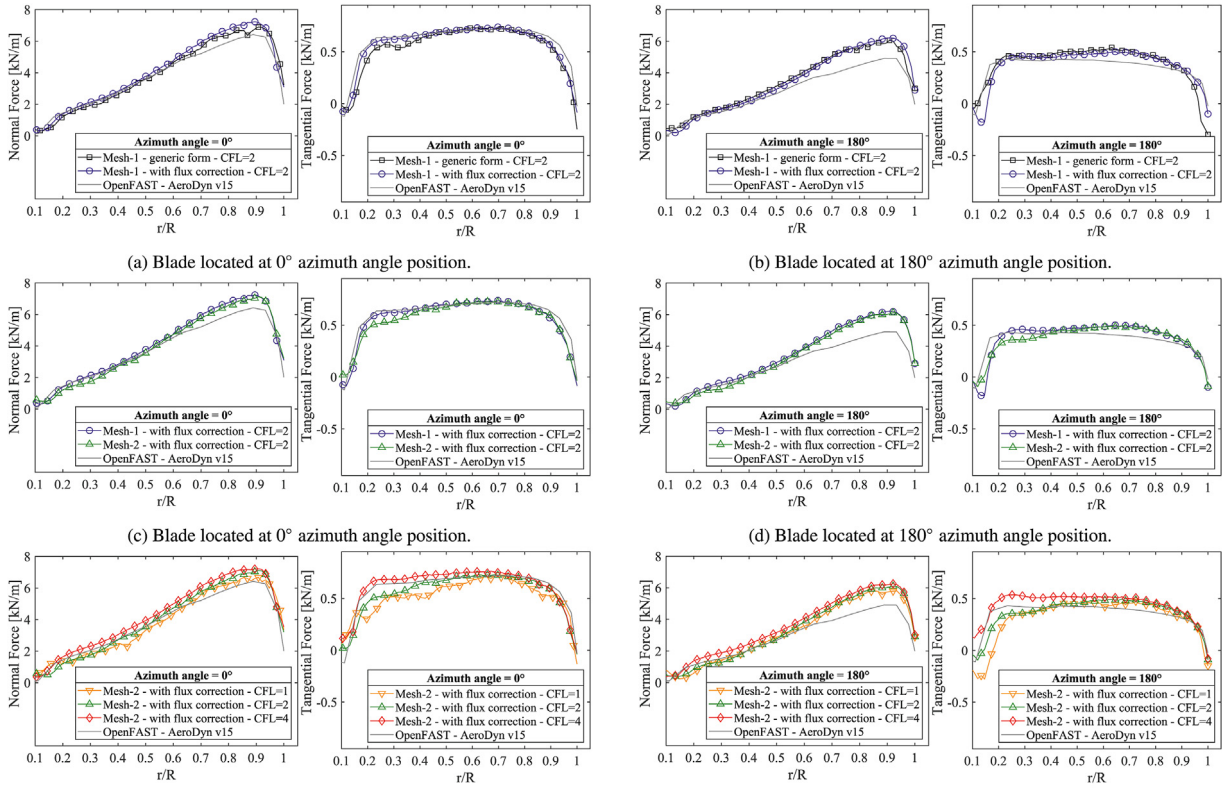

(a) Blade located at 0° azimuth angle position.

(b) Blade located at 180° azimuth angle position.

(c) Blade located at 0° azimuth angle position.

(d) Blade located at 180° azimuth angle position.

(e) Blade located at 0° azimuth angle position.

(f) Blade located at 180° azimuth angle position.

Fig. 8. NREL 5 MW wind turbine comparison of the distributed forces along the blade span for all the CFD simulations benchmarked against the OpenFAST results considering the same environmental conditions.

differences. The force distributions in Fig. 8 c) and d) provide further insight into this result. We can see that the differences in the normal force are more significant than those in the tangential force, so this is consistent with seeing larger differences in thrust than in power. For both forces, the differences are higher close to the tip of the blade, and this can be related to the three-dimensional character of the flow in that region. It is important to remember that OpenFAST employs BEM to calculate the forces, which is an essentially two-dimensional method, with tip correction factors to account for some of the three-dimensional effects [55]. One of the BEM assumptions is that there is very little spanwise pressure variation, and the theory is therefore less accurate for heavily loaded rotors with large pressure gradients across the span. Furthermore, higher differences are seen at 180° azimuth angle position, when compared to 0°. At 180°, the blade is right in front of the tower so the proximity with that structure alters the flow significantly. In OpenFAST, this effect is accounted for considering a potential flow approximation for the field around the tower, but this is certainly not very accurate for this complex flow. In addition, the tip and hub vortex, which are also overlooked in OpenFAST, influence the induced velocities and generates a skewed flow which impacts significantly in the prediction of the wind turbine thrust.

4.2.2. Flow structures

Contours of the axial velocity on a vertical plane, considering the tower influence with the blade located in front of the tower, are presented in Fig. 12 for both meshes investigated. This figure shows that both meshes predicted the wake pattern taking into account perturbations which affect the wake structure as consequence of the influence of the tower, hub-nacelle and blade tip vortices. However, different resolutions in the wake can be observed. For Mesh-1, the velocity field in the centre of the wake presents stronger gradients when compared to the results from Mesh-2.

The primary component of the wake behaviour is captured through the vortex information represented by the second invariant of the velocity gradient tensor, the Q-criterion ($Q = 0.05$), illustrated in Fig. 13. In that figure, we can see different patterns for each mesh being investigated. For Mesh-2 the vortical structures along the blade span are mitigated, whereas Mesh-1 captures better the disturbances which are related with the spanwise flow. These differences between the results for each mesh is due to the resolution of the mesh in the rotor region, which is higher for Mesh-1. However, even though in Mesh-2 this flow features are damped, the wake intensity remains with a similar behaviour and the prediction of the wind turbine performance results were slightly closer to those from OpenFAST.

More details of the blade-tower interaction for both meshes are illustrated in Fig. 14 through the instantaneous axial velocity and normal vorticity contours at different positions along the blade span, indicated by R, and above the ground, indicated by H. By comparing the results for Mesh-1 and Mesh-2, it is possible to observe different behaviour of the vortex pattern shed by the tower in the three regions analyzed, while for the rotor blades the behaviour is similar. In addition, some differences can be noticed in the wake pattern when the normal vorticity contours are compared, such as the wake contour which was more stable for Mesh-2.

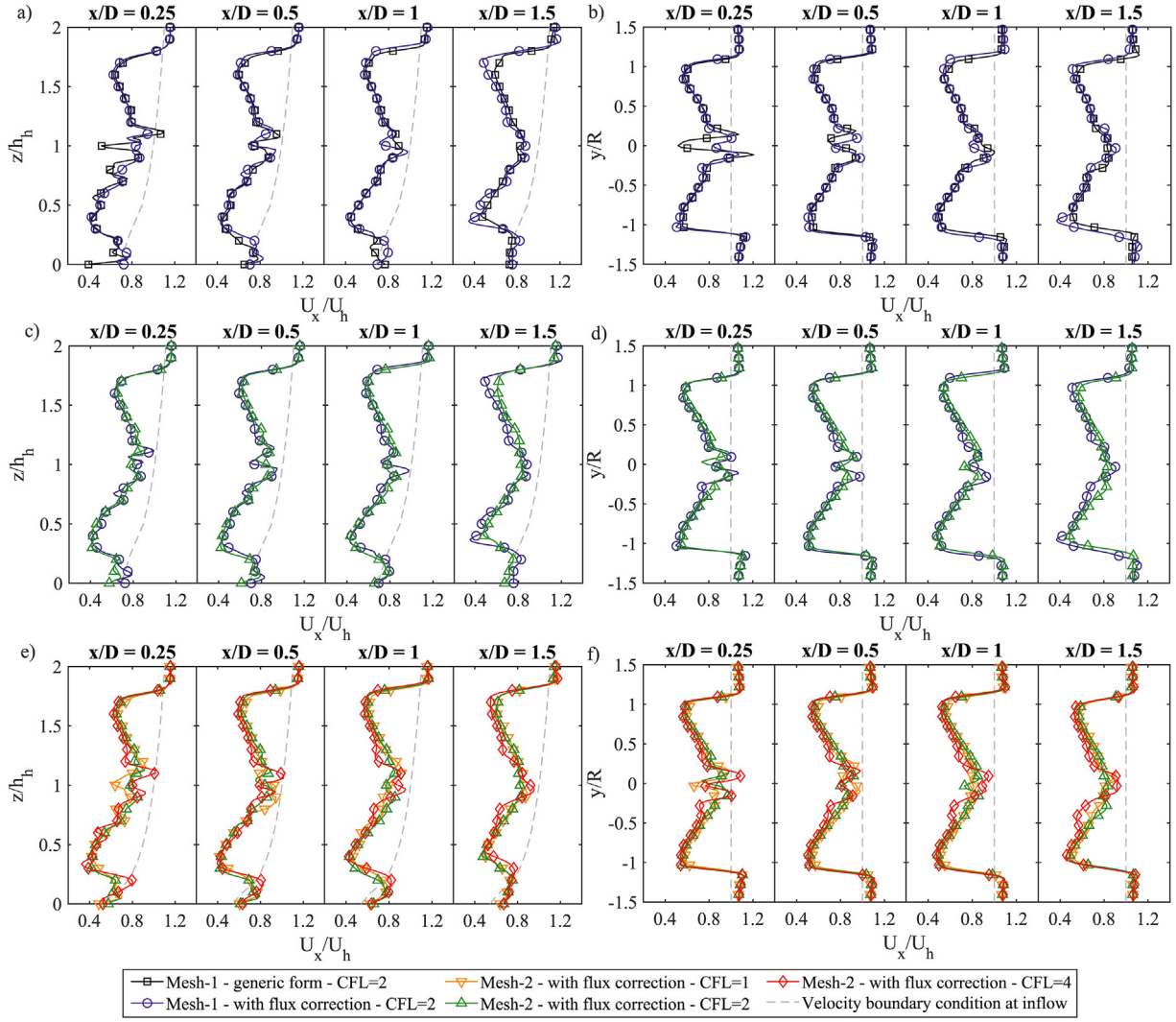

Fig. 9. Comparison of the instantaneous wind velocity profiles after 7 complete rotor revolutions at 4 x/D different positions downstream of the wind turbine, for vertical and horizontal planes. h_h is the hub height and U_h is the velocity at hub height.

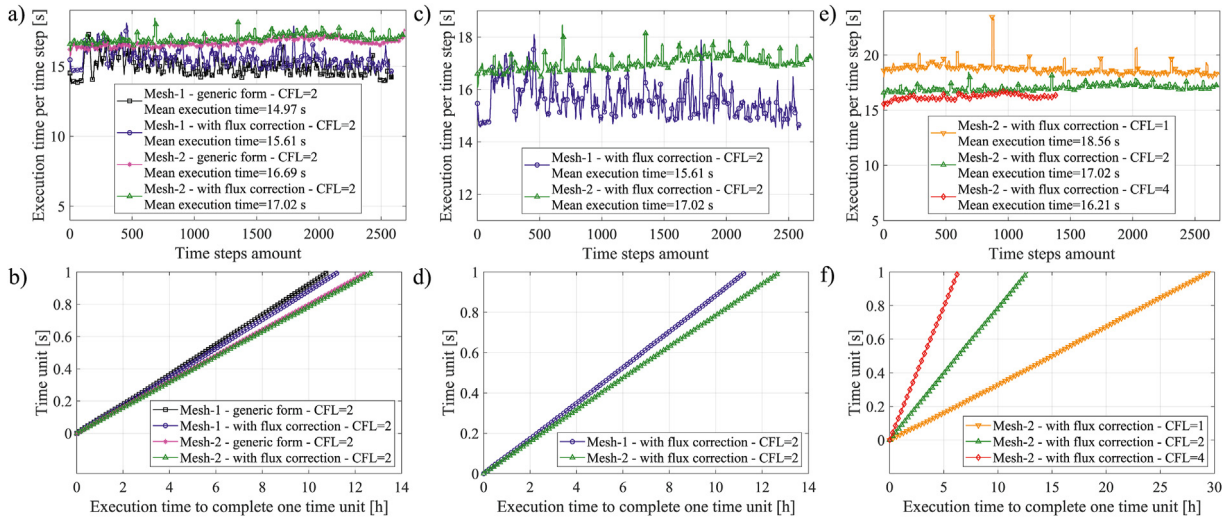

Fig. 10. Computational cost comparison for all the CFD simulations presented in Section 4.

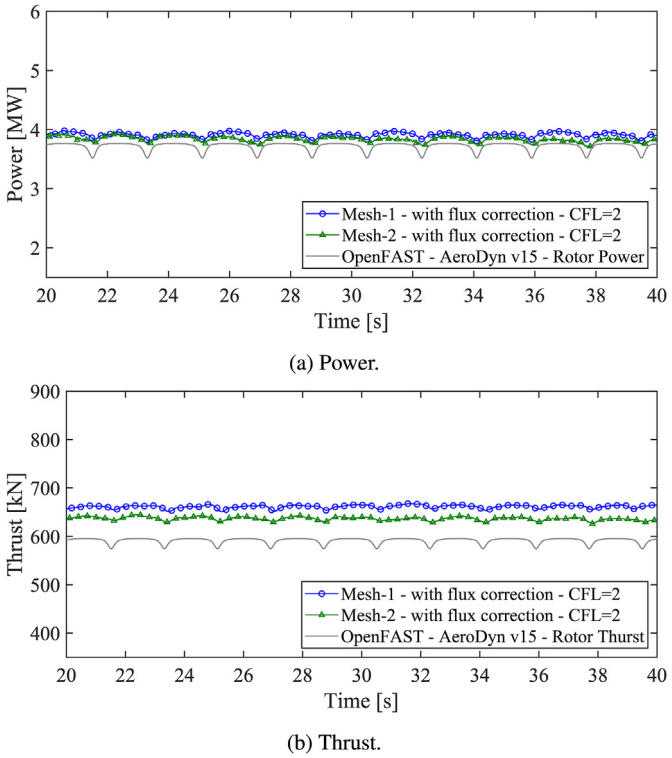

Fig. 11. Generated power and thrust comparison between Mesh-1 and Mesh-2 using the iterative PISO solver with face flux correction benchmarked against OpenFAST results.

The computational cost presented in Fig. 10 c) and d) shows that, even though the time to complete 1 s of the simulation time is around 12 h for both meshes, Mesh-1 presented a slight improvement in the time to calculate one time-step, which was 15.61 s, while for Mesh-2 it was 17.02 s. The most suitable option is here considered as Mesh-2 due to the increase in the results accuracy at an acceptable computational demand.

4.3. Temporal discretization investigation for Mesh-2 and iterative PISO with face flux correction

A temporal discretization analysis, which is strongly recommended in the modeling of transient problems, is performed in this section considering different CFL numbers for Mesh-2. Like in the previous analyses, the results are presented in three parts. First a comparison of performance results in terms of generated thrust, power production and forces distribution along the blade span are presented along the results obtained with OpenFAST, for the same environmental conditions as performed in the CFD simulations. We also analyse the computational cost associated with each case being investigated. Next, a comparison of the flow features for each CFL numbers is presented.

4.3.1. Verification with OpenFAST

A comparison for the wind turbine power production and generated thrust obtained through the CFD simulations for each of the CFL numbers investigated, and the results obtained with OpenFAST, considering the same environmental conditions, are illustrated in Fig. 15. It is possible to notice that with the increase in the CFL number, the accuracy in the results prediction is reduced since the differences between the expected values obtained with OpenFAST and the CFD simulation are considerably increased for both power and thrust (see also the mean values as presented in Table 3). This behaviour is here considered to be a consequence of an unappropriated time step sizing which is increased for higher CFL numbers. The size of the time step is related to the temporal scales that can be captured in the simulations. By increasing the CFL number, the use of a larger time step filtered out some important characteristics of the flow which resulted in loss of accuracy in the results.

Fig. 8 e) and f) show the distribution of the tangential and normal forces along the blades span. These results also vary

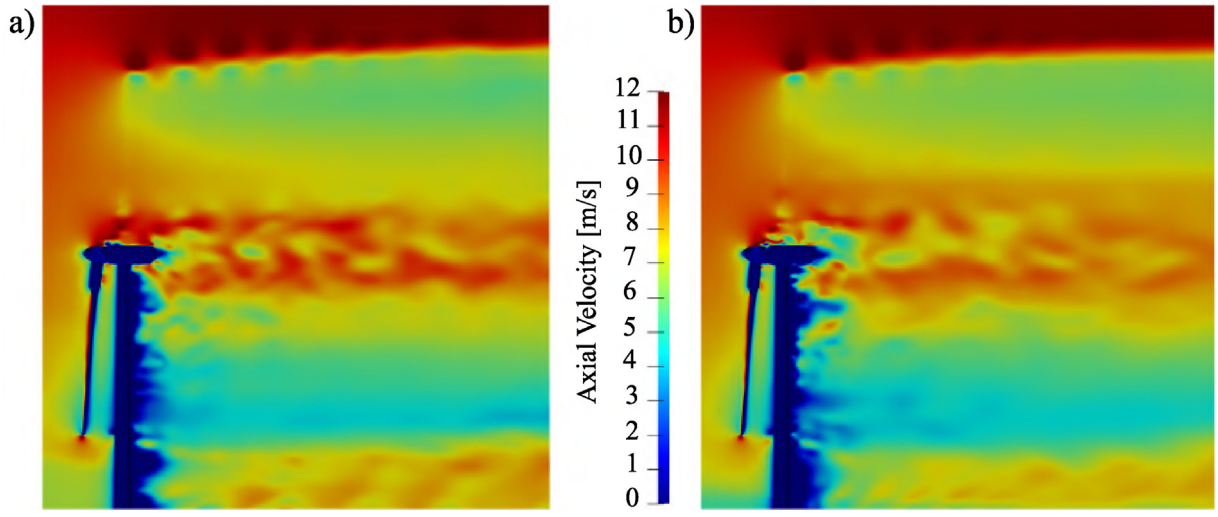

Fig. 12. NREL 5 MW wind turbine results comparison of the instantaneous iso-contours of the axial velocity for a) Mesh-1 and b) Mesh-2.

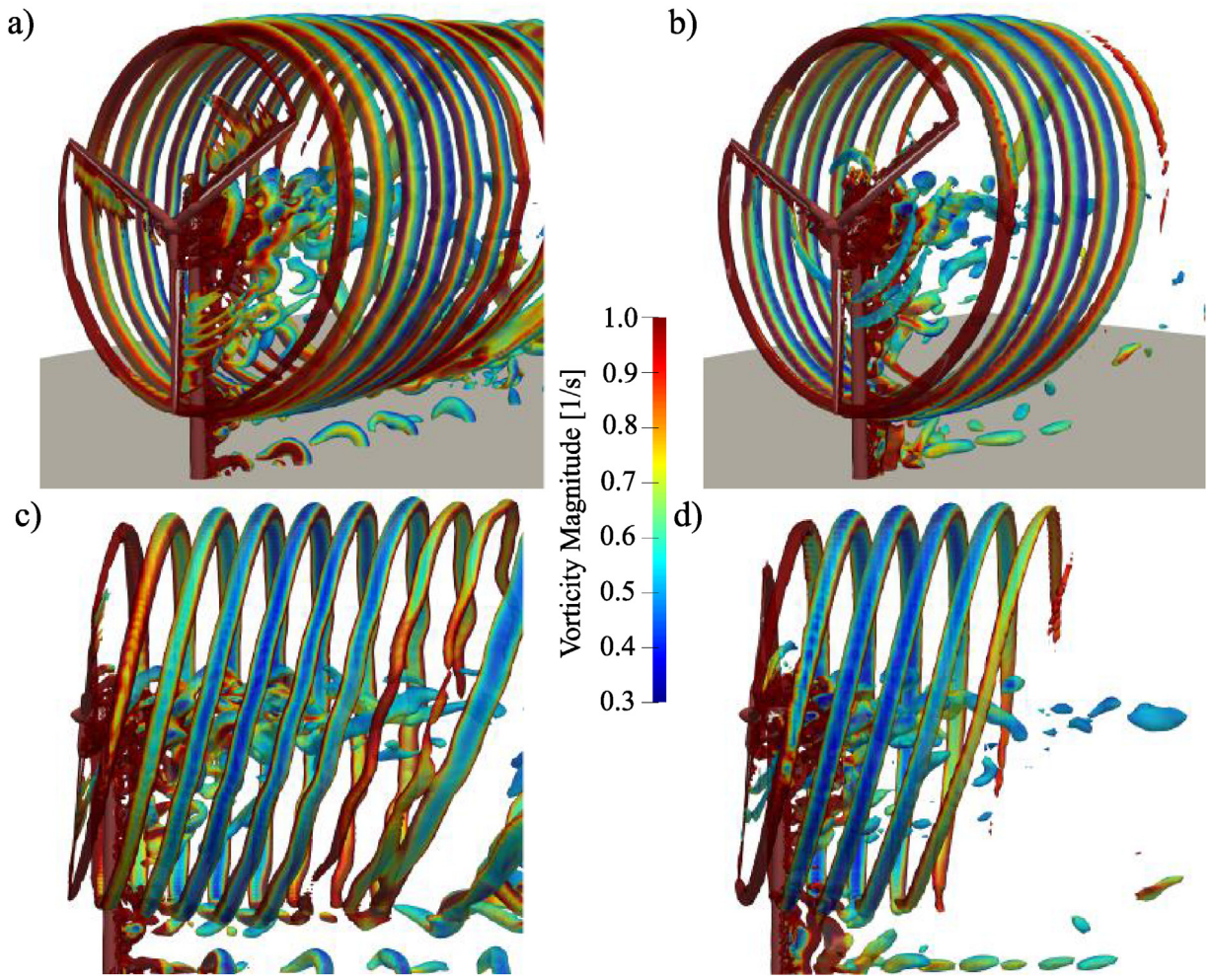

Fig. 13. NREL 5 MW wind turbine results comparison of the instantaneous isosurfaces of the Q-criterion (Q = 0.05) colored by vorticity magnitude shown in perspective and side view for Mesh-1 a) and c) and for Mesh-2 b) and d) respectively.

significantly when the CFL number is increased. When the CFL number was equal to 4, we observed a higher tangential force in the regions close to the blade root for both blade positions. Additionally to the quantitative analyses of the normal and tangential forces acting on the blades, a comparison of the instantaneous velocity profiles after 7 complete revolution is presented for all the CFL numbers investigated in Fig. 9 e) for the vertical plane, and Fig. 9 f) for the horizontal plane at different positions downstream in the wake region. It is possible to notice that with the increase in the CFL number more fluctuations appear manly in the hub region and at the blade regions close to the root.

The computational cost results presented in Fig. 10 e) and f) show that the increase in the CFL number reduces the computational demand. From CFL number of 2–4 the time to execute 1 s of the simulation time was reduced from 12 h to 6 h, due to the reduction in the amount of time steps required to execute the same simulation time. However, the loss of accuracy is significant and the CFL number of 4 is not a suitable option. Following with this analyses, the most suitable option for the temporal discretization is here considered as the CFL number equal to 2 due to the acceptable results accuracy and less computational demand when compared with CFL number equal to 1.

4.3.2. Flow structures

In Fig. 16 a), b) and c), it is possible to notice through the instantaneous axial velocity contours, that the increase in the CFL number changes the gradient of axial velocity significantly in the wake region. With CFL number equals to 4, the reduction in the axial velocity caused by the blades is higher, which resulted in the over estimation of the wind turbine power, thrust, and the forces distributions along the blade span close to the blade root. Looking at the instantaneous iso-surfaces of the Q-criterion ($Q = 0.05$) colored by the vorticity magnitude, Fig. 16 d), e) and f), it is clearly observed that with the increase in the CFL number, less vortical structures are captured. As a consequence, differences in the axial velocity gradient from the blade-tower interaction and vortex shedding pattern are also noticed in Fig. 16 g) to l), respectively.

Therefore, by considering the temporal discretization investigation employed in the analyses of the NREL 5 MW wind turbine, the accuracy in the performance results were better predicted by the numerical model considering the CFL numbers 1 and 2. However, since the differences between the results are not large, when comparing the computational cost for both cases, we consider the most suitable option to conduct future investigations to be the spatial discretization given by Mesh-2 considering a temporal

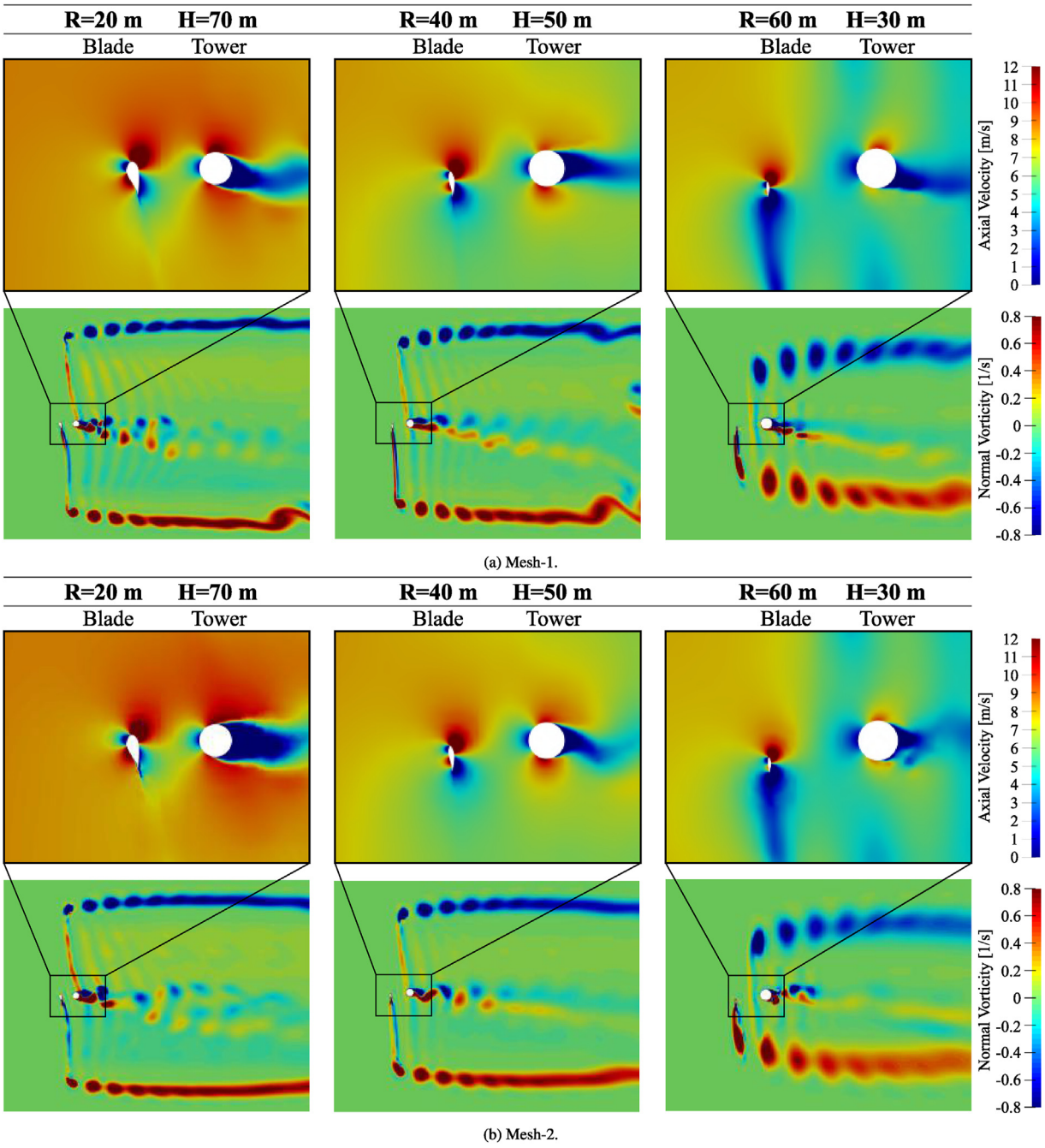

Fig. 14. NREL 5 MW wind turbine results comparison of the instantaneous iso-contours of the axial velocity and normal vorticity in different positions along the blade span indicated by R and above the ground indicated by H, for a) Mesh-1 and b) Mesh-2.

discretization limited by the CFL number equals to 2, and employing the iterative PISO with face flux correction as solver.

5. Conclusions

In this paper, a numerical investigation of the performance of the NREL 5 MW reference wind turbine for offshore applications in full scale considering different approaches of the iterative PISO solver has been carried out. An extra correction for pressure considered through the inclusion of the face flux correction in the algorithm steps presented a more stable numerical behaviour in relation to the convergence of the time series signals for the generated power and thrust. Since the wind profile considered in the investigation was non-turbulent, the instabilities captured by the generic form were attributed to numerical oscillations caused by the solver numerical arrangement. Therefore, as the approach with face flux correction can be performed without significant extra computational demand independent of the spatial discretization chosen, this solver algorithm was chosen for conducting the spatial and temporal discretization investigations.

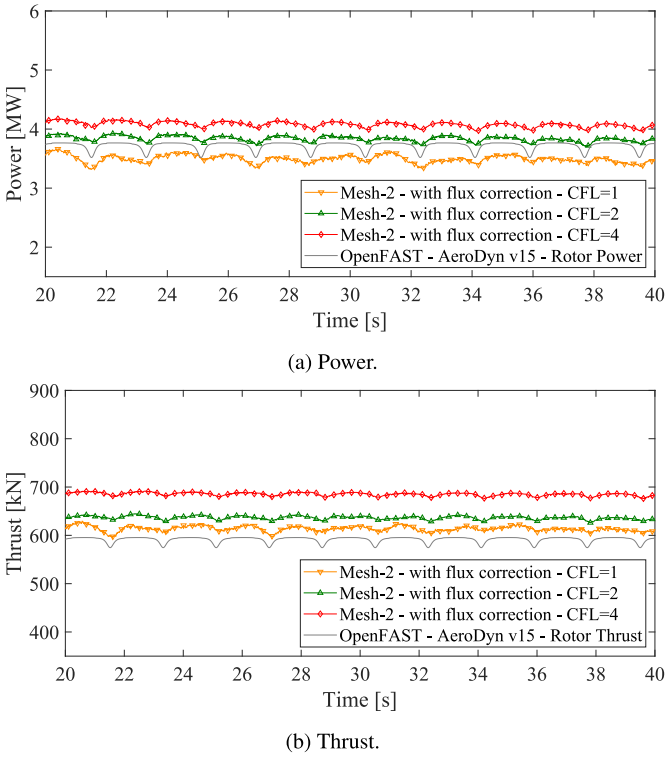

Fig. 15. Generated power and thrust comparison between different CFL numbers considered for Mesh-2 using the iterative PISO solver with face flux correction benchmarked against OpenFAST results.

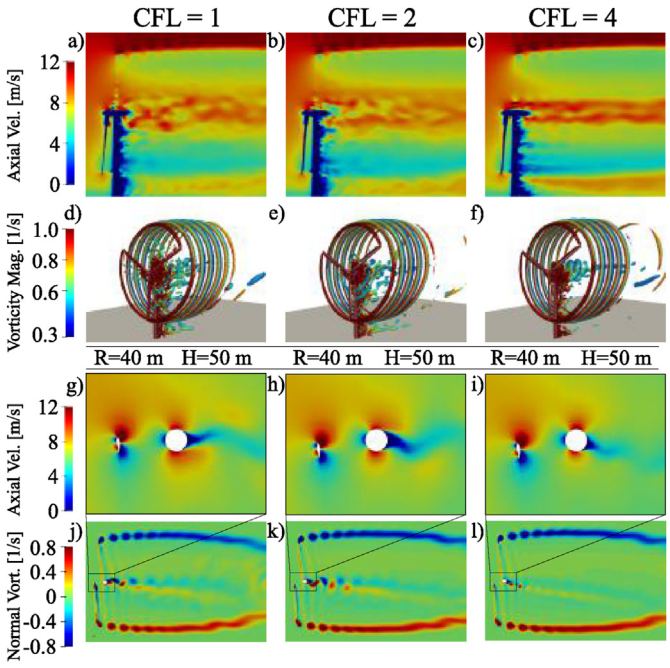

Fig. 16. Comparison of the flow characteristics for Mesh-2 considering different CFL numbers given by a), b) and c) instantaneous axial velocity contours. d), e) and f) instantaneous iso-surfaces of the Q-criterion ($Q = 0.05$) colored by the vorticity magnitude. g), h) and i) instantaneous axial velocity contours and j), k) and l) instantaneous normal vorticity contours, at 40 m of blade span and 50 m from the ground.

By considering the iterative PISO algorithm with face flux correction as pressure-based solver, a spatial discretization investigation was performed by considering different refinement strategies. The performance results in terms of power production, generated thrust, forces distribution along the blade span, and velocity profile in different positions downstream in the wake region were obtained for both meshes being investigated. In addition, a detailed comparison of the results in terms of visualization of the flow characteristics for both meshes was also performed. The comparison between Mesh-1 and Mesh-2 allowed us to identify that if the y^+ is within adequate limits in the near-wall region for the application of the turbulence model, the field close to the WT does not need to be so refined for the prediction of the forces, which allows us to increase the refinement in other regions of the computational domain which will be necessary for the future steps of our research, which intends to apply the CFD methodology considered in this work, without increase the computational cost dramatically. Therefore, Mesh-2 was chosen to conducting the analysis of the temporal discretization by considering different CFL numbers to limit the time step sizing.

Considering Mesh-2, the present work allowed a better interpretation of the influence of the CFL number as a convergence parameter and its influence in the results accuracy for transient analyses. The increase in the CFL number presented a limitation due to the time step which became unappropriated to capture the flow temporal scales which represents the physics of the problem being investigated. CFL numbers close to the unit such as 1 and 2 presented satisfactory results, but the CFL equals to 1 requires higher computational demand than equals to 2.

5.1. Future work

Future work should employ the conclusions presented in this paper in the modeling of the next generation of larger wind turbines, such as IEA 15 MW [56], and the numerical investigations of FOWTs, like the NREL 5 MW mounted on an OC4 platform [57]. We believe that a complete CFD model, capable to predict the dynamic response of a FOWT under aerodynamic and hydrodynamic loads will be very useful to improve the understanding of this type of system, which will certainly become ubiquitous in the next few years.

Credit author statement

Marielle de Oliveira: Conceptualization, Methodology, Software, Simulations, Writing – original draft. Rodolfo C. Puraca: Investigation, Simulations, Data curation, Formal analysis. Bruno S. Carmo: Supervision, Manuscript Revision, Project administration, Funding acquisition.

Declaration of competing interest

The authors declare that they have no known competing financial interests or personal relationships that could have appeared to influence the work reported in this paper.

Acknowledgments

M. de Oliveira acknowledges FAPESP (Fundação de Amparo à Pesquisa do Estado de São Paulo), the São Paulo Research Foundation, for the PhD grant - Process number 2018/26207-4. R. C. Puraca acknowledges FUSP/Petrobras for the PhD grant Project number

2019/00171-6. B. S. Carmo acknowledges the support from FAPESP, Proc. 2019/01507-8, for this research, and thanks the Brazilian National Council for Scientific and Technological Development (CNPq) for financial support in the form of a productivity grant, number 312951/2018-3. The authors also acknowledge the grant from the National Laboratory of Scientific Computing (LNCC), CADASE project, which allowed the use of the Santos Dumont supercomputer to run the simulations that generated the results reported in this paper. This work is part of the European Commission Project "High Performance Computing for Wind Energy (HPCWE)" with agreement no. 828799.

Appendix A. Turbulence Modeling

The incompressible URANS equations are obtained by means of average decomposition. Applying the averaging procedure into the continuity equation and incompressible Navier-Stokes equations given respectively by Eqs. (3) and (4), the averaged form of the equations are obtained:

$$\nabla \cdot \bar{\mathbf{U}} = 0, \tag{A.1}$$

$$\frac{\partial \bar{\mathbf{U}}}{\partial t} + \nabla \cdot (\bar{\mathbf{U}}\bar{\mathbf{U}}) = -\nabla \bar{p} + \nabla \cdot (\nu \nabla \bar{\mathbf{U}}) + \mathbf{f} + \bar{\mathbf{U}'\,\mathbf{U}'}. \tag{A.2}$$

where all the terms were explained previously except the term $\bar{\mathbf{U}'\,\mathbf{U}'}$ which represents the Reynolds stress tensor. This tensor introduces six new unknown variables, consequently the set of equations for the URANS model are not closed and further modeling is necessary.

The Reynolds shear stresses tensor is given by

$$\bar{\mathbf{U}'\,\mathbf{U}'} = \nu_t(\nabla \mathbf{U} + (\nabla \mathbf{U})^T) + \frac{2}{3}k\mathbf{I}, \tag{A.3}$$

where $\mathbf{I}$ is the identity matrix, and k is the specific turbulent kinetic energy given by

$$k = \frac{1}{2}\bar{\mathbf{U}'\,\mathbf{U}'}. \tag{A.4}$$

Thus, the kinematic eddy viscosity and the specific dissipation rate are given by

$$\nu_t = C_\mu \frac{k^2}{\varepsilon}, \tag{A.5}$$

$$\varepsilon = \{\bar{\mathbf{U}'\mathbf{U}'}\} : \{\nabla \mathbf{U}'\}. \tag{A.6}$$

Table A.4
SST k-ω turbulence model auxiliary relations.

$\nu_t = \frac{k}{\omega}\cdot\min\left(\alpha^*, \frac{a_1\omega}{S_2F_2}\right)$
$S_t = \sqrt{\mathbf{S}_t \cdot \mathbf{S}_t}$
$\mathbf{S}_t = \frac{1}{2}\left[(\nabla \mathbf{U}) + (\nabla \mathbf{U})^T\right]$
$\alpha^* = \alpha^*_\infty\left(\frac{\alpha^*_0 + Re_T/R_k}{1 + Re_T/R_k}\right)$
$D^+_\omega = \max(2\rho\sigma_{\omega 2}\frac{1}{\omega}\nabla(k\omega), 10^{-10})$
$P_k = \nu_t \nabla \mathbf{U}\left[(\nabla \mathbf{U}) + (\nabla \mathbf{U})^T\right]$
$\tilde{P}_k = \min\cdot(P_k, 10\beta^*\rho k\omega)$
$\alpha = \frac{\alpha_\infty}{\alpha^*}\left(\frac{\alpha_0 + Re_T/R_\omega}{1 + Re_T/R_\omega}\right); Re_T = \frac{k}{\nu\omega}$
$F_1 = \tanh\left\{\left\{\min\left[\max\left(\frac{\sqrt{k}}{\beta^*\omega d}, \frac{500\nu}{d^2\omega}\right), \frac{4\rho\sigma_{\omega 2}k}{D^+_\omega d^2}\right]\right\}^4\right\}$
$F_2 = \tanh\left\{\left[\max\left(\frac{2\sqrt{k}}{\beta^*\omega d}, \frac{500\nu}{d^2\omega}\right)\right]^2\right\}$

Table A.5
SST k-ω turbulence model constants.

$R_k = 6$	$R_\omega = 2.95$	$\alpha_0 = 1/9$	$\alpha^*_0 = 0.024$	$\sigma_{k,1} = 0.85$	$\sigma_{k,2} = 1.0$	$\alpha_{\infty,1} = 5/9$
$\alpha_{\infty,2} = 0.44$	$\sigma_{\omega,1} = 0.5$	$\sigma_{\omega,2} = 0.856$	$\beta_1 = 0.075$	$\beta_2 = 0.0828$	$\beta^* = 0.09$	$a_1 = 0.31$

Therefore, by considering this model, the governing equations are presented as follows for the ε and ω relation, the specific turbulent kinetic energy k and the specific dissipation rate ω

$$\omega = \frac{\varepsilon}{C_\mu k}, \tag{A.7}$$

$$\frac{\partial k}{\partial t} + \nabla \cdot (\mathbf{U}k) = \nabla \cdot [(\nu + \nu_t\sigma_k)\nabla k] + \tilde{P}_k - \beta^* k\omega, \tag{A.8}$$

$$\frac{\partial \omega}{\partial t} + \nabla \cdot (\mathbf{U}\omega) = \nabla \cdot [(\nu + \nu_t\sigma_\omega)\nabla \omega] + \frac{\alpha}{\nu_t}\tilde{P}_k - \beta\omega^2 + 2(1 - F_1)\frac{\sigma_{\omega,2}}{\omega}\nabla k \cdot \nabla \omega. \tag{A.9}$$

The last term on the right side of Eq. (A.9) denotes the cross-diffusion which represents the standard $k - \epsilon$ into the means of the $k - \omega$, and C_μ is a constant equal to 0.09. The auxiliary relations of the k-ω SST model are presented in Table A.4.

The specific kinetic energy production P_k is considered in the transport equations, Eqs. (A.8) and (A.9), and $\tilde{P}_k$ is a production limiter to prevent the formation of turbulence in stagnation areas. In addition, we use the blending functions F_1 and F_2 defined by Ref. [23]: F_2 is equal to one in boundary layers and zero in free shear layers, and F_1 is blended with the model coefficients, which include σ_k, σ_ω, α_∞, and β by the relation expressed in generic form by

$$\varphi = \varphi_1 F_1 + \varphi_2(1 - F_1), \tag{A.10}$$

where φ represents the coefficients σ_k, σ_ω, α_∞, and β. Finally, to close

all the model requirements, the constants values are presented in Table A.5.

Appendix A.1. Near-wall region treatment

In the current investigations, k and ω were modeled by the low Reynolds wall functions representing a model which can switch between the viscous and logarithmic regions of the boundary layer according to the position of y^+. In addition, ν_t is obtained using the Spalding wall function model [48,49], which also switch between viscous and logarithmic regions based on the value of y^+. Fig. A.17 illustrates the velocity profiles of the near wall regions.

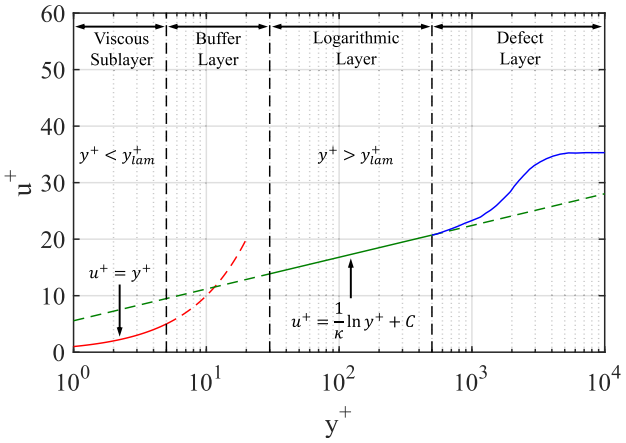

Fig. A.17. Velocity profiles and different regions of a turbulent boundary layer, edited from Ref. [46].

In the OpenFOAM software, this method was implemented as explained in Ref. [58], by considering the y^+_{lam} parameter as reference. The y^+_{lam} is calculated to identify the region of the wall function by,

$$y^+_{\text{lam}} = \frac{\log(\max(Ey^+, 1))}{\kappa},$$

where E is equal to 9.8 for smooth walls and κ is the von Kármán constant, equals to 0.41. The y^+ parameter is given by

$$y^+ = \frac{yu_\tau}{\nu}, \tag{A.11}$$

where u_τ is the friction velocity,

$$u_\tau = C_\mu^{1/4}\sqrt{k}, \tag{A.12}$$

and k is the value of turbulent kinetic energy of the cell centre adjacent to the wall obtained through the relation $k = k^+ \times u_\tau^2$. If $y^+ > y^+_{lam}$, the local turbulent kinetic energy is estimated as

$$k^+ = \frac{C_k}{\kappa}\log(y^+) + B_k,$$

where C_k and B_k are turbulence model constants equal to -0.416 and 8.366 respectively, and the specific dissipation rate is given by

$$\omega = \frac{k^{\frac{1}{2}}}{C_\mu^{1/4}\kappa y}. \tag{A.13}$$

If $y^+ < y^+_{lam}$, the kinetic energy and the dissipation rate are estimated as

$$k^+ = \frac{2400}{C_\epsilon^2 \times C_f} \tag{A.14}$$

and

$$\omega = \frac{6.0\nu}{\beta_1 y^2}, \tag{A.15}$$

where β_1 is a turbulence constant equals to 0.075. Finally, the kinematic eddy viscosity estimation is given by the following relations,

$$\nu_t = \frac{(u_\tau)^2}{\partial \mathbf{U}/\partial n} - \nu, \tag{A.16}$$

$$y^+ = u^+ + \frac{1}{E}\left[e^{\kappa u^+} - 1 - \kappa u^+ - \frac{1}{2}(\kappa u^+)^2 - \frac{1}{6}(\kappa u^+)^3\right], \tag{A.17}$$

where if $y^+ > y^+_{lam}$,

$$u^+ = \frac{Ey^+}{\kappa}, \tag{A.18}$$

while if $y^+ < y^+_{lam}$,

$$u^+ = y^+. \tag{A.19}$$

References

[1] Lund H. Renewable energy strategies for sustainable development. Energy 2007;32(6):912–9.
[2] G. W. E. Council, GWEC| global wind report 2021, Global Wind Energy Council: Brussels, Belgium .
[3] Ostachowicz W, McGugan M, Schröder-Hinrichs J-U, Luczak M. MARE-WINT: new materials and reliability in offshore wind turbine technology. Springer Nature; 2016.
[4] Karimirad M. Offshore energy structures: for wind power, wave energy and hybrid marine platforms. Springer; 2014.
[5] Hand MM, Simms DA, Fingersh LJ, Jager DW, Cotrell JR. Unsteady aerodynamics experiment phase V: test configuration and available data campaigns. Tech. Rep., NREL 2001. https://doi.org/10.2172/787980. https://www.osti.gov/biblio/787980.
[6] Hand MM, Simms DA, Fingersh LJ, Jager DW, Cotrell JR, Schreck S, Larwood SM. Unsteady aerodynamics experiment phase VI: wind tunnel test configurations and available data campaigns. Tech. Rep., NREL 2001. https://doi.org/10.2172/15000240. https://www.osti.gov/biblio/15000240.
[7] Hayes L, Stocks M, Blakers A. Accurate long-term power generation model for offshore wind farms in Europe using ERA5 reanalysis. Energy 2021;229:120603.
[8] Zhang Y, Deng S, Wang X. RANS and DDES simulations of a horizontal-axis wind turbine under stalled flow condition using OpenFOAM. Energy 2019;167:1155–63.
[9] Sanderse B, Van der Pijl S, Koren B. Review of computational fluid dynamics for wind turbine wake aerodynamics. Wind Energy 2011;14(7):799–819.
[10] Thé J, Yu H. A critical review on the simulations of wind turbine aerodynamics focusing on hybrid RANS-LES methods. Energy 2017;138:257–89.
[11] Sorensen N, Hansen M. Rotor performance predictions using a Navier-Stokes method. In: 1998 ASME wind energy symposium, vol. 25; 1998.
[12] Duque E, Van Dam C, Hughes S. Navier-Stokes simulations of the NREL combined experiment phase II rotor. In: 37th aerospace sciences meeting and exhibit, vol. 37; 1999.
[13] Duque EP, Burklund MD, Johnson W. Navier-Stokes and comprehensive

analysis performance predictions of the NREL phase VI experiment. J Sol Energy Eng 2003;125(4):457–67.
[14] Park SH, Kwon JH. Implementation of kw turbulence models in an implicit multigrid method. AIAA J 2004;42(7):1348–57.
[15] Rocha PC, Rocha HB, Carneiro FM, da Silva MV, Bueno AV. k–ω SST (shear stress transport) turbulence model calibration: a case study on a small scale horizontal axis wind turbine. Energy 2014;65:412–8.
[16] Lawson MJ, Melvin J, Ananthan S, Gruchalla KM, Rood JS, Sprague MA. Blade-resolved, single-turbine simulations under atmospheric flow, Tech. Rep.. Golden, CO (United States): National Renewable Energy Lab.(NREL); 2019.
[17] Weihing P, Letzgus J, Bangga G, Lutz T, Krämer E. Hybrid RANS/LES capabilities of the flow solver FLOWer—application to flow around wind turbines. In: Symposium on hybrid RANS-LES methods. Springer; 2016. p. 369–80.
[18] Zhang Y, van Zuijlen A, van Bussel G. Massively separated turbulent flow simulation around non-rotating Mexico blade by means of RANS and DDES approaches in OpenFOAM. In: 33rd AIAA applied aerodynamics conference; 2015. p. 2716.
[19] Jonkman J, Butterfield S, Musial W, Scott G. Definition of a 5-MW reference wind turbine for offshore system development, Tech. Rep.. Golden, CO (United States): National Renewable Energy Lab.(NREL); 2009.
[20] Zhang R-K, Wu VDJ-Z. Aerodynamic characteristics of wind turbine blades with a sinusoidal leading edge. Wind Energy 2012;15(3):407–24.
[21] El Kasmi A, Masson C. An extended k–ϵ model for turbulent flow through horizontal-axis wind turbines. J Wind Eng Ind Aerod 2008;96(1):103–22.
[22] Tachos N, Filios A, Margaris D. A comparative numerical study of four turbulence models for the prediction of horizontal axis wind turbine flow. Proc IME C J Mech Eng Sci 2010;224(9):1973–9.
[23] Menter FR. Two-equation eddy-viscosity turbulence models for engineering applications. AIAA J 1994;32(8):1598–605.
[24] Sørensen NN, Bechmann A, Réthoré P-E, Zahle F. Near wake Reynolds-averaged Navier–Stokes predictions of the wake behind the Mexico rotor in axial and yawed flow conditions. Wind Energy 2014;17(1):75–86.
[25] Moshfeghi M, Song YJ, Xie YH. Effects of near-wall grid spacing on SST-K-ω model using NREL Phase VI horizontal axis wind turbine. J Wind Eng Ind Aerod 2012;107:94–105.
[26] Hansen MOL, Sørensen JN, Voutsinas S, Sørensen N, Madsen HA. State of the art in wind turbine aerodynamics and aeroelasticity. Prog Aero Sci 2006;42(4):285–330.
[27] Latimer B, Pollard A. Comparison of pressure-velocity coupling solution algorithms. Numer Heat Tran 1985;8(6):635–52.
[28] Patankar SV. Numerical heat transfer and fluid flow. CRC press; 2018.
[29] Issa RI. Solution of the implicitly discretised fluid flow equations by operator-splitting. J Comput Phys 1986;62(1):40–65.
[30] Patankar SV, Spalding DB. A calculation procedure for heat, mass and momentum transfer in three-dimensional parabolic flows. In: Numerical prediction of flow, heat transfer, turbulence and combustion. Elsevier; 1983. p. 54–73.
[31] Bertagnolio F, Sørensen NN, Rasmussen F. New insight into the flow around a wind turbine airfoil section. J Sol Energy Eng 2005;127(2):214–22.
[32] Robertson E, Choudhury V, Bhushan S, Walters DK. Validation of OpenFOAM numerical methods and turbulence models for incompressible bluff body flows. Comput Fluids 2015;123:122–45.
[33] Cheng P, Huang Y, Wan D. A numerical model for fully coupled aero-hydrodynamic analysis of floating offshore wind turbine. Ocean Eng 2019;173:183–96.
[34] Versteeg HK, Malalasekera W. An introduction to computational fluid dynamics: the finite volume method. Pearson education; 2007.
[35] Jasak H. Dynamic mesh handling in OpenFOAM. In: 47th AIAA aerospace sciences meeting including the new horizons forum and aerospace exposition, vol. 341; 2009.
[36] Jasak H. Error analysis and estimation for the finite volume method with applications to fluid flows. Ph.D. thesis. Imperial College London (University of London); 1996.
[37] Muratova G, Martynova T, Andreeva E, Bavin V, Wang Z-Q. Numerical solution of the Navier–Stokes equations using multigrid methods with HSS-based and STS-based smoothers. Symmetry 2020;12(2):233.
[38] Zhang Y, Jia Y. Velocity correction coefficients in pressure correction–type model. J Hydraul Eng 2019;145(6):06019008.
[39] Dose B, Rahimi H, Stoevesandt B, Peinke J. Fluid-structure coupled investigations of the NREL 5 MW wind turbine for two downwind configurations. Renew Energy 2020;146:1113–23.
[40] Liu Y. A CFD study of fluid-structure interaction problems for floating offshore wind turbines. Ph.D. thesis. University of Strathclyde; 2018.
[41] Shi W, Jiang J, Sun K, Ju Q. Aerodynamic performance of semi-submersible floating wind turbine under pitch motion. Sustain Energy Technol Assessments 2021;48:101556.
[42] Tran TT, Kim D-H. A CFD study of coupled aerodynamic-hydrodynamic loads on a semisubmersible floating offshore wind turbine. Wind Energy 2018;21(1):70–85.
[43] Liu Y, Xiao Q, Incecik A, Peyrard C, Wan D. Establishing a fully coupled CFD analysis tool for floating offshore wind turbines. Renew Energy 2017;112:280–301.
[44] National Renewable Energy Laboratory. OpenFAST documentation. https://github.com/openfast. [Accessed 17 August 2021].
[45] Moukalled F, Mangani L, Darwish M, et al. The finite volume method in computational fluid dynamics, vol. 113. Springer; 2016.
[46] Wilcox DC, et al. Turbulence modeling for CFD, vol. 2. CA: DCW industries La Canada; 1998.
[47] Menter F. Zonal two equation kw turbulence models for aerodynamic flows. In: 23rd fluid dynamics, plasmadynamics, and lasers conference, vol. 2906; 1993.
[48] Spalding D. Mass transfer through laminar boundary layers—1. The velocity boundary layer. Int J Heat Mass Tran 1961;2(1–2):15–32.
[49] Spalding D, Evans H. Mass transfer through laminar boundary layers—2. Auxiliary functions for the velocity boundary layer. Int J Heat Mass Tran 1961;2(3):199–221.
[50] Hsu M-C, Bazilevs Y. Fluid–structure interaction modeling of wind turbines: simulating the full machine. Comput Mech 2012;50(6):821–33.
[51] Pope SB. Turbulent flows. 2001.
[52] Farrell PE, Maddison JR. Conservative interpolation between volume meshes by local Galerkin projection. Comput Methods Appl Mech Eng 2011;200:89–100. https://doi.org/10.1016/j.cma.2010.07.015.
[53] Coulling AJ, Goupee AJ, Robertson AN, Jonkman JM, Dagher HJ. Validation of a FAST semi-submersible floating wind turbine numerical model with DeepCwind test data. J Renew Sustain Energy 2013;5(2):023116.
[54] National Renewable Energy Laboratory. Wind turbine design codes certified. https://www.nrel.gov/news/press/2005/357.html. [Accessed 10 January 2022].
[55] Moriarty PJ, Hansen AC. AeroDyn theory manual, Tech. Rep.. Golden, CO (US): National Renewable Energy Lab.; 2005.
[56] Gaertner E, Rinker J, Sethuraman L, Zahle F, Anderson B, Barter GE, Abbas NJ, Meng F, Bortolotti P, Skrzypinski W, et al. IEA wind TCP task 37: definition of the IEA 15-megawatt offshore reference wind turbine, Tech. Rep.. Golden, CO (United States): National Renewable Energy Lab.(NREL); 2020.
[57] Robertson A, Jonkman J, Masciola M, Song H, Goupee A, Coulling A, Luan C. Definition of the semisubmersible floating system for phase II of OC4, Tech. Rep.. Golden, CO (United States): National Renewable Energy Lab.(NREL); 2014.
[58] Liu F. A thorough description of how wall functions are implemented in OpenFOAM. Proceedings of CFD with OpenSource Software 2016:1–33.

6 A STUDY ON THE INFLUENCE OF NUMERICAL SCHEMES AND TURBULENCE MODELS ON THE ACCURACY OF BLADE-RESOLVED SIMULATIONS

The interaction between the turbulence model and discretization schemes required for the computation of the nonlinear terms of the momentum equation can impact the accuracy of the results and computational demand of blade-resolved simulations. This chapter presents a comprehensive study of chosen convection discretization schemes. In this regard, a CFD methodology was developed to understand the influence of discretization methods given by the LUD and LUST schemes for the computation of the convective term while considering different turbulence closure models.

Blade-resolved CFD simulations were conducted employing LUD and LUST schemes for the URANS k-ω SST simulations and the LUST scheme for the DES k-ω SST cases. The results obtained from the different numerical arrangements employed in the CFD simulations were compared and benchmarked against the results from the OpenFAST code for the same environmental conditions. The NREL 5 MW reference wind turbine for offshore applications was chosen to conduct the numerical investigations. The wind turbine geometry in its full scale was considered without the tower and nacelle parts to optimize the use of the computational resources available.

The environmental conditions employed in the simulations aimed to represent the operating condition of optimal wind-power conversion efficiency. In addition, different spatial and temporal discretization strategies were tested to evaluate their influence on the numerical arrangements being investigated.

The blade-resolved CFD simulations developed in this chapter are presented through a second paper published in Energy. Further results related to this study, whose paper was also presented at the EPTT-2022 conference, are available in Appendix A of this thesis.

Energy 283 (2023) 128394

Contents lists available at ScienceDirect

Energy

journal homepage: www.elsevier.com/locate/energy

A study on the influence of the numerical scheme on the accuracy of blade-resolved simulations employed to evaluate the performance of the NREL 5 MW wind turbine rotor in full scale

Marielle de Oliveira *, Rodolfo C. Puraca, Bruno S. Carmo

University of São Paulo, Escola Politécnica, Department of Mechanical Engineering, Brazil

ARTICLE INFO

Keywords:
LUST and LUD advection schemes
Blade-resolved simulations
NREL 5 MW wind turbine rotor
Turbulence closure models
URANS *k-ω* SST
DES *k-ω* SST

ABSTRACT

We present a numerical investigation on the influence of the numerical arrangement in the accuracy of the NREL 5 MW wind turbine rotor performance evaluation in full scale, using a Computational Fluid Dynamics (CFD) methodology which employs the Finite Volume Method (FVM) implemented in the OpenFOAM software. The nonlinearity of the Navier–Stokes equation, which requires special treatment and still represents a subject under intense debate in the scientific community, is tackled by using two different discretization schemes for computing the convective term. In addition, since the advection scheme numerically interacts with the turbulence closure model employed in the numerical simulations, we considered the URANS *k-ω* SST and DES *k-ω* SST models to perform the blade-resolved simulations. A hybrid central/upwind scheme, namely the LUST scheme, was considered for discretizing the convective term for both URANS and DES simulations, while the second order accurate upwind given by the LUD scheme was considered only in the URANS simulation. Considering the LUST scheme, an investigation on the temporal and spatial discretization was performed for both turbulence closure models. The performance of the NREL 5 MW rotor for offshore application in full scale was assessed in terms of power production, generated thrust, and forces distribution along the blade span, for the operation condition of optimal wind-power conversion efficiency. We provide detailed information regarding the flow features and computational cost, and verified the results from each case by comparing the CFD results against values obtained using the blade element momentum theory implemented in OpenFAST. For the spatial discretization considered in one of the meshes, the LUD scheme showed low accuracy in the results, being more susceptible to the grid influence for the URANS simulations compared to LUST, while the URANS-LUST and DES-LUST approaches were both suitable options for all the meshes investigated. The DES-LUST approach was less affected by the variation in the size of the time step employed. Additionally, finer flow structures were captured with the DES-LUST simulations at an affordable computational cost.

1. Introduction

In recent years, due to the significant expansion of the wind energy market to offshore sites, and consequent industry requirements to meet this crescent demand, an increase of numerical methods used as a tool to represent the complex system of an offshore wind turbine, and its operational conditions was noticed [1–3]. There are several numerical methods that can be applied to model a wind turbine to predict the aerodynamic forces and estimate its performance when considering a specific operational condition. They can also be used to model the dynamic response of the machine under specific situations, such as when it operates coupled manner to another device, such as fixed, or floating platforms [4,5]. In practice, the applicability of each method is chosen based on the purpose of the numerical simulation. As suggested by Sanderse et al. [3], the methods can be classified according to the type of model applied to represent the blades and the wake regions. For example, in the kinematic method, the simplest one, the far wake is modeled based on an analytical approach, while by applying Blade Element Momentum (BEM), the blade aerodynamics are computed based on 2D blade elements and global momentum balance. In turn, the direct methods include all the Computational Fluid Dynamics (CFD) techniques, which require higher computational demand when compared to the other methods.

Even though the CFD simulations are considerably more expensive, with the increase of the commercial offshore wind turbine (OWT) sizes to scales of power capacity such as SG 8 MW, Vestas 9.5 MW and GE 14 MW [6–8], the high-fidelity CFD numerical models became

* Corresponding author.
E-mail address: mariellededeoliveira@usp.br (M. de Oliveira).

https://doi.org/10.1016/j.energy.2023.128394
Received 28 February 2023; Received in revised form 19 June 2023; Accepted 9 July 2023
Available online 15 July 2023

Nomenclature

BEM	Blade Element Momentum
CDS	Central Discretization Schemes
CFD	Computational Fluid Dynamics
CFL	Courant–Friedrichs–Lewy
DES	Detached Eddy Simulation
DTU	Technical University of Denmark
FVM	Finite Volume Method
IEA	International Energy Agency
LES	Large Eddy Simulation
N-S	Navier Stokes
NREL	National Renewable Energy Laboratory
OWTs	Offshore Wind Turbines
PISO	Pressure Implicit Split Operator
SST	Shear Stress Transport
UDS	Upwind Discretization Schemes
URANS	Unsteady Reynolds-Average Navier–Stokes
Δt	Time step
ν	Kinematic viscosity
ν_t	Turbulent kinematic eddy viscosity
ω	Specific dissipation rate of the SST k-ω turbulence model
ρ	Density
N	Point in the center of the neighboring control volume **N**
P	Point in the center of the control volume **P**
S	Area vector pointing out of the volume cell
U	Velocity vector
$\mathbf{U}_N$	velocity of the neighbor cell **N**
$\mathbf{U}_f$	Control volume velocity at the face cell
$\mathbf{U}_p$	velocity at the center of the cell
f	Body forces
a_N	Matrix coefficient corresponding to the neighbor **N**
a_P	Matrix corresponding to the central coefficient **P**
k	Specific turbulent kinetic energy
p	Kinematic pressure
y^+	Dimensionless wall distance
CL	Linear Interpolation
F	Mass flux through a general face
LUD	Linear-Upwind Differencing
LUST	Linear-Upwind Stabilized Transport
t	Time
R	Blade radius
Re_L	Turbulence Reynolds number parameter
AMI	Arbitrary Mesh Interface
DILU	Simplified Diagonal-based Incomplete LU preconditioner
GAMG	Geometric-Algebraic Multi-Grid
PBiCG	Preconditioned Bi-Conjugate Gradient
SIMPLE	Semi-Implicit Method for Pressure-Linked Equations
GL	Germanischer Lloyd
P_k	Production of specific kinetic energy
ϵ	Specific dissipation rate of the standard k-ϵ turbulence model
κ	von Kármán constant
$\overline{\mathbf{U}'\mathbf{U}'}$	Reynolds shear stresses tensor
$\tilde{P}_k$	Production limiter of specific kinetic energy
u_τ	Friction velocity
C_{DES}	DES approach constant
Δ_{DES}	Spatial step
δ_t	Integral length scale of turbulence
$\delta_x, \delta_y, \delta_z$	Dimension of the grid
$\tilde{l}$	Specific length scale
d_w	Distance of the computational grid cell to the closest wall
l	Length scale
k^+	Dimensionless turbulent kinetic energy
ψ	Blending factor

a useful alternative to understand the flow features of such complex systems, due to the difficulties associated to analyzing a large wind turbine experimentally, and the need of valuable information used to calibrate simpler numerical models [4].

Although the Finite Volume Method (FVM) in CFD has been shown to be a mature approach to investigate the unsteady aerodynamic behavior of the flow around wind turbine blades and generated wakes [3,9], only a few investigations using such method considered the OWT geometry in its full size of a megawatt scale, due the complexity of the numerical simulation, and computational resources required [9,10]. For instance, there are investigations about the multi-physical problem in terms of fluid–structure interaction [11–13], aero-hydrodynamic response [14,15], aeroelasticity effect [16–18], and influence of the turbulence closure model [19–21]. Nonetheless, in these investigations besides the important analyses conducted to understand the physics of the problem, the solver arrangement is briefly presented and no study about the influence of the simulation setup on the accuracy of the results were explore regarding the numerical schemes and solver parameters used.

A recent study on a proper solver configuration to numerically investigate the performance of a megawatt scale offshore wind turbine in terms of power production, generated thrust, and forces distribution along the blade span, was presented by the authors of this paper [10]. In that work, we investigated the effect of different configurations of the Pressure Implicit Split Operator (PISO) solver for treating the pressure–velocity coupling, and different spatial and temporal discretization using a CFD methodology implemented in the OpenFOAM software. We identified the numerical arrangement that presented better accuracy in the results, besides the optimized use of the computational resources. The relevant impact of the numerical schemes on the simulations results and computational demand suggests that further investigations should be conducted to also capture the influence of other parts of the numerical solver, such as the discretization schemes, in the accuracy of the solution.

To date, regarding the solver parameters employed in this type of CFD simulations, most of the investigations exploring the influence of the numerical arrangement on the results accuracy of a OWT in full scale focused on comparing different turbulence models [22–25]. In this regard, unsteady Reynolds-averaged Navier–Stokes (URANS) methods are more commonly used in blade-resolved simulations, instead of Large-eddy simulations (LES), to predict unsteady aerodynamic loads due the difficulties of the LES approach in obtaining a solution in the near-wall region [26]. The hybridization of the unsteady URANS-LES into an improved approach, such as the Detached-Eddy Simulation (DES) model, has enhanced the modeling process of the turbulence effects to a manageable computational demand even for flow at high

Reynolds number regime, which facilitates understanding wind turbine aerodynamics loads [26–29].

There was a promising improvement in the turbulence models used in the blade-resolved simulations, such as the DES model which allows applying the URANS-based models in the boundary layer regions, and LES, where the momentum transfer is dominated by large structures [30]. However, only a few investigations have implemented the DES approach in CFD simulations of a megawatt scaled wind turbine, due the complexity of the numerical arrangement necessary to solve the governing equations [9]. In the numerical investigations performed by [20], the DES turbulence model was used to predict the performance of the OWT NREL 5 MW. However, due to the mismatch between the turbulence model employed and the solver strategies adopted, the quasi-steady regime for the power and thrust, which typically requires around 5–6 rotor revolutions to be established, was not achieved even with the coarsest mesh.

In CFD codes, the solution of the problem investigated is achieved by combining an ample variety of numerical schemes. Discretization schemes are used to split a continuous function into a discrete function, in which the solution values are defined at each point in space and time. In practice, the discretization procedure is separated into spatial and temporal methods. Summarized information on temporal and spatial discretization schemes used accordingly with the turbulence model chosen are presented by Thé and Yu [9].

Even though the fundamentals of the discretization procedure are well comprehended in the finite volume method [31,32], the discretization of the convective term is still a subject under intense debate in the scientific community, because it usually represents the main source of errors among the spatial discretization schemes [33]. Amongst the ample variety of convection discretization schemes, central discretization schemes (CDS) and upwind discretization schemes (UDS), are the two major categories of spatial discretization methods recommended for wind turbine simulations [3,9]. Investigations on similar wind turbine problems usually consider the second-order upwind scheme for computing convective fluxes, while to discretize the viscous terms, a centered second-order differentiation scheme is employed [4,9,10].

Generally, the application of each discretization scheme is related to the turbulence model employed in the numerical simulations [9]. For instance, second-order accurate UDS methods, such as the Linear-Upwind Differencing (LUD) proposed by Warming and Beam [34], are strongly recommended for URANS-based simulations due to its high stability. In turn, the non-dissipative CDS methods, such as Centered Linear interpolation (CL), are preferred for LES-based models since upwind schemes can interfere with the turbulent structures by introducing a considerable amount of numerical diffusion, which can influence the energy cascade from large to small scales, by interacting with the turbulent diffusion introduced by the turbulence model [33,35].

The hybridization of the URANS-LES methods has been of great importance for engineering problems involving complex flows. Intense work has been done to develop advanced discretization methods for the convective term, which presents central-like behavior, except in the regions dominated by strong gradients, whereby the scheme is capable of adjusting to an upwind approach. The Linear-Upwind Stabilized Transport (LUST) scheme proposed by Weller [36] is an advanced method that blends two second-order accurate schemes, providing superior numerical stability while maintaining better accuracy [35,37]. Although the hybrid central/upwind concept of the LUST scheme has been applied to DES simulations and presented very promising results [35], there is still a lack of information about the applicability of the LUST scheme to URANS simulations, in terms of wind turbine performance results accuracy, and computational effort required for high Reynolds dominated flows.

The numerical arrangement interaction between turbulence model and discretization schemes used to compute the nonlinear terms of the momentum equations can thus present a significant impact on the results accuracy of blade-resolved simulations. Hence, the methodology and numerical simulations employed in this work aimed to understand the influence of the discretization methods given by the LUD and LUST schemes on the computation of the convective term, considering different turbulence closure models. Therefore, in the blade-resolved simulations we tested the LUD and LUST schemes for the URANS $k-\omega$ SST simulations to understand the behavior of the scheme related to the computational demand and accuracy of the results. Additionally, we conducted blade-resolved simulations employing the DES $k-\omega$ SST turbulence model, to compare the simulations results with those from the URANS simulations.

To conduct the investigations, we chose the operating condition of optimal wind-power conversion efficiency for the NREL 5 MW wind turbine for offshore applications in full scale, which according to [38], is represented by a constant TSR of 7 and a pitch angle of 0 degrees for a wind speed of 10 m/s. Different spatial and temporal discretization strategies were employed, so we could better understand their influence on the simulation results. Since this type of numerical simulations are computationally expensive, and the increase in the offshore wind turbines power capacity makes the numerical investigations a challenging task, we hope our findings help the development of other large wind turbines simulations.

2. Methodology

As discussed previously, the numerical solution of turbulent flow problems is usually very complex, and require sophisticated computational algorithms [39]. The difficulties in obtaining closed-form solution is particularly pronounced in the boundary layer, where the flow being calculated is characterized by high shear levels, and the estimation of its properties is extremely valuable in design studies, which is the case of blade-resolved simulations. For the latter, we analyze the flow in the near-wall region for the entire wind turbine geometry. In this section, we describe the governing equations, the discretization schemes and turbulence closure models employed in the numerical analyses.

2.1. Governing equations

The governing set of equations for a transient, three-dimensional, and incompressible flow is given by the conservation of mass and conservation of momentum equations. Their differential forms are:

$$\nabla \cdot \mathbf{U} = 0, \tag{1}$$

$$\frac{\partial \mathbf{U}}{\partial t} + \nabla \cdot (\mathbf{U}\mathbf{U}) = -\nabla p + \nabla \cdot (\nu \nabla \mathbf{U}) + \mathbf{f}, \tag{2}$$

where $\mathbf{U}$ is the velocity vector, t is time, p is the kinematic pressure, ν is the kinematic viscosity, and $\mathbf{f}$ represents the body forces.

In this work, the governing equations are discretized by the FVM [40,41]. This practice is applied to transform partial differential equations into a corresponding set of algebraic equations capable of reproduce the original solution for pre-determined locations in time and space [33]. In CFD codes in which the 3D Navier–Stokes equations, here represented by Eqs. (1) and (2), are solved by this discretization procedure, two issues require special treatment: the pressure–velocity coupling, and the treatment of the nonlinear term of the momentum equation [33]. The discretization of the nonlinear convective term of the momentum equation, represented by the second term on the left hand side of Eq. (2), leads to

$$\nabla \cdot (\mathbf{U}\mathbf{U}) = \sum_f \mathbf{S}\left(\mathbf{U}_f\right)\left(\mathbf{U}_f\right) = \sum_f F\left(\mathbf{U}_f\right), \tag{3}$$

where $\mathbf{S}$ is the area vector pointing out of the volume cell with magnitude equal to the face area, F represents the term $\mathbf{S} \cdot (\rho \mathbf{U})_f$, which is the mass flux through a general face, whereas $\mathbf{U}_f$ is the control volume velocity at the face cell. In the OpenFOAM software, which we employ in our simulations, this value is obtained by the Gauss scheme along with the interpolation schemes given by the LUD and LUST schemes.

2.2. Linear-Upwind Differencing (LUD) scheme

The use of upwind schemes to discretize the convective terms brings considerable stability to the convergence process [42,43]. In the blade-resolved simulations conducted in our work, for the simulations cases in which the URANS turbulence model was employed, we applied the LUD scheme as proposed by Warming and Beam [34]. The LUD method uses the information about the local gradient at the cell centroid as an explicit correction to improve the accuracy of the scheme, which makes it stable and second-order accurate. In the LUD scheme, the velocity is interpolated into the cell faces using the following expression:

$$\mathbf{U}_j^{n+1} = \frac{1}{2}\left(\mathbf{U}_j^n + \mathbf{U}_j^{n+1}\right) - \frac{\Delta t}{2}\frac{\nabla^2 F(\mathbf{U}_j)^n}{\Delta x} - \frac{\Delta t}{2}\frac{\nabla F(\mathbf{U}_j)^{n+1}}{\Delta x}, \tag{4}$$

where $\mathbf{U}_j^n$ denotes the approximation of $\mathbf{U}$, in which, $\mathbf{U}_j^n = \mathbf{U}(n\Delta t, j\Delta x)$, while Δt and Δx are the time and mesh increments, $F(\mathbf{U}_j)$ defines the forward and backward difference operators. Therefore, on face of the finite volume cells, $\mathbf{U}_j^{n+1}$ is equal to $\mathbf{U}_f$.

2.3. Linear-Upwind Stabilized Transport (LUST) scheme

For the blade-resolved simulations conducted in our work using the hybrid DES turbulence model, a blended method given by the LUST scheme proposed by Weller [36] was applied to estimate the velocity on the cell faces. This scheme is a blend between two second-order accurate schemes, the linear-upwind (LUD) and centered linear interpolation (CL), as presented by the following relation:

$$\mathbf{U}_{f_{(LUST)}} = \psi \mathbf{U}_{f_{(LUD)}} + (1-\psi)\mathbf{U}_{f_{(CL)}}, \tag{5}$$

where ψ is the blending factor to control the proportion of each scheme, $\mathbf{U}_{f_{(LUST)}}$, $\mathbf{U}_{f_{(LUD)}}$ and $\mathbf{U}_{f_{(CL)}}$ are the velocity on the cell face estimated by the LUST, LUD and CL schemes, respectively.

The expression to estimate the velocity on the cells face by the CL scheme is defined, according to Weller [36], as

$$\mathbf{U}_{f_{(CL)}} = \frac{|\Delta x_d - \Delta x_f|}{|\Delta x_d - \Delta x_u|}\mathbf{U}_{f_u} + \left(1 - \frac{|\Delta x_d - \Delta x_f|}{|\Delta x_d - \Delta x_u|}\right)\mathbf{U}_{f_d}, \tag{6}$$

where Δx_d and Δx_u refer to the mesh increments downwind and upwind from the Δx_f, respectively. Similarly, $\mathbf{U}_f$ is calculated as the difference between $\mathbf{U}_{f_d}$ and $\mathbf{U}_{f_u}$. For the simulations in which the LUST scheme was employed we considered a blending factor $\psi = 0.25$.

2.4. Turbulence modeling

Since the flow studied is governed by high Reynolds numbers, along with the discretization schemes, we also investigated the effect of different turbulence closure methods, the URANS and DES approaches. Previous works have shown that the choice of turbulence model [44] and the values of its parameters [45], affects the prediction of the wind turbine aerodynamics loads and performance. The best turbulence model for a given application should minimize the complexity of the flow field, capture the features of the most significant part of the physical system, and work in an optimized way with the numerical arrangement chosen [39]. There is thus no direct way to choose the most suitable model due the complexity of the numerical arrangement [46–48] and the interaction between the behavior of the numeric schemes and the turbulence modeling, such as the numerical diffusion from the convection discretization and the turbulent diffusion introduced by the turbulence model [33].

2.4.1. URANS $k-\omega$ SST approach

Following the statistical procedure with the averaging operation in the governing set of equations given by the continuity and incompressible Navier–Stokes equations, Eqs. (1) and (2), respectively, the URANS equations result in

$$\nabla \cdot \overline{\mathbf{U}} = 0, \tag{7}$$

$$\frac{\partial \overline{\mathbf{U}}}{\partial t} + \nabla \cdot (\overline{\mathbf{U}}\overline{\mathbf{U}}) = -\nabla \overline{p} + \nabla \cdot (\nu \nabla \overline{\mathbf{U}}) + \mathbf{f} + \overline{\mathbf{U}'\mathbf{U}'}, \tag{8}$$

where the overbar means the ensemble average value of the variable, $\overline{\mathbf{U}'\mathbf{U}'}$ represents the nonlinear Reynolds stress tensor, which introduces six new unknown variables to the governing equations. This results in the closure problem, which requires using proper closure models to establish a sufficient number of equations to solve all the flow properties [39,49].

The solution for the Reynolds stress tensor by means of known quantities can be obtained considering the mean velocity gradient. The turbulent-viscosity hypothesis, introduced by Boussinesq [49,50], one of the most popular approaches, considers the deviatoric part of the Reynolds stress tensor as proportional to the mean rate of strain as

$$\overline{\mathbf{U}'\mathbf{U}'} = \nu_t(\nabla \mathbf{U} + (\nabla \mathbf{U})^T) + \frac{2}{3}k\mathbf{I}, \tag{9}$$

where ν_t is the kinematic eddy viscosity, k the specific turbulent kinetic energy, and $\mathbf{I}$ the identity matrix. Thus, employing this model means that the transfer of momentum due to turbulent fluctuations is represented by a diffusion operator.

The next step is the evaluation of the kinematic eddy viscosity, which requires using auxiliary relations; many of them have been proposed in the literature [39]. For the URANS approach, we here employed the two-equation $k-\omega$ SST model from Menter [51], due to its ability to correctly predict flows with strong adverse pressure gradient. In this closure model, the kinematic eddy viscosity is assumed to be a function of the specific turbulent kinetic energy and its specific dissipation rate. The full expressions of the transport equations of the $k-\omega$ SST model and model constants used in our calculations are presented in Appendix A.1.

2.4.2. DES $k-\omega$ SST approach

Although the URANS turbulence model was the first to be employed in blade-resolved simulations of wind turbines [22,52], the limitations of the URANS approach, such as failure in representing the flow unsteadiness [53,54], and difficulties to represent the physics of the flow in the outer region of the boundary layer [30], have being highlighted by the scientific community [9].

The DES approach from Spalart [26], which combines the LES and URANS methods, presents a superior approach that better captures the features of a transient flow over a wind turbine. Based on the turbulence length scale and mesh sizing, the model behaves as a subgrid-scale LES model in the regions of the computational domain where the mesh resolution is fine enough, switching to the URANS $k-\omega$ SST model in the regions where it is not. Hence, URANS is used in the region of attached eddies in the boundary layer, while LES is applied to regions of massive separations [29].

The definitions of the required mesh resolution is given by the relation between spatial step Δ_{DES} and integral length scale of turbulence δ_t, where the maximum value of Δ_{DES} over the three-directions is much smaller than δ_t, which, by representing the integral length scale, is larger than the Kolmogorov scale [35,39]. The largest dimension of the grid computational cell is given by

$$\Delta_{\mathrm{DES}} = max(\delta_x, \delta_y, \delta_z). \tag{10}$$

By considering the $k-\omega$ SST model, the length scale in terms of k and ω is

$$l_{k,\omega} = \frac{k^{1/2}}{\beta^* \omega}. \tag{11}$$

In addition to replacing the length scale with that from the DES model, a specific length scale parameter based on the mesh spacing is considered,

$$\tilde{l} = \min(l_{k,\omega}, C_{\mathrm{DES}}\Delta_{\mathrm{DES}}), \tag{12}$$

where C_{DES} is a constant of the DES approach to adjust the turbulence model, which changes according to the type of URANS models [35]. For instance, in the $k-\omega$ SST, the constant C_{DES} is based on a combination of the $k-\epsilon$ and the $k-\omega$ constants, which is accomplished with the blending function F_1,

$$C_{\mathrm{DES-SST}} = (1-F_1)C_{\mathrm{DES}}^{k-\epsilon} + F_1 C_{\mathrm{DES}}^{k-\omega}, \tag{13}$$

where $C_{\mathrm{DES}}^{k-\epsilon} = 0.61$ and $C_{\mathrm{DES}}^{k-\omega} = 0.78$. Therefore, as d_w refers to the distance of the computational grid cell to the closest wall, when d_w is close to $\tilde{l}$, the model reduces to the URANS $k-\omega$ SST model. Otherwise, when a computational cell is far from the wall, $d_w > C_{\mathrm{DES-SST}}$, the approach leads to the grid-dependent model LES, allowing the representation of large eddies.

2.5. Near-wall region treatment

Since the turbulent flow close to the blades is considerably different from that of other regions due the no-slip condition applied, special treatment for the near-wall region is required [33]. The appropriate relations chosen to estimate kinematic eddy viscosity ν_t, based on the mesh refinement, local Reynolds number, and the y^+ parameter as presented in Fig. 4, are described in Appendix A.2.

For both URANS and DES turbulence models employed in the blade-resolved simulations performed in our work, ν_t k and ω were modeled by wall functions based on Launder et al. [55], assuming that, in this region, both convection and diffusion of the Reynolds stresses are small, which makes the turbulence energy generation and dissipation rates close to the equilibrium [56].

2.6. Temporal discretization scheme

To conclude the discussion regarding the numerical scheme employed to discretize the transport equation terms, the temporal term, which represents the system's time-dependent behavior, requires consideration. The choice of time-integrator scheme typically depends on the equations being solved [33]. In this study, which deals with high Reynolds numbers near the wind turbine blades, an implicit second-order upwind Euler scheme is utilized to achieve better convergence during the iterative process. In this regard, the Backward approach from [57] is implemented, which involves storing information from the current and previous time steps. Additionally, the convergence stability of the temporal discretization methods is limited by the Courant number,

$$Co = \frac{\mathbf{U}_f \Delta t}{|\mathbf{d}|}, \tag{14}$$

where $\mathbf{U}_f$ is the control volume velocity at the face cell, Δt is the time step and $\mathbf{d}$ is the vector that represents the distance between the center of the control volume cell of interest and its neighboring cells centers. Also, it is worth mentioning that the Courant–Friedrichs–Lewy (CFL) refers to the maximum allowable Courant number that a certain time-integrator scheme can employ and also defines the time-step sizing of the transient simulation.

3. Numerical simulations

This section presents the setup and details of the numerical arrangement considered in the blade-resolved investigations. We considered some simplifications regarding the wind turbine geometry, such as the absence of the tower and nacelle parts to optimize the use of the computational resources available. Thus, the case investigated is illustrated in Fig. 1, which consists of a 5 MW wind turbine rotor operating in a uniform non-turbulent wind profile of 10 m/s. Although the representation of the inflow wind as a non-turbulent and uniform profile is not realistic, the numerical setup of the simulations must first be optimized and tested for simpler environmental conditions. This will help to improve the utilization of computational resources and accuracy of the results before increasing the complexity of the environmental conditions. Once the numerical arrangement is verified, it can then be used to represent the environmental conditions more realistically.

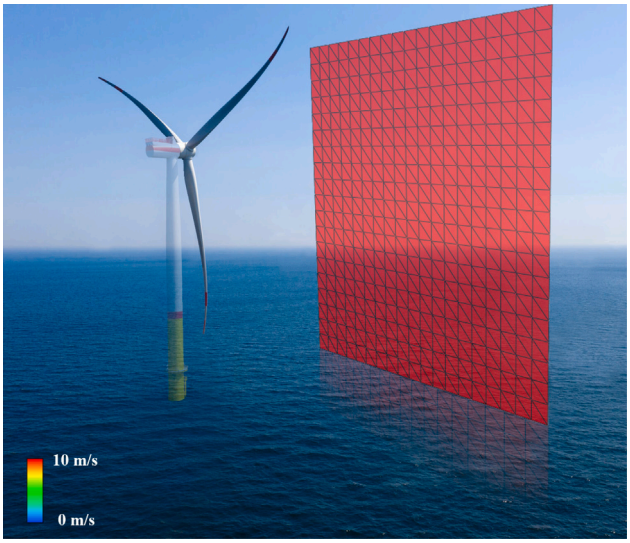

Fig. 1. Representation of the case being investigated, which includes a 5 MW wind turbine rotor in full scale, (without the tower an nacelle parts,) operating under a uniform non-turbulent wind profile.

To conduct the investigations, for the spatial discretization, given by Mesh-1, and temporal discretization given by CFL = 2, we compute the performance of the wind turbine, applying the LUD and LUST schemes in the CFD simulations considering the URANS $k-\omega$ SST as a turbulence closure model. To evaluate the response of the numerical arrangement in terms of accuracy of the results and computational demand associated, for the same numerical arrangement given by Mesh-1, and CFL = 2, we conducted blade-resolved simulation applying the LUST scheme along with the DES $k-\omega$ SST turbulence model.

Therefore, the LUST scheme was applied for discretizing the convective term for both URANS and DES simulations, while the second order accurate LUD scheme was considered only in the URANS simulation. Since the URANS simulations with LUST scheme presented better results and use of the computational resources over URANS simulations with LUD scheme, we used this numerical arrangement to predict the performance of the wind turbine rotor considering a more refined mesh given by Mesh-2. In addition, for the investigations performed for Mesh-2, besides the URANS and DES turbulence models investigated with the LUST scheme, a time discretization investigation was performed by considering different CFL numbers for each case.

The open-source OpenFOAM v.1912 software was used in the investigations, and the performance of the wind turbine rotor-only simulations was evaluated in terms of power production, generated thrust, distributed forces along the blade span, and wind profile in different positions in the wake region. A verification procedure was conducted, comparing the CFD results against the results from OpenFAST [58], which implements the blade element momentum method, considering the same NREL 5 MW wind turbine (rotor-only), with the same environmental conditions. Finally, a computational cost analysis was conducted between the numerical arrangement related to the different turbulence models and discretization schemes, to allow understanding the performance of each.

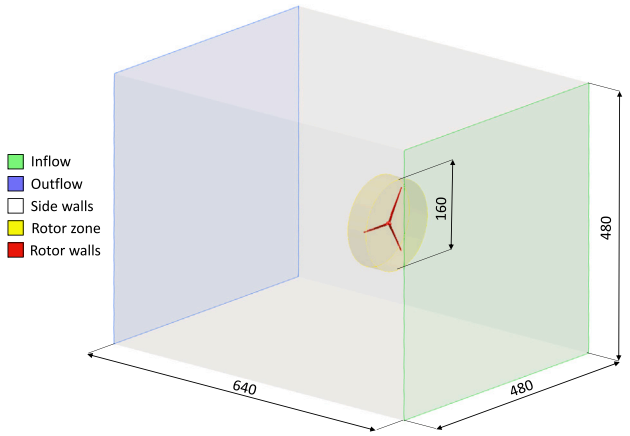

Fig. 2. Computational domain dimensions (in meters) and boundary conditions employed in the blade-resolved simulations of the NREL 5 MW wind turbine rotor.

3.1. Computational domain and boundary conditions

The rotor geometry in full scale is composed of the hub and three blades. Detailed information regarding the rotor properties are available in Jonkman et al. [38]. The rotor part, including the three blades and hub, was built using the software Solid Edge and imported into OpenFOAM, whereas all the other parts of the computational domain were built around the rotor geometry using the snappyHexMesh utility. Fig. 2 illustrates the computational domain dimensions in meters and the boundary conditions, which were defined based on [10,59].

For all the investigations conducted in our work, which are divided by the different meshes analyzed, given by Mesh-1 and Mesh-2, the dimensions of the computational domain were the same: 640 m long, 480 m wide and high, and the rotor region of 160 m to settle the rotor diameter which was considered as 124 m to take into account the hub distance between the blades.

Regarding the boundary conditions, at the inflow a Dirichlet boundary condition, given by a prescribed uniform wind profile of 10 m/s, was imposed. The value of the velocity was chosen based on Jonkman et al. [38] to represent the operational condition of optimal wind-power conversion efficiency, and for the pressure we imposed null gradient (Neumann condition). Based on the most critical Reynolds number (at the blade tip), and considering the turbulence as isotropic, the boundary conditions for the turbulent quantities were estimated based on the relations recommended by the OpenFOAM developers [60], in which as suggested by [49,61], to take into account the effect of the wall, the mixing-length specification l_m was considered as 7% of the blade tip chord. Thus, considering the local Reynolds number, the local velocity and chord length of the blade tip (R = 60 m), as presented in Fig. 4, the turbulence length scale for this region was l_m = 0.084 m, turbulence intensity I = 2%, turbulence kinetic energy k = 3.2651 $m^2\ s^{-2}$, and the specific dissipation rate, ω = 20.5649 s^{-1}, while the kinematic eddy viscosity was calculated based on the internal field everywhere. As the wind profile was uniform, for all the side walls, the boundary conditions for the velocity were the symmetry plane conditions, which correspond to null normal velocity and zero normal gradients for the tangential velocity, pressure, and turbulent quantities. Additionally, since the AMI technique is imposed in the rotor zone region of the mesh to represent its dynamic part, a uniform rotor velocity of 1.1649 rad/s was prescribed, which is the optimal rotor speed for a wind-power conversion for a wind speed of 10 m/s. Thus, for the rotor walls, a moving wall velocity condition was employed, which sets the velocity to the desired value for moving walls when a moving mesh methodology is employed. Regarding this condition, a prescribed value of (0, 0, 0) was imposed for the velocity. Also, in the rotor walls, Neumann boundary condition was applied for the pressure as a null gradient, while the turbulence properties received the proper wall function treatment according with the y^+ value in the near wall region (see Appendix A.2). At the outflow, the Dirichlet condition was applied for the pressure as a fixed value equal to zero, and for the velocity and turbulence quantities, Neumann conditions were employed as a null gradient.

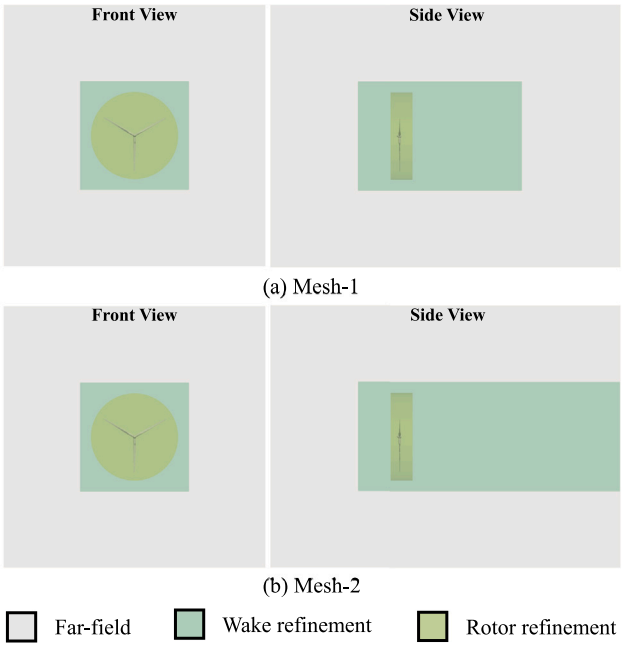

Fig. 3. Strategical partition of the computational domain to apply different mesh refinements considered for (a) Mesh-1 and (b) Mesh-2.

3.2. Spatial discretization

To perform the investigation in which different turbulence approach were employed, and for the URANS method, different discretization schemes for the convective term were tested, we considered two different types of spatial discretizations, given by Mesh-1 and Mesh-2, to capture the influence of the different mesh strategies for the cases investigated. Mesh-1 was built based on de Oliveira et al. [10] and Mesh-2 is the same mesh used in de Oliveira et al. [21]. Both meshes presented good accuracy in similar investigations at an accessible computational cost. However, Mesh-2 is more refined than Mesh-1 in different regions of the computational domain.

One important step to obtain a suitable mesh is regarding the division of the computational domain, in which different refinements are applied. In our work, different partitions of the computational domain were adopted for each mesh, as presented in Fig. 3(a) for Mesh-1 and Fig. 3(b) for Mesh-2. Both meshes had the same cell size close to the blade walls to have y^+ parameter within the adequate range for applying the turbulence models, which in all the cases was the same at the near-wall region. Information about the mesh close to the blades for both Mesh-1 and Mesh-2 along with the flow characteristics at different positions along the blade span are presented in Fig. 4. As can be seen in the region close to the blade walls, the local Reynolds number increases along with the blade radius, due the increment in the local air speed, which consequently increases the value of y^+.

Therefore, the main differences between Mesh-1 and Mesh-2 are related to the cell size in different regions of the computational domain, such as the far-field, wake, and rotor regions. For instance, the cell size in the far-field region was 32 m for Mesh-1 and 25 m for Mesh-2. In addition, in the wake region, the cell size was 2 m for Mesh-1 and 1.6 m

	R=10 m	R=20 m	R=40 m	R=60 m
	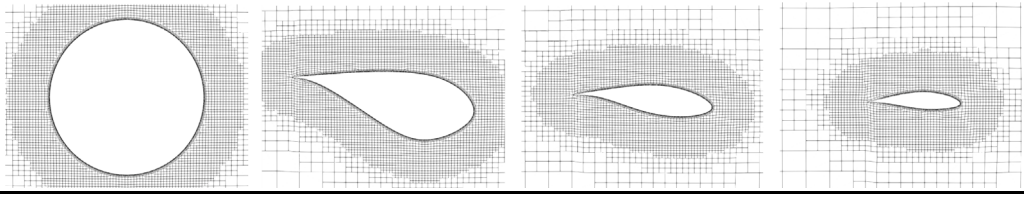			
First cell height	$1 \times 10^{-3}\ m$	$1 \times 10^{-3}\ m$	$1 \times 10^{-3}\ m$	$1 \times 10^{-3}\ m$
Characteristic length	Diameter	Chord	Chord	Chord
	$3.84\ m$	$4.65\ m$	$3.63\ m$	$1.2\ m$
Re_{local}	3.1×10^{6}	7.2×10^{6}	11.3×10^{6}	11.7×10^{6}
Local air speed	$11.6\ m/s$	$23.3\ m/s$	$46.6\ m/s$	$69.9\ m/s$
y^{+}	40	60	120	180

Fig. 4. Spatial discretization information at different positions along the blade span, indicated by R for both Mesh-1 and Mesh-2.

Table 1
Mesh sizing information (in meters) for each region of the computational domain for Mesh-1 and Mesh-2.

Region	Mesh-1	Mesh-2
Far-field	32	25
Wake refinement	2	1.6
Rotor refinement	2	0.5
Total number of cells	15,356,365	25,314,125

for Mesh-2. Different cell sizes were also adopted in the rotor region. For Mesh-1, the cell size was refined from 2 m to 0.0625 m near the blades and to 0.001 m at the first cell height attached to the blade walls. For Mesh-2, the cell size started from 0.5 m in the rotor region and decreased to 0.0625 m near the blades and then to 0.001 m at the first cell height attached to the blade walls. As a result, Mesh-1 and Mesh-2 comprised $15,356,365$ and $25,314,125$ finite volume cells respectively. Table 1 presents the refinement description applied in each region of the computational domain for both meshes.

In addition, the communication between the static and dynamic parts of the mesh, for both meshes, was performed by an arbitrary mesh interface (AMI) methodology based on [62]. More details about the refinement strategy applied to each partition of the computational domain, for each spatial discretization, can be seen in Fig. 5.

3.3. Numerical schemes

For the Mesh-1 investigations performed with the URANS turbulence model, the LUST and LUD schemes were applied to discretize the convective term, while for Mesh-2, the URANS simulations were conducted only with LUST. This is because the results from Mesh-1 investigations using the numerical arrangement given by URANS with the LUD scheme were unsatisfactory. Regarding the DES simulations, only the LUST scheme was considered for the discretization of the convective term in both analyses conducted with Mesh-1 and Mesh-2. This allowed us to improve the use of the computational resources available for Mesh-2 analyses, in which we investigated different time step sizes by testing CFL numbers equal to 1 and 2.

Besides this change in the numerical setup, the other parts of the CFD code related to the numerical methods and algorithms employed were the same in all simulations. The pressure–velocity linear dependence was treated by the iterative PISO algorithm with an extra correction for pressure, as in de Oliveira et al. [10], with 5 sub-iterations and 2 corrections for pressure performed in each time step.

The divergence terms were discretized using a second-order upwind scheme, chosen based on the modeling of similar problems [63]. Second order Gauss scheme was adopted with linear Gaussian integration for the gradient terms, while central differences were employed for the Laplacian terms based on the suggestions from Thé and Yu [9]. The set of linear equations was solved using the geometric-algebraic multi-grid (GAMG) algorithm for the symmetric matrices, and the preconditioned bi-conjugate gradient (PBiCG) with the DILU preconditioner for the non-symmetric matrices, based on Muratova et al. [64] and Moukalled et al. [57]. Regarding the temporal discretization, the second order implicit backward scheme was employed, along with the limited CFL number equals to 2 for the Mesh-1 investigations, and equal to 1 and 2 for the Mesh-2 analyses. The CFL convergence parameter was controlled by an adaptive time step to guarantee stability during the iterative process [40,57,65,66].

The solution of the all simulations conducted in our work were considered converged when the residuals of the set of estimated variables was equal to or less than 10^{-6}. For all the transient simulations cases, the initial conditions for all properties were obtained considering the steady state solution after 500 iterations, calculated with the steady form of the SIMPLE algorithm solver [67].

3.4. Hardware and parallelization

All the computations were carried out in the Brazilian supercomputer SDumont [68]. To perform the simulations, the mesh was partitioned into 240 sub-domains in each case, using the scotch decomposition method, and 10 nodes of the cluster were employed. Each node had two 12 core Intel Xeon Cascade Lake Gold 6252 processors, 3.7 GHz, and 256 Gb of RAM.

4. Results and discussion

In this section, we first report the results from the investigation conducted with Mesh-1 regarding the LUD and LUST schemes employed in the discretization of the convective term in the URANS simulations, and compare them with the results from DES simulation with the LUST scheme. Next, we present a temporal investigation using Mesh-2 considering CFL numbers equal to 1 and 2, along with a comparison between the turbulence models URANS and DES (both using the LUST scheme). We also compare the results from Mesh-2 with those from Mesh-1, to investigate the effects of the spatial discretization in the numerical solution.

The results are presented in terms of the performance of the wind turbine rotor, in which the computations of the aerodynamic loads allowed estimating the rotor power, thrust and distributed forces along the blade span. The flow features are also analyzed in terms of instantaneous iso-contours of the velocity magnitude, isosurfaces of the Q-criterion and normal vorticity. The computational cost associated with each simulation case is also discussed.

To assess the accuracy of the CFD simulations, given the absence of experimental data and similarly to the procedure adopted in de Oliveira

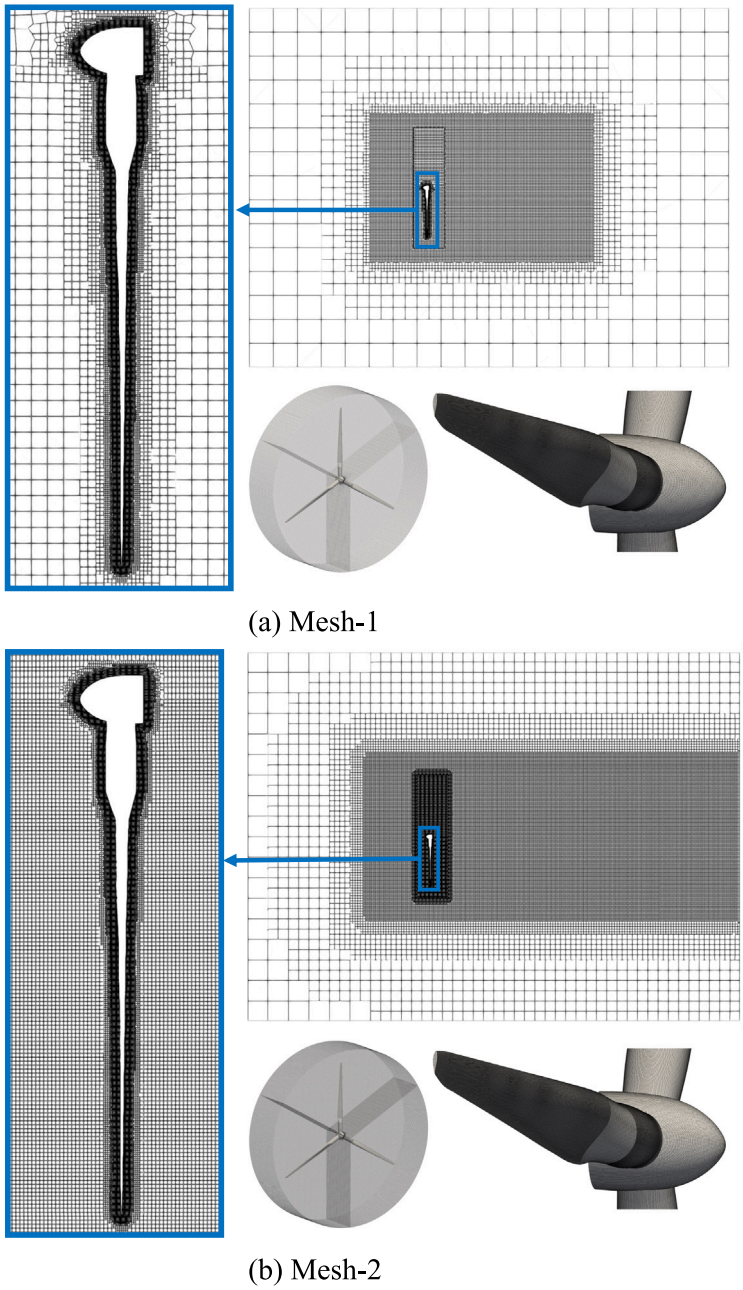

Fig. 5. Spatial discretization of the computational domain regions considered for (a) Mesh-1, and (b) Mesh-2.

et al. [10], our blade-resolved CFD simulations results were benchmarked against the results from the OpenFAST v2.5.0 code [58] for the same environmental conditions. OpenFAST is a certified code by Germanischer Lloyd (GL) [69], and calibrated by Coulling et al. [70]. It uses the blade element momentum theory and tip corrections to calculate the aerodynamic loads, and the calculations were carried out for the same wind turbine and environmental conditions considered in our work, including the absence of the tower.

4.1. LUD and LUST schemes investigation

Fig. 6 shows the power and thrust results from the URANS simulations employing the LUD and LUST schemes, as well as the results from DES simulations and the LUST scheme, and with OpenFAST. All CFD simulations employed Mesh-1. Note that the URANS simulation with the LUD scheme produced considerably different results from those obtained with the other methods. This difference can also be noticed in Fig. 7(a), which shows the distribution of mean normal and tangential forces along the blade span. Due to this disagreement, the URANS LUD simulations were considered less accurate than the others. Small differences are also noticed between the results from the URANS and DES models with the LUST scheme; the DES results were slightly better than URANS in comparison with the results from OpenFAST. A comparison of the power and thrust mean values for all the cases investigated with Mesh-1 is also presented in Table 2.

Fig. 8 shows the instantaneous iso-contours of the velocity magnitude, isosurfaces of the Q-criterion, and normal vorticity obtained from the simulations with Mesh-1. The flow features captured in the wake with the DES model are very different from those obtained with the URANS model; the gradients inside the wake region presented were

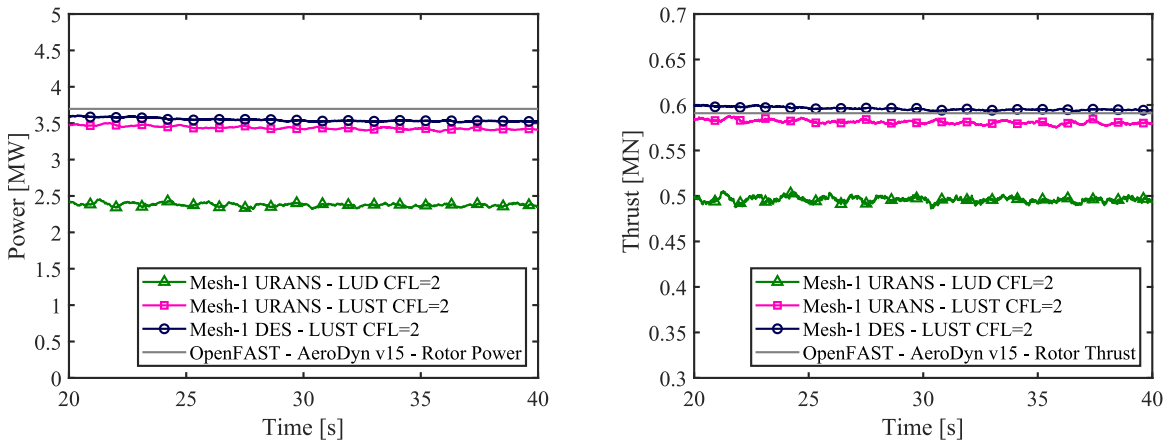

(a) Power. (b) Thrust.

Fig. 6. Mesh-1 generated power and thrust comparison between the LUD and LUST schemes for the URANS $k-\omega$ SST simulations, benchmarked against DES $k-\omega$ SST and OpenFAST results.

Table 2
Mean power production and generated thrust calculated with the CFD simulations and OpenFAST code.

Simulation	Power [MW]	Thrust [kN]
Mesh-1 URANS-LUD CFL 2	2.38 ± 0.02	495.9 ± 2.9
Mesh-1 URANS-LUST CFL 2	3.44 ± 0.02	581.2 ± 2.1
Mesh-1 DES-LUST CFL 2	3.55 ± 0.02	595.9 ± 1.6
Mesh-2 DES-LUST CFL 2	3.67 ± 0.01	626.5 ± 0.9
Mesh-2 DES-LUST CFL 1 [21]	3.75 ± 0.03	635.2 ± 2.1
Mesh-2 URANS-LUST CFL 2	3.81 ± 0.05	663.8 ± 4.6
Mesh-2 URANS-LUST CFL 1 [21]	3.53 ± 0.03	624.6 ± 2.3
OpenFAST-AeroDyn v15	3.70 ± 0.00	590.9 ± 0.0

more pronounced for the DES simulations. Furthermore, a well-defined pattern of the vortex shedding in the center of the wake is observed only for the DES-LUST case, and not so much for the URANS results. In addition, some differences can also be observed between the URANS-LUD and URANS-LUST results, especially in the region behind the blades. The URANS-LUD results show less energy extraction from the incoming flow, and this is more evident in the Q criterion isosurfaces and normal vorticity contours.

A deeper understanding of the influence of the discretization scheme in the computations of the flow in the near-wall region can be achieved by analyzing Figs. 9 and 10, comparing the local axial velocity and local pressure, respectively, at different positions along the blade span defined by R. Important distinctions can be noticed in the regions of R = 40 m, and R = 20 m; with the increase in the blade profile thickness, the boundary layer starts detaching for the URANS simulations with LUD scheme, while for the simulations that employ the LUST scheme, the flow remains attached. A possible explanation for this behavior is the higher numerical diffusion of the LUD schemes at high Reynolds numbers, and another potential cause is inappropriate mesh refinement. Similar investigations conducted by [10], presented satisfactory results for both types of spatial discretization investigated in which URANS turbulence model was employed with the LUD discretization scheme. However, in that work, the size of the cells in the rotor region were considerably smaller than those in the current investigations with Mesh-1, indicating that the LUD scheme is more susceptible to the grid influence for the URANS approach than LUST.

Finally, a computational cost analysis is shown in the first column of Fig. 11. The computational time to calculate one time step was on average 15.16 s for the URANS-LUD, on average, 15.18 s for the URANS-LUST and 17.94 s for the DES-LUST approach. However, the time step size for each of these simulations was not the same, and to compute one time unit, the URANS-LUD approach required many more time-steps. This numerical arrangement thus presented the worst performance, requiring approximately 13 h to complete 1 s of simulation time, against 10 h for the URANS-LUST and 12 h for the DES-LUST.

Therefore, considering the computational cost and numerical accuracy for the simulations conducted with Mesh-1, we concluded that the LUST scheme is superior to LUD for discretizing the convective term, even for the URANS turbulence model simulations. Thus, the LUST scheme was employed to obtain the results discussed in the next subsections of this work. The choice between the URANS-LUST and DES-LUST will depend on the mesh being used and the objective of the simulation, since both approaches presented good accuracy in terms of aerodynamic loads in our calculations, but the DES model captured more detailed information regarding the flow features with a higher computational demand.

4.2. Temporal discretization investigation considering the URANS $k-\omega$ SST turbulence model

This subsection presents the results of simulations carried out to analyze the effect of temporal discretization on the prediction of the wind turbine performance. We employed a different mesh for these calculations, namely Mesh-2, which is more refined than Mesh-1, as shown in Fig. 5. We used the LUST scheme to discretize the convection terms, performed simulations using the URANS $k-\omega$ SST model, and tested two values for the CFL number: 1 and 2.

The results for power and thrust are shown in Fig. 12, together with results from OpenFAST and Mesh-1, CFL = 2 simulations. All the models produced similar results in terms of power production, with the model that employed Mesh-2 with CFL = 2 being the closest to the result from OpenFAST. The difference between the results for thrust was more noticeable, and the CFD model that better approached the OpenFAST result was that which employed Mesh-1 and CFL = 2. These results are also reported in Table 2.

The force distributions in Fig. 7(b), provide further insight into the analysis. The differences in the normal and tangential forces computations are more significant up to approximately 45 m of the blade radius. For Mesh-2, the results from CFL = 1 and 2, were similar from 30 m of the blade radius to the blade tip. The results from Mesh-2 with both CFL numbers were closer to that from OpenFAST for the normal force from the blade root to 40 m of the blade radius, while the computations with Mesh-1 yielded results with better agreement in the region closer to the blade tip. For the tangential force, Mesh-2 with CFL = 2 presented the best agreement with the results from OpenFAST for the entire blade span, and this justifies the best agreement in the power generated. Even though the mesh refinement in the near-wall

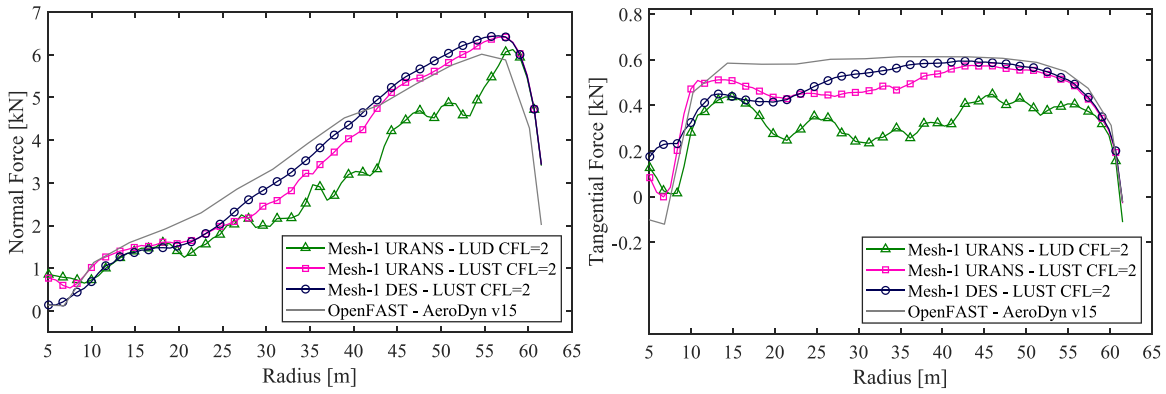

(a) Mesh-1 URANS-LUD, URANS-LUST and DES-LUST comparison.

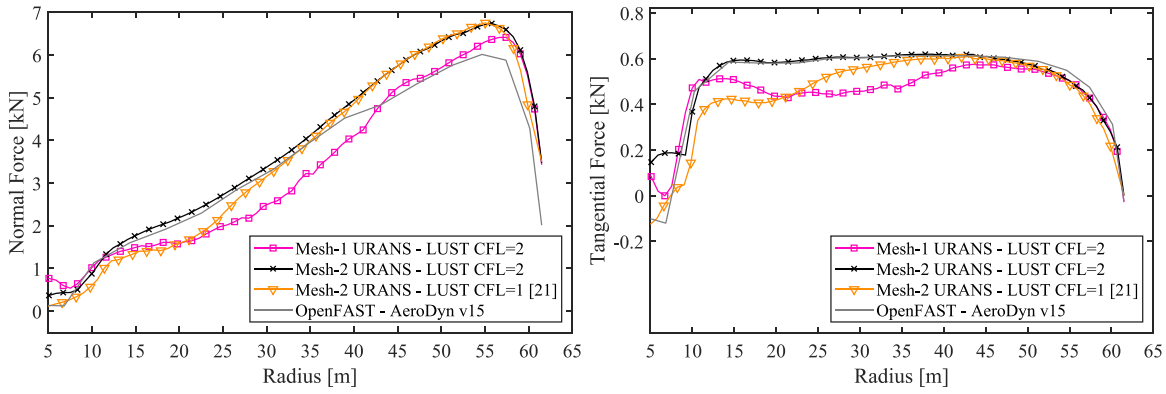

(b) Spatial and Temporal discretization investigation for the URANS-LUST approach.

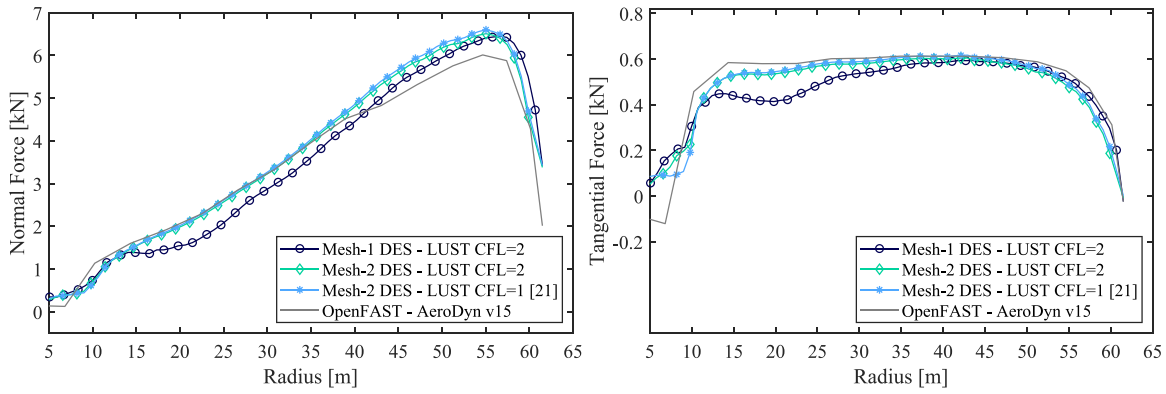

(c) Spatial and Temporal discretization investigation for the DES-LUST approach.

Fig. 7. Distributed forces along the blade span comparison for all the blade-resolved simulations conducted with Mesh-1 and Mesh-2 benchmarked against OpenFAST results.

region is the same for all CFD cases, these results show that the forces prediction can be influenced by the mesh refinement in other regions of the computational domain, such as the rotor region, besides the influence of the time step sizing.

Flow features are shown in Fig. 13(a) and (g), with the instantaneous iso-contours of the velocity magnitude. The most striking differences in the wakes are closer to the centerline (blade root region), and this is consistent with the distributed force results in Fig. 7(b). The results from CFL = 1 show finer structures in that region, in comparison to the results from CFL = 2. This difference can also be observed in the instantaneous isosurfaces of the Q-criterion shown in Fig. 13(c) and (i) and in the normal vorticity contours shown in Fig. 13(e) and (k).

With respect to the computational cost, Fig. 11(e) and (f) show that the time to complete one second of simulation time is about 10 h for Mesh-1, 13 h for Mesh-2 with CFL = 2, and 24 h for Mesh-2 with CFL = 1. The increase in the computational cost with the decrease of CFL number is expected, since the time step is inversely proportional to the CFL number. The computational cost does not follow an exact proportion because for smaller time steps, the number of internal iterations to converge the flow within each time step is usually smaller than it is for larger time steps. Both Mesh-1 with CFL = 2 and Mesh-2 with CFL = 2 are considered suitable options for the URANS simulations when the LUST scheme is employed, due to acceptable results accuracy at an affordable computational demand.

4.3. Temporal discretization investigation considering the DES $k-\omega$ SST turbulence model

We also carried out a temporal discretization analysis for the DES model, employing Mesh-2, the LUST scheme, and CFL numbers equal

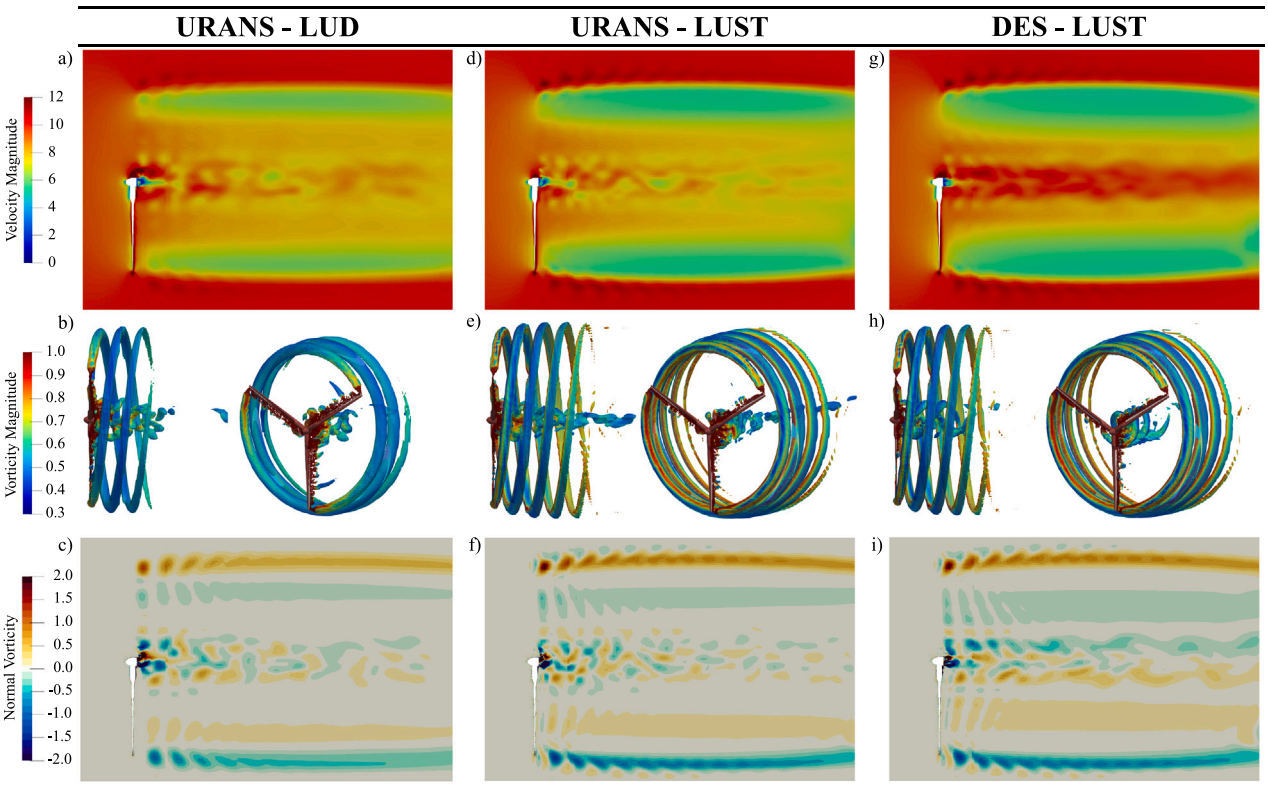

Fig. 8. Flow fields from the simulations performed with Mesh-1. Comparison of the instantaneous iso-contours of the velocity magnitude a), d), and g); isosurfaces of the Q-criterion (Q = 0.05) colored by the vorticity magnitude b), e) and h); normal vorticity c), f) and i), respectively for URANS-LUD, URANS-LUST and DES-LUST.

to 1 and 2. Fig. 14 shows the power and thrust results for these simulations, compared to those obtained with Mesh-1 (CFL = 2) and OpenFAST (see Table 2). All the results for power were very close to that obtained with Mesh-2, CFL = 2 being the closest to the OpenFAST result. For thrust, the differences were more noticeable, but the results were less dispersed than for the URANS simulations reported in Section 4.2. The CFD result for thrust that was closer to the OpenFAST benchmark value was the one from Mesh-1 (CFL = 2). These results indicate that the DES turbulence approach is less sensitive to the influence of the temporal discretization than URANS.

Fig. 7(c) presents the distribution of the normal and tangential forces along the blade span. Note that the results are much more sensitive to the spatial discretization (change of meshes) than to the temporal discretization (change of CFL number). In general, the results from Mesh-2 presented better agreement with those from OpenFAST, compared to Mesh-1.

The similarity of the results from the DES model for Mesh-2 with different CFL numbers can also be seen in the flow features shown in Fig. 13. Instantaneous iso-contours of the velocity magnitude, Fig. 13(b) and (h), instantaneous isosurfaces of the Q-criterion colored by vorticity magnitude, Fig. 13(d) and (j), and normal vorticity contours, Fig. 13(f) and (l), are virtually indistinguishable from each other. Conversely, the effect of the spatial discretization is significant. The results from Mesh-1 for the DES model with CFL = 2, illustrated in Fig. 8, (g), (h) and (i), are notably different from the flow features captured with Mesh-2 for the same DES model with CFL = 2, shown in Fig. 13(h), (j) and (l).

To conclude the analyses, the computational cost of the blade-resolved simulations conducted with the DES model are shown in Fig. 11(c) and (d). The variation in the CFL number from 1 to 2 resulted in a significant increase in the computational cost. The time required to compute one second of the simulation time was approximately 24 h for Mesh-2 with CFL = 1, while with CFL = 2, it was 13 h for Mesh-2 and 12 h for Mesh-1. The reasons for these differences are the same as those given in Section 4.2 for the URANS simulations.

Therefore, for the blade-resolved simulations performed with the DES turbulence model, both Mesh-1 or Mesh-2 with CFL = 2 are considered satisfactory numerical arrangements to be employed in this type of simulation, with satisfactory accuracy and affordable computational cost. However, in comparison with the URANS-LUST approach, whose computational cost can be seen in Fig. 11(f), for Mesh-1, the URANS model was slightly better in the time required to calculate one second of the simulation time, while for Mesh-2, the DES $k-\omega$ SST model was slightly better than the URANS $k-\omega$ SST for both CFL numbers investigated.

5. Conclusions

In this work, different numerical arrangements in CFD simulations were employed to predict the performance of the NREL 5 MW reference wind turbine rotor in full scale, operating in uniform laminar flow. The tower and nacelle were not modeled. The results were benchmarked against those obtained with OpenFAST for the same turbine and environmental conditions. At first, the treatment of the convective term of the momentum equation was investigated considering the LUD and LUST schemes in the URANS $k-\omega$ SST simulations with Mesh-1 and CFL = 2. Our conclusion was that the LUST scheme was superior to the LUD scheme, regarding computational cost and accuracy of the solution. Next, we compared the URANS and DES turbulence approach methods, using LUST and the same spatial and temporal discretization (Mesh-1 and CFL = 2). The aerodynamic loads were similar for both methods, but in terms of flow features, the DES $k-\omega$ SST turbulence model captured more detailed information, at higher computational cost. We then analyzed the spatial and temporal discretization for both turbulence approaches. We employed a more refined mesh, namely

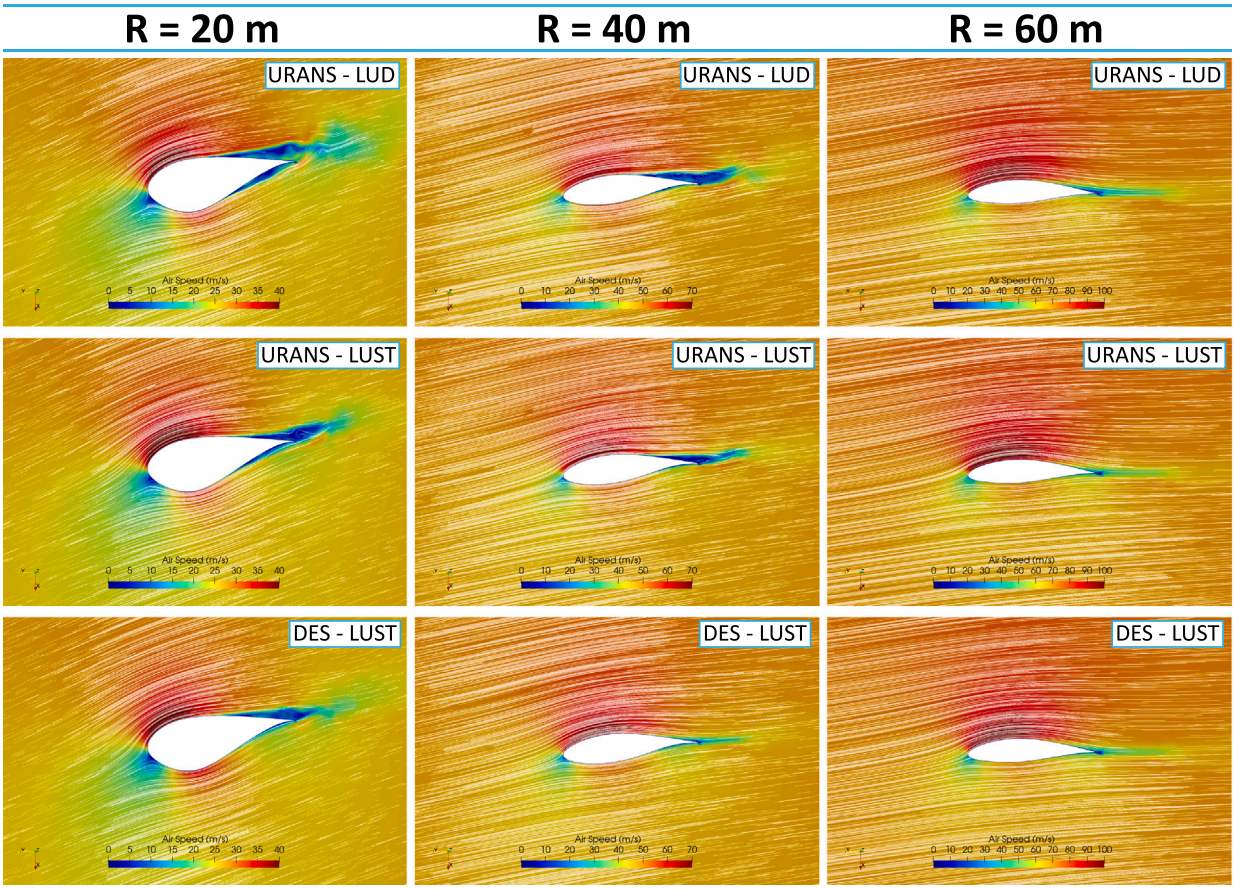

Fig. 9. Results from simulations performed with Mesh-1. Comparison of the local axial velocity field and velocity streamlines after 7 complete rotor revolutions at 3 different positions along of the blade span defined by R, for URANS-LUD, URANS-LUST and DES-LUST.

Mesh-2, the LUST scheme, and performed simulations with CFL = 1 and 2. For the URANS simulations, our conclusion was that both meshes were adequate for the simulations, and CFL = 2 was enough to produce an accurate solution. The DES simulations were more sensitive to the spatial discretization, and Mesh-2 exhibited a better performance than Mesh-1. Regarding the time step size, the conclusion was the same as that for the URANS turbulence closure method: CFL = 2 was sufficient to produce converged results.

Therefore, the numerical arrangement given by the URANS-LUST and DES-LUST approaches are both suitable options to be employed in similar investigations. However, the choice between the URANS-LUST and DES-LUST will depend on the mesh being used and on the main objectives of the blade-resolved simulation. Even though both approaches presented good accuracy in the performance results, higher definition of the flow behavior was captured with the DES-LUST approach at an affordable computational demand, highlighting the DES $k-\omega$ SST turbulence model as an attractive solution to be implemented in the modeling of the new generation of larger wind turbines. Future work will depart from the conclusions presented in this paper in similar investigations, such as modeling of tidal turbines, and the next generation of larger wind turbines, such as IEA 15 MW [71].

CRediT authorship contribution statement

Marielle de Oliveira: Conceptualization, Methodology, Software, Simulations, Writing – original draft. **Rodolfo C. Puraca:** Simulations, Data treatment, Formal analysis. **Bruno S. Carmo:** Supervision, Manuscript revision, Project administration, Funding acquisition.

Declaration of competing interest

The authors declare that they have no known competing financial interests or personal relationships that could have appeared to influence the work reported in this paper.

Data availability

Data will be made available on request.

Acknowledgments

M. de Oliveira acknowledges FAPESP (Fundação de Amparo à Pesquisa do Estado de São Paulo), the São Paulo State Research Foundation, for the Ph.D. grant - process number 2018/26207-4. R. C. Puraca acknowledges FUSP/Petrobras for the Ph.D. grant project number 2019/00171-6. B. S. Carmo acknowledges the support from FAPESP, process number 2019/01507-8, for this research, and thanks the Brazilian National Council for Scientific and Technological Development (CNPq) for financial support in the form of a productivity grant, number 314221/2021-2. The authors also acknowledge the grant from the National Laboratory of Scientific Computing (LNCC), CADASE project, which allowed the use of the Santos Dumont supercomputer to run the simulations that generated the results reported herein. This work is part of the European Commission Project "High Performance Computing for Wind Energy (HPCWE)" project number 828799.

Appendix. Turbulence modeling

This appendix presents the details of the formulation of both turbulence models employed in this work.

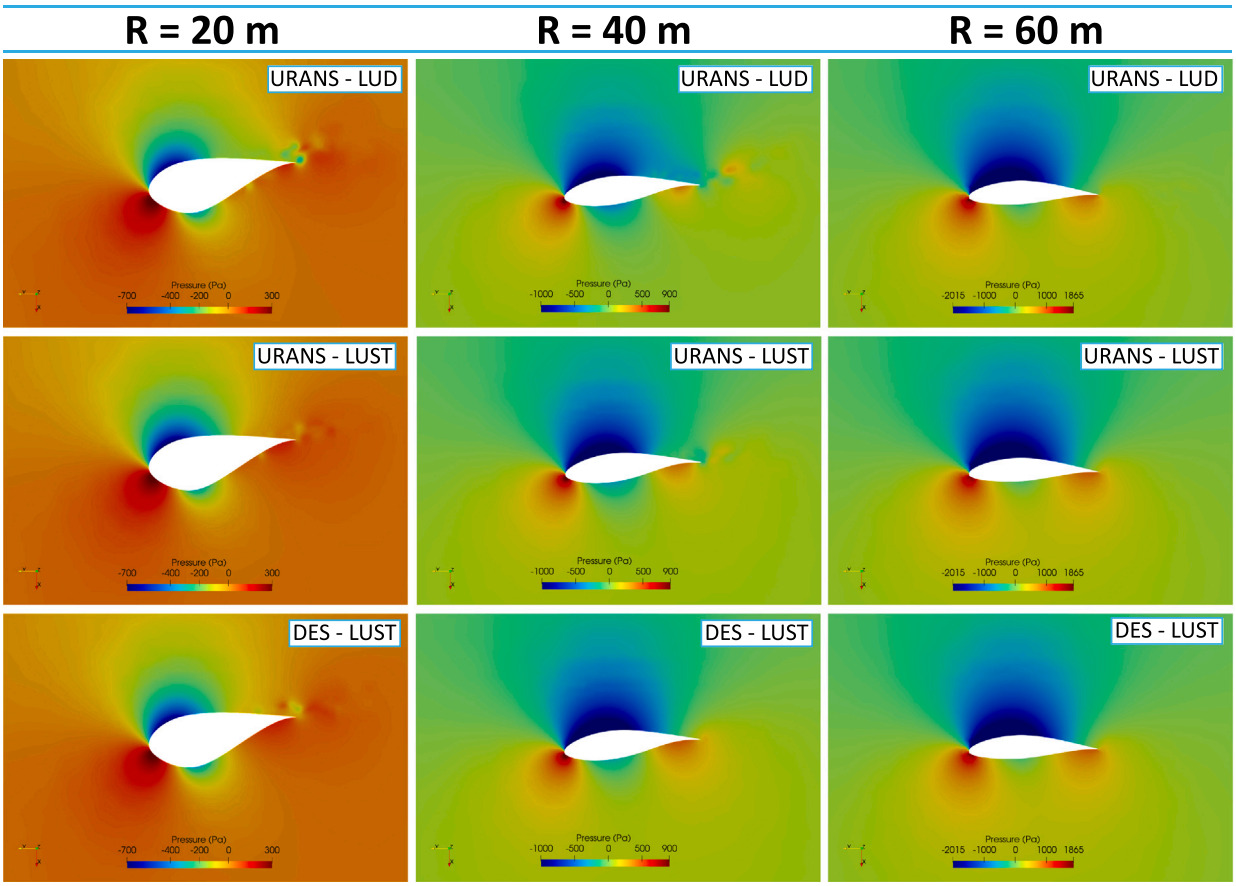

Fig. 10. Results from simulations performed with Mesh-1. Comparison of the local pressure field after 7 complete rotor revolutions at 3 different positions along of the blade span defined by R, for URANS-LUD, URANS-LUST and DES-LUST.

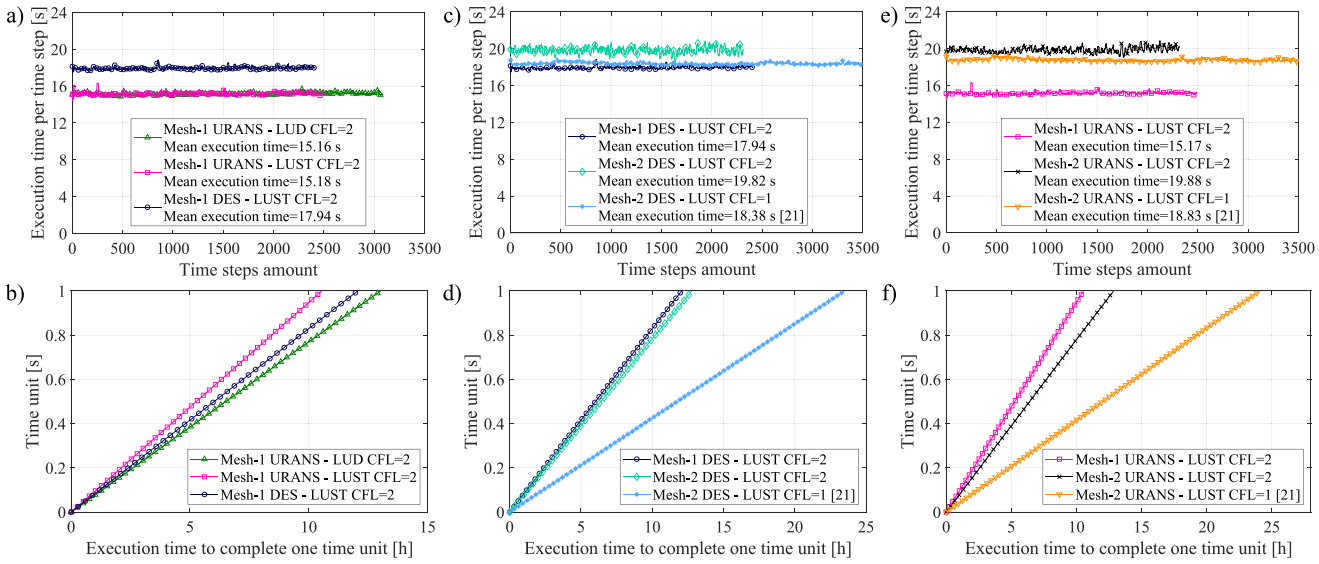

Fig. 11. Computational cost comparison for all the blade-resolved simulations conducted with Mesh-1 and Mesh-2 spatial discretizations.

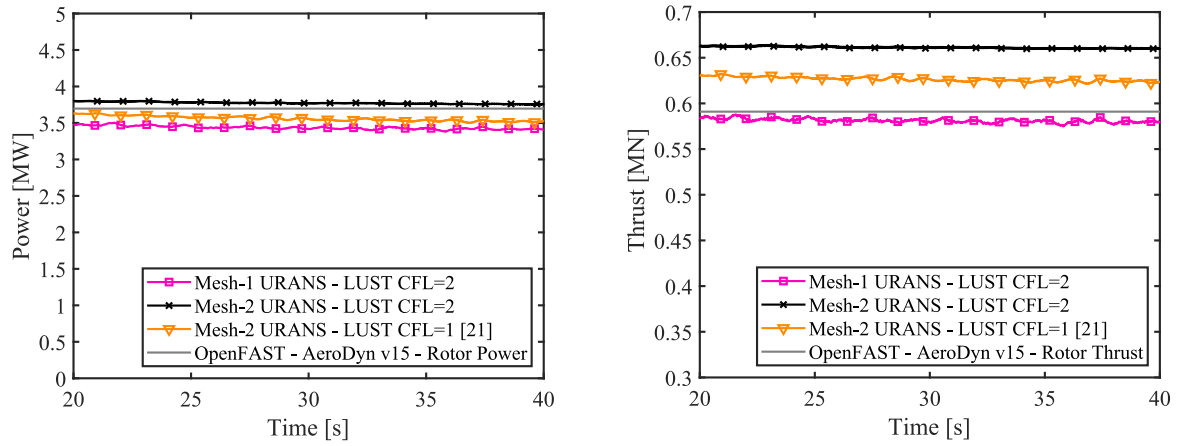

(a) Power. (b) Thrust.

Fig. 12. Results from URANS simulations performed with Mesh-2. Generated power and thrust comparison considering the LUST scheme and URANS $k-\omega$ SST simulations for CFL = 1 and CFL = 2, benchmarked against Mesh-1 and OpenFAST results.

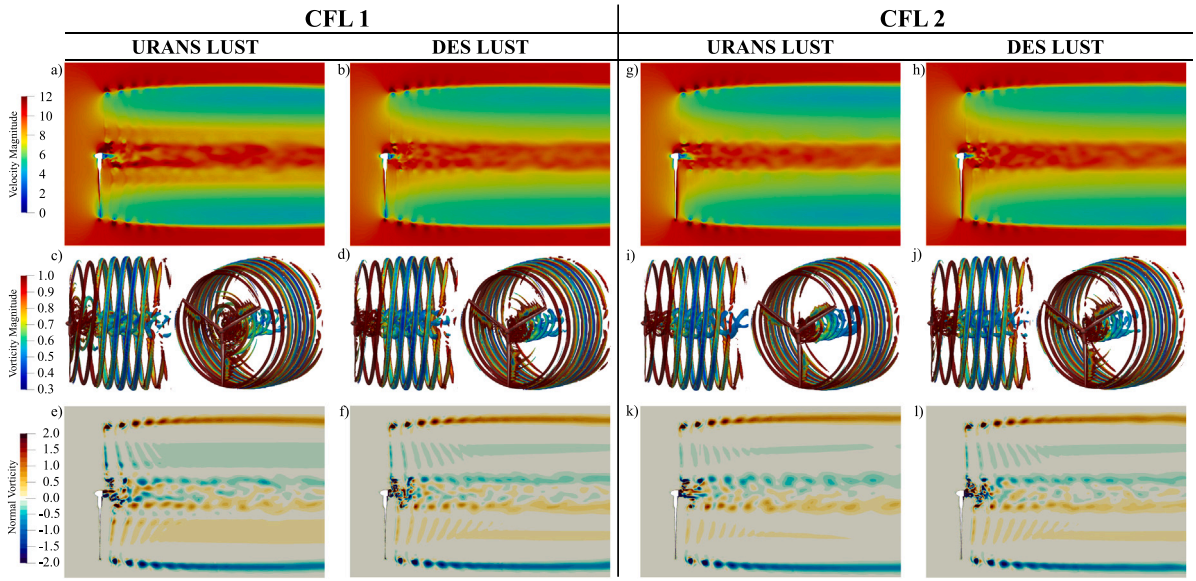

Fig. 13. Flow fields from the simulations performed with Mesh-2. Comparison of the instantaneous iso-contours of the velocity magnitude a), b), g) and h); isosurfaces of the Q-criterion ($Q = 0.05$) colored by the vorticity magnitude c), d), i) and j); normal vorticity e), f), k) and l), respectively for the URANS and DES turbulence approaches and CFL numbers equal to 1 and 2.

A.1. URANS $k-\omega$ SST approach

In the two-equations $k-\omega$ SST turbulence model from Menter [51], the specific turbulent kinetic energy k is given by

$$k = \frac{1}{2}\overline{\mathbf{U}'\mathbf{U}'}. \tag{A.1}$$

The kinematic eddy viscosity ν_t, the dissipation ϵ, and the specific dissipation rate are calculated, respectively, as

$$\nu_t = C_\mu \frac{k^2}{\epsilon}, \tag{A.2}$$

$$\epsilon = \overline{\{\mathbf{U}'\mathbf{U}'\} : \{\nabla\mathbf{U}'\}}, \tag{A.3}$$

$$\omega = \frac{\epsilon}{C_\mu k}, \tag{A.4}$$

where C_μ is a constant equal to 0.09.

The model defines two transport equations for turbulent quantities, namely k and ω:

$$\frac{\partial k}{\partial t} + \nabla\cdot(\mathbf{U}k) = \nabla\cdot[(\nu+\nu_t\sigma_k)\nabla k] + \tilde{P}_k - \beta^* k\omega, \tag{A.5}$$

$$\frac{\partial \omega}{\partial t} + \nabla\cdot(\mathbf{U}\omega) = \nabla\cdot[(\nu+\nu_t\sigma_\omega)\nabla\omega] + \frac{\alpha}{\nu_t}\tilde{P}_k - \beta\omega^2 + 2(1-F_1)\frac{\sigma_{\omega,2}}{\omega}\nabla k\cdot\nabla\omega. \tag{A.6}$$

In these equations, P_k is the specific kinetic energy production and $\tilde{P}_k$ is a production limiter to prevent the formation of turbulence in stagnation areas. We employ the blending functions F_1 and F_2 defined by Menter [51]: F_2 is equal to one in boundary layers and zero in free shear layers, and F_1 is blended with the model coefficients, which include σ_k, σ_ω, α_∞, and β by the relation expressed in generic form by

$$\phi = \phi_1 F_1 + \phi_2(1-F_1), \tag{A.7}$$

where ϕ represents coefficients σ_k, σ_ω, α_∞, and β.

All the auxiliary relations for the $k-\omega$ SST model are presented in Table A.3, and the values of the constants used in this work are given in Table A.4.

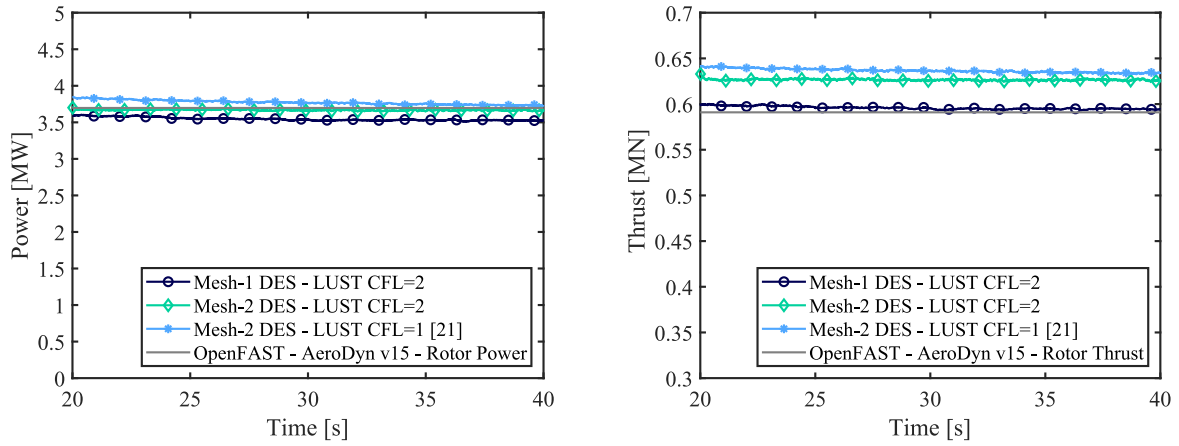

(a) Power. (b) Thrust.

Fig. 14. Results from DES simulations performed with Mesh-2. Generated power and thrust comparison considering the LUST scheme and DES $k-\omega$ SST simulations for CFL = 1 and CFL = 2, benchmarked against Mesh-1 and OpenFAST results.

Table A.3
SST k-ω turbulence model auxiliary relations.

$\nu_t = \frac{k}{\omega} \cdot \min\left(\alpha^*, \frac{a_1\omega}{S_2 F_2}\right)$
$S_t = \sqrt{\mathbf{S}_t \cdot \mathbf{S}_t}$
$\mathbf{S}_t = \frac{1}{2}\left[(\nabla U) + (\nabla U)^T\right]$
$\alpha^* = \alpha^*_\infty \left(\frac{\alpha^*_0 + Re_T/R_k}{1 + Re_T/R_k}\right)$
$D^+_\omega = \max(2\rho\sigma_{\omega 2}\frac{1}{\omega}\nabla(k\omega), 10^{-10})$
$P_k = \nu_t \nabla U \left[(\nabla U) + (\nabla U)^T\right]$
$\tilde{P}_k = \min \cdot (P_k, 10\beta^*\rho k\omega)$
$\alpha = \frac{\alpha_\infty}{\alpha^*}\left(\frac{\alpha_0 + Re_T/R_\omega}{1 + Re_T/R_\omega}\right); Re_T = \frac{k}{\nu\omega}$
$F_1 = \tanh\left\{\left\{\min\left[\max\left(\frac{\sqrt{k}}{\beta^*\omega d}, \frac{500\nu}{d^2\omega}\right), \frac{4\rho\sigma_{\omega 2}k}{D^+_\omega d^2}\right]\right\}^4\right\}$
$F_2 = \tanh\left\{\left[\max\left(\frac{2\sqrt{k}}{\beta^*\omega d}, \frac{500\nu}{d^2\omega}\right)\right]^2\right\}$

A.2. Near-wall region treatment

For both turbulence closure models investigated in our work, the treatment for the near-wall region was the same. As the flow in this region is dominated by high Reynolds number as presented in Fig. 4, the turbulent quantities ν_t, k and ω were modeled by wall functions, whereof the proper relations are employed according with the position of y^+. Initially, the y^+ parameter was set for the logarithmic-layer region, however as the mesh in this region is dynamic, this parameter can vary during the simulation. Therefore, we employed the wall functions approach to model the near-wall region by considering the y^+_{lam} parameter as reference for the y^+ position in the boundary layer. This approach, which is available in the OpenFOAM software as explained by Liu [72], allows the possibility of switch between the viscous and logarithmic regions of the boundary layer (according with the variation of the y^+ during the simulation) to bring stability to the turbulence modeling in the near-wall region by avoiding the buffer region.

Following the same methodology, the eddy viscosity ν_t is estimated by the Spalding wall function [73,74], where the relations are applied based in the y^+ value, which can also switch between the viscous and logarithmic regions. The different velocity profiles at the near-wall regions are illustrated in Fig. A.15.

Therefore, the y^+_{lam} is calculated as

$$y^+_{\text{lam}} = \frac{\log\left(\max\left(Ey^+, 1\right)\right)}{\kappa},$$

where $E = 9.8$ for smooth walls and $\kappa = 0.41$ is the von Kármán constant. The y^+ parameter is given by

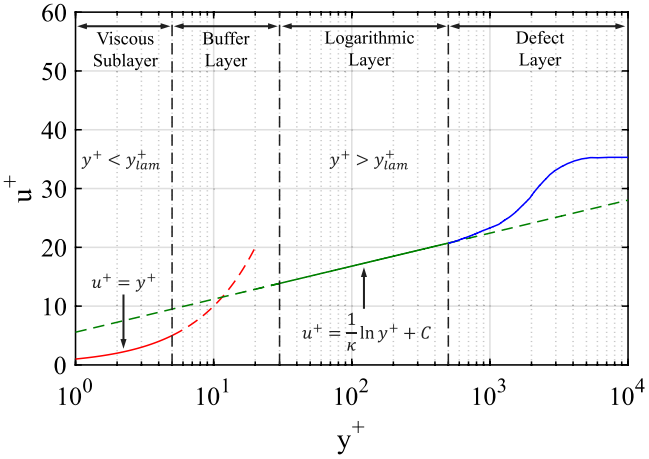

Fig. A.15. Velocity profiles and different regions of a turbulent boundary layer, edited from [10,39].

$$y^+ = \frac{y u_\tau}{\nu}, \tag{A.8}$$

where u_τ is the friction velocity,

$$u_\tau = C_\mu^{1/4}\sqrt{k}, \tag{A.9}$$

and k is the value of turbulent kinetic energy at the center of the cell adjacent to the wall, obtained through the relation $k = k^+ \times u_\tau^2$.

If $y^+ > y^+_{\text{lam}}$, the local turbulent kinetic energy is estimated as

$$k^+ = \frac{C_k}{\kappa}\log\left(y^+\right) + B_k,$$

where C_k and B_k are turbulence model constants equal to −0.416 and 8.366 respectively, and the specific dissipation rate is given by

$$\omega = \frac{k^{\frac{1}{2}}}{C_\mu^{1/4}\kappa y}. \tag{A.10}$$

If $y^+ < y^+_{\text{lam}}$, the kinetic energy and the dissipation rate are estimated as

$$k^+ = \frac{2400}{C_\varepsilon^2 \times C_f} \tag{A.11}$$

and

$$\omega = \frac{6.0\nu}{\beta_1 y^2}, \tag{A.12}$$

Table A.4
SST $k-\omega$ turbulence model constants.

$R_k = 6$	$R_\omega = 2.95$	$\alpha_0 = 1/9$	$\alpha_0^* = 0.024$	$\sigma_{k,1} = 0.85$	$\sigma_{k,2} = 1.0$	$\alpha_{\infty,1} = 5/9$
$\alpha_{\infty,2} = 0.44$	$\sigma_{\omega,1} = 0.5$	$\sigma_{\omega,2} = 0.856$	$\beta_1 = 0.075$	$\beta_2 = 0.0828$	$\beta^* = 0.09$	$a_1 = 0.31$

where β_1 is a turbulence constant equals to 0.075. Finally, the kinematic eddy viscosity is given by

$$\upsilon_t = \frac{\left(u_\tau\right)^2}{\partial \mathbf{U}/\partial n} - \upsilon, \tag{A.13}$$

where $\partial \mathbf{U}/\partial n$ means the gradient of velocity.

References

[1] GWEC. Global wind report 2022. Technical report, Global Wind Energy Council; 2022.
[2] Gomez-Iradi S, Steijl R, Barakos G. Development and validation of a CFD technique for the aerodynamic analysis of HAWT. J Solar Energy Eng 2009;131(3).
[3] Sanderse B, Van der Pijl S, Koren B. Review of computational fluid dynamics for wind turbine wake aerodynamics. Wind Energy 2011;14(7):799–819.
[4] Hansen MOL, Sørensen JN, Voutsinas S, Sørensen N, Madsen HA. State of the art in wind turbine aerodynamics and aeroelasticity. Prog Aerosp Sci 2006;42(4):285–330.
[5] Kalvig S, Manger E, Hjertager B. Comparing different CFD wind turbine modelling approaches with wind tunnel measurements. In: Journal of physics: Conference series, vol. 555. IOP Publishing; 2014, 012056.
[6] SG. Sg 8.0-167 DD Offshore wind turbine. 2022, https://www.siemensgamesa.com/products-and-services/offshore/wind-turbine-sg-8-0-167-dd (accessed: 01.05.2023).
[7] Vestas. V174-9.5 MW Offshore wind turbine. 2022, https://www.vestas.com/en/products/offshore/v174-9-5-mw- (accessed: 01.05.2023).
[8] GE. Haliade-X offshore wind turbine. 2022, https://www.ge.com/renewableenergy/wind-energy/offshore-wind/haliade-x-offshore-turbine (accessed: 01.05.2023).
[9] Thé J, Yu H. A critical review on the simulations of wind turbine aerodynamics focusing on hybrid RANS-LES methods. Energy 2017;138:257–89.
[10] de Oliveira M, Puraca RC, Carmo BS. Blade-resolved numerical simulations of the NREL offshore 5 MW baseline wind turbine in full scale: A study of proper solver configuration and discretization strategies. Energy 2022;124368.
[11] Dose B, Rahimi H, Stoevesandt B, Peinke J. Fluid-structure coupled investigations of the NREL 5 MW wind turbine for two downwind configurations. Renew Energy 2020;146:1113–23.
[12] Liu Y. A CFD study of fluid-structure interaction problems for floating offshore wind turbines (Ph.D. thesis), University of Strathclyde; 2018.
[13] Tran TT, Kim D-H. A CFD study of coupled aerodynamic-hydrodynamic loads on a semisubmersible floating offshore wind turbine. Wind Energy 2018;21(1):70–85.
[14] Tran TT, Kim D-H. Fully coupled aero-hydrodynamic analysis of a semi-submersible FOWT using a dynamic fluid body interaction approach. Renew Energy 2016;92:244–61.
[15] Liu Y, Xiao Q, Incecik A, Peyrard C, Wan D. Establishing a fully coupled CFD analysis tool for floating offshore wind turbines. Renew Energy 2017;112:280–301.
[16] Li Y. Coupled computational fluid dynamics/multibody dynamics method with application to wind turbine simulations. The University of Iowa; 2014.
[17] Liu Y, Xiao Q, Incecik A. A coupled CFD/Multibody Dynamics analysis tool for offshore wind turbines with aeroelastic blades. In: International conference on offshore mechanics and arctic engineering, vol. 57786. American Society of Mechanical Engineers; 2017, V010T09A038.
[18] Li Y, Castro A, Martin J, Sinokrot T, Prescott W, Carrica P. Coupled computational fluid dynamics/multibody dynamics method for wind turbine aero-servo-elastic simulation including drivetrain dynamics. Renew Energy 2017;101:1037–51.
[19] Li Y, Castro A, Sinokrot T, Prescott W, Carrica P. Coupled multi-body dynamics and CFD for wind turbine simulation including explicit wind turbulence. Renew Energy 2015;76:338–61.
[20] Lawson MJ, Melvin J, Ananthan S, Gruchalla KM, Rood JS, Sprague MA. Blade-resolved, single-turbine simulations under atmospheric flow. Technical report, Golden, CO (United States): National Renewable Energy Lab.(NREL); 2019.
[21] de Oliveira M, Puraca RC, Carmo BS. EPTT-2022-0008 Assessment of turbulence models for the simulation of the flow through a megawatt scale wind turbine rotor. In: ABCM, editor. EPTT-2022. Blumenau, SC, Brazil: 13th Spring School on Transition and Turbulence; 2022, p. 11.
[22] Sorensen N, Hansen M. Rotor performance predictions using a Navier-Stokes method. In: 1998 ASME wind energy symposium. 1998, p. 25.
[23] Duque E, Van Dam C, Hughes S. Navier-Stokes simulations of the NREL combined experiment phase II rotor. In: 37th aerospace sciences meeting and exhibit. 1999, p. 37.
[24] Duque EP, Burklund MD, Johnson W. Navier-Stokes and comprehensive analysis performance predictions of the NREL phase VI experiment. J Sol Energy Eng 2003;125(4):457–67.
[25] Zhang Y, Deng S, Wang X. RANS and DDES simulations of a horizontal-axis wind turbine under stalled flow condition using OpenFOAM. Energy 2019;167:1155–63.
[26] Spalart PR. Comments on the feasibility of LES for wings, and on a hybrid RANS/LES approach. In: Proceedings of first AFOSR international conference on DNS/LES. Greyden Press; 1997, p. 11.
[27] Shur M, Spalart P, Strelets M, Travin A. Detached-eddy simulation of an airfoil at high angle of attack. In: Engineering turbulence modelling and experiments 4. Elsevier; 1999, p. 669–78.
[28] Nikitin N, Nicoud F, Wasistho B, Squires K, Spalart PR. An approach to wall modeling in large-eddy simulations. Phys Fluids 2000;12(7):1629–32.
[29] Argyropoulos CD, Markatos N. Recent advances on the numerical modelling of turbulent flows. Appl Math Model 2015;39(2):693–732.
[30] Spalart PR. Strategies for turbulence modelling and simulations. Int J Heat Fluid Flow 2000;21(3):252–63.
[31] Patankar SV, Spalding DB. A calculation procedure for heat, mass and momentum transfer in three-dimensional parabolic flows. In: Numerical prediction of flow, heat transfer, turbulence and combustion. Elsevier; 1983, p. 54–73.
[32] Hirsch C. Numerical computation of internal and external flows: The fundamentals of computational fluid dynamics. Elsevier; 2007.
[33] Jasak H. Error analysis and estimation for the finite volume method with applications to fluid flows (Ph.D. thesis), Imperial College London (University of London); 1996.
[34] Warming R, Beam RM. Upwind second-order difference schemes and applications in aerodynamic flows. AIAA J 1976;14(9):1241–9.
[35] Strelets M. Detached eddy simulation of massively separated flows. In: 39th Aerospace sciences meeting and exhibit. 2001, p. 879.
[36] Weller H. Controlling the computational modes of the arbitrarily structured C grid. Mon Weather Rev 2012;140(10):3220–34.
[37] Georgiadis NJ, Rizzetta DP, Fureby C. Large-eddy simulation: current capabilities, recommended practices, and future research. AIAA J 2010;48(8):1772–84.
[38] Jonkman J, Butterfield S, Musial W, Scott G. Definition of a 5-MW reference wind turbine for offshore system development. Technical report, Golden, CO (United States): National Renewable Energy Lab.(NREL); 2009.
[39] Wilcox DC, et al. Turbulence modeling for CFD, vol. 2. DCW industries La Canada, CA; 1998.
[40] Versteeg HK, Malalasekera W. An introduction to computational fluid dynamics: The finite volume method. Pearson education; 2007.
[41] Patankar SV. Numerical heat transfer and fluid flow. CRC Press; 2018.
[42] Ferziger JH, Perić M, Street RL. Computational methods for fluid dynamics, vol. 3. Springer; 2002.
[43] Robertson E, Choudhury V, Bhushan S, Walters DK. Validation of OpenFOAM numerical methods and turbulence models for incompressible bluff body flows. Comput & Fluids 2015;123:122–45.
[44] Benjanirat S, Sankar LN, Xu G. Evaluation of turbulence models for the prediction of wind turbine aerodynamics. In: Wind energy symposium, vol. 75944. 2003, p. 73–83.
[45] Carneiro F, Moura L, Costa Rocha P, Pontes Lima R, Ismail K. Application and analysis of the moving mesh algorithm AMI in a small scale HAWT: Validation with field test's results against the frozen rotor approach. Energy 2019;171:819–29. http://dx.doi.org/10.1016/j.energy.2019.01.088, URL: https://www.sciencedirect.com/science/article/pii/S0360544219300969.
[46] Srinivasan G, Ekaterinaris J, McCroskey W. Evaluation of turbulence models for unsteady flows of an oscillating airfoil. Comput & Fluids 1995;24(7):833–61.
[47] Rizzetta DP, Visbal MR. Comparative numerical study of two turbulence models for airfoil static and dynamic stall. AIAA J 1993;31(4):784–6.
[48] Sørensen JN. Aerodynamic aspects of wind energy conversion. Annu Rev Fluid Mech 2011;43:427–48.
[49] Pope SB. Turbulent flows. 2001.
[50] Pope S. A more general effective-viscosity hypothesis. J Fluid Mech 1975;72(2):331–40.
[51] Menter FR. Two-equation eddy-viscosity turbulence models for engineering applications. AIAA J 1994;32(8):1598–605.
[52] Hansen M, Sorensen J, Michelsen J, Sorensen N, Hansen M, Sorensen J, Michelsen J, Sorensen N. A global Navier-Stokes rotor prediction model. In: 35th Aerospace sciences meeting and exhibit. 1997, p. 970.
[53] Simms D, Schreck S, Hand M, Fingersh LJ. NREL unsteady aerodynamics experiment in the NASA-Ames wind tunnel: a comparison of predictions to measurements. Technical report, Golden, CO (United States): National Renewable Energy Lab.(NREL); 2001.

[54] Sumner J, Watters CS, Masson C. CFD in wind energy: the virtual, multiscale wind tunnel. Energies 2010;3(5):989–1013.
[55] Launder BE, Reece GJ, Rodi W. Progress in the development of a Reynolds-stress turbulence closure. J Fluid Mech 1975;68(3):537–66.
[56] Bremhorst K. Modified form of the k-ϵ model for predicting wall turbulence. J Fluid Eng 1981;103:456–60.
[57] Moukalled F, Mangani L, Darwish M, et al. The finite volume method in computational fluid dynamics, vol. 113. Springer; 2016.
[58] National Renewable Energy Laboratory. OpenFAST documentation. 2021, URL: https://github.com/openfast (accessed: 17.08.2022).
[59] Hsu M-C, Bazilevs Y. Fluid–structure interaction modeling of wind turbines: simulating the full machine. Comput Mech 2012;50(6):821–33.
[60] OpenFOAM User Guide - OpenCFD Ltd. k-omega shear stress transport (SST) boundary conditions relations. 2017, URL: https://www.openfoam.com/documentation/guides/latest/doc/guide-turbulence-ras-k-omega-sst.html (accessed: 03.03.2023).
[61] Wilcox D. Turbulence modelling for CFD. DCW Industries Inc; 1993.
[62] Farrell PE, Maddison JR. Conservative interpolation between volume meshes by local Galerkin projection. Comput Methods Appl Mech Engrg 2011;200:89–100. http://dx.doi.org/10.1016/j.cma.2010.07.015.
[63] Bertagnolio F, Sørensen NN, Rasmussen F. New insight into the flow around a wind turbine airfoil section. J Sol Energy Eng 2005;127(2):214–22.
[64] Muratova G, Martynova T, Andreeva E, Bavin V, Wang Z-Q. Numerical solution of the Navier–Stokes equations using multigrid methods with HSS-based and STS-based smoothers. Symmetry 2020;12(2):233.
[65] OpenFOAMcom. Discretization schemes in OpenFOAM. 2022, URL: https://www.openfoam.com/documentation/user-guide/6-solving/6.2-numerical-schemes#x23-870273 (accessed: 07.06.2022).
[66] OpenFOAMcom. Upwind divergence scheme by OpenFOAM. 2022, URL: https://www.openfoam.com/documentation/guides/latest/doc/guide-schemes-divergence-linear-upwind.html (accessed: 07.06.2022).
[67] Van Doormaal JP, Raithby GD. Enhancements of the SIMPLE method for predicting incompressible fluid flows. Numer Heat Transfer 1984;7(2):147–63.
[68] SDumont - Sistema Brasileiro de Computacao Petaflopica. Configuracao do SDumont. 2023, URL: https://sdumont.lncc.br/machine.php?pg=machine# (accessed: 05.07.2023).
[69] National Renewable Energy Laboratory. Wind turbine design codes certified. 2005, URL: https://www.nrel.gov/news/press/2005/357.html (accessed: 10.01.2022).
[70] Coulling AJ, Goupee AJ, Robertson AN, Jonkman JM, Dagher HJ. Validation of a FAST semi-submersible floating wind turbine numerical model with DeepCwind test data. J Renew Sustain Energy 2013;5(2):023116.
[71] Gaertner E, Rinker J, Sethuraman L, Zahle F, Anderson B, Barter GE, Abbas NJ, Meng F, Bortolotti P, Skrzypinski W, et al. IEA wind TCP task 37: definition of the IEA 15-megawatt offshore reference wind turbine. Technical report, Golden, CO (United States): National Renewable Energy Lab.(NREL); 2020.
[72] Liu F. A thorough description of how wall functions are implemented in OpenFOAM. In: Proceedings of CFD with opensource software. 2016, p. 1–33.
[73] Spalding D. Mass transfer through laminar boundary layers—1. The velocity boundary layer. Int J Heat Mass Transfer 1961;2(1–2):15–32.
[74] Spalding D, Evans H. Mass transfer through laminar boundary layers—2. Auxiliary functions for the velocity boundary layer. Int J Heat Mass Transfer 1961;2(3):199–221.

7 BLADE-RESOLVED NUMERICAL SIMULATIONS OF THE IEA 15 MW WIND TURBINE FOR OFFSHORE APPLICATION IN FULL SCALE

In the process of developing larger wind turbines, such as of power capacity of 15 MW, numerical simulations play an important role as they can be used as a tool to predict the system's operation, efficiency, and reliability under different wind conditions. In this regard, different methodologies of numerical simulation are often used to investigate the aerodynamic behavior of wind turbine blades and wakes. However, as mentioned in the previous investigations conducted for the NREL 5 MW wind turbine in full scale, the accuracy of the obtained results depends on the numerical arrangement used, which includes mesh refinement, numerical schemes, algorithms, and solver parameters.

Therefore, based on the findings regarding the solver configuration from the previous investigations conducted for the NREL 5 MW wind turbine, this chapter presents blade-resolved CFD simulations for the IEA 15 MW reference wind turbine for offshore applications. In order to provide valuable insights into the unsteady aerodynamic behavior of the flow, different types of blade-resolved investigations were considered to evaluate the performance of the IEA 15 MW wind turbine at full scale. Initially, rotor-only simulations were performed considering a temporal discretization investigation. Next, the influence of the tower was included in the blade-resolved simulations. The results from the CFD simulation are presented in terms of power production, generated thrust, and forces distribution along the blade span and benchmarked against the results from the OpenFAST code for the same environmental conditions.

The blade-resolved CFD simulations developed in this chapter are presented in two stages. First, the rotor-only investigations are presented in a paper accepted for the OMAE 2023 international conference. In the sequence, the CFD investigation considering the tower influence for the same reference wind turbine is presented.

Proceedings of the ASME 2023 International Conference on Ocean, & Offshore and Arctic Engineering
OMAE2023
June 11-16, 2023, Melbourne, Australia

OMAE2023-105084

CFD INVESTIGATION OF THE IEA OFFSHORE 15 MW REFERENCE WIND TURBINE PERFORMANCE IN FULL SCALE: A TEMPORAL DISCRETIZATION ANALYSIS

Marielle de Oliveira*
Escola Politécnica
Dept. of Mechanical Engineering
University of São Paulo
05508-010, Brazil

Leandro S.P. da Silva
Delmar Systems
Perth 6000, Australia

Rodolfo Puraca
Escola Politécnica
Dept. of Mechanical Engineering
University of São Paulo
05508-010, Brazil

Bruno Carmo
Escola Politécnica
Dept. of Mechanical Engineering
University of São Paulo
05508-010, Brazil

ABSTRACT

A significant increase in wind turbine size was noticed in the past decade due to the expansion of the wind energy market to offshore sites, where steadier and stronger wind resources are available. This continuous rising in the wind turbines size leads to several design and manufacturing challenges. From the design perspective, the prediction of the flow behavior and wind turbine performance is a difficult task, since the use of reduced-scale experimental testing may not lead to a proper representation of the physics in the full scale. In this context, numerical simulations in full scale became a valuable tool to assist the design process and performance analysis of the wind turbine. This paper presents a Computational Fluid Dynamics (CFD) methodology to perform blade-resolved simulations of the IEA 15 MW Offshore Reference Wind Turbine to predict its performance. In this regard, a temporal discretization investigation is performed by testing three different values of Courant–Friedrichs–Lewy (CFL) number. The rotor performance is assessed when the turbine operates in optimal wind-power conversion efficiency, for a wind speed of 10 m/s at hub height. The results are compared against those obtained using the blade element momentum theory implemented in OpenFAST, in terms of power production, generated thrust, and distribution of forces along the blade span. The adequacy of each CFL number is assessed considering the computational cost and accuracy of the results in capturing the physics of the flow. Amongst the CFL numbers investigated, the results obtained with $\mathrm{CFL} = 1$ *and 2 presented similar behavior and satisfactory accuracy, while those obtained with* $\mathrm{CFL} = 4$ *presented unsatisfactory results. Detailed information of the flow field in the wake internal gradient region and the flow structures that detach along the blade span were noticed using* $\mathrm{CFL} = 1$*, while a significant reduction in the computational demand was achieved with* $\mathrm{CFL} = 2$*. Based on the results presented, we concluded that for the cases being investigated in this paper, a good balance between accuracy and computational demand can be achieved using a CFL number equal to 2.*

*Address all correspondence to this author: marielledeoliveira@usp.br.

1 INTRODUCTION

A continuous expansion of the offshore wind market has occurred over the past decades. Environmental conditions at offshore locations are more beneficial for wind energy harvesting, where the wind speeds are stronger, consistent, and less turbulent [1, 2]. In addition, offshore wind turbines are less restricted by logistical constraints and can increase their size, leading to cost reduction in construction, installation, operation, and maintenance [3, 4]. Since a significant amount of offshore wind potential is located in deep waters [5], the new generation of offshore wind turbines (OWT) is moving from near-shore to further offshore. At such locations, challenges associated with the prototype's design and operation are more complex, and numerical models to understand the underlying dynamics are extremely valuable. In this regard, significant research efforts have been made to support the growing interest in offshore wind power [6, 2], where several numerical models with distinct levels of fidelity have been created and used to predict the response of offshore wind turbines.

Up to date, many numerical methods to predict the dynamics of offshore wind turbines exist, and their application depends on the development stage and purpose of the numerical investigation. For instance, frequency domain models can be used to analyze the wind and wave-induced responses of Floating Offshore Wind Turbines (FOWT) during the conceptual design [7]. In further assessments and stages of development, time domain models can be applied for higher accuracy in estimating the OWT dynamics, where a more detailed analysis is conducted [7, 8, 9]. Such models rely on a numerical representation of the loads that can be validated or calibrated using experimental data or computational fluid dynamics (CFD). However, since the fluid-structure interactions of such structures are complex, the underlying physics may not be accurately described by lower-fidelity models. In addition, high-fidelity experimental testing may not be feasible due to the incompatibility of the Reynolds and Froude scales. In this regard, CFD models are extremely valuable to improve the design and reduce risks of the project that are particularly important for the analysis of larger wind turbines, which are currently ranging from 10 MW (DTU) [10] to 15 MW (IEA) [11]. For such turbines, a better understanding of the wind turbine aerodynamics at the blade and wake regions is required to promote the design of more efficient wind turbines [12, 13]. However, there is still a lack of information regarding CFD simulations of 10 MW and 15 MW OWTs using the full scale, due to the challenging setting up of the region close to the blade walls and the considerable computational demand required.

In this general context, this paper presents a CFD study to investigate the accuracy and computational cost for different temporal discretizations. Blade-resolved CFD simulations were carried out to predict the performance of the baseline wind turbine rotor IEA 15 MW for offshore applications at full scale. The work investigates the temporal discretization effects on the power production, generated thrust, and forces distributed along the blade span when the wind turbine is operating at optimal wind-power conversion efficiency. Amongst the CFD discretizations, the Finite Volume Method (FVM) is employed in this work. The FVM has been shown to be a mature and reliable method to investigate the performance of offshore wind turbines at full scale by modeling the unsteady aerodynamic flow around the wind turbine rotor blades and generated wake [12, 14, 15].

This work is structured as follows. First, the methodology is discussed, along with the governing equations, temporal discretization, the pressure-velocity coupling problem, and turbulence modeling. Second, the main characteristics of the numerical simulation for the 15 MW wind turbine are presented containing the computational domain, boundary conditions, spatial discretization, numerical schemes, and solver information. Third, a comparison of the results is made and discussed in terms of performance and flow features. The work finishes with a conclusion of the main results and deliverables of this paper. It should be noted that the effects of tower influence, wind turbulence, and wind shear are not investigated in this work due to the computational requirement of the simulations. However, future investigations to understand those effects are planned.

2 METHODOLOGY

In this section, the governing equations, the solver parameters, and the discretization schemes employed in this work are described. In order to investigate the accuracy and computational demand, a temporal discretization analysis is carried out and CFL numbers equal to 1, 2, and 4 are investigated to capture the effects of the time step sizing in the transient simulations of the IEA 15 MW wind turbine rotor. Therefore, the same numerical discretization schemes and also the same spatial discretization strategy for each case are used to simulate the blade-resolved cases. The computations were carried out using the open-source software OpenFOAM and the performance of the wind turbine (rotor-only) simulations was evaluated in terms of power production, generated thrust, force distribution along the blade span, and wind profile at different positions in the wake. In addition, the flow characteristics are illustrated and compared for all the CFL numbers investigated, through the instantaneous iso-contours of the velocity magnitude, isosurfaces of the Q-criterion, and normal vorticity. To establish the accuracy of the obtained results, the CFD results are benchmarked (verified) against the results obtained with OpenFAST [16], which implements the blade element momentum method, considering the same IEA 15 MW wind turbine (rotor-only) and environmental conditions. Finally, a computational cost analysis is conducted to identify the effect of the time step size regarding the performance of the numerical arrangement employed in the simulations.

2.1 Governing equations

Since compressibility effects can be neglected for the case being investigated [17], the problem is here represented by a transient three-dimensional incompressible flow. Therefore, the set of governing equations is determined by the conservation of mass and conservation of momentum equations, as:

$$\nabla \cdot \mathbf{U} = 0, \tag{1}$$

$$\frac{\partial \mathbf{U}}{\partial t} + \nabla \cdot (\mathbf{U}\mathbf{U}) = -\nabla p + \nabla \cdot (\nu \nabla \mathbf{U}) + \mathbf{f}, \tag{2}$$

where $\mathbf{U}$ represents the velocity vector, t denotes the time, p is the kinematic pressure, ν is the kinematic viscosity, and $\mathbf{f}$ represents the body forces. In this work, the governing equation set given by Eqs. (1) and (2) is discretized in space using the FVM method, as detailed in [18, 19], and which has been proved to be a mature approach to investigate the unsteady behavior of the flow around wind turbine blades and generated wakes [14, 2].

The discretization of the convective term in Eq. (2) is described as:

$$\nabla \cdot (\mathbf{U}\mathbf{U}) = \sum_f \mathbf{S}(\mathbf{U}_f)(\mathbf{U}_f) = \sum_f F(\mathbf{U}_f), \tag{3}$$

$$\nabla \cdot (\mathbf{U}\mathbf{U}) = a_P \mathbf{U}_P + \sum_N a_N \mathbf{U}_N, \tag{4}$$

where $\mathbf{U}_f$ is the control volume velocity at the face cell, $\mathbf{S}$ is the area vector pointing out of the volume cell with magnitude equal to the face area, the coefficients a_P and a_N which are related to the values interpolated at the faces of the control volume P and its neighbors indicated by N, are also functions of the velocity $\mathbf{U}$, while F represents the mass flux through a general face, given by the term $\mathbf{S} \cdot (\rho U)_f$. Since the complexity of the non-linear solvers results in complexity and a consequent increase in computational effort required, a linearization of the convective term is recommended. In this regard, the calculation of the F term is performed using a numerical upwind-based method for the type of flow being investigated, to guarantee the boundedness of the solution [20].

The discretized form of the continuity equation, Eq. (1), is given by:

$$\nabla \cdot \mathbf{U} = \sum_f \mathbf{S}\mathbf{U}_f = 0. \tag{5}$$

More details about the step-by-step discretization process by the FVM can be found in [12, 18].

Based on Eq. (5), the discretized form of the incompressible Navier-Stokes equations is:

$$a_P \mathbf{U}_P = \mathbf{H}(\mathbf{U}) - \sum_f \mathbf{S}(p)_f, \tag{6}$$

$$\sum_f \mathbf{S}\left[\left(\frac{1}{a_P}\right)_f (\nabla p)_f\right] = \sum_f \mathbf{S}\left(\frac{\mathbf{H}(\mathbf{U})}{a_P}\right)_f, \tag{7}$$

with the calculation of the face fluxes F given by:

$$F = \mathbf{S}\mathbf{U}_f = \mathbf{S}\left[\left(\frac{\mathbf{H}(\mathbf{U})}{a_P}\right)_f - \left(\frac{1}{a_P}\right)_f (\nabla p)_f\right]. \tag{8}$$

2.2 Temporal discretization investigation

In this work, CFL numbers equal to 1, 2, and 4 are considered for conducting the temporal discretization investigation. Since the choice of the time-integrator scheme depends on the type of equations being solved [20], the robust implicit second-order upwind Euler scheme is employed to achieve better stability in time marching for the transient calculations. Therefore, the temporal discretization investigation is carried out employing the backward scheme with an adaptive time step, in which the information from the current and previous time steps are stored. More information regarding the method can be found in [21, 18].

In OpenFOAM, the convergence of the temporal discretization method is limited by the Courant number,

$$Co = \frac{\mathbf{U}_f \Delta t}{|\mathbf{d}|}, \tag{9}$$

where Δt is the time step, $\mathbf{U}_f$ is the control volume velocity at the face cell, and $\mathbf{d}$ is the vector that represents the distance between the cell center of the control volume of interest, denominated by P, and its neighbor cell center. As can be observed in Eq. (9), the Courant number represents a measure of the flow properties being carried at each time step, which transverses a volume cell of the mesh. In addition, the CFL number refers to the maximum allowable Courant number that a certain time-integrator scheme can employ. While for the explicit methods, the CFL condition needs to be close or less than 1, for implicit schemes, as the one employed in this work, the parameter can be larger than 1 since it is less sensitive to numerical instabilities [18, 20].

2.3 Pressure-velocity coupling problem

Once the flow is treated as incompressible, density is assumed as a constant, inducing a lack of one equation to estimate the pressure field directly. By considering the discretized form of the Navier-Stokes set of equations given by Eqs. (6) and (7), a linear simultaneous dependence between velocity and pressure is observed. Therefore, special treatment is required to handle this inter-equation coupling problem. One way to solve this problem is through a segregated solution, where, according to [22], the mass flow rate across the cell faces is given by the aforementioned variable F as shown in Eq. (8), which can be estimated without any interpolation process. Based on [18] and [20], among the family of pressure-based solvers that can be implemented in OpenFOAM through the PIMPLE solver utility, the iterative form of the PISO solver for the treatment of the coupling problem in transient flow is considered, as recommended by [18]. With the iterative PISO solver, in each time step of the algorithm, the pressure corrections are solved twice, in an iterative approach until the desired tolerance is reached. In addition, an extra correction for the pressure, which is done before the start of the iterative PISO steps, can be made by taking into account the face flux velocity vector from the previous time step, as shown by [12]. Such a strategy is applied in this work due to the possibility of established stability to the convergence process, with no considerable increase in the computational cost. More information about the algorithm steps is given in [12].

2.4 Turbulence modeling

To complete the numerical arrangement required to solve the governing equations, an additional set of transport relations to represent the turbulence is employed. The URANS approach, which comes from a statistical procedure applied to the Navier-Stokes equations, is the most common and vastly used method to represent the physics of similar investigation [23, 24, 25, 12]. However, as a consequence of this procedure, the nonlinear Reynolds stresses tensor term and consequent closure problem arise, requiring turbulence closure models to establish a sufficient number of equations to solve all flow properties [26, 27]. To obtain a solution for the Reynolds stresses tensor in terms of known quantities, one possibility is to use the mean velocity gradient. In this regard, the turbulent-viscosity hypothesis, introduced by Boussinesq [28], is one of the most popular approaches, which assumes the deviatoric part of the Reynolds stress tensor as proportional to the mean rate of strain [27]. Thus, according to the hypothesis, the transfer of momentum by diffusion at the molecular level is similar to the transfer of momentum in a turbulent flow due to the turbulent fluctuations by correlating the turbulent tensor and the turbulent viscosity, also called as eddy viscosity. In this regard, the evaluation of the kinematic eddy viscosity ν_t, is obtained by solving the transport equations applying auxiliary relations. Hereby, the most common method to obtain the kinematic eddy viscosity stands out for the so-called two-equations turbulent model, in which a function correlates the ν_t with the specific turbulent kinetic energy and its specific dissipation rate [26, 27].

Therefore, to capture the physics of the system in which unsteady aerodynamic loads are calculated for a flow under the supercritical regime, the Unsteady Reynolds-Average Navier-Stokes (URANS) method from [29], along with the two-equations k-ω SST turbulence model from [30], is employed in the blade-resolved simulations conducted in our work.

Additionally, it is worth mentioning that the features of the flow are considerably different in the region close to the walls due to the no-slip condition applied on the rotor walls, therefore special treatment for this region is required. In the current investigations, in the near-wall region k and ω were estimated by the low-Reynolds wall functions by [31], while the eddy viscosity was obtained using the Spalding wall function model [32, 33]. In the OpenFOAM software, these wall functions represent a model which can switch between the viscous and logarithmic regions of the boundary layer according to the position of y^+ parameter. The equations of the URANS turbulence modeling including the near-wall treatment by the low-Reynolds corrections and the k-ω SST auxiliary relations which are employed in our work are presented in detail in [12, 34].

3 NUMERICAL SIMULATIONS

The main objective of the blade-resolved simulations conducted in this work is to predict the performance of the IEA 15 MW offshore wind turbine rotor at full scale in terms of power production, generated thrust, and blade loading analysis considering a temporal discretization investigation. The rotor geometry at full scale is composed of the hub and three blades, more detailed information regarding the rotor design is available in [11]. In this section, the setup and parameters considered in each numerical investigation are presented. The case is modeled through blade-resolved CFD simulations, as illustrated in Fig. 1, and consists of a 15 MW wind turbine rotor for offshore application (without the tower interference), under the influence of a uniform non-turbulent wind profile. The numerical analysis was carried out considering the problem as presented in Fig. 1, where the simplifications are typical of rotor-only CFD investigations [35, 36, 37].

3.1 Computational Domain and Boundary Conditions

The simplified geometry of the IEA 15MW wind turbine given by the rotor and hub geometries was built using the software Solid Edge and imported into OpenFOAM, whereas all other parts of the computational domain, such as the refinement regions, were built around the rotor geometry using the snappyHexMesh utility. The computational domain dimensions,

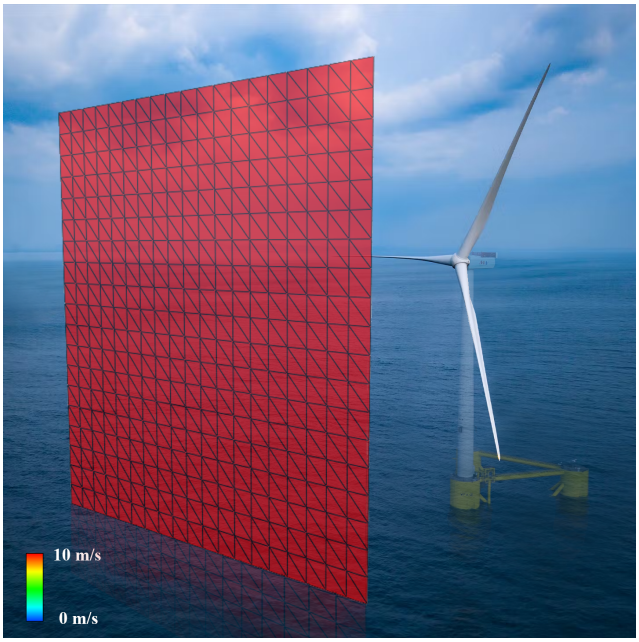

FIGURE 1: Visualization of the case being investigated, which includes a 15 MW wind turbine rotor in full scale, (without the tower) operating under a uniform non-turbulent wind profile.

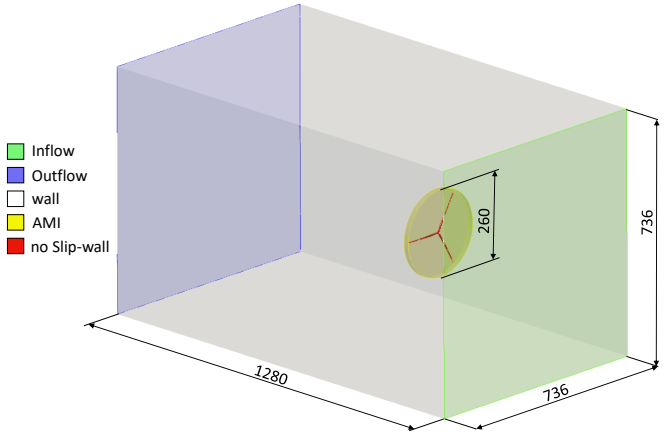

(a) Computational domain (in meters) and boundary conditions.

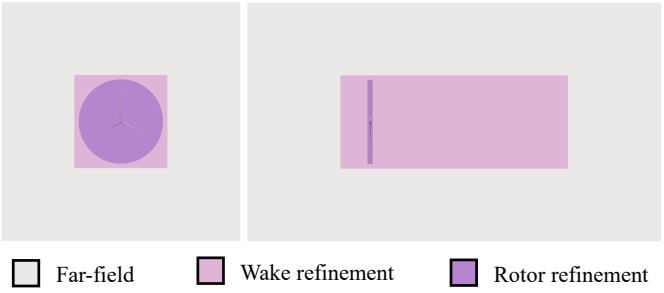

(b) Strategical partition of the computational domain.

FIGURE 2: IEA 15 MW reference offshore wind turbine rotor, computational domain dimensions (in meters), boundary conditions, and strategical partition to assemble the mesh refinements.

which were estimated based on similar investigations conducted by [12], are illustrated in Fig. 2a in meters, along with the boundary conditions applied for each region. The dimensions of the computational domain are 736 m wide and high and 1280 m long. The wind turbine rotor has a diameter equal to 240 m. In terms of the mesh generation, we employed a refined region around the rotor which was a disk with diameter 260 m.

The boundary conditions at the inflow were Dirichlet for the velocity, given by a prescribed uniform wind profile of 10 m/s, which was chosen based on [11] to represent the operational condition of optimal wind-power conversion efficiency, and for the pressure was a null gradient (Neumann condition). Based on the most critical Reynolds number (at the blade tip), and considering the turbulence as isotropic, the boundary conditions for the turbulent quantities were estimated based on the relations recommended by the OpenFOAM developers [38], in which as suggested by [27, 39], to take into account the effect of the wall, the mixing-length specification l_m was considered as 7% of the blade tip chord. Thus, considering the local Reynolds number, the local velocity and chord length of the blade tip ($R = 120\,\text{m}$), as presented in Table 1, the turbulence length scale for this region was $l_m = 0.0994\,\text{m}$, turbulence intensity $I = 0.021\%$, turbulence kinetic energy $k = 7.4789\,\text{m}^2\text{s}^{-2}$, and the specific dissipation rate, $\omega = 50.2312\,\text{s}^{-1}$, while the kinematic eddy viscosity was calculated based on the internal field everywhere. As the wind profile was uniform, for all the side walls, the boundary conditions for the velocity were symmetry plane conditions, which correspond to null normal velocity and zero normal gradients for the tangential velocity, pressure, and turbulent quantities. No slip condition was imposed for the rotor walls, to represent the velocity equal to $(0,0,0)$. Additionally, since the AMI technique is imposed in the rotor region of the mesh to represent its dynamic part, a uniform rotor velocity of $0.7494\,\text{rad/s}$ was prescribed, which is the optimal rotor speed for a wind-power conversion for a wind speed of $10\,\text{m/s}$. Neumann boundary condition was applied for the pressure as a null gradient, while the turbulence properties receive the proper wall function treatment according with the y^+ value in the near wall region. At the outflow, a Dirichlet condition was applied for the pressure as a fixed value equal to zero, and for the velocity and turbulence quantities we employed Neumann condition as a null gradient.

TABLE 1: Mesh properties information for each region of the blade span for the R15Mesh-1 spatial discretization.

	R = 20 m	R = 60 m	R = 120 m	Unit
First cell height	1×10^{-3}	1×10^{-3}	1×10^{-3}	[m]
Chord length	5.76	3.96	1.42	[m]
Re_{local}	8.7×10^{6}	1.8×10^{7}	1.3×10^{7}	[-]
Local air speed	17.98	53.95	107.9	[m/s]
y^{+}	60	160	350	[-]

3.2 Spatial discretization

To perform the temporal discretization investigation, the same spatial discretization was considered for all CFL numbers. To assemble the mesh, a similar strategy as that employed in Mesh-2 from [12] was considered, due to the accuracy in the predicted results at an accessible computational cost. In addition, since one of the most important steps during the mesh design is the division of the computational domain in which the different stages of refinement are applied, to build the mesh being used in the present investigations, the computational domain was decomposed in three main regions as presented in Fig. 2b.

Therefore, the R15Mesh-1 is composed of finite volume cells of the size of 32 m in the far-field region, which decreases into 2 m in the wake and rotor, in which the cells were refined from 1 m to 0.0625 m close to the blades and into 0.001 m at the first cell attached to the wall of the blade in order to respect the y^{+} parameter restriction for the application of the turbulence model at the near-wall region. Additionally, the communication between the static and dynamic parts of the mesh was accomplished by an arbitrary mesh interface (AMI) methodology, based on [40], where the dynamic part is given by the rotor region and the static parts are the other regions of the computational domain as presented in Fig. 2.

As a result, considering the spatial discretization strategy chosen, the R15Mesh-1 is composed of 35,446,717 finite volume cells, with a maximum aspect ratio of 65, skewness of 3.9, and non-orthogonality of 64.4. Additionally, the details about the refinement strategy applied in each partition of the computational domain which composes the R15Mesh-1 are illustrated in Fig. 3, while the information of the mesh at different positions along the blade span, indicated by R, and its local discretization parameters are shown in Fig. 4.

3.3 Numerical schemes

The arrangement employed in all the CFD simulations was the same regarding the numerical schemes, to isolate the influence of the time step sizing. Thus, based on the modeling of similar problems, the convective fluxes were discretized using

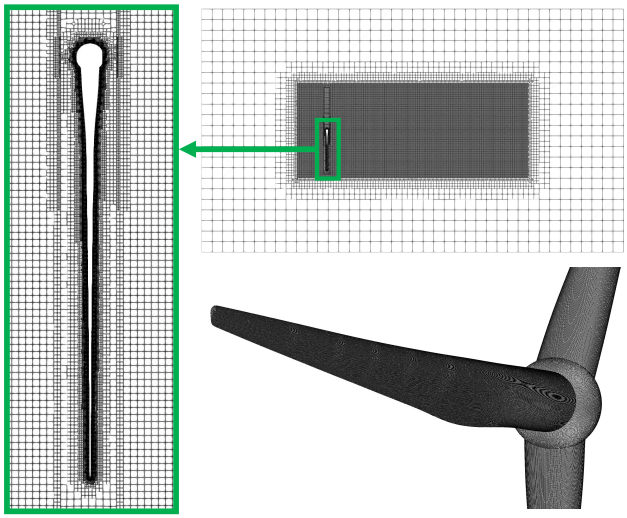

FIGURE 3: Spatial discretization of the computational domain regions.

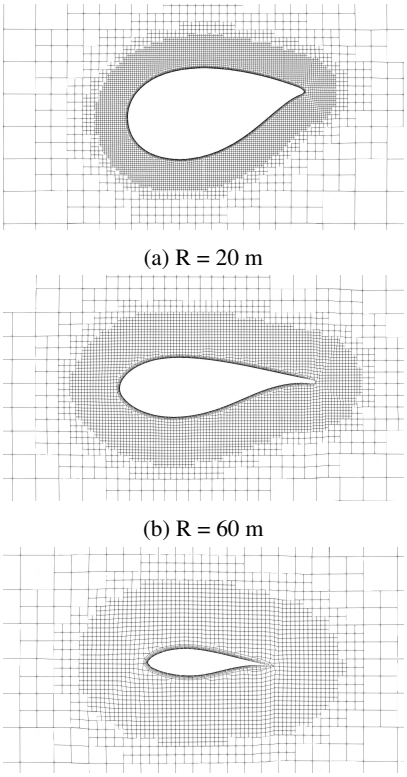

(a) R = 20 m

(b) R = 60 m

(c) R = 120 m

FIGURE 4: Spatial discretization information at different positions along the blade span, indicated by R.

a second-order upwind scheme, while for the diffusive terms, central differences were employed. For the gradient terms, the second-order Gauss scheme was adopted with linear Gaussian integration. Finally, based on [41] and [21], the set of linear equations were solved using the geometric-algebraic multi-grid (GAMG) algorithm for the symmetric matrices, and the preconditioned bi-conjugate gradient (PBiCG) with the DILU preconditioner for the non-symmetric matrices.

3.4 Solver information

As employed by [12] and [42] in similar investigations, the iterative PISO solver with face flux correction was chosen, in which 5 sub-iterations and 2 corrections for pressure were performed in each time step for all the CFL numbers being considered. Regarding the adaptive time step considered in the temporal discretization investigation, for CFL $= 1$ the time step sizing variation was between 1×10^{-4} to 2×10^{-4}, for CFL $= 2$ it was from 3×10^{-4} to 4×10^{-4}, and for CFL $= 4$ from 5×10^{-4} to 7×10^{-4}. Since the problem being investigated is transient, the solution was considered converged when the residuals of the set of estimated variables were equal or less than 10^{-6} as suggested by [18]. In addition, the initial conditions for the transient problem for all properties were obtained considering the steady state solution for the problem after 500 iterations, calculated with the steady form of the SIMPLEC algorithm solver from [43].

The Brazilian supercomputer SDumont was used to carry out the simulations. In each case, the mesh was partitioned into 240 sub-domains using scotch decomposition, using 10 nodes, where each node had two 12 core Intel Xeon Cascade Lake Gold 6252 processors, 3.7 GHz, and 256 Gb of RAM.

4 RESULTS AND DISCUSSION

Firstly, the results obtained with the different CFL numbers tested in the temporal discretization investigation are presented for power production, generated thrust, and distributed forces along the blade span considering a comparison with the results obtained from OpenFAST in order to accomplish a verification procedure. In addition, the flow characteristics and the vortical structures are illustrated along with the analysis of the wind velocity profile at different positions of the wake region. Finally, the computational cost for each CFD simulation is compared in terms of execution time to compute one physical time unit of simulation, and consequent time steps amount to accomplish the required convergence.

4.1 IEA 15 MW performance results comparison

The results for the temporal investigation in terms of the generated power and thrust are illustrated in Fig. 5, as a comparison for the CFL numbers investigated and the results obtained through the OpenFAST code, which employs the blade element momentum theory and tip corrections to calculate the aerodynamic loads for the same IEA 15 MW wind turbine rotor at the same environmental conditions.

The CFL numbers equal to 1 and 2 presented similar results in terms of integral power and thrust. As illustrated in Fig. 5a, the mean value for the power was of 10.28 MW and 10.22 MW with CFL 1 and 2, while for the thrust, Fig. 5b, the mean values were of 1.91 MN and 1.92 MN, respectively. However, with CFL $= 4$, the results were more distant from the expected solution, being 9.13 MW for power and 1.85 MN for thrust. This similarity in the results for the CFL number equal to 1 and 2 was also captured by [12], in which the performance of the NREL 5 MW wind turbine was evaluated considering the tower interference and different CFL numbers. In that work, the results obtained with CFL $= 4$ also presented discrepancies when compared to lower values of CFL such as 1 or 2. Additionally, the mean forces distribution along the blades was also investigated and compared. Considering the position of 0° of azimuth angle which represents the blade aligned in the z-direction, Fig. 6 illustrates the mean normal force in Fig. 6a, and the mean tangential force in 6b. As presented in Fig. 6a, both time step sizes considered through the different CFL numbers presented similar behavior in predicting the normal force, while for the tangential force, CFL $= 4$ presented noticeable discrepancies in the prediction of the force in the region of the blade root up to 60 m of the blade span radius.

Even though a better agreement was accomplished with CFL equal to 1 and 2 in this particular region, all cases being investigated sub-estimate the prediction of the forces along the blade span for both normal and tangential forces when compared with the values from OpenFAST.

4.2 Comparison of the flow features

Besides the performance investigation in which quantitative analyses were employed for the estimation of the generated power and thrust, normal and tangential forces acting on the blades, a comparison of the instantaneous iso-contours of the velocity magnitude, normal vorticity, and isosurfaces of the Q-criterion ($Q = 0.05$) colored by the vorticity magnitude, both after 7 complete revolutions, are illustrated in Fig. 7, for all the CFL numbers investigated. In this regard, as can be seen in Fig. 7 a), b), and c), with the increase in the CFL number a different gradient is observed for the iso-contours of the velocity magnitude, in the inner and central region of the wake region, where higher values of flow velocity are identified with CFL $= 4$ in Fig. 7c), and lower values with CFL $= 1$ in Fig. 7 a). Differences in the flow behavior in these regions are also noticed in the normal vorticity plots where it is possible to see regions of higher fluid rotation velocity for the results obtained with CFL $= 4$.

Additionally, more insights about the vortex efforts are illustrated through the isosurfaces of the Q-criterion ($Q = 0.05$) colored by the vorticity magnitude and illustrated in Figs. 7 g),

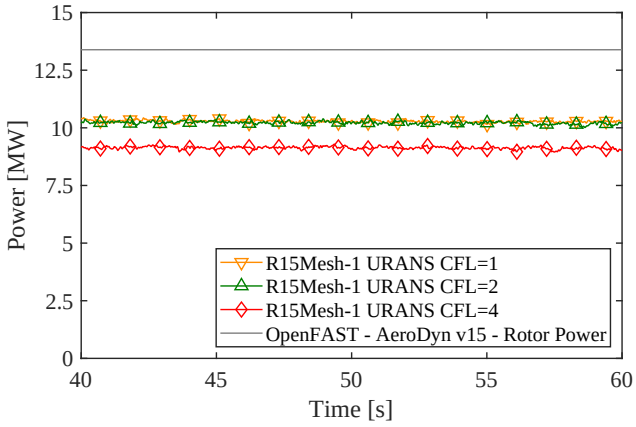

(a) Power.

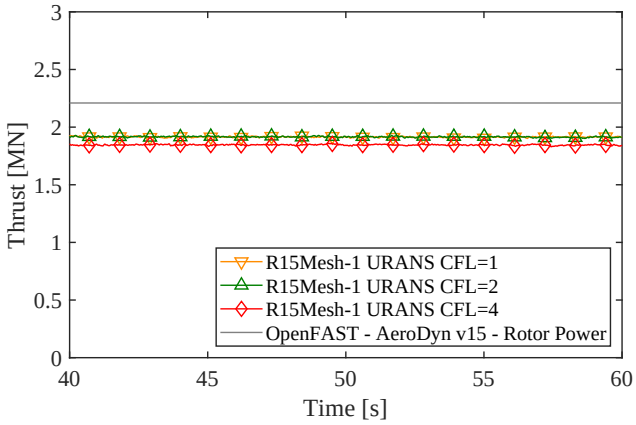

(b) Thrust.

FIGURE 5: R15Mesh-1 Temporal discretization investigation comparison for the generated power and thrust results, benchmarked against the OpenFAST results.

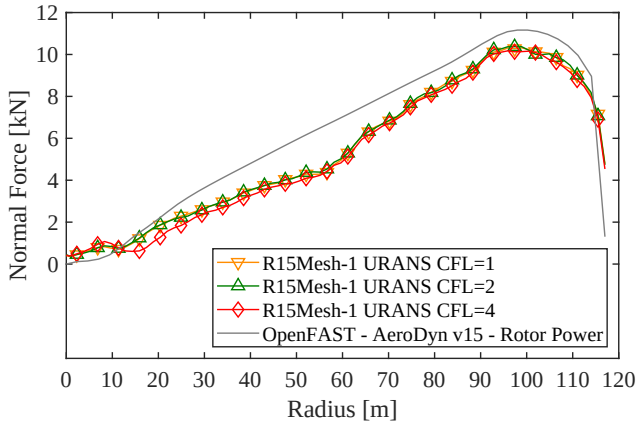

(a) Normal force.

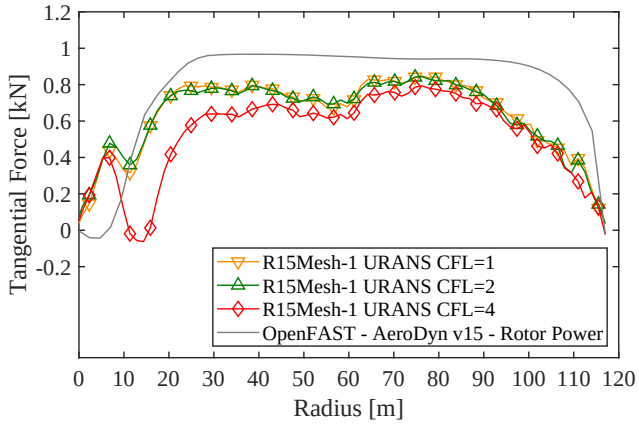

(b) Tangential force.

FIGURE 6: R15Mesh-1 Temporal discretization investigation comparison for the mean distributed forces along the blade span, benchmarked against the OpenFAST results.

h) and i), in which the vortical structures located in the center of the wake are more affected by the time step sizing given by the different CFL numbers tested, than the vortex at the tip of the blades that form the outer region of the wake.

Furthermore, for the same quasi-steady regime, instantaneous iso-contours of the mean velocity field, and wind velocity profiles are compared at 5 different positions downstream in the wake region as presented in Fig. 8 a), and b), respectively. As can be seen, CFL numbers closer to the unit such as 1 and 2, presented more similar results for both iso-contours of the mean velocity field and wind velocity profile, for all the wake regions, while with CFL $= 4$ dissimilarity in the flow pattern were captured for the regions far from the rotor, such as $x/D = 1.5$. The evaluation of the computational resources required for the blade-resolved simulations conducted in our work in which different CFL numbers were tested, showed that the execution time to compute one time unit of simulation time is approximately 89 h for CFL number equals to 1, while with higher values of CFL such as 4, the computational demand reduces to about 23 h. The reduction in the time to execute 1 s of the simulation time was of approximately 89 h to 43 h from CFL number of 1 to 2, due the decrease in time steps amount required to execute the same simulation time as can be seen in Fig. 9.

Therefore, since the use of a CFL number equal to 4 resulted in the loss of accuracy and discrepancies in the flow behavior, this choice for the convergence parameter is considered not suitable. Considering this temporal discretization analysis, a CFL number equal to 2 presented satisfactory accuracy in the obtained results with less computational demand when compared with a CFL number equal to 1.

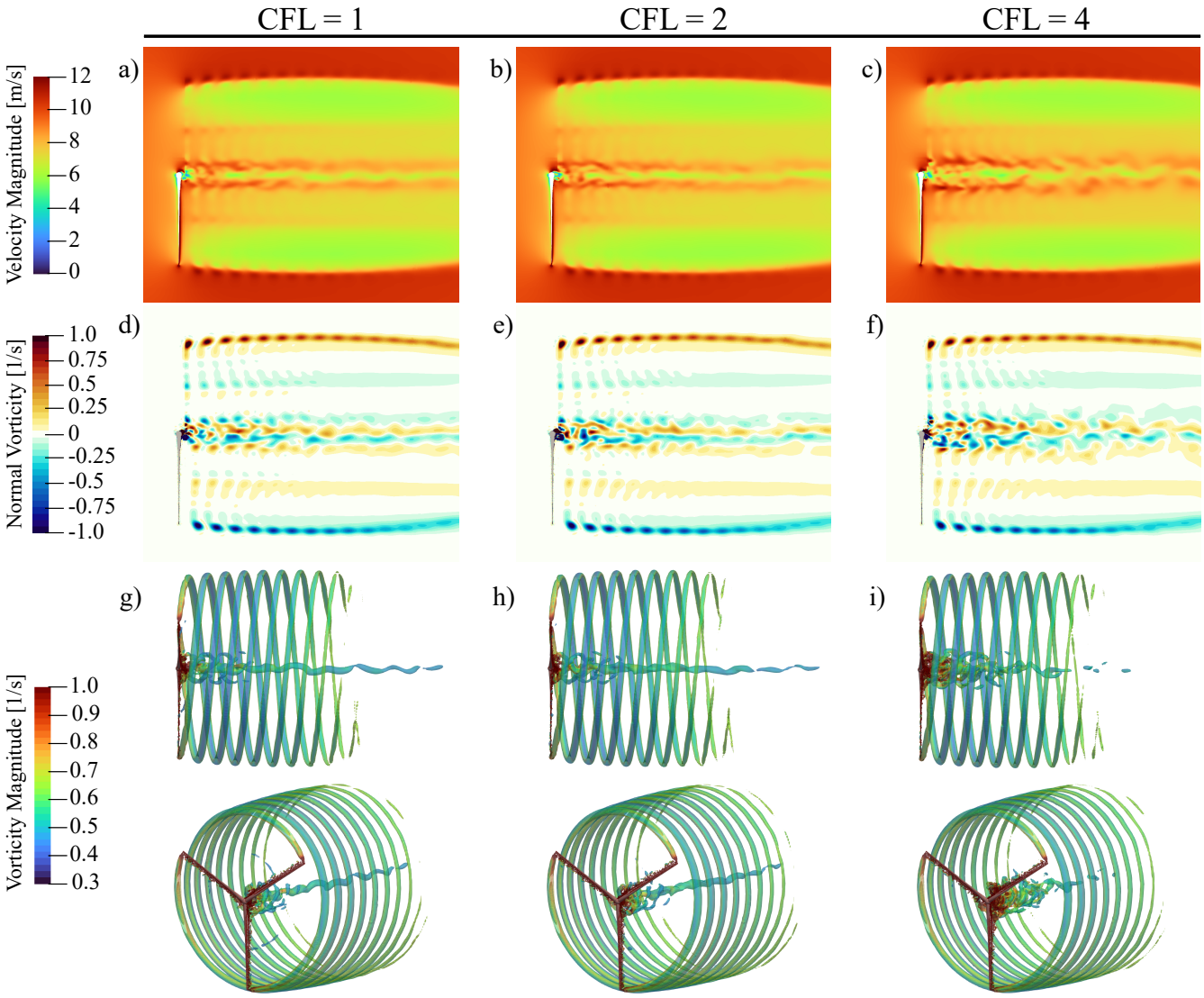

FIGURE 7: Comparison of instantaneous iso-contours of the velocity magnitude a), b), and c); normal vorticity d), e) and f), isosurfaces of the Q-criterion colored by the vorticity magnitude g), h) and i), respectively for CFL number equals to 1, 2 and 4.

5 CONCLUSION

As the blade-resolved simulations employed in the modeling of the new generation of wind turbines in full scale are still a challenging task, in this paper, the performance of the 15 MW wind turbine rotor was evaluated considering a temporal discretization investigation where CFL numbers equal to 1, 2 and 4 were tested. To conduct the numerical analysis, the FVM was employed through the OpenFOAM software where the governing equations were solved considering the URANS k-ω SST turbulence model. The rotor-only CFD simulations were performed considering the IEA 15 MW reference wind turbine for offshore applications in full scale, whereof besides the quantitative analyses of the power production, generated thrust, blade loading and wake aerodynamics pattern, significant data regarding the flow features were captured considering different time step sizing.

The vortical structures presented different behavior according to the CFL number employed in each simulation case and consequently, different integrated values were achieved for the estimation of the rotor performance. In this regard, CFL numbers closer to the unit, such as 1 or 2, presented more similar results than CFL equal to 4, for which some discrepancies were observed. Even though the computational demand was consid-

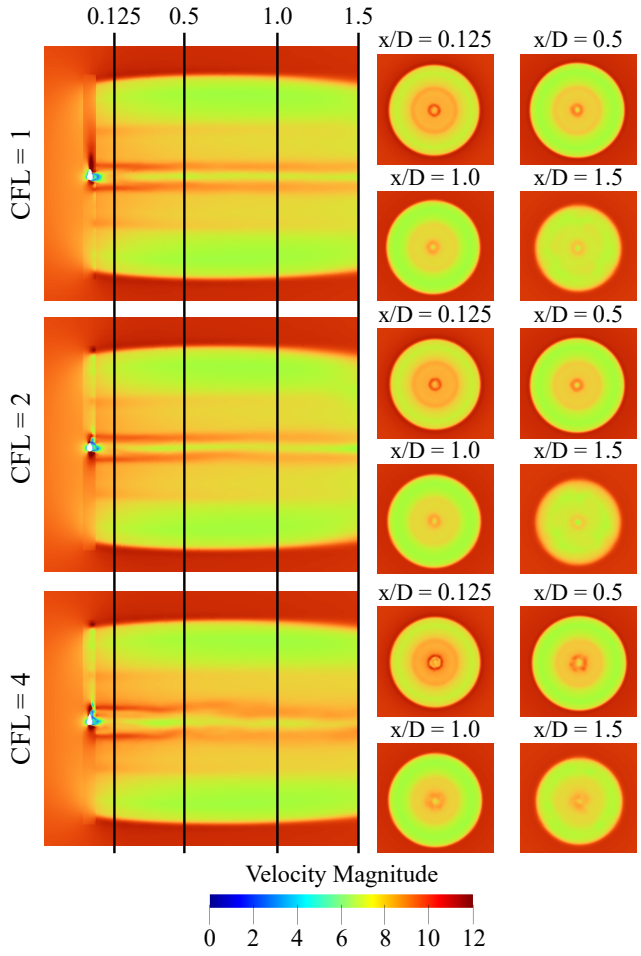

(a) Iso-contours of the mean velocity field at different positions downstream in the wake denominated by x/D.

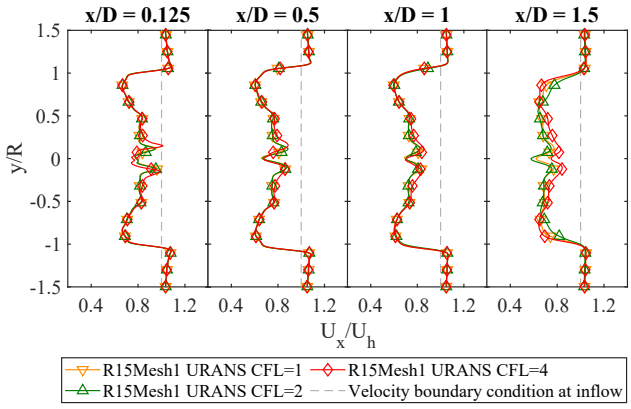

(b) Wind velocity profiles at different positions downstream in the wake denominated by x/D.

FIGURE 8: Comparison of instantaneous iso-contours of the mean velocity field, and wind velocity profiles in the quasi-steady regime at five x/D different positions downstream in the wake region for all CFL numbers investigated.

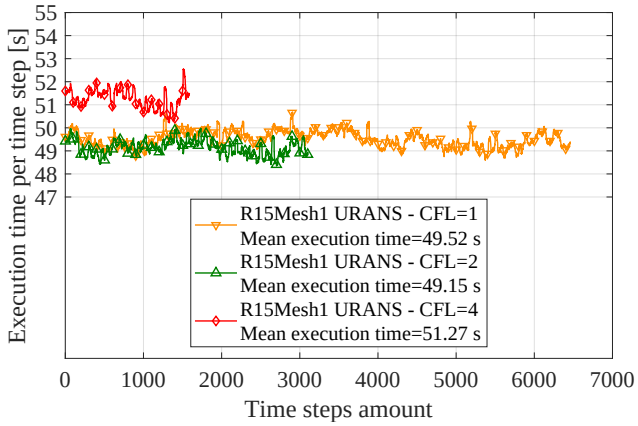

(a) Number of time steps to converge 1 s of simulation time.

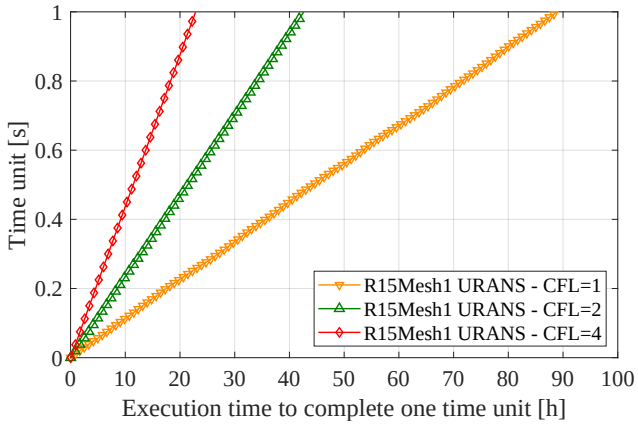

(b) Time in hours to compute 1 s of the simulation time.

FIGURE 9: Computational cost comparison for all the CFL numbers tested in the temporal discretization investigation.

erably reduced with the increase in the CFL number, the loss in accuracy makes the use of CFL equal to 4 unfeasible.

Nevertheless, the similarity in results obtained with CFL 1 and 2 indicated that a CFL number equal to 2 is a promising choice, due to the possibility of achieving accuracy in the numerical solution and also a valuable reduction in the use of the computational resources, which is desired in this type of simulation wherein the inclusion of the tower in future investigations will significantly increase the cost of the CFD simulations.

ACKNOWLEDGMENT

M. de Oliveira acknowledges FAPESP (Fundação de Amparo à Pesquisa do Estado de São Paulo), the Sao Paulo Research Foundation, for the Ph.D. grant - Process number 2018/26207-4. R. C. Puraca acknowledges FUSP/Petrobras for the Ph.D. grant

Project number 2019/00171-6. B. S. Carmo acknowledges the support from FAPESP, Proc. 2019/01507-8, for this research, and thanks the Brazilian National Council for Scientific and Technological Development (CNPq) for the financial support in the form of a productivity grant, number 314221/2021-2. The authors also acknowledge the grant from the National Laboratory of Scientific Computing (LNCC), CADASE project, which allowed the use of the Santos Dumont supercomputer to run the simulations that generated the results reported in this paper. This work is part of the European Commission Project "High Performance Computing for Wind Energy (HPCWE)" with agreement no. 828799.

REFERENCES

[1] Council, G. W. E., 2022. "Gwec— global wind report 2022". *Global Wind Energy Council: Brussels, Belgium*.

[2] Thé, J., and Yu, H., 2017. "A critical review on the simulations of wind turbine aerodynamics focusing on hybrid rans-les methods". *Energy,* ***138***, pp. 257–289.

[3] Musial, W., Spitsen, P., Beiter, P., Duffy, P., Marquis, M., Cooperman, A., Hammond, R., and Shields, M., 2021. Offshore wind market report: 2021 edition. Tech. rep., National Renewable Energy Lab.(NREL), Golden, CO (United States).

[4] Sergiienko, N., da Silva, L., Bachynski-Polić, E., Cazzolato, B., Arjomandi, M., and Ding, B., 2022. "Review of scaling laws applied to floating offshore wind turbines". *Renewable and Sustainable Energy Reviews,* ***162***, p. 112477.

[5] The Global Wind Atlas, 2020. Accessed on 26/10/2020.

[6] Holttinen, H., 2019. "Wind integration: experience, issues, and challenges". *Advances in Energy Systems: The Large-scale Renewable Energy Integration Challenge*, pp. 341–354.

[7] da Silva, L., de Oliveira, M., Cazzolato, B., Sergiienko, N., Amaral, G., and Ding, B., 2022. "Statistical linearisation of a nonlinear floating offshore wind turbine under random waves and winds". *Ocean Engineering,* ***261***, p. 112033.

[8] Oguz, E., Clelland, D., Day, A. H., Incecik, A., López, J. A., Sánchez, G., and Almeria, G. G., 2018. "Experimental and numerical analysis of a tlp floating offshore wind turbine". *Ocean Engineering,* ***147***, pp. 591–605.

[9] Jonkman, J., Butterfield, S., Musial, W., and Scott, G., 2009. Definition of a 5-mw reference wind turbine for offshore system development. Tech. rep., National Renewable Energy Lab. (NREL), Golden, CO (United States).

[10] Bak, C., Zahle, F., Bitsche, R., Kim, T., Yde, A., Henriksen, L. C., Hansen, M. H., Blasques, J. P. A. A., Gaunaa, M., and Natarajan, A., 2013. "The dtu 10-mw reference wind turbine". In Danish wind power research 2013.

[11] Gaertner, E., Rinker, J., Sethuraman, L., Zahle, F., Anderson, B., Barter, G. E., Abbas, N. J., Meng, F., Bortolotti, P., Skrzypinski, W., et al., 2020. Iea wind tcp task 37: definition of the iea 15-megawatt offshore reference wind turbine. Tech. rep., National Renewable Energy Lab.(NREL), Golden, CO (United States).

[12] de Oliveira, M., Puraca, R. C., and Carmo, B. S., 2022. "Blade-resolved numerical simulations of the nrel offshore 5 mw baseline wind turbine in full scale: A study of proper solver configuration and discretization strategies". *Energy*, p. 124368.

[13] Farrugia, R., Sant, T., and Micallef, D., 2016. "A study on the aerodynamics of a floating wind turbine rotor". *Renewable energy,* ***86***, pp. 770–784.

[14] Sanderse, B., Van der Pijl, S., and Koren, B., 2011. "Review of computational fluid dynamics for wind turbine wake aerodynamics". *Wind energy,* ***14***(7), pp. 799–819.

[15] Cheng, P., Huang, Y., and Wan, D., 2019. "A numerical model for fully coupled aero-hydrodynamic analysis of floating offshore wind turbine". *Ocean Engineering,* ***173***, pp. 183–196.

[16] National Renewable Energy Laboratory, 2021. OpenFAST documentation. (accessed: 10.05.2021).

[17] Hansen, M. O. L., Sørensen, J. N., Voutsinas, S., Sørensen, N., and Madsen, H. A., 2006. "State of the art in wind turbine aerodynamics and aeroelasticity". *Progress in aerospace sciences,* ***42***(4), pp. 285–330.

[18] Versteeg, H. K., and Malalasekera, W., 2007. *An introduction to computational fluid dynamics: the finite volume method*. Pearson education.

[19] Patankar, S. V., 2018. *Numerical heat transfer and fluid flow*. CRC press.

[20] Jasak, H., 1996. "Error analysis and estimation for the finite volume method with applications to fluid flows.". PhD thesis, Imperial College London (University of London).

[21] Moukalled, F., Mangani, L., Darwish, M., et al., 2016. *The finite volume method in computational fluid dynamics*, Vol. 113. Springer.

[22] Patankar, S. V., and Spalding, D. B., 1983. "A calculation procedure for heat, mass and momentum transfer in three-dimensional parabolic flows". In *Numerical prediction of flow, heat transfer, turbulence and combustion*. Elsevier, pp. 54–73.

[23] Rocha, P. C., Rocha, H. B., Carneiro, F. M., da Silva, M. V., and Bueno, A. V., 2014. "k–ω sst (shear stress transport) turbulence model calibration: A case study on a small scale horizontal axis wind turbine". *Energy,* ***65***, pp. 412–418.

[24] Sorensen, N., and Hansen, M., 1998. "Rotor performance predictions using a navier-stokes method". In 1998 ASME Wind Energy Symposium, p. 25.

[25] Robertson, E., Choudhury, V., Bhushan, S., and Walters, D. K., 2015. "Validation of openfoam numerical methods and turbulence models for incompressible bluff body

flows". *Computers & Fluids,* ***123***, pp. 122–145.
[26] Wilcox, D. C., et al., 1998. *Turbulence modeling for CFD*, Vol. 2. DCW industries La Canada, CA.
[27] Pope, S. B., 2001. Turbulent flows.
[28] Pope, S., 1975. "A more general effective-viscosity hypothesis". *Journal of Fluid Mechanics,* ***72***(2), pp. 331–340.
[29] Spalart, P. R., 2000. "Strategies for turbulence modelling and simulations". *International journal of heat and fluid flow,* ***21***(3), pp. 252–263.
[30] Menter, F. R., 1994. "Two-equation eddy-viscosity turbulence models for engineering applications". *AIAA journal,* ***32***(8), pp. 1598–1605.
[31] Launder, B. E., Reece, G. J., and Rodi, W., 1975. "Progress in the development of a reynolds-stress turbulence closure". *Journal of fluid mechanics,* ***68***(3), pp. 537–566.
[32] Spalding, D., and Evans, H., 1961. "Mass transfer through laminar boundary layers—2. auxiliary functions for the velocity boundary layer". *International Journal of Heat and Mass Transfer,* ***2***(3), pp. 199–221.
[33] Spalding, D., 1961. "Mass transfer through laminar boundary layers—1. the velocity boundary layer". *International Journal of Heat and Mass Transfer,* ***2***(1-2), pp. 15–32.
[34] Liu, F., 2016. "A thorough description of how wall functions are implemented in openfoam". *Proceedings of CFD with OpenSource Software*, pp. 1–33.
[35] Duque, E., Van Dam, C., and Hughes, S., 1999. "Navier-stokes simulations of the nrel combined experiment phase ii rotor". In 37th Aerospace Sciences Meeting and Exhibit, p. 37.
[36] Duque, E. P., Burklund, M. D., and Johnson, W., 2003. "Navier-stokes and comprehensive analysis performance predictions of the nrel phase vi experiment". *J. Sol. Energy Eng.,* ***125***(4), pp. 457–467.
[37] Zhang, Y., Deng, S., and Wang, X., 2019. "Rans and ddes simulations of a horizontal-axis wind turbine under stalled flow condition using openfoam". *Energy,* ***167***, pp. 1155–1163.
[38] OpenFOAM User Guide - OpenCFD Ltd, 2017. k-omega shear stress transport (sst) boundary conditions relations. https://www.openfoam.com/documentation/guides/latest/doc/guide-turbulence-ras-k-omega-sst.html (accessed: 03.03.2023).
[39] Wilcox, D., 1993. *Turbulence Modelling for CFD*. DCW Industries Inc.
[40] Farrell, P. E., and Maddison, J. R., 2011. "Conservative interpolation between volume meshes by local Galerkin projection". *Computer Methods in Applied Mechanics and Engineering,* ***200***, pp. 89–100.
[41] Muratova, G., Martynova, T., Andreeva, E., Bavin, V., and Wang, Z.-Q., 2020. "Numerical solution of the navier–stokes equations using multigrid methods with hss-based and sts-based smoothers". *Symmetry,* ***12***(2), p. 233.
[42] de Oliveira, M., Puraca, R. C., and Carmo, B. S., 2022. "Assessment of Turbulence Models for the Simulation of the Flow Through a Megawatt Scale Wind Turbine Rotor". In Proceedings of the EPTT2022 – 13th Spring School on Transition and Turbulence.
[43] Van Doormaal, J. P., and Raithby, G. D., 1984. "Enhancements of the simple method for predicting incompressible fluid flows". *Numerical heat transfer,* ***7***(2), pp. 147–163.

7.1 IEA 15 MW Investigations Considering the Tower Influence

In this section, the investigations of the IEA wind 15MW offshore reference wind turbine in full scale are presented considering the tower influence. The full wind turbine system includes the rotor part composed of three blades as presented in Section 7, along with the inclusion of the nacelle and tower parts. More details of the complete wind turbine system are outlined in [41].

Fig. 7.1 illustrates the case considered in the investigations, given by a 15 MW wind turbine designed for offshore applications, considering the tower influence, and subject to a prescribed non-turbulent logarithmic wind profile, as described in Eq. (2.4), where the roughness height was set 0.001 m to represent the ocean rugosity, the velocity at 150 m height was set to be 10 m/s, which represents the region closer to the optimal wind-power conversion efficiency, with a TSR=9 and a blade pitch angle of zero degrees [41].

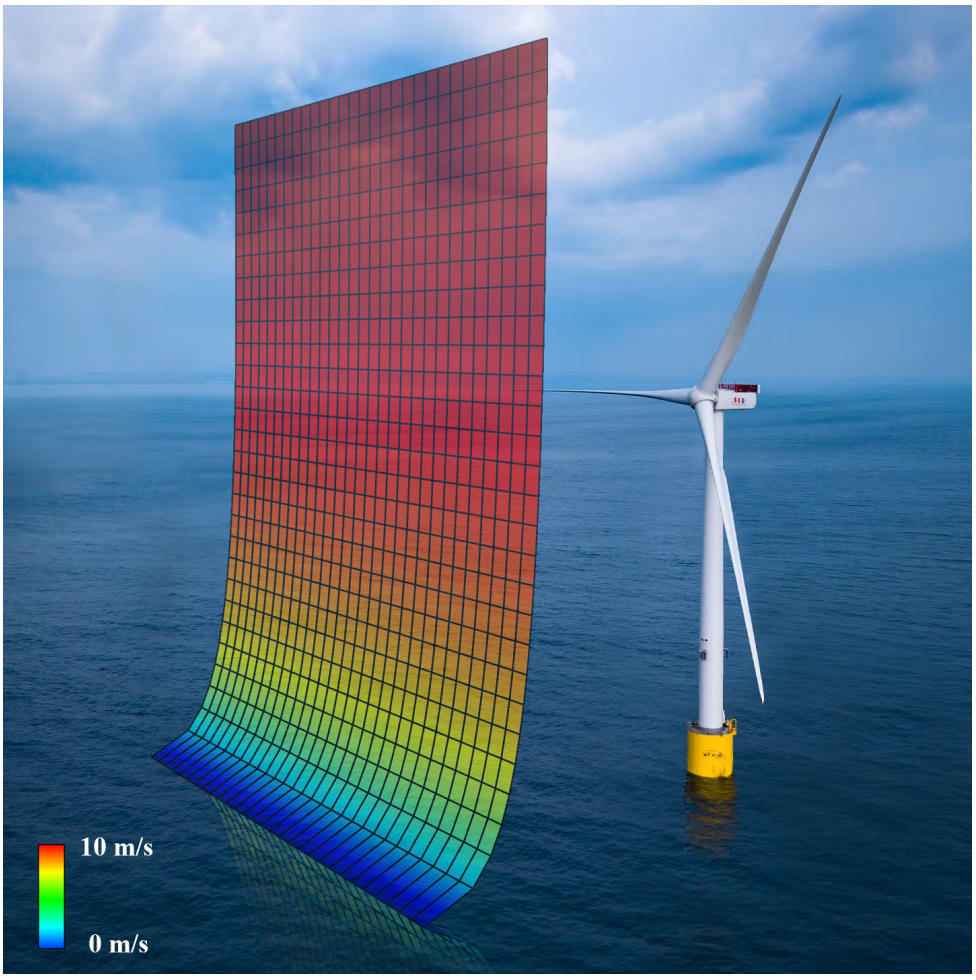

Figure 7.1: Visualization of the case being investigated, which includes a 15 MW offshore wind turbine in full scale operating under a logarithmic non-turbulent wind profile.

7.1.1 Computational Domain and Boundary Conditions

The IEA 15MW wind turbine geometry, which includes the tower, rotor, hub, and nacelle parts, was built in the Solid Edge software and then imported into OpenFOAM, where the snappyHexMesh utility was employed to define all other parts of the computational domain, including the refinement regions surrounding the wind turbine geometry.

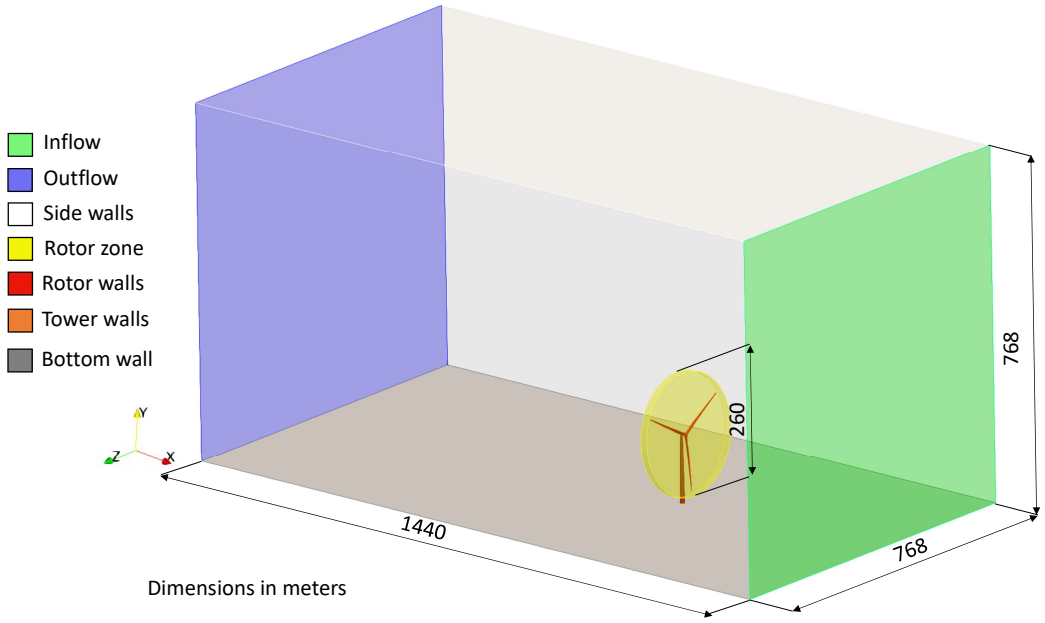

Figure 7.2: IEA wind 15 MW wind turbine computational domain dimensions (in meters) and boundary conditions.

The computational domain dimensions and the boundary conditions used to perform the investigations were chosen based on [66]. The dimensions of the computational domain were 768 m wide and high and 1440 m long. Similarly to the previous investigation presented in Section 7, a region of higher refinement was employed around the blades of 260 m of diameter. The boundary conditions were set as follows: at the inflow, for the velocity, a prescribed non-turbulent logarithmic wind profile of 10 m/s was employed, and for the pressure, a null gradient (Neumann condition) was considered. For the turbulent quantities, the same considerations were employed as presented previously in Section 7. The most critical Reynolds number (at the blade tip) was considered, and the turbulence was assumed to be isotropic. Thus, considering the local Reynolds number, the local velocity and chord length of the blade tip ($R = 120\,\mathrm{m}$), the turbulence kinetic energy $k = 7.4789\,\mathrm{m^2 s^{-2}}$, and the specific dissipation rate, $\omega = 50.2312\,\mathrm{s^{-1}}$, while the kinematic

eddy viscosity was calculated based on the internal field everywhere. For the side walls, the boundary conditions for the velocity were symmetry plane conditions, which correspond to null normal velocity and zero normal gradients for the tangential velocity, pressure, and turbulent quantities, while the slip condition was considered for the bottom wall. No slip condition was imposed on the tower walls. In addition, as considered in the rotor-only investigations, the AMI technique was employed in the rotor zone of the mesh to represent its dynamic part with a uniform rotor velocity of 0.7494 rad/s, which is the optimal rotor speed for a wind velocity of 10 m/s. Thus, for the rotor walls, a moving wall velocity condition was used, where the relative velocity of the flow with respect to the moving walls was set to the desired value of (0, 0, 0) to represent a no-slip condition. Neumann boundary condition was applied for the pressure as a null gradient, while the turbulence properties received the proper wall function treatment according to the y^+ value in the near wall region. At the outflow, a Dirichlet condition was applied for the pressure as a fixed value equal to zero, while for the velocity and turbulence quantities, Neumann conditions were considered as a null gradient.

7.1.2 Spatial Discretization

To perform the blade-resolved investigations of the IEA 15MW in full scale, including the tower influence, a different mesh refinement from the previous rotor-only investigations was considered. The non-uniform structured mesh was developed for the rotor part considering the strategies previously presented, but the refinement for the wake regions was employed, focusing on obtaining better resolution at these regions. Figure 7.3 depicts the strategical partition of the computational domain utilized to employ different levels of refinement in the mesh used in this study.

The spatial discretization of T15Mesh-1 is composed of finite volume cells of the size of 32 m in the far-field region that decrease to 4 m upstream of the wind turbine, then to 2 m in the wake region. In the rotor zone, as in the previous investigations of the rotor-only, the cells were refined from 1 m to 0.0625 m close to the blades and to 0.001 m at the first cell attached to the wall of the blade in order to respect the y^+ value recommendation for the application of the turbulence model at the near-wall region.

To communicate the dynamic part of the mesh, given by the rotor zone, with the static parts, an arbitrary mesh interface methodology was employed. The refinement in the rotor zone region was carried out carefully to ensure good communication between the AMI interfaces. As a result, T15Mesh-1 is composed of 47,389,262 finite volume cells, with

a maximum aspect ratio of 67, skewness of 3.9, and non-orthogonality of 64.6. Figure 7.4 illustrates different views of the spatial discretization employed in T15Mesh-1, including different positions along the blade span placed in front of the tower.

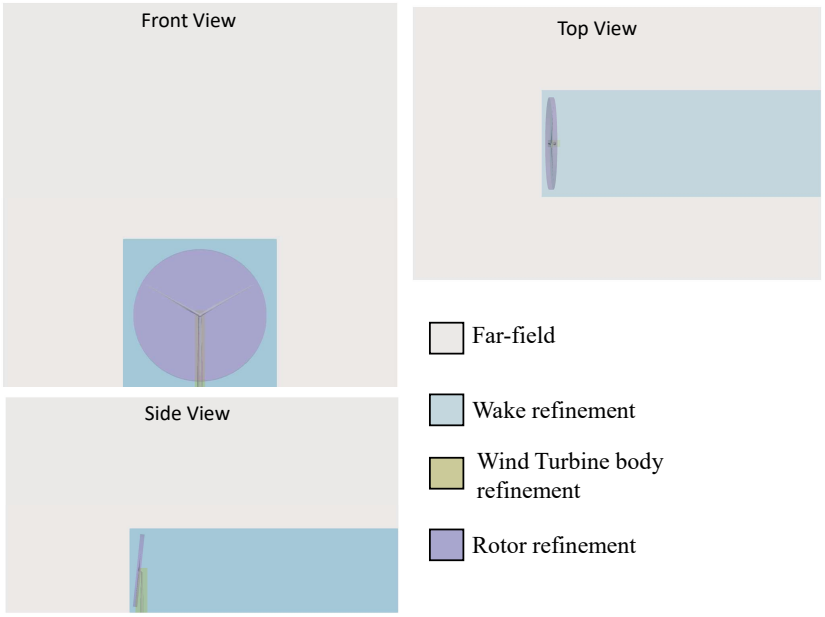

Figure 7.3: IEA wind 15 MW wind turbine partition of the computational domain.

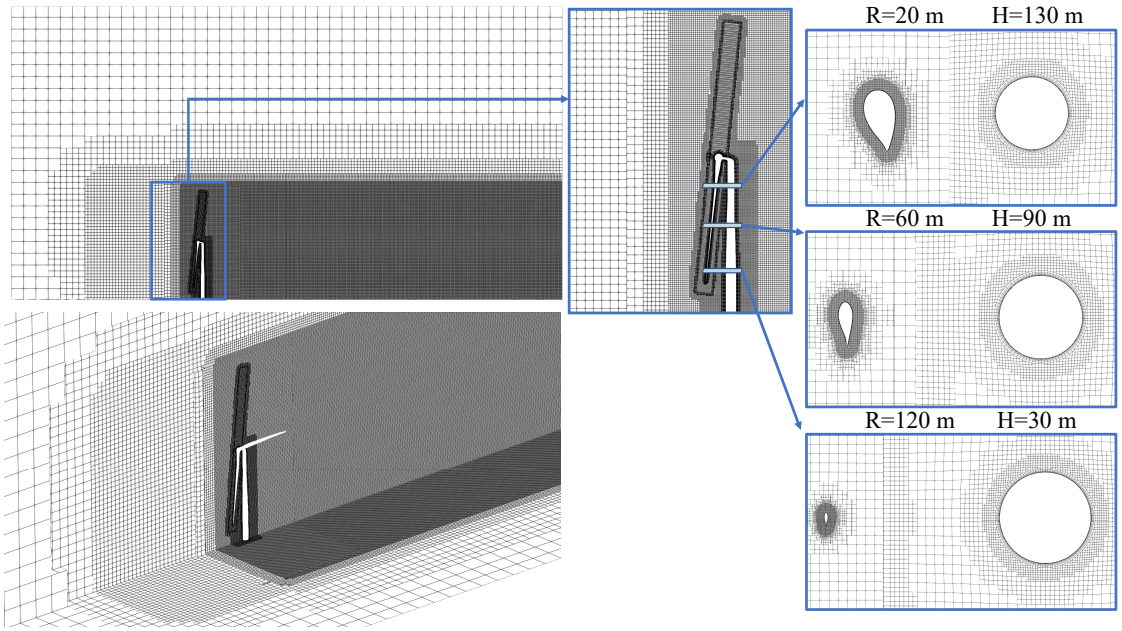

Figure 7.4: IEA wind 15 MW wind turbine spatial discretization of different regions of the computational domain.

7.1.3 Numerical Schemes and Solver Information

The numerical schemes employed in this study were chosen based on the modeling of the previously presented blade-resolved simulations. The convective fluxes were discretized using the LUST scheme along with DES k-ω SST turbulence model and CFL=2. The turbulence modeling for the near-wall region was the same as employed in the rotor-only investigations presented previously in Section 7. Regarding the other schemes employed in the numerical arrangement, for the diffusive terms, central differences were employed, while for the gradient terms, a second-order Gauss scheme was adopted with linear Gaussian integration. The set of linear equations was solved using the geometric-algebraic multi-grid (GAMG) method for the symmetric matrices and the preconditioned bi-conjugate gradient (PBiCG) with the DILU preconditioner for the non-symmetric matrices. The iterative PISO solver with face flux correction was employed, the same as considered in [66], with 5 sub-iterations and 2 corrections for pressure.

The initial conditions for the transient simulation for all properties were obtained from the steady state solution for the problem after 1500 iterations, calculated with the steady form of the SIMPLEC algorithm solver from [76]. The solution of the transient simulations was considered converged when the residuals of the set of estimated variables were equal or less than 10^{-6}.

The Brazilian supercomputer SDumont, was used to carry out the simulation. The mesh was partitioned into 240 sub-domains using scotch decomposition, using 10 nodes, where each node had two 12-core Intel Xeon Cascade Lake Gold 6252 processors, 3.7GHz, and 256Gb of RAM.

7.1.4 Results and Discussion

Initially, the results are presented in terms of power production, generated thrust, and distributed forces along the blade span and compared with those obtained from OpenFAST to accomplish a verification procedure. The main characteristics of the flow and its vortical structures are illustrated. In the sequence, an analysis of the instantaneous iso-contours of the axial velocity and normal vorticity in different positions along the blade span is presented. Lastly, the computational costs are discussed in terms of the execution time required to calculate one physical time unit of simulation and the corresponding number of time steps necessary to achieve convergence.

7.1.4.1 Verification with OpenFAST

A comparison of the CFD simulation results for the IEA 15 MW wind turbine considering the tower influence is presented in Fig. 7.5 and benchmarked against the OpenFAST results for the same environmental conditions. Fig. 7.5 a) and b) present the time series for the generated power and thrust considering the quasi-steady regime, while Fig. 7.5 c) and d) present the mean normal and tangential forces distributed along the blade span for different azimuth angles.

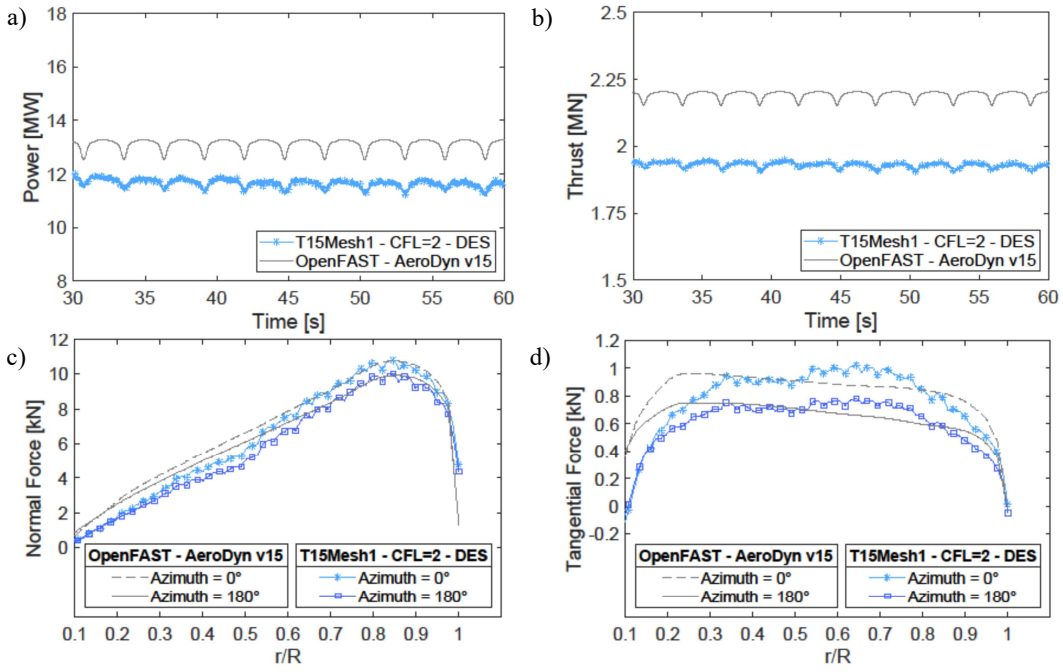

Figure 7.5: IEA wind 15 MW wind turbine comparison of CFD simulations results for: a) Power, b) Thrust, c) Normal force, and d) Tangential force distributed along the blade span, benchmarked against the OpenFAST results considering the same environmental conditions.

As can be seen in Fig. 7.5, a) and b), both performance results, power, and thrust present good agreement with the results from OpenFAST. However, the power estimation presented closer values when compared with the results from OpenFAST than the generated thrust. The results for the mean power and thrust from the CFD simulations were 11.616 $\pm$0.13 MW and 1.92 $\pm$0.0096 MN, against 13.114 $\pm$0.21 MW and 2.19 $\pm$0.0143 MN from the OpenFAST code. The more noticeable differences in the estimation of the generated thrust were also captured in the investigations of the NREL 5 MW conducted in [66]. Further insights about this result are shown in Fig. 7.5 c) and d) through the mean normal and tangential forces. The discrepancies amongst the results from the different

numerical methods can be attributed to the computations of the normal and tangential forces in the region close to the root of the blades, where the aerodynamic profile of the blade is considerably more circular, and for that reason, the BEM method, which employed a two-dimensional method with tip correction factors to account some of the three-dimensional effects, presented results that differ more significantly from the CFD results regarding the calculations of the aerodynamic loads in these regions.

Furthermore, the differences are observed to be higher at 180° azimuth angle position compared to 0° position, mainly due to the position of the blade in front of the tower, in which the flow around the blade is directly affected by the proximity of the tower. Although OpenFAST accounts for this effect by using a potential flow approximation, the complexity of the field around the tower is not well determined by this model. Moreover, the tip and hub vortex, which are not considered in OpenFAST, have a considerable impact on the induced velocities, leading to discrepancies in predicting the wind turbine's thrust.

7.1.4.2 Flow Structures

In order to capture the primary aspects of wake behavior, the second invariant of the velocity gradient tensor, the Q-criterion, was used to represent the vortex structures contained in the flow. The instantaneous isosurfaces of the Q-criterion, as well the iso-contours of the axial velocity, were depicted after 7 complete revolutions considering the tower influence with the blade located at 180° azimuth (blade in front of the tower).

Figure 7.6 a), b), and c) illustrates different views of the Q-criterion (Q = 0.05) colored by vorticity magnitude. Additionally, a vertical plane of the iso-contours of the velocity magnitude is also shown in Fig. 7.6 a). As can be seen in Fig. 7.6 a), vortical structures detaching from the tip of the blade are responsible for the wake external pattern, while the vortices being detached close to the root of the blades are responsible for the wake internal gradient. Also, perturbations in the wake structure can be noticed as a consequence of the vortex detached from the tower. Additional vortex structures detaching along the blade span in the region close to the blade tip can be visualized in Fig. 7.6 a) and c). Further insights about the wake internal gradient are shown through the iso-contours of the axial velocity in Fig. 7.6 d). For instance, the decrease in the velocity field behind the blades is observed considering the influence of the tower.

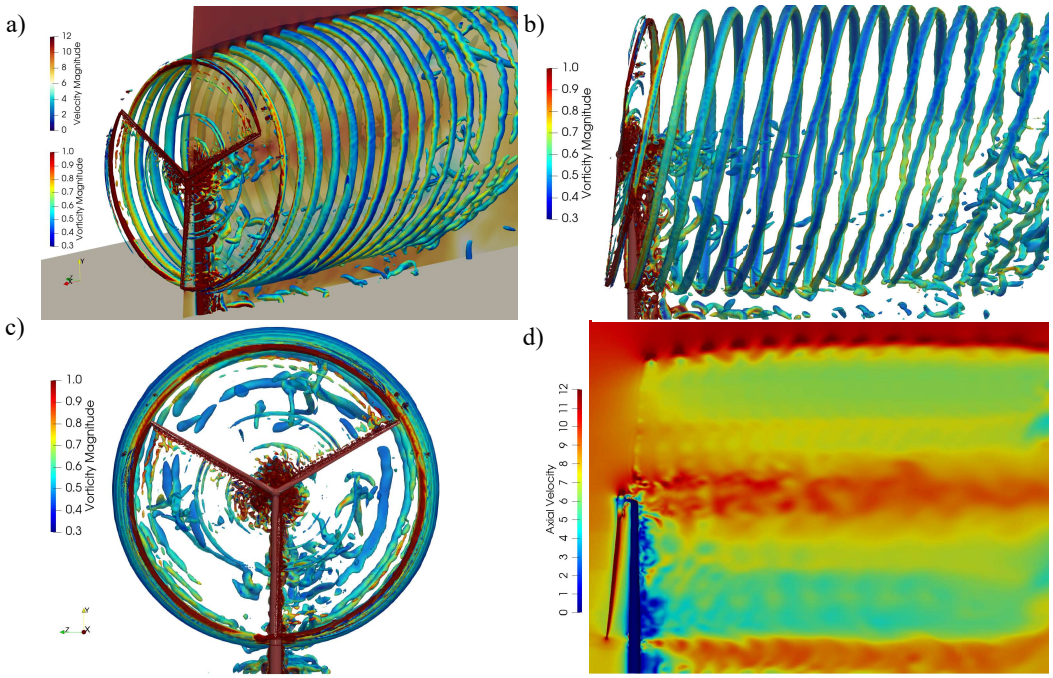

Figure 7.6: IEA wind 15 MW wind turbine CFD simulations results for a), b) and C) instantaneous isosurfaces of the Q-criterion (Q=0.05) colored by vorticity magnitude shown in different views and d) instantaneous iso-contours of the axial velocity.

More details about the blade-tower interaction are illustrated in Fig. 7.7 through the instantaneous iso-contours of the axial velocity and normal vorticity at different positions along the blade span, indicated by R and above the ground, indicated by H. In this regard, different vortex shedding patterns were observed for the tower at the different positions, as well as the interaction between the blade and tower as the distance among them changes along the tower height due to the inclination of the rotor. For instance, in regions close to the blade root (R=20 m) and (H=130 m), the interaction between the blade and tower is more intense. Conversely, in the region closer to the blade tip (R=120 m) and (H=30 m), the interaction is less intense, but it still affects the wake.

The evaluation of the computational resources required for the blade-resolved simulation conducted in this study is shown in Fig. 7.8. The execution time for computing one-time unit of the simulation time was approximately 48 hours considering the tower influence and the DES turbulence model with CFL=2.

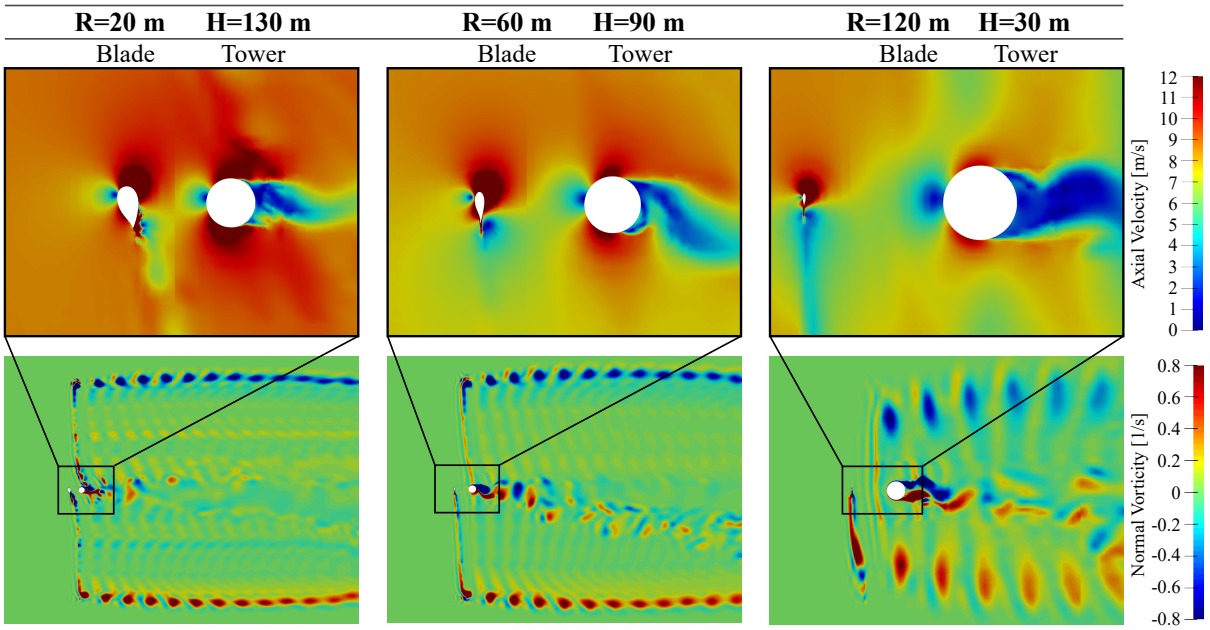

Figure 7.7: IEA wind 15 MW wind turbine CFD simulations results of the instantaneous iso-contours of the axial velocity and normal vorticity in different positions along the blade span indicated by R and above the ground indicated by H.

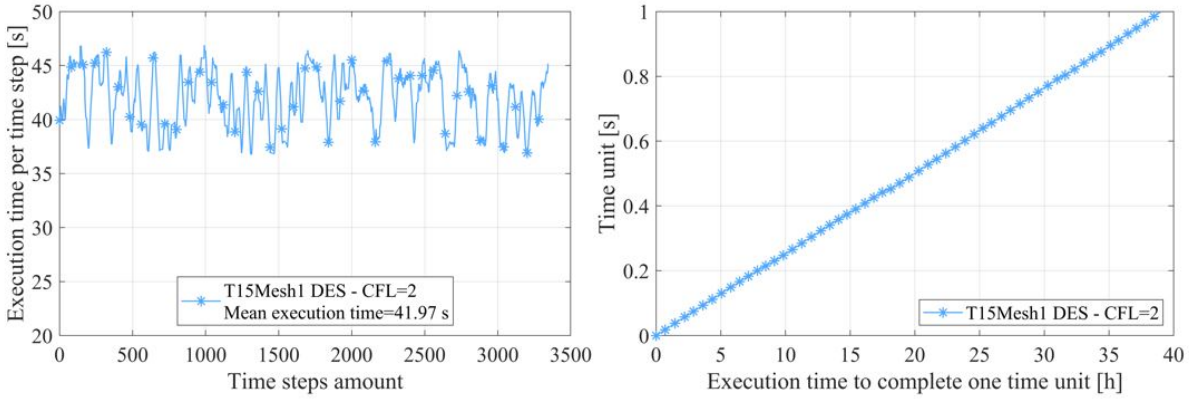

Figure 7.8: IEA wind 15 MW wind turbine CFD simulation computational cost.

Considering the results previously presented of the rotor-only simulations, it is possible to notice that the numerical arrangement, which employed the DES turbulence model with CFL=2 and considers the tower influence, required a similar level of computation demand as the rotor-only case with URANS and CFL=2, where the execution time for computing one-time unit of simulation time was approximately 43 h.

This comparison regarding the use of computational demand, along with the good accuracy achieved in this study, highlights the influence of the simulation's numerical arrangement on both accuracy of the results and the use of the computational resources.

PART IV

CONCLUDING REMARKS

8 CONCLUSION

Offshore wind energy has emerged as a promising solution among the renewable energy sources to contribute to the world's energy supply. However, improving the efficiency and reliability of offshore wind turbines is crucial to ensure their viability as a sustainable source of energy. In this regard, as the size of commercial wind turbines for offshore applications have increased considerably in terms of scale of power capacity, numerical simulations have become an essential tool for predicting the aerodynamic behavior of the wind turbine in full scale, under different wind conditions, due to the limitations of experimental tests in representing the wind turbine's operating conditions. Therefore, this thesis provided different types of investigation regarding the substantial impact of the numerical schemes and solver parameters on the accuracy of the simulations results and its computational costs, to maximize the reliability of the CFD methodology as a tool in the development of offshore wind turbines.

Thus, to evaluate the performance of the NREL 5 MW and IEA 15 MW reference wind turbines for offshore applications, a CFD methodology was developed considering the FVM implemented in the OpenFOAM software, in which different investigations were conducted to evaluate the influence of the simulation setup on the accuracy of the obtained results and computational demand required.

Initially, blade-resolved CFD simulations were conducted to estimate the performance of the NREL 5 MW in terms of power production, generated thrust, forces distribution along the blade span and visualization of the flow features with high resolution at different regions of interest, including around the blades and wake regions. Regarding the influence of the numerical setup on the accuracy of the obtained results, at first the pressure-velocity coupling problem was investigated considering different approaches of the iterative PISO solver. Thus, an extra correction for pressure considered through the inclusion of the face flux correction in the algorithm steps presented a more stable numerical behaviour in relation to the convergence of the time series signals for the generated power and thrust.

Additionally, considering the iterative PISO algorithm with face flux correction as solver, a spatial discretization investigation was performed through different refinement strategies. The findings from the comparison of the results from both meshes investigated have shown that if the y^+ value is within the adequate limits in the near-wall region for the application of the turbulence model, there is no need to significantly refine the field close to the wind turbine for the prediction of aerodynamic forces. Such insight led to the possibility of optimize the spatial discretization strategy and also highlighted that the methodology adopted for the mesh refinement at the regions close to the blades walls were appropriated for the turbulence modeling implemented in this region.

Further understanding with regard to the influence of the solver parameters in the accuracy of the simulation results was achieved through the temporal discretization investigation. The influence of the CFL number as a convergence parameter was evaluated for the transient simulations, and the increase in the CFL number presented a limitation, due to the time step sizing, which became unappropriated to capture the physics of the flow regarding its temporal scales. While CFL=4 was considered unsuitable, CFL numbers close to the unit such as 1 and 2 presented satisfactory results, but the CFL equals to 1 required higher computational demand than equals to 2. Additionally, the same conclusions regarding the CFL parameter was obtained for the temporal discretization investigations performed for the blade-resolved simulations of the IEA 15 MW.

Next, blade-resolved CFD simulations were conducted to estimate the performance of the NREL 5 MW and evaluate the influence of different turbulence models and discretizations schemes for the convective term of the Navier-Stokes equations on the accuracy of the simulation's results and computational demand. Thus, the simulations that employed the LUD and LUST schemes for the URANS k-ω SST turbulence model were able to capture the interaction between the turbulence model and the discretization schemes, and the LUST scheme was identified as superior to the LUD scheme, regarding computational cost and accuracy of the obtained results.

In addition, a comparison of the results from URANS and DES turbulence models, using LUST have shown that the prediction of aerodynamic loads were very similar for both models, but in terms of flow features, the DES k-ω SST turbulence model captured more detailed information at higher computational cost. Moreover, further spatial and temporal discretizations investigations performed for both turbulence models also showed that the DES simulations were more sensitive to the spatial discretization, than URANS. With respect to the temporal discretization analyses, the conclusion was that both URANS-LUST and DES-LUST approaches are suitable options to be employed with

CFL=2. Thus, the choice between the URANS-LUST and DES-LUST will depend on the mesh being used and the main objectives of the blade-resolved simulation. However, higher definition of the flow was captured with DES-LUST approach at an affordable computational demand, which led the DES k-ω SST turbulence model as an attractive solution to be implemented in the modeling of the new generation of larger wind turbines.

In this regard, with the increase in the wind turbine power capacity, the sizes of computational domain and spatial mesh also increased considerably, making the CFD simulations more challenging. However, based on the findings regarding the solver configuration from the investigations conducted for the NREL 5 MW, blade-resolved CFD simulations of the IEA 15 MW reference wind turbine for offshore applications were performed. The simulations including the tower influence for the IEA 15 MW reference wind turbine employed a strategical refinement of the computational domain, the DES k-ω SST turbulence model with LUST scheme and CFL=2. The results presented good agreement with the results from OpenFAST code in terms of power production, generated thrust, and forces distribution along the blade span. The discrepancies amongst the results from the different numerical methods were attributed to the computations of the normal and tangential forces, in the region close to blade's root, where the aerodynamic profile of the blade is considerably more circular, and for that reason, the BEM method presented a different estimation than the CFD of the aerodynamic loads in these regions. Further details about the aerodynamic behavior of the IEA 15 MW in full scale was observed through the flow characteristics depicted in different views of the flow. Regarding the computational costs, even though the mesh employed in the investigations, which considered the tower influence was bigger, the simulation required a similar level of computation demand as the rotor-only case with URANS and CFL=2. This finding highlights the substantial impact of the simulation's numerical arrangement on both accuracy of the obtained results and use of the computational resources.

8.1 Future work

The results illustrated in this thesis have provided valuable insights into the aerodynamic behavior of offshore wind turbines and the accuracy of numerical simulations for predicting its performance. Therefore, the CFD methodology developed in this thesis can be extended to future work, in which is required to evaluate the performance of other wind turbines in full scale, including different wind turbine designs, power capacities, environmental factors, and operating conditions.

However, as the wind turbines investigated in this thesis were modeled as rigid bodies, future work should employ the conclusions presented in this thesis to model the new generation of large wind turbines, considering the wind turbines system through a proper aeroelastic model, and assessing the influence of structural aeroelasticity on its performance. In addition, the methodology developed in the blade-resolved simulations can be applied in the numerical investigations of offshore wind turbines, considering different platform concepts in its analysis. As the inclusion of the platform in the numerical model increases the use of computational resources, an optimized CFD methodology is necessary to improve the capability of the simulation to predict the dynamic response of offshore wind turbine under aerodynamic and hydrodynamic loads.

The CFD methodology developed in this thesis, which identifies a relation between the numerical model and several solver parameters, such as, spatial and temporal discretizations, can also be adapted for other types of investigations that are also important for the development of renewable sources of energy, such as tidal turbines.

Furthermore, as the turbulence models implemented in the blade-resolved simulations were adjusted for the most critical Reynolds number, which occurs at the blade tip and is of the order of millions, the CFD methodology developed in this thesis can be applied to other types of numerical simulations involving the flow governed by high Reynolds numbers. For instance, the same methodology can be used to investigate the flow around circular cylinders at supercritical and postcritical Reynolds regimes, since the phenomenon of vortex shedding has been extensively investigated in the scientific community.

REFERENCES

[1] AL-SHETWI, A. Q. Sustainable development of renewable energy integrated power sector: Trends, environmental impacts, and recent challenges. *Science of The Total Environment*, Elsevier, p. 153645, 2022.

[2] IRENA. Irena releases renewable capacity statistics 2022. March 2022. Disponível em: <https://taiyangnews.info/business/irena-releases-renewable-capacity-statistics-2022/>. Acesso em: 14 Apr. 2022.

[3] LEE, J.; ZHAO, F. *Global Offshore Wind Report 2022*. [S.l.]: Global Wind Energy Council, 2022.

[4] HUTCHINSON, M.; ZHAO, F. *Global Offshore Wind Report 2023*. [S.l.]: Global Wind Energy Council, 2023.

[5] KARIMIRAD, M. *Offshore energy structures: for wind power, wave energy and hybrid marine platforms*. [S.l.]: Springer, 2014.

[6] STATISTICS, R. C. *International Renewable Energy Agency (IRENA)*. [S.l.]: ed, 2016.

[7] HATZIARGYRIOU, N.; ZERVOS, A. Wind power development in europe. *Proceedings of the IEEE*, IEEE, v. 89, n. 12, p. 1765–1782, 2001.

[8] DUTTON, A.; BACKWELL, B.; QIAO, L.; LIM, S.; LATHIGARALEAD, A.; LIANG, W. *Global Offshore Wind Report 2020*. [S.l.]: Global Wind Energy Council, 2020.

[9] RICH, N. H.; MOELLER, T. K. Danish wind power in Brazil. part 2. experience with danish 75 kw wind turbine-the first modern turbine in Brazil. 1996.

[10] SILVA, N. F. da; ROSA, L. P.; ARAÚJO, M. R. The utilization of wind energy in the Brazilian electric sector's expansion. *Renewable and Sustainable Energy Reviews*, Elsevier, v. 9, n. 3, p. 289–309, 2005.

[11] OHLENFORST, K.; SAWYER, S.; DUTTON, A.; BACKWELL, B.; FIESTAS, R.; LEE, J.; QIAO, L.; ZHAO, F.; BALACHANDRAN, N. Global wind report 2018. *Global Wind Energy Council, Brussels, Belgium, Tech. Rep*, 2019.

[12] IBAMA. Mapas de projetos em licenciamento ambiental federal de complexos eólicos offshore. March 2023. Disponível em: <https://www.gov.br/ibama/pt-br/assuntos/laf/consultas/mapas-de-projetos-em-licenciamento-complexos-eolicos-offshore>. Acesso em: 12 Apr. 2023.

[13] IBAMA. Licenciamento ambiental federal de complexos eólicos offshore - mapa. March 2023. Disponível em: <https://www.gov.br/ibama/pt-br/assuntos/laf/consultas/arquivos/20230328_Usinas_Eolicas_Offshore_reduzido.pdf>. Acesso em: 12 Apr. 2023.

[14] LIMA, D. K.; LEÃO, R. P.; SANTOS, A. C. dos; MELO, F. D. de; COUTO, V. M.; NORONHA, A. W. de; JR, D. S. O. Estimating the offshore wind resources of the State of Ceará in Brazil. *Renewable Energy*, Elsevier, v. 83, p. 203–221, 2015.

[15] PIMENTA, F.; KEMPTON, W.; GARVINE, R. Combining meteorological stations and satellite data to evaluate the offshore wind power resource of southeastern Brazil. *Renewable Energy*, Elsevier, v. 33, n. 11, p. 2375–2387, 2008.

[16] DEWAN, A.; ASGARPOUR, M.; SAVENIJE, R. *Commercial proof of innovative offshore wind installation concepts using ECN Install Tool*. [S.l.]: ECN The Hague, The Netherlands, 2015.

[17] CASTRO-SANTOS, L.; DIAZ-CASAS, V. *Floating offshore wind farms*. [S.l.]: Springer, 2016.

[18] OSTACHOWICZ, W.; MCGUGAN, M.; SCHRÖDER-HINRICHS, J.-U.; LUCZAK, M. *MARE-WINT: new materials and reliability in offshore wind turbine technology*. [S.l.]: Springer, 2016.

[19] SG. Sg 8.0-167 dd offshore wind turbine. May 2022. Disponível em: <https://www.siemensgamesa.com/products-and-services/offshore/wind-turbine-sg-8-0-167-dd>. Acesso em: 01 May 2023.

[20] VESTAS. V174-9.5 mw offshore wind turbine. May 2022. Disponível em: <https://www.vestas.com/en/products/offshore/v174-9-5-mw->. Acesso em: 01 May 2023.

[21] GE. Haliade-x offshore wind turbine. May 2022. Disponível em: <https://www.ge.com/renewableenergy/wind-energy/offshore-wind/haliade-x-offshore-turbine>. Acesso em: 01 May 2023.

[22] HANSEN, M. O. L.; SØRENSEN, J. N.; VOUTSINAS, S.; SØRENSEN, N.; MADSEN, H. A. State of the art in wind turbine aerodynamics and aeroelasticity. *Progress in aerospace sciences*, Elsevier, v. 42, n. 4, p. 285–330, 2006.

[23] SANDERSE, B.; PIJL, S. Van der; KOREN, B. Review of computational fluid dynamics for wind turbine wake aerodynamics. *Wind energy*, Wiley Online Library, v. 14, n. 7, p. 799–819, 2011.

[24] THÉ, J.; YU, H. A critical review on the simulations of wind turbine aerodynamics focusing on hybrid rans-les methods. *Energy*, Elsevier, v. 138, p. 257–289, 2017.

[25] BURTON, T.; JENKINS, N.; SHARPE, D.; BOSSANYI, E. *Wind energy handbook*. [S.l.]: John Wiley & Sons, 2011.

[26] KELLY, M. C. From standard wind measurements to spectral characterization: turbulence length scale and distribution. *Wind Energy Science*, Copernicus GmbH, v. 3, n. 2, p. 533–543, 2018.

[27] MÖLLERSTRÖM, E.; OTTERMO, F.; GOUDE, A.; ERIKSSON, S.; HYLANDER, J.; BERNHOFF, H. Turbulence influence on wind energy extraction for a medium size vertical axis wind turbine. *Wind Energy*, Wiley Online Library, v. 19, n. 11, p. 1963–1973, 2016.

[28] BASSE, N. T. Scaling of global properties of fluctuating and mean streamwise velocities in pipe flow: Characterization of a high reynolds number transition region. *Physics of Fluids*, AIP Publishing LLC, v. 33, n. 6, p. 065127, 2021.

[29] WILCOX, D. C. *Turbulence modeling for CFD Third Edition*. [S.l.]: DCW industries La Canada, CA, 2006.

[30] HASAGER, C. B.; NYGAARD, N. G.; VOLKER, P. J.; KARAGALI, I.; ANDERSEN, S. J.; BADGER, J. Wind farm wake: the 2016 horns rev photo case. *Energies*, Multidisciplinary Digital Publishing Institute, v. 10, n. 3, p. 317, 2017.

[31] MANWELL, J. F.; MCGOWAN, J. G.; ROGERS, A. L. *Wind energy explained: theory, design and application*. [S.l.]: John Wiley & Sons, 2010.

[32] VERMEER, L.; SØRENSEN, J. N.; CRESPO, A. Wind turbine wake aerodynamics. *Progress in aerospace sciences*, Elsevier, v. 39, n. 6-7, p. 467–510, 2003.

[33] BRAND, A. J.; PEINKE, J.; MANN, J. Turbulence and wind turbines. In: IOP PUBLISHING. *Journal of Physics: Conference Series*. [S.l.], 2011. v. 318, n. 7, p. 072005.

[34] JOHNSON, K. E.; THOMAS, N. Wind farm control: Addressing the aerodynamic interaction among wind turbines. In: IEEE. *American Control Conference, 2009. ACC'09.* [S.l.], 2009. p. 2104–2109.

[35] SHADMAN, M.; AMIRI, M. M.; SILVA, C.; ESTEFEN, S. F.; ROVERE, E. L. et al. Environmental impacts of offshore wind installation, operation and maintenance, and decommissioning activities: A case study of brazil. *Renewable and Sustainable Energy Reviews*, Elsevier, v. 144, p. 110994, 2021.

[36] NG, C.; RAN, L. *Offshore wind farms: Technologies, design and operation*. [S.l.]: Woodhead Publishing, 2016.

[37] KREIDER, M.; OTERI, F.; ROBERTSON, A.; CONSTANT, C.; GILL, E. *Offshore Wind Energy: Technology Below the Water*. [S.l.], 2022.

[38] CHEN, X.; JIANG, Z.; LI, Q.; LI, Y.; REN, N. Extended environmental contour methods for long-term extreme response analysis of offshore wind turbines. *Journal of Offshore Mechanics and Arctic Engineering*, American Society of Mechanical Engineers, v. 142, n. 5, p. 052003, 2020.

[39] SHAH, K. A.; MENG, F.; LI, Y.; NAGAMUNE, R.; ZHOU, Y.; REN, Z.; JIANG, Z. A synthesis of feasible control methods for floating offshore wind turbine system dynamics. *Renewable and Sustainable Energy Reviews*, Elsevier, v. 151, p. 111525, 2021.

[40] JONKMAN, J.; BUTTERFIELD, S.; MUSIAL, W.; SCOTT, G. *Definition of a 5-MW reference wind turbine for offshore system development*. [S.l.], 2009.

[41] GAERTNER, E.; RINKER, J.; SETHURAMAN, L.; ZAHLE, F.; ANDERSON, B.; BARTER, G. E.; ABBAS, N. J.; MENG, F.; BORTOLOTTI, P.; SKRZYPINSKI, W. et al. *IEA wind TCP task 37: definition of the IEA 15-megawatt offshore reference wind turbine*. [S.l.], 2020.

[42] ROBERTSON, A.; JONKMAN, J.; MASCIOLA, M.; SONG, H.; GOUPEE, A.; COULLING, A.; LUAN, C. *Definition of the semisubmersible floating system for phase II of OC4*. [S.l.], 2014.

[43] ROBERTSON, A.; JONKMAN, J.; MUSIAL, W.; VORPAHL, F.; POPKO, W. *Offshore code comparison collaboration, continuation: Phase II results of a floating semisubmersible wind system*. [S.l.], 2013.

[44] JOHLAS, H. M.; MARTÍNEZ-TOSSAS, L. A.; CHURCHFIELD, M. J.; LACKNER, M. A.; SCHMIDT, D. P. Floating platform effects on power generation in spar and semisubmersible wind turbines. *Wind Energy*, Wiley Online Library, v. 24, n. 8, p. 901–916, 2021.

[45] ALLEN, C.; VISCELLI, A.; DAGHER, H.; GOUPEE, A.; GAERTNER, E.; ABBAS, N.; HALL, M.; BARTER, G. *Definition of the UMaine VolturnUS-S reference platform developed for the IEA Wind 15-megawatt offshore reference wind turbine*. [S.l.], 2020.

[46] MORIARTY, P. J.; HANSEN, A. C. *AeroDyn theory manual*. [S.l.], 2005.

[47] NREL. Openfast code documentation. Feb. 2023. Disponível em: <https://openfast.readthedocs.io/en/main/>. Acesso em: 28 mar. 2023.

[48] NUKALA, V. B.; MADDULA, S. P. Influence of rotor solidity on trailing edge noise from wind turbine blades. *Advances in Aerodynamics*, Springer, v. 2, n. 1, p. 15, 2020.

[49] COULLING, A. J.; GOUPEE, A. J.; ROBERTSON, A. N.; JONKMAN, J. M.; DAGHER, H. J. Validation of a fast semi-submersible floating wind turbine numerical model with deepcwind test data. *Journal of Renewable and Sustainable Energy*, American Institute of Physics, v. 5, n. 2, p. 023116, 2013.

[50] NREL. Wind turbine design code certified. Aug. 2005. Disponível em: <https://www.nrel.gov/news/press/2005/357.html>. Acesso em: 28 mar. 2023.

[51] HAND, M. M.; SIMMS, D.; FINGERSH, L.; JAGER, D.; COTRELL, J.; SCHRECK, S.; LARWOOD, S. *Unsteady aerodynamics experiment phase VI: wind tunnel test configurations and available data campaigns*. [S.l.], 2001.

[52] CORDLE, A.; JONKMAN, J. et al. State of the art in floating wind turbine design tools. In: INTERNATIONAL SOCIETY OF OFFSHORE AND POLAR ENGINEERS. *The Twenty-first International Offshore and Polar Engineering Conference*. [S.l.], 2011.

[53] SEBASTIAN, T.; LACKNER, M. A comparison of first-order aerodynamic analysis methods for floating wind turbines. In: *48th AIAA Aerospace Sciences Meeting Including the New Horizons Forum and Aerospace Exposition*. [S.l.: s.n.], 2010. p. 998.

[54] SEBASTIAN, T.; LACKNER, M. Offshore floating wind turbines-an aerodynamic perspective. In: *49th AIAA Aerospace Sciences Meeting Including the New Horizons Forum and Aerospace Exposition*. [S.l.: s.n.], 2011. p. 720.

[55] CAI, X.; GU, R.; PAN, P.; ZHU, J. Unsteady aerodynamics simulation of a full-scale horizontal axis wind turbine using cfd methodology. *Energy Conversion and Management*, Elsevier, v. 112, p. 146–156, 2016.

[56] SORENSEN, N.; HANSEN, M. Rotor performance predictions using a navier-stokes method. In: *1998 ASME wind energy symposium*. [S.l.: s.n.], 1998. p. 25.

[57] DUQUE, E.; DAM, C. V.; HUGHES, S. Navier-stokes simulations of the nrel combined experiment phase ii rotor. In: *37th Aerospace Sciences Meeting and Exhibit*. [S.l.: s.n.], 1999. p. 37.

[58] DUQUE, E. P.; BURKLUND, M. D.; JOHNSON, W. Navier-stokes and comprehensive analysis performance predictions of the nrel phase vi experiment. *J. Sol. Energy Eng.*, v. 125, n. 4, p. 457–467, 2003.

[59] ZHANG, Y.; DENG, S.; WANG, X. Rans and ddes simulations of a horizontal-axis wind turbine under stalled flow condition using openfoam. *Energy*, Elsevier, v. 167, p. 1155–1163, 2019.

[60] LI, Y.; CASTRO, A.; SINOKROT, T.; PRESCOTT, W.; CARRICA, P. Coupled multi-body dynamics and cfd for wind turbine simulation including explicit wind turbulence. *Renewable Energy*, Elsevier, v. 76, p. 338–361, 2015.

[61] LAWSON, M. J.; MELVIN, J.; ANANTHAN, S.; GRUCHALLA, K. M.; ROOD, J. S.; SPRAGUE, M. A. *Blade-resolved, single-turbine simulations under atmospheric flow*. [S.l.], 2019.

[62] LI, Y. *Coupled computational fluid dynamics/multibody dynamics method with application to wind turbine simulations*. [S.l.]: The University of Iowa, 2014.

[63] LIU, Y.; XIAO, Q.; INCECIK, A. A coupled cfd/multibody dynamics analysis tool for offshore wind turbines with aeroelastic blades. In: AMERICAN SOCIETY OF MECHANICAL ENGINEERS. *International Conference on Offshore Mechanics and Arctic Engineering*. [S.l.], 2017. v. 57786, p. V010T09A038.

[64] LI, Y.; CASTRO, A.; MARTIN, J.; SINOKROT, T.; PRESCOTT, W.; CARRICA, P. Coupled computational fluid dynamics/multibody dynamics method for wind turbine aero-servo-elastic simulation including drivetrain dynamics. *Renewable Energy*, Elsevier, v. 101, p. 1037–1051, 2017.

[65] VERSTEEG, H. K.; MALALASEKERA, W. *An introduction to computational fluid dynamics: the finite volume method*. [S.l.]: Pearson education, 2007.

[66] OLIVEIRA, M.; PURACA, R. C.; CARMO, B. S. Blade-resolved numerical simulations of the nrel offshore 5 mw baseline wind turbine in full scale: A study of proper solver configuration and discretization strategies. *Energy*, Elsevier, v. 254, p. 124368, 2022.

[67] PATANKAR, S. V.; SPALDING, D. B. A calculation procedure for heat, mass and momentum transfer in three-dimensional parabolic flows. In: *Numerical prediction of flow, heat transfer, turbulence and combustion*. [S.l.]: Elsevier, 1983. p. 54–73.

[68] MOUKALLED, F.; MANGANI, L.; DARWISH, M. et al. *The finite volume method in computational fluid dynamics*. [S.l.]: Springer, 2016. v. 6.

[69] JASAK, H. Error analysis and estimation for the finite volume method with applications to fluid flows. Imperial College London (University of London), 1996.

[70] WARMING, R.; BEAM, R. M. Upwind second-order difference schemes and applications in aerodynamic flows. *AIAA Journal*, v. 14, n. 9, p. 1241–1249, 1976.

[71] WELLER, H. Controlling the computational modes of the arbitrarily structured c grid. *Monthly Weather Review*, American Meteorological Society, v. 140, n. 10, p. 3220–3234, 2012.

[72] STRELETS, M. Detached eddy simulation of massively separated flows. In: *39th Aerospace sciences meeting and exhibit*. [S.l.: s.n.], 2001. p. 879.

[73] GEORGIADIS, N. J.; RIZZETTA, D. P.; FUREBY, C. Large-eddy simulation: current capabilities, recommended practices, and future research. *AIAA journal*, v. 48, n. 8, p. 1772–1784, 2010.

[74] PATANKAR, S. *Numerical heat transfer and fluid flow*. [S.l.]: Taylor & Francis, 2018.

[75] ISSA, R. I. Solution of the implicitly discretised fluid flow equations by operator-splitting. *Journal of computational physics*, Elsevier, v. 62, n. 1, p. 40–65, 1986.

[76] DOORMAAL, J. P. V.; RAITHBY, G. D. Enhancements of the simple method for predicting incompressible fluid flows. *Numerical heat transfer*, Taylor & Francis, v. 7, n. 2, p. 147–163, 1984.

[77] JASAK, H. Dynamic mesh handling in openfoam. In: *47th AIAA aerospace sciences meeting including the new horizons forum and aerospace exposition*. [S.l.: s.n.], 2009. p. 341.

[78] TENNEKES, H.; LUMLEY, J. L. *A first course in turbulence*. [S.l.]: MIT press, 2018.

[79] POPE, S. B. *Turbulent flows*. [S.l.]: IOP Publishing, 2001.

[80] SPALART, P. R. Strategies for turbulence modelling and simulations. *International journal of heat and fluid flow*, Elsevier, v. 21, n. 3, p. 252–263, 2000.

[81] MENTER, F. R. *Improved two-equation k-omega turbulence models for aerodynamic flows*. [S.l.], 1992.

[82] MENTER, F. Zonal two equation kw turbulence models for aerodynamic flows. In: *23rd fluid dynamics, plasmadynamics, and lasers conference*. [S.l.: s.n.], 1993. p. 2906.

[83] MENTER, F. R. Two-equation eddy-viscosity turbulence models for engineering applications. *AIAA journal*, v. 32, n. 8, p. 1598–1605, 1994.

[84] ROCHA, P. C.; ROCHA, H. B.; CARNEIRO, F. M.; SILVA, M. V. D.; BUENO, A. V. k–ω sst (shear stress transport) turbulence model calibration: A case study on a small scale horizontal axis wind turbine. *Energy*, Elsevier, v. 65, p. 412–418, 2014.

[85] SPALART, P. R. Comments on the feasibility of les for wings and on the hybrid rans/les approach. In: *Proceedings of the First AFOSR International Conference on DNS/LES, 1997*. [S.l.: s.n.], 1997. p. 137–147.

[86] SHUR, M.; SPALART, P.; STRELETS, M.; TRAVIN, A. Detached-eddy simulation of an airfoil at high angle of attack. In: *Engineering turbulence modelling and experiments 4*. [S.l.]: Elsevier, 1999. p. 669–678.

[87] LIU, F. A thorough description of how wall functions are implemented in openfoam. *Proceedings of CFD with OpenSource Software*, Chalmers University of Technology, Gothenburg Sweden, v. 34, 2016.

[88] OPENFOAM. Running applications in parallel. March 2023. Disponível em: <https://www.openfoam.com/documentation/user-guide/3-running-applications/3.2-running-applications-in-parallel>. Acesso em: 26 Apr. 2023.

[89] AXTMANN, G.; RIST, U. Scalability of openfoam with large eddy simulations and dns on high-performance systems. In: SPRINGER. *High Performance Computing in Science and Engineering´ 16: Transactions of the High Performance Computing Center, Stuttgart (HLRS) 2016*. [S.l.], 2016. p. 413–424.

Appendices

APPENDIX A – ASSESSMENT OF TURBULENCE MODELS FOR THE SIMULATION OF THE FLOW THROUGH A MEGAWATT SCALE WIND TURBINE ROTOR

Escola de Primavera de Transição e Turbulência
Blumenau 2022

ABCM
13th Spring School on Transition and Turbulence
September 19th-23rd, 2022, Blumenau, SC, Brazil

EPTT-2022-0008
Assessment of Turbulence Models for the Simulation of the Flow Through a Megawatt Scale Wind Turbine Rotor

Marielle de Oliveira
mariellededoliveira@usp.br
Rodolfo C. Puraca
rodolfo.puraca@usp.br
Bruno S. Carmo
bruno.carmo@usp.br
Department of Mechanical Engineering, Escola Politécnica - University of São Paulo - Brazil

Abstract. *The increase of the size of wind turbines to deliver power at megawatt scale, particularly for offshore application, brings a number of engineering challenges. The numerical modeling of these systems, considering the wind turbine geometry in full scale, is a valuable tool for design and performance analysis. To properly model the interaction between the turbine and the wind we need a proper turbulence model. This paper presents a comparison of two of the most used turbulence models, the Unsteady Reynolds Averaged Navier-Stokes (URANS) k-ω SST and the two-equation Detached Eddy Simulation (DES) applied in blade-resolved simulations of the NREL 5 MW reference wind turbine, in order to predict the rotor performance when it operates in optimal wind-power conversion efficiency, for a wind speed of 10 m/s at hub height. The power production, generated thrust, and forces distribution along the blade span were estimated. The computational analyses were carried out using a Computational Fluid Dynamics (CFD) methodology employing the Finite Volume Method (FVM) implemented in the OpenFOAM software. A numerical verification was conducted by comparing the CFD results against values obtained using the blade element momentum theory, implemented in OpenFAST. The performance of each turbulence model was assessed considering the computational cost and accuracy of the results. Both turbulence models presented satisfactory results when comparing with the results from OpenFAST, for the same environmental condition investigated. However the wake internal gradient present different patterns. For the DES model it was possible to observe with higher resolution the effects of the blade in the near wake region. In addition, a different behavior of the flow that detaches along the blade span and transitions to the wake external pattern was also observed when comparing the turbulence models.*

Keywords: *NREL 5 MW Wind Turbine Rotor, Blade-resolved Simulations, Iterative PISO Solver, Turbulence Models, Computational Cost Analysis*

1. INTRODUCTION

With the continued expansion of the wind energy industry over the past decade, which aims to contribute significantly to the global energy transition, besides the increase of wind power in emerging markets such as China, India, and Brazil, the growth of wind turbines operating in offshore installations was also noticed (Council, 2022; El Bassam, 2021). Consequently, due to the development of wind energy in offshore areas, which can present outstanding wind resources (Ostachowicz *et al.*, 2016; Karimirad, 2014), the changes in the size of wind turbines to higher scales present intrinsic challenges.

The offshore sites present environmental conditions such as atmospheric boundary layer and turbulence varying spatially, which directly affects the prediction of the aerodynamic loads and wake behaviour of the wind turbines. Therefore, along with the arising of the new generation of wind turbines which include higher costs associated in both fabrication and installation process, the need of better tools to accurately predict the loads acting in the offshore wind turbines (OWT) become an important task.

Up to date, the experimental campaigns which were conducted to obtain information about the unsteady three-dimensional aerodynamic behaviour of horizontal-axis wind turbine (HAWT), such as presented by Hand *et al.* (2001a,b), have shown that the aerodynamic loads and that 3D effects are prevalent, resulting in a complex system to be accurately represented experimentally. Even though the data have been used to validate and enhance engineering models, due to the ever increasing power capacity of OWTs to scales of 3 MW, 6 MW (Hayes *et al.*, 2021), and more recently DTU 10 MW, GE's Haliade-X 14 MW, and IEA 15 MW (Bak *et al.*, 2013; Jiang, 2021; Gaertner *et al.*, 2020), the development of high fidelity numerical models capable of capturing the influence of these three-dimensional effects to better predict the OWT performance is necessary as a reliable tool in the OWT design (Hand *et al.*, 2001b; Zhang *et al.*, 2019). Among the numerical options to deal with these effects, computational fluid dynamics (CFD) has been applied through different methods, and has shown to be a mature approach to investigate the unsteady aerodynamic behaviour of the flow around wind turbine blades and generated wakes (Sanderse *et al.*, 2011; Thé and Yu, 2017).

The numerical investigations available in the literature which considered a CFD approach to investigate the flow around

a wind turbine rotor blade with a blade-resolved modeling (Sorensen and Hansen, 1998; Duque *et al.*, 1999, 2003; Zhang *et al.*, 2019) showed that the numerical solution of the Navier-Stokes (N-S) equations, which needs special treatment to proper represent the turbulence effects, still requires efforts since the solution through the direct numerical simulations (DNS) to analyse the wind turbine performance is yet not feasible.

A different approach is given by the large-eddy simulation (LES) method, in which the equations are solved taking into account a filtered velocity field, so the larger scales of the turbulent motion are represented, whereas the smaller scales of the turbulent motions, also called as subgrid-scales (SGS), are modeled (Pope, 2001; Wilcox *et al.*, 1998). As part of the turbulence modeling technique considered in the numerical investigations of engineering problems, the Reynolds-Average Navier-Stokes (RANS) procedure is vastly applied, due to the solution of the Reynolds equations which determines the mean velocity field (Pope, 2001). In sequence, the Unsteady Reynolds-Averaged Navier-Stokes (URANS) nomenclature started to be used, since the RANS models are unsteady even when considering steady boundary conditions (Spalart, 2000). In addition, as a result of this mathematical procedure, the Reynolds stress tensor requires the use of turbulence models to be evaluated (Wilcox *et al.*, 1998; Pope, 2001).

Among the ample variety of turbulence models, to represent the aerodynamic loads under the influence of considerably adverse pressure gradient, the URANS approach is commonly linked to the two-equation k-ω SST turbulence model (Menter, 1992, 1993, 1994). To date, the URANS k-ω SST turbulence model has been used in the modeling of wind turbines conducted in the OpenFOAM software for a small-scale HAWT and presented good agreement in terms of the wind turbine performance coefficient between the CFD results and the calibrated experimental tests (Rocha *et al.*, 2014).

More qualitative and quantitative agreement between the results from the CFD modeling of a similar problem, considering the same turbulence modeling and experimental tests, were found also in the prediction of the velocity profiles in the wake region in the MEXICO project (Sørensen *et al.*, 2014). More recently, the URANS k-ω SST turbulence model was successfully applied to represent the turbulence effects in the numerical modeling of the NREL 5 MW wind turbine in full scale, including the tower influence, to represent the flow around the blades and in the wake region. Since there was no experimental data available, the authors conducted a verification procedure benchmarking the blade-resolved results against the results obtained with the OpenFAST software for the same environmental conditions, and presented good agreement in terms of the power production, generated thrust and distributed forces along the blade span (de Oliveira *et al.*, 2022).

Usually, the preference for URANS-based models instead of LES or DNS approaches is related to the computational costs which is largely determined by the resolution requirements (Pope, 2001). Even though LES is advantageous when comparing to URANS in the modeling of anisotropic turbulent flow, in which large-scale structures are dominant, in the numerical analysis of the flow around wind turbines, the model is recommended to be applied only in the wake region (Sanderse *et al.*, 2011), due to the fact that the LES approach present difficulties to determine the flow properties in the wall region of the boundary layer (Wilcox *et al.*, 1998; Spalart, 2000).

In this regard, since LES even when implemented with a proper wall-region modeling is not viable to predict unsteady aerodynamic loads (Spalart, 1997), the hybridization of LES into a improved approach such as the Detached-Eddy Simulation (DES) model allow the numerical modeling of the turbulence effects to a manageable computational demand even for flows at high Reynolds numbers (Shur *et al.*, 1999; Nikitin *et al.*, 2000; Spalart, 1997).

Whereas the application of DES in aerodynamics is promising due to the possibility of applying the URANS-based models in the large areas of the boundary layer while in the regions in which the momentum transfer is dominated by large structures LES is efficiently applied (Spalart, 2000), few investigations have implemented the DES approach in the blade-resolved CFD simulations of a megawatt scale wind turbine, due the difficulties of proper connecting the numerical model setup with the more suitable spatial and temporal discretization. For example, in the investigations performed by Lawson *et al.* (2019), the authors used DES to represent the flow around the NREL 5 MW wind turbine blades and wake region. However, the quasi-steady regime for the power and thrust, which typically requires around 5-6 rotor revolutions to be established, was not achieved even for the coarsest mesh tested, due to the mesh strategy employed, which presented a high computational demand, indicating that more efforts were still required to better comprehend the efficiency of the method when comparing the results accuracy and computational costs.

With the increase in the wind turbines scale such as 15 MW, the numerical modeling in full scale becomes even more challenging, and the need of a optimized turbulent model to represent the unsteady aerodynamics load more evident. Therefore, in order to cover these needs, the target of this paper is to present a comparison between the URANS k-ω SST and DES-two equations turbulence models applied in the blade-resolved CFD simulations to adequately predict the aerodynamic loads of the baseline NREL 5 MW wind turbine rotor in full scale (Jonkman *et al.*, 2009), under the operating condition of optimal wind-power conversion efficiency.

Since these simulations are computationally expensive and challenging to set up the turbulence model properly, in the present investigation we are not taking into account the tower influence, nevertheless we hope the discussion and results presented in the next sections regarding the rotor-only investigation, considering different turbulence models, can be used to help in the modeling and simulation of other large wind turbines.

2. METHODOLOGY

To conduct the numerical investigations and capture the effects of the different turbulence models tested, we considered the same numerical discretization schemes and also the same spatial and temporal discretization strategies for each case. The investigations were carried out considering the open source OpenFOAM software and the performance of the wind turbine rotor-only simulations was evaluated in terms of power production, generated thrust, distributed forces along the blade span and wind profile in different positions in the wake region. As a verification procedure, the CFD results were benchmarked against the results obtained with OpenFAST (National Renewable Energy Laboratory, 2021), which implements the blade element momentum method, considering the same NREL 5 MW wind turbine rotor-only, at the same environmental conditions. Finally a computational cost analysis was conducted between the two different turbulence models to allow us to understand the performance of each one considering the numerical arrangement chosen.

In this section we describe the governing equations considered to model the problem and also some details about the solver parameters and discretizations schemes employed in the CFD investigation.

2.1 Governing Equations

As the problem being investigated is represented by a transient three-dimensional incompressible flow, the governing set of equations is given respectively by the conservation of mass and conservation of momentum equations, as:

$$\nabla \cdot \mathbf{U} = 0, \tag{1}$$

$$\frac{\partial \mathbf{U}}{\partial t} + \nabla \cdot (\mathbf{U}\mathbf{U}) = -\nabla p + \nabla \cdot (\nu \nabla \mathbf{U}) + \mathbf{f}, \tag{2}$$

where t is time, ν is the kinematic viscosity, $\mathbf{U}$ is the velocity vector, p is the kinematic pressure and $\mathbf{f}$ represents the body forces.

In this work we discretize the governing equation given by Eqs. 1 and 2 considering the finite volume method (FVM) in which detailed information can be found in Versteeg and Malalasekera (2007); Patankar (2018). In this regard, the discretization of the non-linear term given by the convective term in Eq. (2) leads to

$$\nabla \cdot (\mathbf{U}\mathbf{U}) = \sum_f \mathbf{S}(\mathbf{U}_f)(\mathbf{U}_f) = \sum_f F(\mathbf{U}_f), \tag{3}$$

$$\nabla \cdot (\mathbf{U}\mathbf{U}) = a_P \mathbf{U}_P + \sum_N a_N \mathbf{U}_N, \tag{4}$$

where the coefficients a_P and a_N are related to the values interpolated at the faces of the control volume P and its neighbors indicated by N, and are functions of the velocity $\mathbf{U}$. $\mathbf{U}_f$ is the control volume velocity at the face cell, and $\mathbf{S}$ is the area vector pointing out of the volume cell with magnitude equal to the face area, while F represents the term $\mathbf{S} \cdot (\rho U)_f$, which is the mass flux through a general face.

Due to the complexity of the non-linear solvers and consequent computation effort required, a linearisation of the convective term is recommended. Considering the type of flow being investigated, the calculation of the F term is performed using a numerical upwind-based method, to guarantee the boundedness of the solution by preserving positive coefficients in the linear algebraic equation matrices (Jasak, 1996; Versteeg and Malalasekera, 2007).

The discretized form of the continuity equation, Eq. (1), is given by

$$\nabla \cdot \mathbf{U} = \sum_f \mathbf{S}\mathbf{U}_f = 0. \tag{5}$$

More details about the step-by-step in the discretization process by the FVM can be found in de Oliveira *et al.* (2022); Versteeg and Malalasekera (2007). Therefore, the discretized form of the incompressible Navier-Stokes equations are given by

$$a_P \mathbf{U}_P = \mathbf{H}(\mathbf{U}) - \sum_f \mathbf{S}(p)_f, \tag{6}$$

$$\sum_f \mathbf{S}\Big[\Big(\frac{1}{a_P}\Big)_f (\nabla p)_f\Big] = \sum_f \mathbf{S}\Big(\frac{\mathbf{H}(\mathbf{U})}{a_P}\Big)_f, \tag{7}$$

with the calculation of the face fluxes F given by

$$F = \mathbf{S}\mathbf{U}_f = \mathbf{S}\Big[\Big(\frac{\mathbf{H}(\mathbf{U})}{a_P}\Big)_f - \Big(\frac{1}{a_P}\Big)_f (\nabla p)_f\Big]. \tag{8}$$

2.2 Turbulence Modeling

To complete the numerical arrangement to conduct the blade-resolved CFD simulations, an additional set of transport equations to represent the turbulence are required in order to obtain an approximate solution for the Navier-Stokes set of equations. According to Wilcox *et al.* (1998), an ideal turbulence model should minimize the complexity of the flow field in order to capture the features of the most significant part of the physical system. As aforementioned mentioned in the section 1, the main objective of our work is to compare different turbulence modeling approaches in the blade-resolved simulation of a megawatt scale wind turbine rotor, focusing on the estimate of the rotor performance through the prediction of the power production, generated thrust, distributed forces along the blades, wind profile at different positions of the wake region and the comparison of the flow structures obtained by each approach.

Even though the URANS method along with the two-equations k-ω SST turbulence model is the most common and vastly used method to represent the physics of similar investigation (Rocha *et al.*, 2014; Sorensen and Hansen, 1998; Robertson *et al.*, 2015; de Oliveira *et al.*, 2022), with the increase in the wind turbine scale to cover the offshore application needs, the DES model has been put forward as a promising solution since it improves the accuracy of the results prediction, with less computational cost than LES (Zhang *et al.*, 2015).

2.2.1 URANS k-ω SST Approach

The URANS approach comes from a statistical averaging procedure applied to the Navier-Stokes equations, from which the nonlinear Reynolds stresses tensor term and consequent closure problem arise requiring the turbulence models to establish a sufficient number of equations to solve all the flow properties (Wilcox *et al.*, 1998; Pope, 2001).

One way to obtain a solution for the Reynolds stresses tensor in means of known quantities is using the mean velocity gradient. In this regard, the most popular approach is to use the turbulent-viscosity hypothesis, introduced by Boussinesq (Pope, 1975) which, according to the hypothesis, the deviatoric part of the Reynolds stress tensor is proportional to the mean rate of strain (Pope, 2001).

Therefore, the relation between the turbulent tensor and the turbulent viscosity, also called as eddy viscosity, imposes the idea that the transfer of momentum by diffusion in molecular level is similar to the transfer of momentum in a turbulent flow due to the turbulent fluctuations. The evaluation of the kinematic eddy viscosity, ν_t, can be made by solving the transport equations with the use of auxiliary relations. However, the most common method to obtain the kinematic eddy viscosity is considering a function which correlates it with the specific turbulent kinetic energy and its specific dissipation rate, such approach stands out for the so called two-equations turbulent model (Wilcox *et al.*, 1998; Pope, 2001).

In this work for the URANS turbulence modeling approach we employed the two-equations k-ω SST model from Menter (1994), due its ability of predict flows with strong adverse pressure gradient with higher performance when compared to the variation of the k-ω models from Wilcox *et al.* (1998), and the baseline from Menter (1993). Thus, by considering the k-ω SST model, a new set of governing equations is obtained. In the flow region close to the rotor walls, low-Reynolds corrections are applied due to the near-wall region treatment.

2.2.2 DES k-ω SST Approach

According to Spalart (2000), the limitations of the RANS approach to represent the physics in the boundary layer region relies in the outer region, where LES captures well the straining, cross-flow and curvature effects, although with a considerable computational demand over RANS. Therefore, by thanking into account the idea of entrust the RANS approach in the attached eddies region of the boundary layer, which refers to the region close to the walls, while LES is applied in the separated region, also called as the detached eddies region, the hybridization of the LES and RANS models brings out the DES hybrid approach (Spalart, 1997). In addition, DES is an attractive solution for external flows, since the model is simple to be implemented, and preset stability for both URANS turbulence models, such as, one and two-equations (Robertson *et al.*, 2015). However, the main challenge in the use of DES model is regarding the user skills in the determination of a suitable mesh resolution (Spalart, 1997).

Therefore, based on the results obtained by the authors in previous investigations about the blade-resolved simulations of the NREL 5 MW wind turbine, including the tower interference (de Oliveira *et al.*, 2022), we designed a strategical spatial discretization, in order to capture the influence of the hybrid model over the RANS model in terms of the results accuracy and less computational demand, to be able to perform blade-resolved simulations of a megawatt scale wind turbine rotor with a more robust turbulence model. Thus, we employed for DES the same turbulence model used for the URANS approach model, the k-ω SST turbulence model, which is also the reason the approach is called as DES 2-Equations.

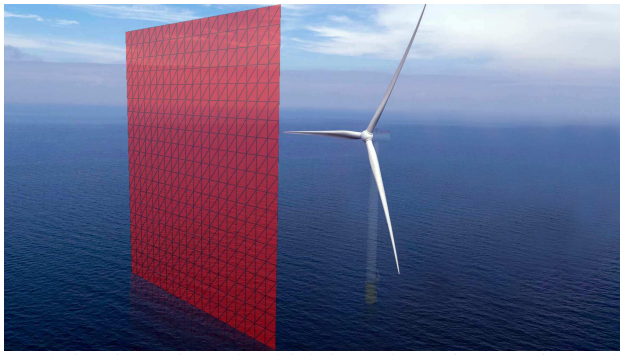

Figure 1: Visualization of the case being investigated, which includes a 5 MW wind turbine rotor in full scale, (without the tower an nacelle parts,) operating under a uniform non-turbulent wind profile.

2.3 Near-wall region treatment

As well mentioned in the previous section, the features of the turbulent flow changes considerably by getting closer to the wall region, in which an appropriated model is required for the estimation of the kinematic eddy viscosity ν_t. Thus, a strategical mesh refinement must be considered to estimate the turbulent flow close to the wall, which must satisfy the requirement of the turbulence model based on the y^+ variable. In the current investigations, for both turbulence models being investigated, k and ω were modeled by the low Reynolds wall functions, which represents a model which can switch between the viscous and logarithmic regions of the boundary layer according to the position of y^+, and also avoid the buffer layer region at the same time.

Following the same methodology, the kinematic eddy viscosity ν_t was calculated using the Spalding wall function model (Spalding, 1961), which can also switch between viscous and logarithmic regions based on the value of y^+.

3. NUMERICAL SIMULATIONS

In this section the setup and parameters considered in each numerical investigations are presented. The main objective of the CFD simulations were to predict the performance of the NREL baseline 5 MW offshore wind turbine rotor in full scale, in terms of power production, generated thrust, blade loading and wake aerodynamics pattern analysis considering two different turbulence models. The rotor geometry in full scale is composed by three blades and the hub, more detailed information regarding the rotor design are available in Jonkman *et al.* (2009).

Fig. 1 illustrates the case being investigated, which consists of a 5 MW wind turbine rotor for offshore application (without the tower interference), placed on an site of operation, under the influence of a uniform non-turbulent wind profile.

The simplifications which were made in the case being modeled, such as, the consideration of a uniform wind profile and the absence of the tower and nacelle parts in the wind turbine geometry, are typical of rotor-only CFD investigations (Duque *et al.*, 1999, 2003; Zhang *et al.*, 2019).

3.1 Computational Domain and Boundary Conditions

The rotor and hub geometries were built using the software Solid Edge and imported into OpenFOAM, whereas all other parts of the computational domain were built around the rotor geometry using the snappyHexMesh utility. Fig. 2 illustrates the computational domain dimensions in meters and the boundary conditions, which were defined based in Hsu and Bazilevs (2012); de Oliveira *et al.* (2022).

For both turbulence model investigation, the dimensions of the computational domain were the same, $480\,\mathrm{m}$ wide, $640\,\mathrm{m}$ long, $480\,\mathrm{m}$ high, and the rotor region of $160\,\mathrm{m}$ to settle the rotor diameter which is considered as $124\,\mathrm{m}$ to take into account the hub distance between the blades. The same boundary conditions were also considered in the turbulence models investigation for both cases, in which for the inflow the boundary condition for the velocity was of Dirichlet type, given by a prescribed uniform wind profile of 10 m/s, which was chosen based on Jonkman *et al.* (2009). According to the authors, at this wind speed the rotor operates in optimal wind-power conversion efficiency. Still at the inflow, the boundary condition for the pressure was a null gradient (Neumann condition). For the turbulent quantities, Dirichlet conditions were employed, with prescribed values estimated based on the most critical Reynolds number (at the blade tip), through the turbulence Reynolds number parameter (Re_L) as suggested by Pope (2001). Based on that, the turbulence length scale for this region was 0.175 m, the turbulence kinetic energy $k = 3.2651\,\mathrm{m^2 s^{-2}}$, and the dissipation rate, $\omega = 20.5649\,\mathrm{s^{-1}}$, while the kinematic eddy viscosity was calculated based on the internal field everywhere. As the wind profile is uniform for all the side walls, the boundary conditions for the velocity were symmetric plane condition, which corresponds to null normal velocity and zero normal gradient for the tangential velocity, pressure and turbulent quantities. For the rotor walls,

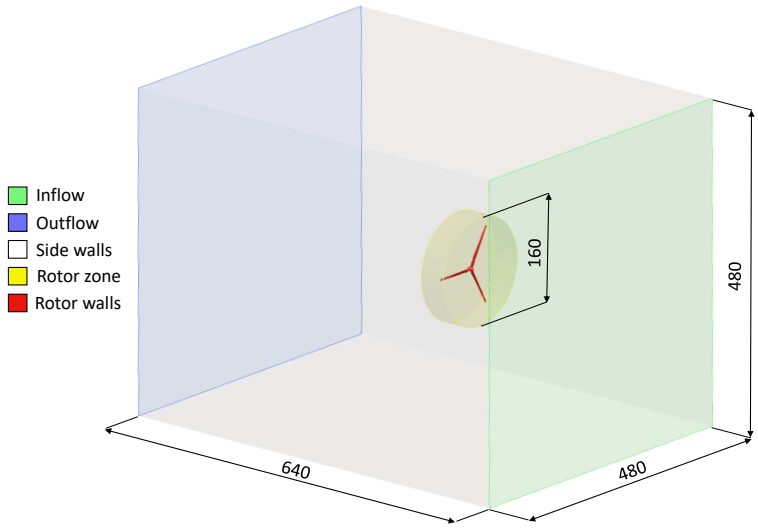

Figure 2: NREL baseline 5 MW offshore wind turbine rotor, computational domain dimensions (in meters) and boundary conditions.

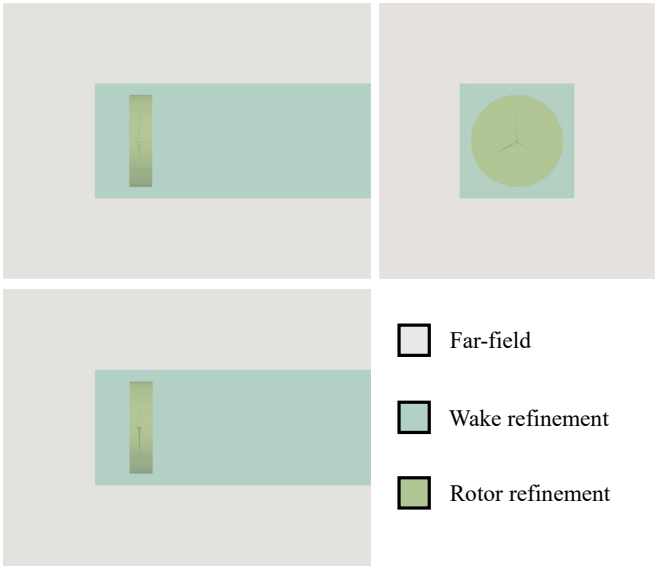

Figure 3: Strategic partition of the computational domain to apply different mesh refinements.

no slip condition was imposed. Since the mesh around this region is dynamic, a uniform rotor velocity of 1.1649 rad/s was prescribed, which is the rotor speed for a wind speed of 10 m/s, and Neumann boundary condition is applied for the pressure as a null gradient, while the turbulence properties receive the proper wall function treatment according with the y^+ value in the near wall region. At the outflow, Dirichlet condition was applied for the pressure as a fixed value equal to zero, and for the velocity and turbulence quantities had Neumann condition as null gradient.

3.2 Spatial discretization

To perform the turbulence model investigation, for both blade-resolved simulations the same spatial discretization were considered. The mesh was built considering a strategy similar to the one which was employed by de Oliveira *et al.* (2022) in Mesh-2, since it was adequate to present both accuracy in the predicted results at a accessible computational cost. One of the most important steps during the mesh design is related with the division of the the computational domain in which the different stages of refinement are applied.

In this regard, for the mesh being used in the present investigations, the computational domain was decomposed in three main regions as presented in Fig. 3, where in the far-field region the finite volume cells are of the size of $25\,\mathrm{m}$ which decreases into $1.6\,\mathrm{m}$ in the wake region and to $0.5\,\mathrm{m}$ in the rotor region. In the rotor region the cells size are refined from $0.5\,\mathrm{m}$ to $0.0625\,\mathrm{m}$ close to the blades and into $0.001\,\mathrm{m}$ at the first cell attached to the blades wall in order to respect the y^+ parameter within the adequate range for the application of the turbulence model at the near-wall region.

Regarding the mesh communication between the static and dynamic parts of the mesh, an arbitrary mesh interface (AMI) methodology was considered based in (Farrell and Maddison, 2011). Therefore, the spatial discretization strategy applied resulted in a mesh composed by $25,314,125$ finite volume cells, with a maximum aspect ratio of 75, skewness of 3.9 and non-orthogonality of 64.4.

3.3 Numerical schemes

The same numerical arrangement regarding the discretization schemes were employed for both turbulence models. The divergence terms were discretized using a second-order upwind scheme, chosen based on the modeling of similar problems to compute the convective fluxes. Central differences were employed for the Laplacian terms, and the second order Gauss scheme was adopted with linear Gaussian integration for the gradient terms. The set of linear equations was solved based on Muratova *et al.* (2020); Moukalled *et al.* (2016), using the geometric-algebraic multi-grid (GAMG) algorithm for the symmetric matrices, and the preconditioned bi-conjugate gradient (PBiCG) with the DILU preconditioner for the non-symmetric matrices.

Regarding the temporal discretization, the second order implicit backward scheme was employed, along with the limited CFL number equal to 1, which was controlled by an adaptive time step to guarantee stability during the iterative process.

3.4 Solver information

The iterative PISO with face flux correction, as presented in (de Oliveira *et al.*, 2022), was chosen as solver, in which 5 sub-iterations and 2 corrections for pressure was performed in each time step for both turbulence models being considered. For both DES and URANS turbulence models, the solution was considered converged when the residuals of the set of estimated variables was equal or less than 10^{-6} based in the convergence parameters for transient problems suggest by Versteeg and Malalasekera (2007). For each case, the initial conditions for the transient problem for all properties were obtained considering the steady state solution for the problem after 500 iterations, calculated with the steady form of the SIMPLE algorithm solver. The computations were carried out in the Brazilian supercomputer SDumont. To run the simulations, in each case the mesh was partitioned into 240 sub-domains using scotch decomposition, using 10 nodes, where each node had two 12 core Intel Xeon Cascade Lake Gold 6252 processors, 3.7 GHz, and 256 Gb of RAM.

4. RESULTS AND DISCUSSION

First, the results obtained by the two different turbulence models are presented in terms of power production and generated thrust. Next, a comparison between the computations of the distributed normal and tangential forces are presented. In sequence, the flow pattern and the vortical structures captured by the URANS and DES are illustrated along with the analysis of the wind velocity profile at different positions of the wake region. Finally, a comparison in terms of computational cost is shown in order to understand the performance of each turbulence model considered in the blade-resolved simulations to predict the unsteady aerodynamic loads of a megawatt scale wind turbine rotor.

4.1 Verification with OpenFAST

In order to understand the accuracy in the obtained results by the CFD simulations, the verification and validation are the main recommended methods to quantify the errors and uncertainties (Versteeg and Malalasekera, 2007). However, in our case there is no experimental data available, so we performed a verification procedure by making a comparison between the results obtained with each turbulence model against the results obtained with a different numerical method for the same environmental conditions, which was the OpenFAST v2.5.0 code by NREL (National Renewable Energy Laboratory, 2021). OpenFAST is a code certified by Germanischer Lloyd (GL) National Renewable Energy Laboratory (2005), and calibrated by Coulling *et al.* (2013), which uses the blade element momentum theory and tip corrections to calculate the aerodynamic loads of three-bladed HAWT, including different environmental conditions in the time domain.

Figure 4 illustrates a comparison of the wind turbine power production and the generated thrust for both turbulence models tested, the DES 2-Equations, and the URANS $k-\omega$ SST. Both turbulence models presented similar results in terms of integral power and thrust. The mean value for the power was of 3.75 MW by DES and 3.53 MW by the URANS model, while for the thrust the mean value was of 635 kN, 624.6 kN for both DES and URANS respectively. This similarity between in results by boh turbulence models were also obtained by (Mittal *et al.*, 2016) for a comparable CFD simulation, where the author investigated the same turbulence models for a reduced scale wind turbine. Probably the similarity in the performance results is due to the modeling of the region close to the blades wall, since both turbulence models solve the same equations.

In addition, the distribution of the mean forces along the blades were also investigated and compared. As presented in Fig. 5, both methodologies presented similar behaviour in the normal and tangential forces prediction along the blade span, for the positions of the blade being analyzed. The 0° azimuth angle represents the blade aligned in the z-direction

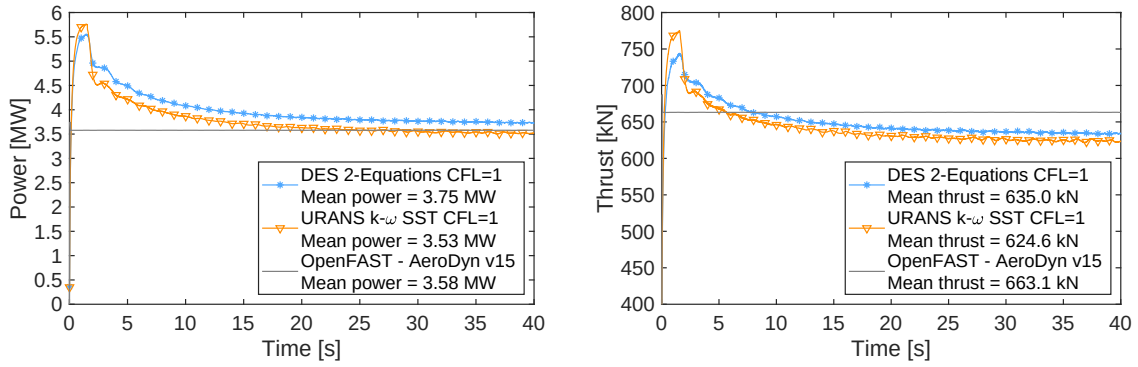

(a) Power. (b) Thrust.

Figure 4: Generated power and thrust comparison between the DES 2-Equations and URANS $k-\omega$ SST turbulence models, benchmarked against OpenFAST results.

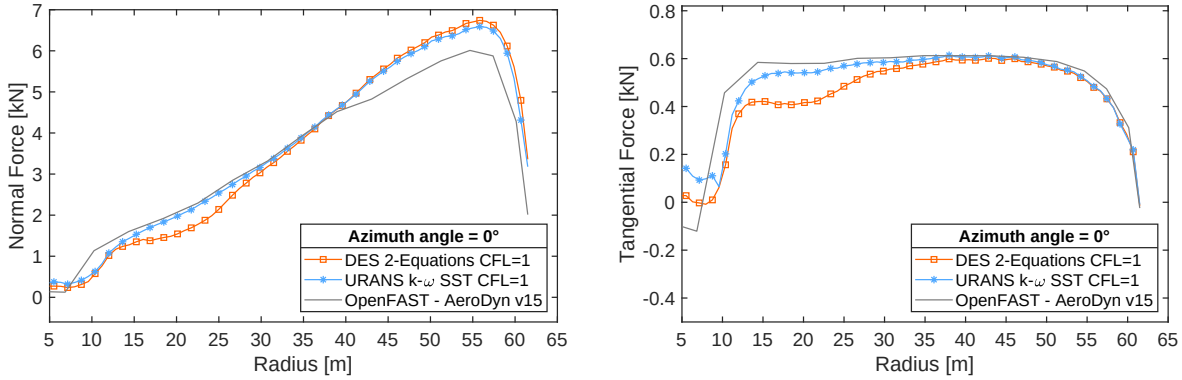

(a) Normal Force. (b) Tangential Force.

Figure 5: Distributed forces along the blade span comparison between the DES 2-Equations and URANS $k-\omega$ SST turbulence models, benchmarked against OpenFAST results.

orthogonal with the flow in the x-direction. The agreement between the results is remarkable.

Besides the quantitative analyses of the normal and tangential forces acting on the blades, we performed a comparison about the instantaneous wind velocity profiles after 7 complete revolution at 5 different positions downstream in the wake region. These results are presented in Fig. 6 along with the instantaneous iso-contours of the mean velocity field for both turbulence models being investigated considering approximately the last 20 seconds of the simulation. It is possible to observe that both turbulence approach led to similar results in terms of the mean velocity field properties. However, differences in the flow pattern ca also be observed in all positions of the wake region.

A computational cost analysis considering the performance of each of the tested turbulence models showed that both approaches took approximated 24 hours to complete the simulation of one time unit. However, the execution time to calculate one time step was on average 18.38 s for the DES 2-Equations, against 18.83 s for the URANS $k-\omega$ SST. Therefore, considering the computational cost comparison, the performance of DES $k-\omega$ SST model was slightly better over the URANS $k-\omega$ SST.

5. CONCLUSIONS

A numerical investigation about the performance of a 5 MW wind turbine rotor was conducted considering for the same numerical arrangement two difference turbulence models, one vastly applied in the investigation of similar blade-resolved simulations, and another yet being implemented in the simulations of the new generation of wind turbines modeled in its full scale. In this paper, the rotor-only blade-resolved simulations were performed considering the NREL 5 MW reference wind turbine for offshore applications. The CFD simulations provided significant data from which the performance of the NREL 5 MW offshore wind turbine rotor in full scale was evaluated, in terms of, power production, generated thrust, blade loading and wake aerodynamics pattern analysis considering the two different turbulence models tested.

In terms of the computations of the power production, generated thrust and distributed mean tangential and normal forces along the blade span, both turbulence models presented similar and satisfactory results. However significant amount

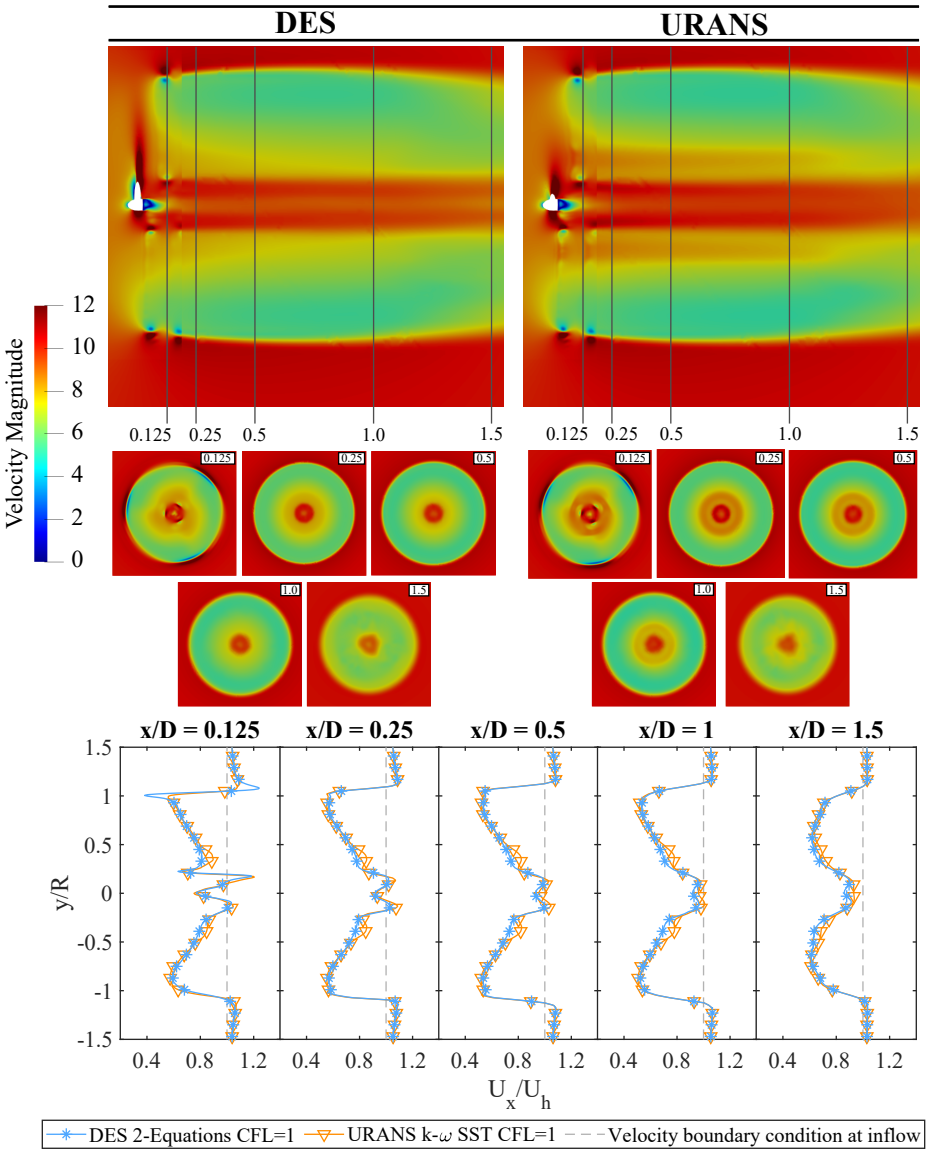

Figure 6: Comparison of the instantaneous wind velocity profiles after 7 complete rotor revolutions at 5 x/D different positions downstream in the wake region along with the iso-contours of the mean velocity field at the same positions for both turbulence models being investigated.

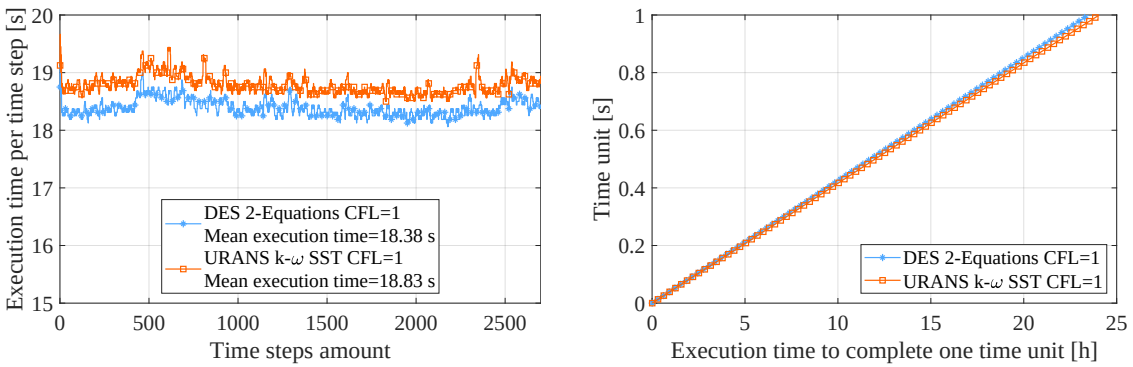

(a) Execution time per time step.

(b) Execution time to complete one time unit of simulation.

Figure 7: Computational demand comparison between the DES 2-Equations and URANS $k-\omega$ SST turbulence models.

of flow structures with indicated with higher definition the flow behaviour were captured considering the DES $k-\omega$ SST over RANS $k-\omega$ SST with less computational demand, becoming an attractive solution to be implemented in the modeling of the new generation of larger wind turbines.

6. ACKNOWLEDGEMENTS

M. de Oliveira acknowledges FAPESP (Fundação de Amparo à Pesquisa do Estado de São Paulo), the São Paulo Research Foundation, for the PhD grant - Process number 2018/26207-4. R. C. Puraca acknowledges FUSP/Petrobras for the PhD grant Project number 2019/00171-6. B. S. Carmo acknowledges the support from FAPESP, Proc. 2019/01507-8, for this research, and thanks the Brazilian National Council for Scientific and Technological Development (CNPq) for financial support in the form of a productivity grant, number 312951/2018-3. The authors also acknowledge the grant from the National Laboratory of Scientific Computing (LNCC), CADASE project, which allowed the use of the Santos Dumont supercomputer to run the simulations that generated the results reported in this paper. This work is part of the European Commission Project "High Performance Computing for Wind Energy (HPCWE)" with agreement no. 828799.

7. REFERENCES

Bak, C., Zahle, F., Bitsche, R., Kim, T., Yde, A., Henriksen, L.C., Hansen, M.H., Blasques, J.P.A.A., Gaunaa, M. and Natarajan, A., 2013. "The dtu 10-mw reference wind turbine". In *Danish wind power research 2013*.

Coulling, A.J., Goupee, A.J., Robertson, A.N., Jonkman, J.M. and Dagher, H.J., 2013. "Validation of a fast semi-submersible floating wind turbine numerical model with deepcwind test data". *Journal of Renewable and Sustainable Energy*, Vol. 5, No. 2, p. 023116.

Council, G.W.E., 2022. "Gwec| global wind report 2022". *Global Wind Energy Council: Brussels, Belgium*.

de Oliveira, M., Puraca, R.C. and Carmo, B.S., 2022. "Blade-resolved numerical simulations of the NREL offshore 5 MW baseline wind turbine in full scale: A study of proper solver configuration and discretization strategies". *Energy*, p. 124368.

Duque, E., Van Dam, C. and Hughes, S., 1999. "Navier-stokes simulations of the nrel combined experiment phase ii rotor". In *37th Aerospace Sciences Meeting and Exhibit*. p. 37.

Duque, E.P., Burklund, M.D. and Johnson, W., 2003. "Navier-stokes and comprehensive analysis performance predictions of the nrel phase vi experiment". *J. Sol. Energy Eng.*, Vol. 125, No. 4, pp. 457–467.

El Bassam, N., 2021. "Wind energy". In *Distributed Renewable Energies for Off-Grid Communities*, Elsevier, pp. 149–163.

Farrell, P.E. and Maddison, J.R., 2011. "Conservative interpolation between volume meshes by local Galerkin projection". *Computer Methods in Applied Mechanics and Engineering*, Vol. 200, pp. 89–100. doi:10.1016/j.cma.2010.07.015.

Gaertner, E., Rinker, J., Sethuraman, L., Zahle, F., Anderson, B., Barter, G.E., Abbas, N.J., Meng, F., Bortolotti, P., Skrzypinski, W. *et al.*, 2020. "Iea wind tcp task 37: definition of the iea 15-megawatt offshore reference wind turbine". Technical report, National Renewable Energy Lab.(NREL), Golden, CO (United States).

Hand, M.M., Simms, D.A., Fingersh, L.J., Jager, D.W. and Cotrell, J.R., 2001a. "Unsteady aerodynamics experiment phase v: Test configuration and available data campaigns". Technical report, NREL. doi:10.2172/787980. URL `https://www.osti.gov/biblio/787980`.

Hand, M.M., Simms, D.A., Fingersh, L.J., Jager, D.W., Cotrell, J.R., Schreck, S. and Larwood, S.M., 2001b. "Unsteady aerodynamics experiment phase vi: Wind tunnel test configurations and available data campaigns". Technical report, NREL. doi:10.2172/15000240. URL `https://www.osti.gov/biblio/15000240`.

Hayes, L., Stocks, M. and Blakers, A., 2021. "Accurate long-term power generation model for offshore wind farms in europe using era5 reanalysis". *Energy*, Vol. 229, p. 120603.

Hsu, M.C. and Bazilevs, Y., 2012. "Fluid–structure interaction modeling of wind turbines: simulating the full machine". *Computational Mechanics*, Vol. 50, No. 6, pp. 821–833.

Jasak, H., 1996. *Error analysis and estimation for the finite volume method with applications to fluid flows.* Ph.D. thesis, Imperial College London (University of London).

Jiang, Z., 2021. "Installation of offshore wind turbines: A technical review". *Renewable and Sustainable Energy Reviews*, Vol. 139, p. 110576.

Jonkman, J., Butterfield, S., Musial, W. and Scott, G., 2009. "Definition of a 5-mw reference wind turbine for offshore system development". Technical report, National Renewable Energy Lab.(NREL), Golden, CO (United States).

Karimirad, M., 2014. *Offshore energy structures: for wind power, wave energy and hybrid marine platforms*. Springer.

Lawson, M.J., Melvin, J., Ananthan, S., Gruchalla, K.M., Rood, J.S. and Sprague, M.A., 2019. "Blade-resolved, single-turbine simulations under atmospheric flow". Technical report, National Renewable Energy Lab.(NREL), Golden, CO (United States).

Menter, F.R., 1992. "Improved two-equation k-omega turbulence models for aerodynamic flows". Technical report, NASA Ames.

Menter, F.R., 1994. "Two-equation eddy-viscosity turbulence models for engineering applications". *AIAA journal*, Vol. 32, No. 8, pp. 1598–1605.

Menter, F., 1993. "Zonal two equation kw turbulence models for aerodynamic flows". In *23rd fluid dynamics, plasmadynamics, and lasers conference*. p. 2906.

Mittal, A., Sreenivas, K., Taylor, L.K., Hereth, L. and Hilbert, C.B., 2016. "Blade-resolved simulations of a model wind turbine: effect of temporal convergence". *Wind Energy*, Vol. 19, No. 10, pp. 1761–1783.

Moukalled, F., Mangani, L., Darwish, M. *et al.*, 2016. *The finite volume method in computational fluid dynamics*, Vol. 113. Springer.

Muratova, G., Martynova, T., Andreeva, E., Bavin, V. and Wang, Z.Q., 2020. "Numerical solution of the navier–stokes equations using multigrid methods with hss-based and sts-based smoothers". *Symmetry*, Vol. 12, No. 2, p. 233.

National Renewable Energy Laboratory, 2005. "Wind turbine design codes certified". URL `https://www.nrel.gov/news/press/2005/357.html`. (accessed: 10.01.2022).

National Renewable Energy Laboratory, 2021. "Openfast documentation". URL `https://github.com/openfast`. (accessed: 17.08.2021).

Nikitin, N., Nicoud, F., Wasistho, B., Squires, K. and Spalart, P.R., 2000. "An approach to wall modeling in large-eddy simulations". *Physics of fluids*, Vol. 12, No. 7, pp. 1629–1632.

Ostachowicz, W., McGugan, M., Schröder-Hinrichs, J.U. and Luczak, M., 2016. *MARE-WINT: new materials and reliability in offshore wind turbine technology*. Springer Nature.

Patankar, S.V., 2018. *Numerical heat transfer and fluid flow*. CRC press.

Pope, S., 1975. "A more general effective-viscosity hypothesis". *Journal of Fluid Mechanics*, Vol. 72, No. 2, pp. 331–340.

Pope, S.B., 2001. "Turbulent flows".

Robertson, E., Choudhury, V., Bhushan, S. and Walters, D.K., 2015. "Validation of openfoam numerical methods and turbulence models for incompressible bluff body flows". *Computers & Fluids*, Vol. 123, pp. 122–145.

Rocha, P.C., Rocha, H.B., Carneiro, F.M., da Silva, M.V. and Bueno, A.V., 2014. "k–ω sst (shear stress transport) turbulence model calibration: A case study on a small scale horizontal axis wind turbine". *Energy*, Vol. 65, pp. 412–418.

Sanderse, B., Van der Pijl, S. and Koren, B., 2011. "Review of computational fluid dynamics for wind turbine wake aerodynamics". *Wind energy*, Vol. 14, No. 7, pp. 799–819.

Shur, M., Spalart, P., Strelets, M. and Travin, A., 1999. "Detached-eddy simulation of an airfoil at high angle of attack". In *Engineering turbulence modelling and experiments 4*, Elsevier, pp. 669–678.

Sorensen, N. and Hansen, M., 1998. "Rotor performance predictions using a navier-stokes method". In *1998 ASME Wind Energy Symposium*. p. 25.

Sørensen, N.N., Bechmann, A., Réthoré, P.E. and Zahle, F., 2014. "Near wake reynolds-averaged navier–stokes predictions of the wake behind the mexico rotor in axial and yawed flow conditions". *Wind Energy*, Vol. 17, No. 1, pp. 75–86.

Spalart, P.R., 1997. "Comments on the feasibility of les for wings, and on a hybrid rans/les approach". In *Proceedings of first AFOSR international conference on DNS/LES*. Greyden Press.

Spalart, P.R., 2000. "Strategies for turbulence modelling and simulations". *International journal of heat and fluid flow*, Vol. 21, No. 3, pp. 252–263.

Spalding, D., 1961. "Mass transfer through laminar boundary layers—1. the velocity boundary layer". *International Journal of Heat and Mass Transfer*, Vol. 2, No. 1-2, pp. 15–32.

Thé, J. and Yu, H., 2017. "A critical review on the simulations of wind turbine aerodynamics focusing on hybrid rans-les methods". *Energy*, Vol. 138, pp. 257–289.

Versteeg, H.K. and Malalasekera, W., 2007. *An introduction to computational fluid dynamics: the finite volume method*. Pearson education.

Wilcox, D.C. *et al.*, 1998. *Turbulence modeling for CFD*, Vol. 2. DCW industries La Canada, CA.

Zhang, Y., Deng, S. and Wang, X., 2019. "Rans and ddes simulations of a horizontal-axis wind turbine under stalled flow condition using openfoam". *Energy*, Vol. 167, pp. 1155–1163.

Zhang, Y., van Zuijlen, A. and van Bussel, G., 2015. "Massively separated turbulent flow simulation around non-rotating mexico blade by means of rans and ddes approaches in openfoam". In *33rd AIAA Applied Aerodynamics Conference*. p. 2716.

8. RESPONSIBILITY NOTICE

The authors are the only responsible for the printed material included in this paper.